

# Improving the seismic response of masonry piers with single sided FRCM coating using Innovative clamping details

---

**Hafner, Ivan**

**Doctoral thesis / Disertacija**

**2024**

*Degree Grantor / Ustanova koja je dodijelila akademski / stručni stupanj:* **University of Zagreb, Faculty of Civil Engineering / Sveučilište u Zagrebu, Građevinski fakultet**

*Permanent link / Trajna poveznica:* <https://um.nsk.hr/um:nbn:hr:237:718685>

*Rights / Prava:* [In copyright](#)/[Zaštićeno autorskim pravom.](#)

*Download date / Datum preuzimanja:* **2024-06-25**

*Repository / Repozitorij:*

[Repository of the Faculty of Civil Engineering,  
University of Zagreb](#)





University of Zagreb

Faculty of Civil Engineering

Ivan Hafner

**IMPROVING THE SEISMIC RESPONSE  
OF MASONRY PIERS WITH SINGLE  
SIDED FRCM COATING USING  
INNOVATIVE CLAMPING DETAILS**

DOCTORAL DISSERTATION

Supervisor:

prof. dr. sc. Tomislav Kišiček

Zagreb, 2024.



Sveučilište u Zagrebu

Građevinski fakultet

Ivan Hafner

**UNAPRJEĐENJE POTRESNOGA  
ODGOVORA ZIDA S JEDNOSTRANIM  
FRCM POJAČANJEM POMOĆU  
INOVATIVNOGA DETALJA  
PRIHVAĆANJA**

DOKTORSKI RAD

Mentor:

prof. dr. sc. Tomislav Kišiček

Zagreb, 2024.

## **DECLARATION OF ORIGINALITY**

I declare that my thesis is the original result of my work and that I have used no sources other than those indicated in the thesis.

## **IZJAVA O IZVORNOSTI**

Izjavljujem da je moj doktorski rad izvorni rezultat mojeg rada te da se u izradi istoga nisam koristio drugim izvorima osim onih koji su u njemu navedeni.

---

Ivan Hafner, mag.ing.aedif.

## **INFORMATION ABOUT THE MENTOR**

Tomislav Kišiček has been employed at the University of Zagreb, Faculty of Civil Engineering, since 1997. Currently, he holds the position of a tenured Full Professor at the Department of Structures and serves as the Head of the Chair of Concrete and Masonry Structures.

He teaches courses in the field of concrete and masonry structures at the undergraduate, graduate, and doctoral levels. His active involvement in scientific research and professional projects has resulted in authoring or co-authoring more than 80 papers and two university textbooks.

He actively participates in international scientific conferences and is involved in the work of the fib (International Federation for Structural Concrete) Working Group 5.1 on "FRP (Fibre Reinforced Polymer) reinforcement for concrete structures." Additionally, he is a member of technical subcommittees at the Croatian Institute for Norms and contributes to laboratory accreditation procedures by the Croatian Accreditation Agency.

He serves on the editorial board of the journal "Građevinar" and is a guest editor for three publications by MDPI publishing house. Furthermore, he is actively engaged in reviewing scientific papers and research projects.

In addition to his academic and teaching activities, he is actively involved in professional work. Together with his team, he works on damage assessments from recent earthquakes, analyses the current state of damaged structures, and participates in projects for their restoration.

## ACKNOWLEDGMENTS / ZAHVALE

Vjerujem da je svaki doktorski rad pa tako i ovaj, plod želje za inovacijom, uloženog vremena i potrošenih živaca. No, ono što ovaj rad nije, jest djelo jednog čovjeka lišeno tuđih zasluga. Na mojem putu koji je trajao oko četiri i pol godine pomogli su mi brojni ljudi koji su ostavili svoj neizbrisiv trag unutar ovih stranica. Mogu se samo nadati da nikoga nisam izostavio, a ako i jesam siguran sam da mi neće zamjeriti.

Za početak, volio bih se zahvaliti svom mentoru, prof. dr. sc. Tomislavu Kišičeku, što mi je uopće pružio šansu da napišem doktorski rad te što je svojim prijedlozima, savjetima, znanjem i moralnom podrškom bio ključan čimbenik u izradi ovog rada. Od jednog skijaša drugom, hvala Vam na svemu profesore.

Nakon toga zahvalio bih se izr. prof. dr. Matiji Gamsu koji mi je dao samu ideju za ovu doktorsku disertaciju te izv. prof. dr. sc. Mislavu Stepincu koji me zapravo zaposlio na fakultetu kao i većinu ljudi koji na njemu rade. Makar on tako tvrdi.

Veliko hvala Mihelu Bosankiću i tvrtki Röfix na doniranim materijalima, Ivanu Ćuriću i tvrtki Massa na izradi uzoraka, prof. dr. sc. Ivici Guljašu i njegovom timu iz laboratorija Građevinskog i arhitektonskog fakulteta u Osijeku na provedenim ispitivanjima te Francescu Messaliju i Michele Longu s TU Delft na pruženoj pomoći prilikom numeričkog modeliranja. Bez njih bi ovaj rad ostao samo zamisao.

Hvala mojim kolegama i prijateljima Karlu, Tvrtku, Antoneli, Luki, Nikoli, Dominiku, Juri i Zdravku. Od savjeta i danih ideja do ručkova, kavica, termina padela i sauna, svaki doprinos se osjetio prilikom izrade ovog rada. Bio taj doprinos dobar ili loš.

Hvala svim mojim prijateljima. Neprospavane noći, brojna putovanja i smijeh do suza obilježili su ovo razdoblje, a i moj život. Svako tko me poznaje zna koliko vas ima pa bi bilo nemoguće sve vas nabrojati. Stoga jedno veliko hvala i puse svima vama.

Hvala mojoj Vedrani na beskrajnom strpljenju, zagrljajima i ljubavi u trenucima slabosti i velikom interesu za moj doktorski rad. Sada kada je sve gotovo vjerujem da će mi priznati da ju nije previše briga za zidove u potresu.

Na kraju najveće hvala mojoj obitelji, a poglavito mami Ledisi i tati Gorazdu. Ovaj rad je posvećen vama jer znam da vama znači i više nego meni. Bez vas ne bih upisao doktorski studij, a kamoli postao čovjek koji danas i jesam. Stoga, bez imalo zadržke mogu tvrditi da je ovaj doktorski rad naš, a ne moj. Voli vas od srca vaš Ivek.

## THESIS SUMMARY

Masonry is globally recognized as one of the most extensively used building materials in the world. Despite its widespread application, masonry structures face a notable challenge concerning seismic vulnerability. The low tensile strength of masonry makes these structures susceptible to horizontal forces, a vulnerability amplified by their construction predating comprehensive seismic regulations.

The most vulnerable parts of these buildings are piers located at the ground floor. Therefore, masonry piers that may be defined as structural elements between windows, are considered one of the most vulnerable elements in an unreinforced masonry (URM) building when subjected to horizontal actions such as earthquakes. Therefore, the assessment and retrofitting of masonry piers needs to be conducted on a very high level.

One of the most used methods for retrofitting are TRMs or textile reinforced mortars. In this dissertation, a subgroup of TRMs is used called Fibre Reinforced Cementitious Matrix (FRCM) methods. The main purpose of FRCMs is the improvement of tensile behaviour. In this dissertation, an increase in the in-plane shear capacity and ductility of URM elements was sought and an improvement of the one-sided application of the FRCM system was introduced using innovative clamping details.

For the purposes of this dissertation, a theoretical analysis was conducted analysing the behaviour of unreinforced and strengthened masonry piers. After that, an experimental campaign was carried out involving nine full-scale pier samples that were tested. Three samples were unreinforced, three were strengthened with the FRCM system on one side and three were strengthened with the FRCM system on one side with new and innovative clamping details added on the sides of the pier. Utilizing a quasi-static displacement-controlled testing protocol, the campaign yielded key results, including initial stiffness, maximum displacement, and maximum in-plane horizontal force. To validate the results, a numerical model was developed for all types of samples. By comparing the results, it is concluded that by adding clamping details the ductility of masonry piers improves while the in-plane force capacity is not influenced.

Keywords: FRCM, masonry piers, ductility, in-plane shear capacity, seismic strengthening, numerical modelling

# EXTENDED ABSTRACT IN CROATIAN

Ključne riječi: FRCM, potresno djelovanje, posmična nosivost, duktilnost

## 1. Uvod

Približno 70 % svih zgrada na svijetu čine različite vrste zidanih zgrada prema Yavartanoo i Kang [1]. Vlačna čvrstoća kod takvih građevina prilično je mala, što ih čini ranjivima na horizontalna djelovanja, posebno potrese. Sukladno tome, procjena stanja i pojačanje postojećih zidanih građevina moraju se provoditi na visokoj razini. Metode pojačanja postojećih zidanih građevina mogu se podijeliti na tradicionalne i suvremene metode temeljene na upotrebi kompozitnih materijala. Vrhunac tehnologije u području suvremenih metoda su tkaninom armirane cementne matrice (Fabric-Reinforced Cementitious Matrix ili FRCM). FRCM sustavi se sastoje od jednog ili većeg broja slojeva mrežica utisnutih u cementnu matricu. Mrežice su najčešće staklene ili ugljične. Osnovni zadatak FRCM sustava je povećanje posmične nosivosti u ravnini te povećanje duktilnosti nepojačanog zida, a imaju i niz drugih prednosti. Moguće ih je koristiti i kod zidova od opeke i kod kamenih zidova, ugradnja je jednostavna i oni usporavaju propadanje zidanih građevina u agresivnim okolišima. Što se same ugradnje tiče, FRCM sustavi se najčešće postavljaju samo sa jedne strane zida pošto je postavljanje sa više strana teško ostvarivo (iseljavanje stanara, uklanjanje prozora itd.). U ovom radu predstavljen je poboljšani koncept jednostrano postavljenog FRCM sustava s inovativnim detaljima stezanja sa strane zida. Osnovni cilj je povećati duktilnost i posmičnu nosivost zidova u usporedbi s, prvo, nepojačanim zidovima, i, drugo, zidovima pojačanim tipičnim jednostrano postavljenim FRCM sustavom. Svaka vrsta zida ima po tri uzorka, a svaka vrsta bit će eksperimentalno i numerički istražena te će sve vrste zidova bit uspoređene.

U skladu s navedenim ciljevima predložene su sljedeće hipoteze:

**H<sub>1</sub>:** Povećanje duktilnosti zidova od opeke pojačanih novim rasporedom FRCM sustava s inovativnim detaljima stezanja veće je od povećanja duktilnosti zidova od opeke pojačanih standardnim jednostranim FRCM sustavom.

**H<sub>2</sub>:** Povećanje posmične nosivosti zidova od opeke pojačanih novim rasporedom FRCM sustava s inovativnim detaljima stezanja veće je od povećanja posmične nosivosti zidova od opeke pojačanih standardnim jednostranim FRCM sustavom.



## 2. Pregled stanja područja

Ponašanje FRCM sustava ovisi o međudjelovanju između pojedinačnih ili višestrukih mreža i cementne matrice unutar koje se nalaze. Uz to, ponašanje sustava ovisi i o interakciji između čitavog sustava i zidanog elementa. Pojedinačno, cementna matrica i mreže imaju svoje zasebne uloge. Cementna matrica omogućava postavljanje mreža i zaštitu od djelovanja iz okoline. Mreže karakteriziraju vrlo visoka vlačna čvrstoća i krutost duž smjera pružanja vlakana, što je glavni cilj korištenja ovog sustava pojačanja. Vlakna u mrežama apsorbiraju većinu vlačnog djelovanja, dok u samoj matrici može doći do stvaranja pukotina. Prema Parisi et al. [44], to ne predstavlja problem. Ponašanje čitavog FRCM sustava opterećenog vlačnim djelovanjem može se podijeliti u tri faze prema Carozzi i Poggi [45]. U prvoj fazi ne dolazi do formiranja pukotina i čitav FRCM sustav se ponaša kao kompozitni materijal u kojem krutost uzorka određuju svojstva cimente matrice. U drugoj fazi dolazi do prvih pukotina u cementnoj matrici i smanjenja krutosti. U trećoj fazi dolazi do širenja pukotina te vlakna u mrežama preuzimaju cijelo vlačno djelovanje. Nakon toga dolazi do otkazivanja čitavog sustava.

Osnovni zadatak FRCM sustava je povećanje posmične nosivosti i duktilnosti nepojačanih zidova opterećenih horizontalnim djelovanjima. Prema Celano et al. [47] zidovi mogu imati tri oblika otkazivanja tj. sloma: otkazivanje savijanjem, dijagonalni slom i slom klizanjem. Najčešći oblik otkazivanja je dijagonalni slom [47] te će se on pokušati spriječiti u ovom radu. Kako bi se to i ostvarilo, FRCM sustav mora biti postavljen na odgovarajući način i nekoliko stvari treba uzeti u obzir prilikom definiranja samog sustava.

Proračun i dimenzioniranje FRCM sustava provodi se prema talijanskim CNR normama [51]. Na temelju niza istraživanja [52-54] dokazano je da su trenutne norme konzervativne kada se govori o povećanju posmične nosivosti i duktilnosti zidova pojačanih FRCM sustavom.

Nakon analitičke i teoretske obrade FRCM sustava, ponašanje u praksi je obrađeno kroz niz istraživanja. Postoji nekoliko načina otkazivanja samog sustava koja je potrebno uzeti u obzir, no na temelju niza eksperimenata Ceroni i Salzano [56], Carozzi et al. [57] i Pelin et al. [59] zaključili su da je pucanje vlakana u mreži FRCM sustava najčešći oblik otkazivanja što se želi postići i u ovom radu. Ono što se želi izbjeći je delaminacija tj. odvajanje čitavog FRCM sustava od zida. Ovom tematikom su se u

svojim istraživanjima bavili Mandor i El Rafai [60], Grande i Milani [61], Colombi i D'Antino [62] te brojni drugi. Zaključak svih istraživanja je da je, kako bi iskoristivost FRM sustava bila maksimalna, potrebno čitavi sustav odgovarajuće povezati sa samim zidom. Kako bi se to postiglo, razvijeni su različiti tipovi mehaničkih sidara. Dokazano je da je, pravilnim postavljanjem i rasporedom te dovoljno velikim brojem sidara, mogućnost delaminacije uvelike smanjenja [64-69]. Navedena istraživanja i brojna druga uzeta su u obzir prilikom definiranja novog rasporeda FRM sustava predstavljenog u ovom radu. Proširivanje znanja u području potresnog pojačavanja zidova FRM sustavom bit će od velikog značaja i važnosti za građevinsku i znanstvenu zajednicu.

### 3. Teorijska analiza zidova

Prije eksperimenata provest će se preliminarna teorijska analiza kako bi se definirale odgovarajuće dimenzije, broj i detalji uzoraka za testiranje. Prvo, to uključuje opsežan pregled literature koji je prikazan u prethodna dva odjeljka. Drugo, dimenzije i detalji opečnih zidova također su definirani provedbom terenske procjene i mjerenja na brojnim stambenim i kulturnim nepojačanim zidanim zgradama u gradu Zagrebu. Osnovni cilj ove teorijske analize jest dobiti procjenu ponašanja opečnih zidova prije provođenja eksperimenta. S takvom analizom ideja je postići dijagonalni slom opečnih zidova kako bi se potvrdile hipoteze disertacije. No, kako bi se to postiglo, potrebno je uzeti u obzir sva tri oblika sloma na temelju kojih će se dobiti interakcijski dijagrami i rezultirajuća anvelopa nosivosti promatranih zidova. Nakon što se definira ponašanje nepojačanog opečnog zida, potrebno je izračunati i doprinos FRM pojačanja.

Kao što je već definirano, razlikuju se tri grupe uzoraka. U prvoj grupi nalaze se tri nepojačana opečna zida dimenzija  $l/h/t = 142/186,5/25$  cm zidani pomoću pune opeke dimenzija  $b/h/l = 12/6,5/25$  cm povezane vapnenim mortom debljine 1 cm. Iznad i ispod zida nalaze se armiranobetonske grede dimenzija  $b/h/l = 45/25/172$  cm sa uzdužnom armaturom u obliku šipki  $8\phi 12$  i poprečnom armaturom u vidu vilica  $\phi 8$  svakih 15 cm. Isti takvi uzorci se koriste u ostale dvije grupe. U drugoj grupi nalaze se zidovi pojačani FRM sustavom duž jednog lica zida. Koriste se mreže sa  $12 \text{ mm} \times 12 \text{ mm}$  otvorima izrađene od staklenih vlakana promjera  $d = 0,6 \text{ mm}$ . Za povezivanje mreža sa zidom koristi se cementa matrica u dva sloja ukupne debljine 15 mm, a čitav sustav je povezan sa zidom pomoću staklenih sidara promjera  $d = 10 \text{ mm}$  i duljine  $l = 150 \text{ mm}$  kojih se treba

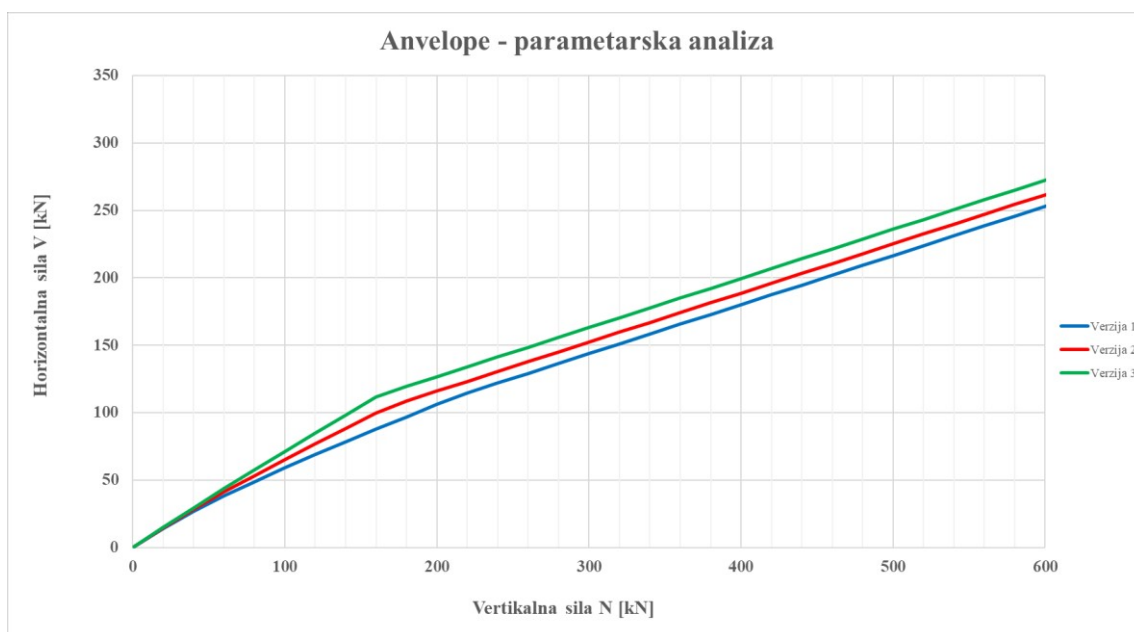
postaviti  $4/m^2$ . Treću skupinu uzoraka čine zidovi koji uz jednostrano postavljeni FRCC sustav, imaju dodani FRCC sustav do polovice debljine zida uključujući staklena sidra. Osim dimenzija uzoraka, potrebno je definirati i mehaničke karakteristike materijala koji se koriste. U preliminarnoj teorijskoj analizi sve potrebne vrijednosti uzete su iz literature i tehničkih listova prodavača. Beton kod greda je C25/30, a armatura je B500B. Zidani opečni elementi imaju tlačnu čvrstoću  $f_b = 40 \text{ N/mm}^2$  i težinu od 2,95 kg po elementu. Korišteni mort je klase M5. Komponente FRCC sustava su također definirane od strane proizvođača. Staklena mreža ima težinu od  $300 \text{ g/m}^2$ , vlačnu čvrstoću od  $1400 \text{ N/mm}^2$  i modul elastičnosti od  $E_f = 74000 \text{ N/mm}^2$ . Cementa matrica ima tlačnu čvrstoću od  $15 \text{ N/mm}^2$  i modul elastičnosti od  $E_{mm} = 6000 \text{ N/mm}^2$ . Mehanička sidra imaju vlačnu čvrstoću od  $800 \text{ N/mm}^2$  i modul elastičnosti od  $68500 \text{ N/mm}^2$ .

Na temelju iznad navedenih parametara i mehaničkih karakteristika materijala, definiraju se interakcijski dijagrami za nepojačane zidove. Na x osi se nalaze vrijednosti vertikalne tlačne sile  $N$  [kN], a na y osi se nalaze vrijednosti horizontalne poprečne sile duž zida  $V$  [kN]. Sedam različitih oblika otkazivanja i pripadajućih poprečnih sila je potrebno uzeti u obzir u ovoj analizi:

- 1) poprečna sila koja odgovara slomu savijanjem  $V_f$
- 2) poprečna sila koja odgovara slomu klizanjem (veliki ekscentricitet  $e_n$ ,  $f_{vk} < f_{vt}$ )  $V_{Rd,1A}$
- 3) poprečna sila koja odgovara slomu klizanjem (veliki ekscentricitet  $e_n$ ,  $f_{vk} = f_{vt}$ )  $V_{Rd,1B}$
- 4) poprečna sila koja odgovara slomu klizanjem (mali ekscentricitet  $e_n$ ,  $f_{vk} < f_{vt}$ )  $V_{Rd,2A}$
- 5) poprečna sila koja odgovara slomu klizanjem (mali ekscentricitet  $e_n$ ,  $f_{vk} = f_{vt}$ )  $V_{Rd,2B}$
- 6) poprečna sila koja odgovara dijagonalnom slomu  $V_d$
- 7) granična vrijednost poprečne sile koja odgovara dijagonalnom slomu  $V_{d, \text{lim}}$

Uz to, provodi se parametarska analiza gdje se karakteristične vrijednosti mehaničkih karakteristika materijala (Verzija 2) kod nepojačanih zidova umanjuju za 25 % (Verzija 1) i povećavaju za 25 % (Verzija 3) kako ne bi došlo do podcjenjivanja vrijednosti vertikalne tlačne sile koju je potrebno unijeti u zid sa ciljem postizanja dijagonalnog sloma. Ovo pojednostavljenje napravljeno je prema Soriću [93] i prema EN 1052-3:2002 [91]. Na temelju dobivenih interakcijskih dijagrama, uzimajući u obzir maksimalne vrijednosti u pojedinim dijelovima dijagrama, dobivaju se anvelope za sve tri verzije odnosno slučaja. Anvelope su prikazane na slici 3.8.

Maksimalna vertikalna sila koja se može postići u laboratoriju je 300 kN. Kako je težina samog zida 30 kN, odabire se sila od 250 kN. S ukupnom vrijednošću od 280 kN vertikalne sile, sve tri verzije u parametarskoj analizi imaju dijagonalni slom (klizanje prestaje u području od 150 do 200 kN vertikalne sile  $N$  ovisno o verziji kada dolazi do promjene u nagibu anvelope). Budući da se laboratorijski eksperiment provodi kontroliranjem pomaka, horizontalna sila  $H$  u ravnini dobiva se kao rezultat eksperimenta. Očekivane vrijednosti  $H$  za  $N = 280$  kN za različite verzije navedene su u tablici 3.4.



Slika 3.8 Anvelope iz parametarske analize

Tablica 3.4 Vrijednosti  $H$  za  $N = 280$  kN kod nepojačanih zidova

|                            | <b>Verzija 1</b> | <b>Verzija 2</b> | <b>Verzija 3</b> |
|----------------------------|------------------|------------------|------------------|
| <b><math>H</math> (kN)</b> | 136,42           | 145,04           | 155,41           |

Nakon nepojačanih zidova, potrebno je procijeniti i ponašanje jednostrano pojačanih zidova FRCCM sustavom. Doprinos FRCCM sustava od 119 kN koji je dobiven na temelju karakterističnih vrijednosti mehaničkih karakteristika materijala korištenih u FRCCM sustavu dodaje se kapacitetu nepojačanih zidova na horizontalna djelovanja tj. vrijednostima iz tablice 3.4. Utjecaj inovativnih detalja stezanja na posmičnu otpornost zidova ne može se uzeti u obzir trenutno raspoloživim normama i izrazima.

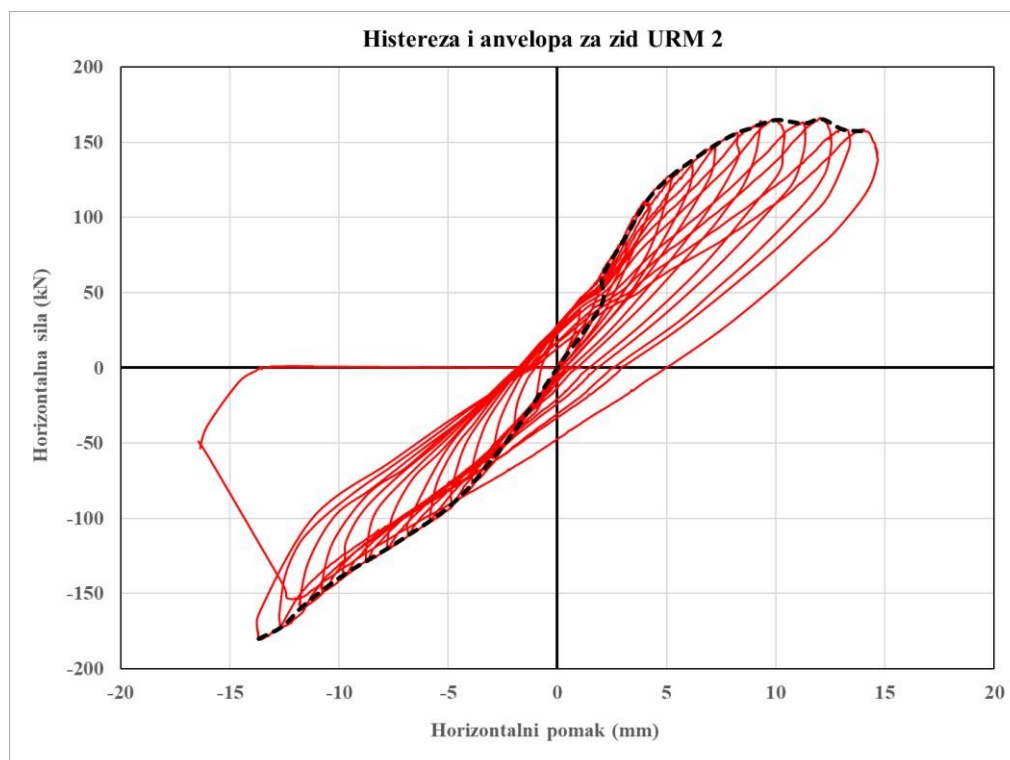
## 4. Eksperimentalno ispitivanje

Eksperimentalni dio ovog istraživanja može se podijeliti u dvije faze. U prvoj fazi provode se ispitivanja mehaničkih karakteristika materijala koji su korišteni prilikom izgradnje zidova. Prva vrijednost koja je dobivena je tlačna čvrstoća betona koji je korišten za izgradnju betonskih greda. Na temelju ispitivanja dobivena je prosječna vrijednost  $f_{cm} = 38,87 \text{ N/mm}^2$  te je obradom rezultata beton smješten u razred C30/37. Nakon toga dobivena je tlačna čvrstoća zidnih elemenata. Srednja vrijednost tlačne čvrstoće dobivena iz devet uzoraka, nakon obrade rezultata je  $f_b = 37,02 \text{ N/mm}^2$ . U idućem koraku dobivena je tlačna čvrstoća morta na temelju 12 uzoraka sa vrijednošću  $f_m = 6,12 \text{ N/mm}^2$ . Zadnje vrijednost koja je dobivena je početna posmična čvrstoća zidova. Ispitivanje je provedeno na 12 uzoraka, a na temelju obrađenih rezultata dobivena je vrijednost od  $f_{vk0} = 0,23 \text{ N/mm}^2$ .

Nakon provedenih ispitivanja na malim uzorcima, devet zidova u punoj veličini su sazidani i prevezeni u laboratorij Građevinskog i arhitektonskog fakulteta Sveučilišta u Osijeku gdje će se provoditi ispitivanja. Zidovi se mogu podijeliti u tri kategorije po tri zida. Nepojačani zidovi (URM) ispitani su u lipnju 2023. godine, zidovi pojačani jednostranim FRCC-om (FRCC) u lipnju i srpnju 2023. godine, a zidovi sa inovativnim detaljima stezanja (CFRCC) u rujnu 2023. godine. Eksperiment se provodi kao ravninsko nazovistatičko cikličko pomakom kontrolirano ispitivanje svih zidova. Takvo ispitivanje se provodi u dva osnovna koraka. U prvom koraku, vertikalno opterećenje od 250 kN se postupno nanosi pomoću dvije vertikalne preše. U idućem koraku horizontalni pomak se nanosi pomoću dvije horizontalne preše svaka sa svoje strane zida. Povijest nanošenja horizontalnog pomaka sastojala se od postupno rastućih amplituda. U jednom ciklusu opterećivanja, ciljani pomak je nanesen u pozitivnom i negativnom smjeru opterećivanja, s povratkom u početni položaj zida. Kako bi se postigli najtočniji rezultati, koristi se velika količina opreme i mjernih uređaja. Sveukupno, koristi se već navedenih četiri preše, a od opreme se koristi pet žičanih senzora (draw-wire), dva linearna pretvarača promjenjivog pomaka (LVDT) i četiri mjerača tlaka.

Nakon što su mjerni uređaji postavljeni i oprema namještena, provode se ispitivanja. Rezultati ispitivanja mogu se podijeliti na grafičke i numeričke rezultate. Grafički rezultati prikazani su u obliku histereza u pozitivnom i negativnom smjeru te anvelope koje su iz njih izvedene. Anvelope su dobivene povezivanjem vršnih točaka

tijekom opterećenja u ciklusima pri rastućim deformacijama. Na horizontalnoj osi se nalaze horizontalni pomak u milimetrima (mm), a na vertikalnoj osi horizontalna sila u ravnini zida u kilonewtonima (kN). Prikaz histereze i izvedene anvelope za URM 2 zid (nepojačani zid koji je drugi ispitan) kao primjer prikaza rezultata dan je na slici 4.30. Histereza je prikazana crvenom bojom, a anvelopa crnom bojom.



Slika 4.30 Histereza i anvelopa za zid URM 2

Nakon što je provedeno svih devet ispitivanja, uspoređuju se dobiveni rezultati. U prvom koraku uspoređuju se anvelope svih zidova. Prikaz svih anvelopa dan je na slici 4.66. Crnom bojom su prikazani nepojačani zidovi (URM), narančastom bojom zidovi pojačani jednostranim FRCM-om (FRCM), a zidovi sa inovativnim detaljima stezanja (CFRCM) prikazani su ljubičastom bojom.

Na temelju prikazanih anvelopa, dobivaju se najvažniji numerički rezultati. Oni uključuju maksimalnu horizontalnu silu, maksimalni pomak i inicijalnu krutost u pozitivnom i negativnom smjeru. Srednje vrijednosti po pojedinoj grupi zidova su prikazane u tablici 4.13.



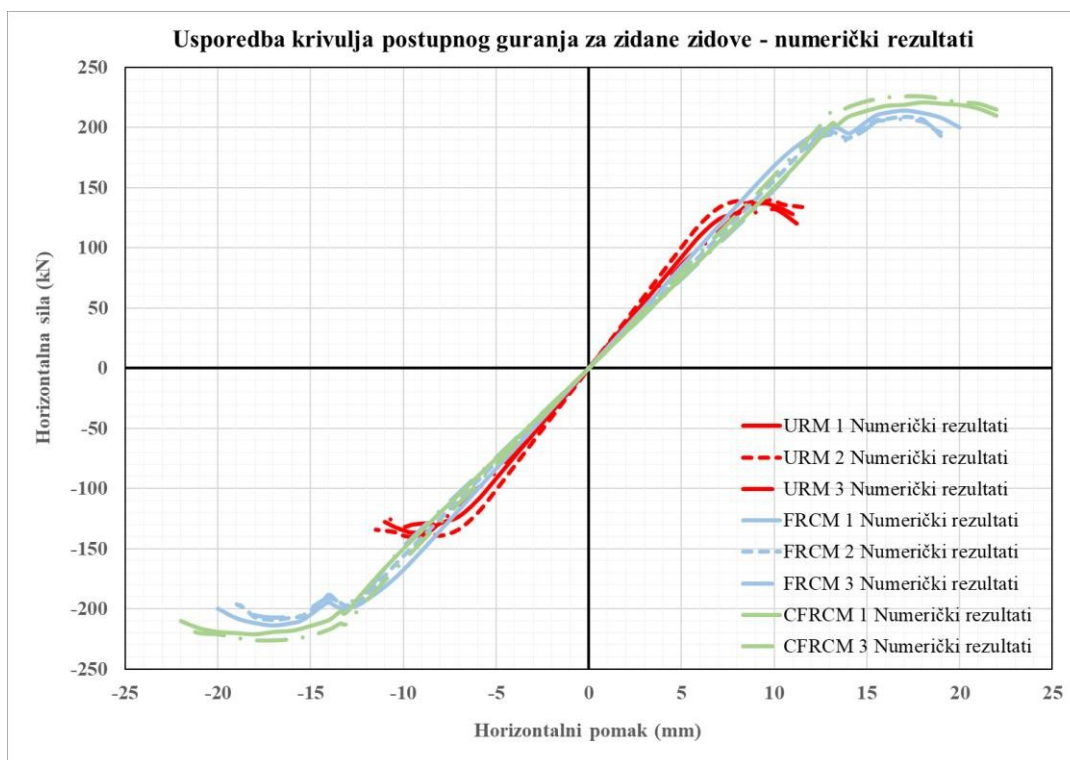
Slika 4.66 Usporedba anvelopa svih ispitanih zidova

Tablica 4.13 Usporedba rezultata za sve vrste zidova

| Vrijednost   | URM    | FRCM   | CFRCM  |
|--|--------|--------|--------|
| <b>Maksimalna horizontalna sila – pozitivan smjer [kN]</b> | 153,39 | 204,52 | 215,69 |
| <b>Maksimalni pomak – pozitivan smjer [mm]</b>             | 14,25  | 20,77  | 21,02  |
| <b>Pomak pri popuštanju – pozitivan smjer [mm]</b>         | 10,38  | 15,59  | 15,18  |
| <b>Duktilnost – pozitivan smjer</b>                        | 1,38   | 1,34   | 1,39   |
| <b>Početna krutost – pozitivan smjer [kN/mm]</b>           | 19,60  | 17,55  | 16,18  |
| <b>Maksimalna horizontalna sila – negativan smjer [kN]</b> | 160,45 | 206,40 | 206,40 |
| <b>Maksimalni pomak – negativan smjer [mm]</b>             | 16,35  | 19,29  | 18,80  |
| <b>Pomak pri popuštanju – negativan smjer [mm]</b>         | 14,17  | 16,85  | 13,05  |
| <b>Duktilnost – negativan smjer</b>                        | 1,16   | 1,15   | 1,44   |
| <b>Početna krutost – negativan smjer [kN/mm]</b>           | 17,93  | 21,49  | 21,33  |

## 5. Numeričko modeliranje

Numeričko modeliranje provedeno je u DIANA FEA 10.4 računalnom programu. Za potrebe ove doktorske disertacije korišten je princip mikro modeliranja. Nakon što je kreiran model, zadani su rubni uvjeti i opterećenja kao i u eksperimentu. Po provođenju analize, rezultati se mogu podijeliti na grafičke i numeričke. Kao grafičke rezultate, za sve zidove, nacrtane su krivulje postupnog guranja prikazane na slici 5.37 u pozitivnom smjeru. Ista takva krivulja prikazana je i u negativnom smjeru za kvalitetniju usporedbu sa rezultatima eksperimenta. Iz dobivenih krivulja dobivaju se i najvažniji numerički rezultati. Uz to, praćene su i vrijednosti maksimalnih širina pukotina kod svih zidova. Srednje vrijednosti po pojedinoj grupi zidova su prikazane u tablici 5.6.



Slika 5.37 Usporedba krivulja postupnog guranja za zidane zidove – numerički rezultati

Tablica 5.9 Usporedba rezultata za sve vrste zidova – numeričko modeliranje

| Vrijednost                        | URM    | FRCM   | CFRCM  |
|-----------------------------------|--------|--------|--------|
| Maksimalna širina pukotina [mm]   | 2,95   | 2,99   | 3,19   |
| Maksimalna horizontalna sila [kN] | 135,67 | 210,00 | 223,50 |
| Maksimalni pomak [mm]             | 11,23  | 19,47  | 22,15  |
| Duktilnost                        | 1,41   | 1,44   | 1,64   |



## 6. Usporedba rezultata i zaključci

Na temelju provedene teorijske analize, eksperimentalnih ispitivanja i numeričkog modeliranja može se zaključiti da i kod FRCM zidova i CFRCM zidova dolazi do povećanja posmične nosivosti i duktilnosti u odnosu na URM zidove. Kako je cilj postići povećanje posmične nosivosti i duktilnosti CFRCM zidova u odnosu na FRCM zidove, potrebno je usporediti rezultate tih dviju skupina zidova. Prosječne vrijednosti za duktilnost prikazane su u tablici 6.5, a prosječne vrijednosti za maksimalne posmične sile dane su u tablici 6.6.

Tablica 6.5 Usporedba duktilnosti FRCM i CFRCM zidova

| Vrijednost                                 | FRCM | CFRCM | $\Delta$ | %     |
|--|------|-------|----------|-------|
| Duktilnost – pozitivan smjer (eksperiment) | 1,34 | 1,39  | 0,05     | 3,73  |
| Duktilnost – negativan smjer (eksperiment) | 1,15 | 1,44  | 0,29     | 25,22 |
| Duktilnost (numerika)                      | 1,44 | 1,64  | 0,20     | 13,89 |

Tablica 6.6 Usporedba posmične nosivosti FRCM i CFRCM zidova

| Vrijednost  | FRCM   | CFRCM  | $\Delta$ [kN] | %    |
|---|--------|--------|---------------|------|
| Maksimalna horizontalna sila – pozitivan smjer [kN] (eksperiment) | 204,52 | 215,69 | 11,17         | 5,46 |
| Maksimalna horizontalna sila – negativan smjer [kN] (eksperiment) | 206,40 | 206,40 | 0,00          | 0,00 |
| Maksimalna horizontalna sila [kN] (numerika)                      | 210,00 | 223,50 | 13,50         | 6,43 |

Na temelju provedene usporedbe može se zaključiti da dolazi do povećanja duktilnosti kod CFRCM zidova u odnosu na FRCM zidove. S druge strane, ne može se sa sigurnošću utvrditi da dolazi i do povećanja posmične nosivosti. Uz to, kao rezultat ove doktorske disertacije moguće je donijeti još nekoliko zaključaka. Kao prvo, korištenje FRCM armature rezultira povećanjem posmične nosivosti i duktilnosti nepojačanih zidova. Drugo, kada se koristi FRCM pojačanje dolazi do savršenog dijagonalnog sloma. Konačno, dodavanjem detalja stezanja osigurava se stabilnije ponašanje zidova u potresu.

# TABLE OF CONTENT

|  |      |
|--|------|
| THESIS SUMMARY .....   | VI   |
| EXTENDED ABSTRACT IN CROATIAN .....  | VII  |
| LIST OF FIGURES .....  | XX   |
| LIST OF TABLES .....   | XXIV |
| 1 INTRODUCTION .....   | 1    |
| 2 STATE-OF-THE-ART .....   | 7    |
| 3 THEORETICAL EVALUATION OF MASONRY PIERS .....  | 15   |
| 3.1 Definition of masonry pier samples .....   | 15   |
| 3.1.1 Series 1 – URM – Unreinforced masonry piers .....                                | 16   |
| 3.1.2 Series 2 – FRCM – Masonry piers with single sided FRCM reinforcement .....       | 17   |
| 3.1.3 Series 3 – CFRCM – Masonry piers with new clamping details (C shaped FRCM) ..... | 18   |
| 3.2 Mechanical properties of materials .....   | 19   |
| 3.2.1 Mechanical properties of concrete .....  | 19   |
| 3.2.2 Mechanical properties of steel reinforcement.....                                | 20   |
| 3.2.3 Mechanical properties of masonry elements (bricks) .....                         | 20   |
| 3.2.4 Mechanical properties of masonry mortar.....                                     | 20   |
| 3.2.5 Mechanical properties of FRCM components .....                                   | 21   |
| 3.3 Mechanical properties of masonry piers .....                                       | 22   |
| 3.4 In-plane shear resistance of masonry piers .....                                   | 24   |
| 3.4.1 Elements failing in flexure .....  | 24   |
| 3.4.2 Elements failing by shear sliding .....  | 25   |
| 3.4.3 Elements failing due to diagonal cracking .....                                  | 28   |
| 3.5 In-plane shear resistance of the FRCM system .....                                 | 29   |
| 3.6 Compression-shear interaction diagrams and envelope curves for URM piers           |      |
| 30   |      |
| 3.6.1 Compression-shear interaction diagrams for different failure modes .....         | 30   |
| 3.6.2 Envelope curve for data used in subsection 3.6.1 .....                           | 32   |
| 3.6.3 Parametric analysis and discussion .....   | 34   |
| 3.7 Contribution of the FRCM reinforcement .....                                       | 36   |
| 4 EXPERIMENTAL CAMPAIGN .....  | 38   |
| 4.1 Construction of pier samples .....   | 38   |

|       |  |     |
|-------|--|-----|
| 4.2   | Testing of mechanical properties of materials .....  | 43  |
| 4.2.1 | Compressive strength of concrete .....   | 43  |
| 4.2.2 | Compressive strength of masonry units .....  | 44  |
| 4.2.3 | Compressive strength of hardened mortar.....   | 46  |
| 4.2.4 | Initial shear strength of masonry .....  | 48  |
| 4.3   | Quasi-static cyclic displacement-controlled testing of masonry piers –<br>Preparation and testing protocol ..... | 51  |
| 4.3.1 | Transportation and placement of samples .....  | 51  |
| 4.3.2 | The experiment setup and the testing equipment .....   | 53  |
| 4.3.3 | The quasi-static cyclic testing protocol .....   | 56  |
| 4.4   | Quasi-static cyclic displacement-controlled testing of masonry piers – Results<br>56                             |     |
| 4.4.1 | Series 1 – URM – Unreinforced masonry piers .....  | 57  |
| 4.4.2 | Series 2 – FRCM – Masonry piers with single sided FRCM reinforcement .....                                       | 70  |
| 4.4.3 | Series 3 – CFRCM – Masonry piers with new clamping details (C shaped FRCM) .....                                 | 82  |
| 4.4.4 | Comparison of the experimental results .....   | 92  |
| 4.4.5 | Analysis of the boundary conditions in the test setup .....  | 96  |
| 5     | NUMERICAL MODELLING.....   | 102 |
| 5.1   | Introduction .....   | 102 |
| 5.2   | Numerical modelling of Series 1 – URM piers .....  | 104 |
| 5.2.1 | Geometry .....   | 104 |
| 5.2.2 | Mechanical properties of materials .....   | 106 |
| 5.2.3 | Boundary conditions and applied loads .....  | 109 |
| 5.2.4 | Mesh settings and the nonlinear analysis .....   | 112 |
| 5.2.5 | Results of the nonlinear pushover analysis .....   | 113 |
| 5.3   | Numerical modelling of Series 2 – FRCM piers .....   | 117 |
| 5.3.1 | Geometry .....   | 117 |
| 5.3.2 | Mechanical properties of materials .....   | 120 |
| 5.3.3 | Boundary conditions and applied loads .....  | 121 |
| 5.3.4 | Mesh settings and the nonlinear analysis .....   | 122 |
| 5.3.5 | Results of the nonlinear pushover analysis .....   | 123 |
| 5.4   | Numerical modelling of Series 3 – CFRCM piers .....  | 130 |
| 5.4.1 | Geometry .....   | 130 |
| 5.4.2 | Mechanical properties of materials .....   | 131 |

|       |  |     |
|-------|--|-----|
| 5.4.3 | Boundary conditions and applied loads .....                          | 131 |
| 5.4.4 | Mesh settings and the nonlinear analysis .....                       | 132 |
| 5.4.5 | Results of the nonlinear pushover analysis .....                     | 133 |
| 5.5   | Comparison of the numerical modelling results .....                  | 139 |
| 6     | COMPARISON OF RESULTS.....   | 143 |
| 6.1   | The update of the theoretical evaluation results .....               | 143 |
| 6.2   | Comparison of theoretical, experimental, and numerical results ..... | 145 |
| 6.3   | Research Hypothesis Verification .....                               | 152 |
| 6.3.1 | Ductility .....  | 152 |
| 6.3.2 | Shear load capacity .....  | 153 |
| 7     | CONCLUSION .....   | 155 |
| 8     | RECOMMENDATIONS FOR FUTURE RESEARCH .....                            | 156 |
|       | LITERATURE .....   | 157 |
|       | CURRICULUM VITAE .....   | 168 |
|       | LIST OF PUBLISHED WORKS BY THE AUTHOR .....                          | 169 |

# LIST OF FIGURES

|  |    |
|--|----|
| Figure 2.1 The phases of the stress-strain curves of the FRCM subjected to tensile loading. ....   | 8  |
| Figure 2.2 In-plane failure modes of URM walls/piers – a) flexural failure b) diagonal shear failure – stair-step pattern c) diagonal shear failure – diagonal straight crack d) sliding shear failure. .... | 10 |
| Figure 3.1 Dimensions of the masonry pier samples – Series 1 – front and side view .....   | 16 |
| Figure 3.2 Cross section of the reinforced concrete beams .....  | 17 |
| Figure 3.3 Single sided FRCM strengthening – Series 2 – front and side view .....  | 18 |
| Figure 3.4 Single sided FRCM strengthening with clamping details (CFRCM) – Series 3 – front and side view .....  | 19 |
| Figure 3.5 Interaction diagrams $N/V$ for seven different failure modes .....  | 31 |
| Figure 3.6 Envelope curves for a) walls with $h/l = 2/1$ b) walls with $h/l = 1/1$ c) walls with $h/l = 1/3$ ...   | 32 |
| Figure 3.7 Envelope curve for the analysed URM pier.....   | 33 |
| Figure 3.8 Envelope curves for the parametric analysis .....   | 35 |
| Figure 4.1 Construction of reinforcement cages.....  | 38 |
| Figure 4.2 Formwork of the reinforced concrete beams .....   | 39 |
| Figure 4.3 Construction process of the masonry piers .....   | 40 |
| Figure 4.4 URM piers .....   | 40 |
| Figure 4.5 Application of the glass fibre mesh .....   | 41 |
| Figure 4.6 Installation of transversal connectors and application of the final layer of the mortar matrix  | 42 |
| Figure 4.7 Strengthened masonry piers .....  | 42 |
| Figure 4.8 Compression strength testing of concrete cubes .....  | 43 |
| Figure 4.9 Test specimens for the determination of the compressive strength of masonry units .....   | 45 |
| Figure 4.10 Test specimens before and after the testing .....  | 45 |
| Figure 4.11 Three samples for the compressive strength test of hardened mortar .....   | 47 |
| Figure 4.12 Nine test specimens for the initial shear strength test of masonry .....   | 48 |
| Figure 4.13 Test setup for the initial shear strength test of masonry .....  | 49 |
| Figure 4.14 Test specimens after the testing .....   | 49 |
| Figure 4.15 Shear strength/precompression diagram for masonry .....  | 51 |
| Figure 4.16 Transportation of masonry piers to the laboratory .....  | 52 |
| Figure 4.17 Transportation of masonry piers inside the laboratory .....  | 52 |
| Figure 4.18 Schematic display of the experimental setup .....  | 53 |
| Figure 4.19 Overview of measured values .....  | 55 |
| Figure 4.20 Loading history in the testing protocol .....  | 56 |
| Figure 4.21 Testing of an URM pier .....   | 57 |
| Figure 4.22 First and second crack of URM 1 pier.....  | 58 |
| Figure 4.23 URM 1 a) Crack propagation - step 7 b) Crack propagation step - 10 c) Crack propagation - failure .....  | 59 |
| Figure 4.24 Final failure mechanism of URM 1 pier .....  | 59 |
| Figure 4.25 Hysteresis curve and envelope curve for URM 1 pier .....   | 60 |

|  |    |
|--|----|
| Figure 4.26 Trilinearization of the envelope curve for URM 1 pier .....  | 61 |
| Figure 4.27 First and second crack of URM 2 pier.....  | 62 |
| Figure 4.28 URM 2 a) Crack propagation – step 7 b) Crack propagation step – 10 c) Crack propagation – failure .....    | 63 |
| Figure 4.29 Final failure mechanism of URM 2 pier .....  | 63 |
| Figure 4.30 Hysteresis curve and envelope curve for URM 2 pier .....   | 64 |
| Figure 4.31 Trilinearization of the envelope curve for URM 2 pier .....  | 65 |
| Figure 4.32 First crack of URM 3 pier .....  | 66 |
| Figure 4.33 URM 3 a) Crack propagation – step 5 b) Crack propagation – failure .....                                   | 66 |
| Figure 4.34 Final failure mechanism of URM 3 pier .....  | 67 |
| Figure 4.35 Hysteresis curve and envelope curve for URM 3 pier .....   | 67 |
| Figure 4.36 Trilinearization of the envelope curve for URM 3 pier .....  | 68 |
| Figure 4.37 Envelope curves for all three URM piers .....  | 69 |
| Figure 4.38 Testing of a FRCCM pier .....  | 70 |
| Figure 4.39 First crack of FRCCM 1 pier.....   | 71 |
| Figure 4.40 FRCCM 1 a) Crack propagation – step 10 b) Crack propagation step – 15 c) Crack propagation – failure.....  | 72 |
| Figure 4.41 Final failure mechanism of FRCCM 1 pier .....  | 72 |
| Figure 4.42 Hysteresis curve and envelope curve for FRCCM 1 pier .....   | 73 |
| Figure 4.43 Trilinearization of the envelope curve for FRCCM 1 pier .....  | 74 |
| Figure 4.44 First crack of FRCCM 2 pier.....   | 75 |
| Figure 4.45 FRCCM 2 a) Crack propagation – step 12 b) Crack propagation step – 15 c) Crack propagation – failure.....  | 76 |
| Figure 4.46 Final failure mechanism of FRCCM 2 pier .....  | 76 |
| Figure 4.47 Hysteresis curve and envelope curve for FRCCM 2 pier .....   | 77 |
| Figure 4.48 Trilinearization of the envelope curve for FRCCM 2 pier .....  | 78 |
| Figure 4.49 Final failure mechanism of FRCCM 3 pier .....  | 79 |
| Figure 4.50 Hysteresis curve and envelope curve for FRCCM 3 pier .....   | 79 |
| Figure 4.51 Trilinearization of the envelope curve for FRCCM 3 pier .....  | 80 |
| Figure 4.52 Envelope curves for all three FRCCM piers .....  | 81 |
| Figure 4.53 Testing of a CFRCCM pier .....   | 82 |
| Figure 4.54 CFRCCM 1 a) Crack propagation – step 10 b) Crack propagation – step 15 c) Crack propagation – failure..... | 83 |
| Figure 4.55 Final failure mechanism of CFRCCM 1 pier .....   | 84 |
| Figure 4.56 Hysteresis curve and envelope curve for CFRCCM 1 pier .....  | 84 |
| Figure 4.57 Trilinearization of the envelope curve for CFRCCM 1 pier .....   | 85 |
| Figure 4.58 CFRCCM 2 a) Crack propagation – step 7 b) Crack propagation – failure .....                                | 86 |
| Figure 4.59 Final failure mechanism of CFRCCM 2 pier .....   | 87 |
| Figure 4.60 Hysteresis curve and envelope curve for CFRCCM 2 pier .....  | 87 |
| Figure 4.61 CFRCCM 3 a) Crack propagation – step 10 b) Crack propagation – failure .....                               | 89 |

|   |     |
|---|-----|
| Figure 4.62 Final failure mechanism of CFRCM 3 pier .....   | 89  |
| Figure 4.63 Hysteresis curve and envelope curve for CFRCM 3 pier .....  | 90  |
| Figure 4.64 Trilinearization of the envelope curve for CFRCM 3 pier .....   | 91  |
| Figure 4.65 Envelope curves for CFRCM 1 and 3 piers .....   | 92  |
| Figure 4.66 Envelope curves for all considered piers .....  | 94  |
| Figure 4.67 Hysteresis curve and envelope curve of the bending moment – URM 1 pier .....  | 97  |
| Figure 4.68 Hysteresis curve and envelope curve of the bending moment – URM 2 pier .....  | 98  |
| Figure 4.69 Hysteresis curve and envelope curve of the bending moment – URM 3 pier .....  | 98  |
| Figure 4.70 Hysteresis curve and envelope curve of the bending moment – FRCM 1 pier .....   | 99  |
| Figure 4.71 Hysteresis curve and envelope curve of the bending moment – FRCM 2 pier .....   | 99  |
| Figure 4.72 Hysteresis curve and envelope curve of the bending moment – FRCM 3 pier .....   | 100 |
| Figure 4.73 Hysteresis curve and envelope curve of the bending moment – CFRCM 1 pier .....  | 100 |
| Figure 4.74 Hysteresis curve and envelope curve of the bending moment – CFRCM 3 pier .....  | 101 |
| Figure 5.1 URM pier (Series 1) in DIANA FEA 10.4 software a) Isometric view 7 b) Front view .....   | 104 |
| Figure 5.2 Interfaces between brick elements – green (vertical joints), red (horizontal joints), blue (connection between two pieces of the same brick) and magenta (brick elements).....                 | 105 |
| Figure 5.3 Detail of the imprint between the lowest row of bricks and the concrete foundation.....  | 106 |
| Figure 5.4 Fixed support at the bottom face of the foundation beam (red colour).....  | 111 |
| Figure 5.5 Support at the upper face of the top beam (red colour) .....   | 111 |
| Figure 5.6 Pushover curve of the bending moment for URM 1 pier – numerical model .....  | 111 |
| Figure 5.7 Meshing configuration for URM pier: a) isometric view b) front view .....  | 112 |
| Figure 5.8 Total vertical stresses of the URM piers: a) isometric view b) front view .....  | 114 |
| Figure 5.9 Deformed shape of the URM 1 pier at 21,50 mm: a) isometric view b) front view .....  | 114 |
| Figure 5.10 Deformed shape of the URM 2 pier at 21,50 mm: a) isometric view b) front view .....   | 115 |
| Figure 5.11 Deformed shape of the URM 3 pier at 21,50 mm: a) isometric view b) front view .....   | 115 |
| Figure 5.12 Pushover curves for the URM piers from the numerical modelling .....  | 116 |
| Figure 5.13 Interface relative displacements of mortar joints: a) URM 1 pier b) URM 2 pier c) URM 3 pier .....  | 117 |
| Figure 5.14 FRCM pier (Series 2) in DIANA FEA 10.4 software a) Isometric view b) Front view of the FRCM matrix pattern .....  | 118 |
| Figure 5.15 Composition of fibres for FRCM piers (Series 2) in DIANA FEA 10.4 software a) Isometric view 7 b) Front view c) Detail of the fibre composition at the bottom right corner (front view) ..... | 119 |
| Figure 5.16 Meshing configuration for FRCM pier: a) isometric view b) front view .....  | 122 |
| Figure 5.17 Total vertical stresses of the FRCM piers: a) isometric view b) front view.....   | 124 |
| Figure 5.18 Deformed shape of the FRCM 1 pier at 23 mm: a) front view of the FRCM pier - glass fibres b) front view of the FRCM pier - mortar matrix failure .....  | 124 |
| Figure 5.19 Deformed shape of the FRCM 2 pier at 23 mm: a) front view of the FRCM pier - glass fibres b) front view of the FRCM pier - mortar matrix failure .....  | 125 |
| Figure 5.20 Deformed shape of the FRCM 3 pier at 23 mm: a) front view of the FRCM pier - glass fibres b) front view of the FRCM pier - mortar matrix failure .....  | 125 |

|   |     |
|---|-----|
| Figure 5.21 Pushover curves for the FRCM piers from the numerical modelling .....   | 126 |
| Figure 5.22 Interface relative displacements of the FRCM 1 pier a) in the mortar joints of the masonry pier b) in the mortar matrix interfaces .....  | 127 |
| Figure 5.23 Interface relative displacements of the FRCM 2 pier a) in the mortar joints of the masonry pier b) in the mortar matrix interfaces .....  | 128 |
| Figure 5.24 Interface relative displacements of the FRCM 3 pier a) in the mortar joints of the masonry pier b) in the mortar matrix interfaces .....  | 128 |
| Figure 5.25 Total stresses in the glass reinforcement in the in-plane direction for a) FRCM 1 pier b) FRCM 2 pier c) FRCM 3 pier.....   | 129 |
| Figure 5.26 CFRCM pier (Series 3) in DIANA FEA 10.4 software a) Isometric view (front matrix in red and side matrix in green) b) Front view of the FRCM matrix pattern in CFRCM piers .....             | 130 |
| Figure 5.27 Composition of fibres for CFRCM piers (Series 3) in DIANA FEA 10.4 software a) Isometric view b) Front view c) Detail of the fibre composition at the bottom right corner (side view) ..... | 131 |
| Figure 5.28 Meshing configuration for CFRCM piers: a) isometric view b) front view.....   | 132 |
| Figure 5.29 Total vertical stresses of the CFRCM piers: a) isometric view b) front view .....   | 134 |
| Figure 5.30 Deformed shape of the CFRCM 1 pier at 23 mm: a) front view of the CFRCM pier - glass fibres b) front view of the CFRCM pier - mortar matrix failure.....                                    | 134 |
| Figure 5.31 Deformed shape of the CFRCM 3 pier at 23 mm: a) front view of the CFRCM pier - glass fibres b) front view of the CFRCM pier - mortar matrix failure.....                                    | 135 |
| Figure 5.32 Pushover curves for the CFRCM piers from the numerical modelling .....  | 136 |
| Figure 5.33 Interface relative displacements of the CFRCM 1 pier a) in the mortar joints of the masonry pier b) in the mortar matrix interfaces .....   | 137 |
| Figure 5.34 Interface relative displacements of the CFRCM 3 pier a) in the mortar joints of the masonry pier b) in the mortar matrix interfaces .....   | 138 |
| Figure 5.35 Total stresses in the glass reinforcement in the in-plane direction for a) CFRCM 1 pier b) CFRCM 3 pier.....  | 138 |
| Figure 5.36 Crack patterns at the final step of the analysis a) URM 1 pier b) URM 2 pier c) URM 3 pier d) FRCM 1 pier e) FRCM 2 pier f) FRCM 3 pier g) CFRCM 1 pier h) CFRCM 3 pier .....               | 140 |
| Figure 5.37 Comparison of pushover curves for masonry piers – numerical results .....   | 142 |
| Figure 6.1 Updated interaction diagrams $N/V$ for seven different failure modes.....  | 144 |
| Figure 6.2 Updated envelope curve for the analysed URM pier .....   | 144 |
| Figure 6.3 Comparison of envelope and pushover curves for URM piers – experimental and numerical results .....  | 147 |
| Figure 6.4 Comparison of envelope and pushover curves for FRCM piers – experimental and numerical results .....   | 150 |
| Figure 6.5 Comparison of envelope and pushover curves for CFRCM piers – experimental and numerical results .....  | 152 |



# LIST OF TABLES

|  |     |
|--|-----|
| Table 3.1 Strength class of concrete C25/30 .....  | 20  |
| Table 3.2 Properties of masonry units, mortar and masonry piers.....                                 | 31  |
| Table 3.3 Values of properties for the parametric analysis .....                                     | 34  |
| Table 3.4 Values of $H$ for $N = 280$ kN in URM piers (Series 1) .....                               | 35  |
| Table 3.5 Mechanical properties of the FRCM system .....   | 36  |
| Table 3.6 Values of $H$ for $N = 280$ kN in strengthened masonry piers (Series 2) .....              | 36  |
| Table 4.1 Results of the compressive strength testing of concrete cubes. ....                        | 43  |
| Table 4.2 Classification of concrete based on the results of cube testing .....                      | 44  |
| Table 4.3 Results of the compressive strength testing of masonry units .....                         | 45  |
| Table 4.4 Mean values and variation coefficients for the compressive strength of masonry units ..... | 46  |
| Table 4.5 Results of the compressive strength testing of hardened mortar samples .....               | 47  |
| Table 4.6 Results of the initial shear strength testing of masonry test specimens .....              | 50  |
| Table 4.7 Dimension and testing dates of URM piers .....   | 57  |
| Table 4.8 Results of the experimental campaign for URM piers.....                                    | 61  |
| Table 4.9 Dimension and testing dates of FRCM piers .....  | 70  |
| Table 4.10 Results of the experimental campaign for FRCM piers .....                                 | 74  |
| Table 4.11 Dimension and testing dates of CFRCM piers .....  | 82  |
| Table 4.12 Results of the experimental campaign for CFRCM piers .....                                | 85  |
| Table 4.13 Comparison of results for all masonry piers .....   | 93  |
| Table 5.1 Linear elastic properties of concrete and masonry .....                                    | 106 |
| Table 5.2 Mechanical properties of mortar joints .....   | 109 |
| Table 5.3 Results of the numerical modelling for URM piers.....                                      | 117 |
| Table 5.4 Linear elastic properties of glass fibres and mortar matrix (FRCM system) .....            | 120 |
| Table 5.5 Mechanical properties of the brick-to-matrix interface .....                               | 120 |
| Table 5.6 Mechanical properties of the matrix-to-matrix interface .....                              | 121 |
| Table 5.7 Results of the numerical modelling for FRCM piers .....                                    | 127 |
| Table 5.8 Results of the numerical modelling for CFRCM piers .....                                   | 136 |
| Table 5.9 Comparison of results for all masonry piers .....  | 141 |
| Table 6.1 Updated properties of masonry units, mortar and masonry piers .....                        | 143 |
| Table 6.2 Theoretical, experimental, and numerical results for URM piers.....                        | 147 |
| Table 6.3 Theoretical, experimental, and numerical results for FRCM piers .....                      | 149 |
| Table 6.4 Theoretical, experimental, and numerical results for CFRCM piers .....                     | 151 |
| Table 6.5 Comparison of the ductility of FRCM and CFRCM piers .....                                  | 153 |
| Table 6.6 Comparison of the shear load capacities of FRCM and CFRCM piers .....                      | 154 |

# 1 INTRODUCTION

According to various literature, it is well established that masonry as a material is one of the most used building materials in the world. Approximately, 70 % of the worlds building stock are buildings built in different types of masonry according to Yavartanoo and Kang [1]. The main reason for this is the simplicity of building with masonry and due to the high-quality characteristics of the material itself. The most noteworthy advantages of masonry include fire resistance, weather resistance (heavy storms or high temperatures) and great ability of sound proofing. Even though masonry building's usability period is quite long, there are some disadvantages. Besides the fact that masonry absorbs moisture that can cause cracking, the tensile strength of such structures is quite poor leaving them vulnerable to horizontal actions, specifically earthquakes. Barbieri et al. [2] defined seismic vulnerability as a measure of inadequacy of a given structure to resist seismic actions. Even though earthquakes are not a problem in every part of the world, most of the European region is well known for its high seismicity. In Europe, most of the buildings that have cultural and historical value are built in masonry, as well as the great portion of the residential building stock. Therefore, in case of seismic events, both economic and cultural aspects are at risk. Because of poor tensile strength, often insufficient tying, and since most of these buildings were built before the development of seismic codes, they are highly vulnerable to earthquakes. Drougkas et al. [3] came to the same conclusion during their experimental study of the in plane seismic behaviour of masonry walls subjected to subsidence-induced damage. With everything mentioned above, it is obvious that the assessment process for the existing masonry buildings must be conducted at a very high level.

Valluzzi [4] explained in the detail the importance of the assessment procedures and their applicability in historical masonry buildings in order to define the improvement techniques in hopes of increasing the safety level of buildings and meeting rigorous preservation and restoration criteria. Therefore, in case of an earthquake the data that needs to be gathered is quite large. The first step is a rapid post-earthquake visual assessment with a specific and detailed methodology which is explained by Stepinac et al. [5]. The next step includes the use of a variety of non-destructive methods including rebound hammer for masonry and mortar, ground penetrating radar, ultrasonic pulse velocity test, impact hammer with an accelerometer, thermography cameras, flat jacks and many more. Most of these methods are well described by Stepinac et al. [6]. These methods are a powerful tool in gathering important information about the condition of the building and material characteristics. With these data, the numerical

modelling of an existing masonry building is more precise. Lulić et al. [7] explained the importance of a post-earthquake visual assessment and non-destructive surveys in the numerical modelling process. A very similar study conducted by Hafner et al. [8] came to the same conclusion that for a proper analysis of an existing building's condition, great amount of information needs to be gathered.

Once the structure and the masonry material have been thoroughly inspected, a strengthening strategy is chosen. The first step in the retrofitting process is always to ensure a proper tying of structural elements so that the entire structure can maintain its integrity during an earthquake and respond to seismic loads with a box-like behaviour [9]. Tying consists of connecting walls to the floors, connecting of two perpendicular walls, or in case of weak wooden floors, also the stiffening of floor structures. When the structural elements are not connected, each of them responds to a seismic activity on their own and the collapse occurs when the weakest structural element fails. On the other hand, when they are connected, seismic loads are distributed among all the elements. The crucial information is that the in-plane loaded walls provide nearly all the resistance. Therefore, even properly tied structures can fail under seismic loads if the masonry is not strong enough. In such cases, structural elements need to be strengthened.

There are numerous traditional methods for masonry strengthening which are used to this day. Confinement of masonry is one of the most used methods in the world. The method is based on adding of vertical and horizontal concrete ties to unstrengthen walls to enclose them. Marques and Lourenco [10] conducted a review of the method, specifically theoretical approaches and experimental investigations, and concluded that the method shows an increase in vertical compressive strength and shear strength of masonry walls. Matošević et al. [11], on the other hand, studied the effect of the connection details between the masonry and concrete part of the confined masonry wall on the shear capacity during cyclic testing. It was concluded that the method is very effective, increasing the stiffness of the wall by 10 to 26 %, lateral load-bearing capacity by 70 to 90 % and ductility by 78 to 88 %. The differences in connection detailing did not show any significant deviations in the results. Unfortunately, this method is very rarely applicable when talking about historic masonry structures due to high interference into the structure of the masonry [12] and poor design and construction [13]. The second method that is used very often is concrete jacketing or shotcrete. In this method, steel meshes are placed on the walls surface and concrete is applied under high pressures. The method can be applied from one or two sides of the wall. It is desirable to apply the coating on both sides of the wall to achieve a symmetrical cross-section, a more ductile response and larger energy dissipation

[14]. Even though this method is quite good in increasing the load-bearing capacity of the wall, the concrete jackets add both stiffness and mass to the structure, increasing seismic forces and modifying the global behaviour of the structure as it is reported by D'Ambra et al. [15]. In addition, this method adds durability issues to a material that is very durable. Finally, the drawbacks are high costs, labour intensiveness, inability to use the space while the method is conducted and dirtiness which was reported by Maras [16] and Chuang and Zhuge [17].

Numerous other traditional methods exist, but the field of seismic strengthening of masonry structures is going in the direction of more reversible and sustainable methods and materials as it is explained by Babatunde [18]. Some modern methods are based on the use of composite fibre reinforced polymer (FRP) materials. FRPs consist of fibres embedded in a polymeric resin matrix [19]. Resin has a dual purpose. It is primarily used as a bonding agent that also provides protection to the fibres. The main distinction between different types of FRP is the material of the fibres. The most common types are Aramid Fibre Reinforced Polymer (AFRP), Carbon Fibre Reinforced Polymer (CFRP), Glass Fibre Reinforced Polymer (GFRP) and Basalt Fibre Reinforced Polymer (BFRP) [20–23]. Different forms and shapes of FRP products exist such as bars, strips in the form of fibres, strips in the form of laminates and fibres in mesh configurations [22]. Methods based on the Fibre Reinforced Polymers (FRPs) provide a simpler, faster, and cleaner application when compared to traditional strengthening techniques according to Triller et al. [24]. They also reported that even though in the early beginnings the problem of FRPs stemmed from the financial aspect, the cost of FRP materials has been steadily dropping making them more affordable. Nonetheless, it was reported that the FRP materials have several disadvantages making them non applicable in masonry structures. Firstly, high and low temperatures compromise the efficiency of the FRP system and wet lay-up applications are impossible on moist surfaces or at low temperatures as it is reported by Garcia-Ramonda et. al [25]. In addition, FRP systems typically act as a vapor barrier and therefore cannot be used when permeability is required, as it is the case with existing masonry structures. These problems are mainly caused by the epoxy matrix, which acts both as the binder of the fibres and the bonding agent between the composite (fibres) and the substrate. FRPs irreversibility and possible early debonding from a weak substrate are also problems that are derived from the epoxy matrix. Maljaee et. al [26] studied the effect of hygrothermal conditions on the durability of FRP-strengthened brick masonry by performing accelerated aging tests. The degradation trend in epoxy resin and GFRP was observed to be in direct relation with moisture absorption which is also a great problem when using FRPs. A paper by Ramirez et al. [27] displays an overview of the experimental activities on durability of externally bonded FRP to masonry

components subjected to water immersion and accelerated hygrothermal exposure. Both the hygrothermal environment and moist were found to be extremely deteriorating and led to a significant degradation of mechanical properties and loss in bond strength. Due to the need to improve some of FRPs' shortcomings, the Fibre Reinforced Cementitious Matrix (FRCM) was developed. By using an inorganic matrix instead of an epoxy resin, the installation of FRCMs is possible under unfavourable conditions such as cold and damp masonry surfaces. Additionally, under the influence of high temperatures the inorganic matrix shows better properties than the FRPs epoxy matrix as it is reported by Kišiček et al. [28].

FRCMs may be used for both brick and stone masonry walls. In brick masonry walls the application of FRCMs on one or both sides of the walls result in an significant ductility enhancement as it is concluded by De Lorenzis et al. [29]. The results of the diagonal compression tests that were analysed by Cucuzza et al. [30] confirmed the efficiency of the FRCM systems used in brick masonry walls. Specimens showed a massive improvement of the shear behaviour and the global ductile behaviour. A similar study was conducted by Incerti et al. [31], where the effectiveness of the FRCM system on already damaged masonry walls was examined. The results showed that the presence of FRCM reinforcements on damaged masonry panels influenced the shear behaviour of the samples, which experienced a more ductile failure. In stone masonry, the use of FRCM reinforcement, in comparison to the unstrengthen walls, resulted in a significant increase in shear modulus, shear strength and load bearing capacity as it was reported by Angiolilli et al. [32]. Additionally, as it is reported by Estevan et al. [33], the use of FRCMs as stone masonry confinement resulted with an increase of ductility of stone masonry walls. Ferretti et al. [34] came to the same conclusions seeing that the stone masonry walls strengthened with FRCM resulted with an increase in failure load and shear stiffness. In addition to seismic strengthening of walls and piers, the FRCM system is applied in masonry structures [35] and can be used for other structural elements. In [36] Toska et al. concluded that the FRCM system has the ability of restoring the majority of strength that RC columns had in the undamaged state. A positive effect of the FRCM system on the strength of columns, but in this case masonry columns, was also reported by Murgu and Mazzotti [37]. They reported that the use of FRCM wrapping resulted in an increase of strength ranging from 5 to 10 %. Grande and Milani [38] developed a simple modelling approach of the bond behavior of FRCM reinforcements externally applied to curved substrates. They highlighted that the modelling of the interface is quite complex, while Zampieri [39] underlined the importance of friction in FRCM application on single-span masonry bridges with intrados. Conclusively, the use of

FRCM is possible for curved structures if great attention is given to the interface modelling between the strengthening system and the substrate.

Apart from the apparent advantages of FRCMs regarding the improvement of the behaviour of masonry walls, use of FRCMs helps in slowing down the deterioration of masonry in aggressive environments. This fact was verified by Garavaglia et al. [40] who formed a probabilistic model that predicted a lower degradation of masonry when FRCM was used. When talking about the effect of different environmental exposures on the FRCM material itself, Donnini [41] conducted a number of single shear bond tests to determine the effect of the environment on the properties of the materials and on the shear bond behaviour at the fibre-to-matrix and matrix-to-substrate interfaces. All the aging protocols that were adopted did not influence the mechanical properties of the inorganic hydraulic matrix which is the most exposed part of the FRCM system. In FRCMs a problem might be the water saturation that can lead to salt crystallization patterns, but Franzoni et al. [42] showed that when a cementitious mortar matrix is used, water saturation seems to lead to no consequences.

With everything stated above, it is clear why FRCMs play a key role in today's strengthening and rehabilitation of the masonry-built environment which is why they have been extensively researched in recent years [43]. It is reported that the most common problem that was observed when using FRCM systems was the debonding issue. To be more precise, the bond between the coating and the masonry (matrix-to-substrate interface) is usually the weak link causing the entire system to perform poorly and become less effective. The debonding issue is most acute when single-sided FRCM strengthening is used. And even though the use of the FRCM system on both sides of the wall is more effective as it was reported by Ferretti et al. [44], the single-sided strengthening is less intrusive and more convenient for the residents. Since masonry piers are going to be observed in this dissertation, additional advantages of the single-sided strengthening need to be considered. Unfortunately for piers, two-sided strengthening is usually not feasible since the façade needs to be removed and four-sided strengthening is even less feasible since, in that case, the windows between piers need to be removed. Therefore, the debonding issue in single-sided FRCM systems needs to be solved. To address this problem, mechanical anchors were introduced in hopes of achieving a better connection between the FRCM system and the masonry substrate. Unfortunately, the bond between the FRCM system and the masonry substrate may be lost even when connectors are used in the single-sided FRCM strengthening system as it was reported by Gattesco et al. [45]. With that in mind, a novelty layout of the FRCM system with innovative clamping details is developed and examined in this dissertation. The main goal of the new method is to increase

the ductility and shear capacity of masonry piers while solving the debonding issues that appear in single-sided FRCM strengthened piers. To have a proper comparison, the increase in ductility and shear capacity when using the new clamping details are compared to URM piers and piers reinforced with a typical single-sided FRCM layout. All three types of piers are experimentally and numerically investigated and finally compared.

This research is conducted with the following goals:

- to experimentally examine the influence of the novelty layout of the FRCM system with innovative clamping details on the ductility and shear force capacity of masonry piers
- to numerically validate the increase of the ductility and shear force capacity of masonry piers when using the novelty FRCM layout with innovative clamping details
- to recommend in what direction should the future research on this topic move and to conclude if the use of such FRCM layouts is justified

With the above defined goals of this research and all the research that has already been published on this subject, the following hypotheses are proposed:

**H<sub>1</sub>:** Increase in ductility of the brick masonry pier strengthened with the novelty layout of the FRCM system with innovative clamping details is larger than the increase in ductility of the brick masonry pier strengthened with a standard single sided FRCM system.

**H<sub>2</sub>:** Increase in shear load capacity of the brick masonry pier strengthened with the novelty layout of the FRCM system with innovative clamping details is larger than the increase in shear load capacity of the brick masonry pier strengthened with a standard single sided FRCM system.

## 2 STATE-OF-THE-ART

The mechanical behaviour of Fibre Reinforced Cementitious Matrix (FRCM) systems depends on the composite action of single or multiple fibre grids that are embedded within a cementitious matrix. Their behaviour is also dependent on the interaction that the system has with the masonry substrate. The matrix is usually a cement or lime-based mortar, while the composite grid is made from usually artificial fibres (aramid, basalt, carbon, glass etc.). The most common composition in which the grid itself is produced is the mesh composition. This geometry has a dual purpose. First, the bidirectional shape of such a grid provides a better strain distribution and has equal strength in both directions. Secondly, with a larger contact area between the grid and the matrix and between the grid and the substrate, the bond efficiency increases drastically.

The application process of the FRCM system is quite simple. After the first layer of the matrix is applied, the dry reinforcing mesh is placed and pressed against the matrix which acts as a bonding agent between the mesh and the substrate. At this point, mechanical anchors should be installed with the main purpose of achieving a better connection of the reinforcing system to the substrate. The final stage of the application includes the placement of another layer of the matrix which covers the mesh providing the much-needed environmental protection.

The meshes/fibres/grids that are used in FRCM systems are characterized by a very high tensile strength along the fibre direction which is the main purpose of using this type of seismic strengthening system. On the other hand, the matrix usually exhibits a poor tensile behaviour that is characterized by crack formation. According to Parisi et al. [46] this does not pose a problem because, while a FRCM specimen is subjected to tensile loading, the fibres absorb most of the tensile stresses. The matrix on the other hand has the role of protecting the fibres and distributing the stresses amongst them.

The behaviour of the FRCM composite subjected to tensile loads can be represented with most accuracy by the uniaxial tensile tests on prismatic specimens. There are different variations of these tests and a commonly accepted testing procedure for characterizing the tensile behaviour of FRCMs is still not agreed upon. Most problems derive from the gripping system that is used for anchoring of the specimens during testing. More on that subject is explained in detail by Parisi et al. [46]. The stress-strain curves of the FRCM specimens are obtained by dividing the uniaxial tensile forces with the cross-sectional area of the embedded fibre ( $A_f$ ). This way, by avoiding the area of the full specimen, the dependency of the tensile stresses on the actual dimensions of the cracked cross section are also avoided. The resulting



behaviour of the FRCM composite under tensile loading is idealized by a trilinear curve which was reported by Parisi et al. [46] and Carozzi and Poggi [47].

The three phases representing three physical states are defined as follows (Figure 2.1):

- 1) The initial stress-strain phase (Phase 1 – magenta line) – linear and represents the uncracked state of the specimen where the FRCM behaves as a composite material in which the stiffness of the specimen is dictated by the matrix properties.
- 2) The crack development phase (Phase 2 – blue line) – initial transverse (normal to loading direction) cracks appear in the matrix and a significant decrease of stiffness due to the loss of the resisting area because of matrix cracking.
- 3) The crack widening phase (Phase 3 – green line) – besides the widening of the existing cracks in the matrix, the fibres withstand most of the overall tensile load which is the reason why the slope of the final phase reflects the Young's modulus of the dry fibre.

In the final part of the stress-strain curve, the propagation of cracks increases rapidly resulting in the ultimate failure of the FRCM. There are six typical failure modes of FRCM [48]: debonding inside the masonry, debonding at FRCM-masonry interface, debonding inside the coating, pure fibre slippage within coating, fibre slippage with cracking of substrate, and tensile fracture of fibres.

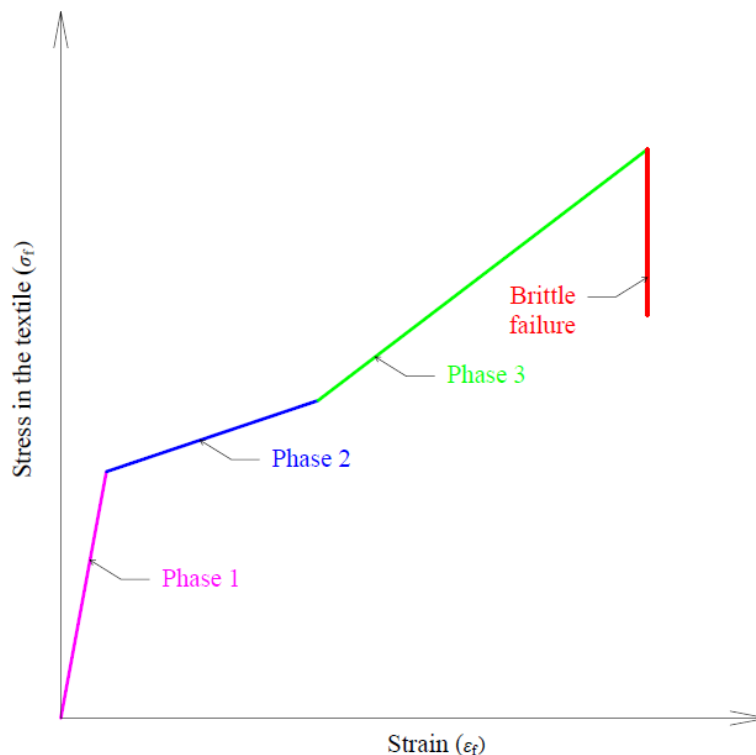


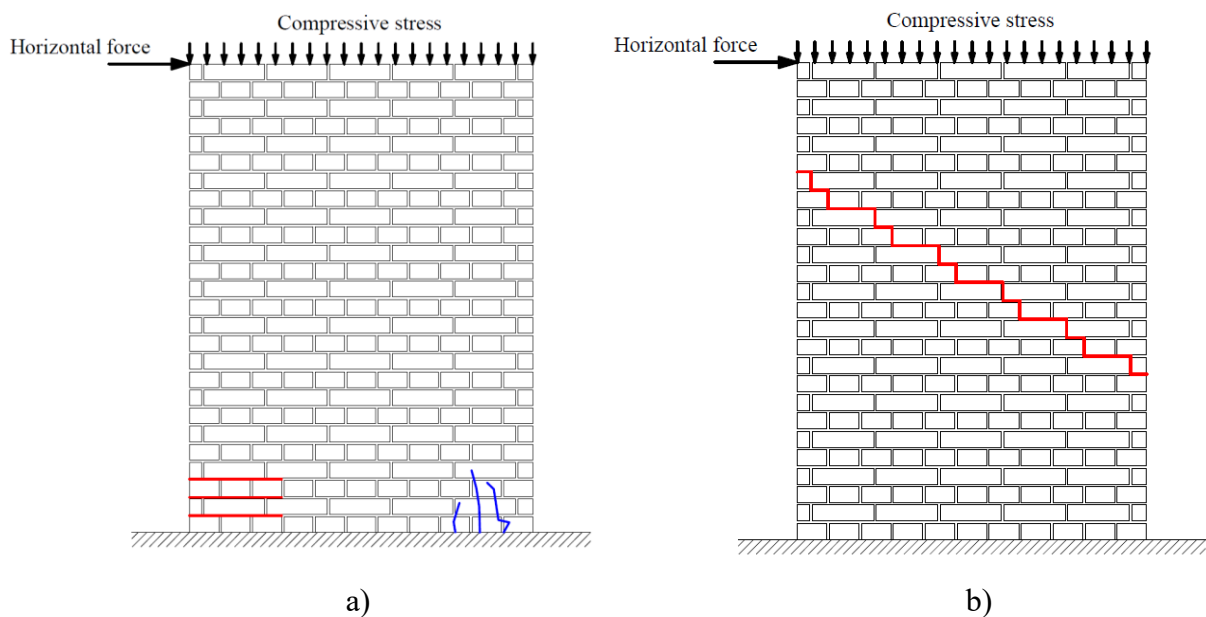
Figure 2.1 The phases of the stress-strain curves of the FRCM subjected to tensile loading.

The main reason for using FRCM systems in URM walls is that masonry walls lack the capacity for absorbing shear/horizontal actions. In that regard, URM structures are quite faulty and can exhibit three typical in plane failure modes according to Celano et al. [49].

The in-plane failure modes are categorized as follows:

- 1) Flexural failure (rocking or toe crushing): failure due to the achievement of the tensile (horizontal cracks – Figure 2.2a – red lines) or compressive (vertical cracks – Figure 2.2a – blue lines) strength along the cross end-sections of the wall. The failure mode is typical for slender walls with high compressive stress. In case that the compressive stress is low, a crack opens on the tensile side, but there is no crushing on the compressed side. Such a response is called rocking.
- 2) Diagonal shear failure: failure related to the achievement of the tensile strength of masonry along the principal direction and characterized by diagonal cracks along the wall that may occur in a stair-step manner through the mortar joints (Figure 2.2b) or as cracks that propagate in a diagonal straight line (through the bricks as well, Figure 2.2c).
- 3) Sliding shear failure: failure occurs along the mortar joints according to horizontal cracks because of the low bond strength at the mortar-masonry interface or due to the reduced values of the compressive stresses acting in the wall (Figure 2.2d).

The typical in-plane failure modes for URM walls are shown in Figure 2.2.



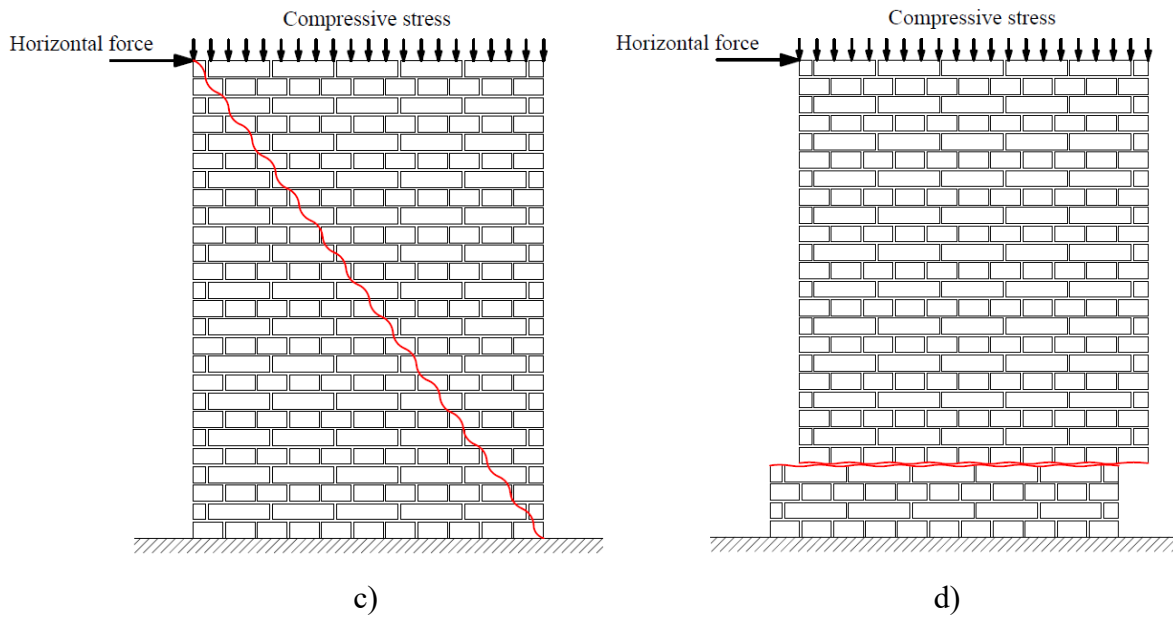


Figure 2.2 In-plane failure modes of URM walls/piers – a) flexural failure b) diagonal shear failure – stair-step pattern c) diagonal shear failure – diagonal straight crack d) sliding shear failure.

It was found by Pirsaeheb et al. [50] that the most important parameters that affect the failure modes are the geometry of the walls, the level of compressive stress and the compressive and tensile strength of the masonry units. Celano et al. [49] conducted an extensive literature review on the in-plane behaviour of masonry walls where they compared theoretical results to the experimental results. It is concluded that, for regular masonry walls, the diagonal shear failure is the most common type of in-plane failure. They also observed that the dimensions of the masonry units have a significant effect on the failure modes. The same authors studied the in-plane behaviour of masonry walls through a numerical campaign in Celano et al. [51]. They found that the agreement between the numerical and experimental results is quite satisfactory and that again the diagonal shear failure was the most common in URM walls. Da Porto et al. [52] found that the decrease in unit strength also has an effect on the dominant failure mode. They concluded that for lower unit strengths, the dominant failure mode was mostly rocking, whereas for the higher unit strengths, diagonal shear failure was the most dominant one.

With the idea of increasing the in-plane ductility and shear force capacity of masonry walls the application of FRCM strengthening systems must be conducted on a high level and several things need to be considered in the very design of such strengthening.

The analytical part of FRCM design is quite important. The most recent design guidelines, CNR guidelines, were developed by the National Research Council in Italy [53]. They are quite conservative as it is often the case with design guidelines. This fact was verified by Casacci et al. [54] who performed a comparison between analytical and experimental results for shear strengthening of masonry wallets using the FRCM strengthening system. Ramaglia et

al. [55] conducted a preliminary study with the idea of highlighting some typical issues that are often overlooked in the strengthening of masonry members that are purely based on design guidelines. They concluded that the ductility capacity of the strengthening techniques such as FRCMs are not considered properly. This may lead to over reinforcing of the masonry substrate leading to brittle behaviour.

Besides the conservative nature of the design guidelines, in some of them adjustments need to be made. Ferretti and Mazzotti [56] proposed a new analytical approach for the evaluation of the shear capacity of strengthened masonry panels on the basis of an extensive experimental campaign. The strengthened masonry panels were tested in diagonal compression. The important outcome of this study was related to the fact, that in most tests, the cracking of the mortar matrix corresponded to the shear capacity of strengthened masonry panels. Since the matrix contribution is not considered in the formulations available today, a new analytical approach is therefore developed. Grande et al. [57] also proposed a theoretical model for studying the tensile behaviour of FRCM systems where the local behaviour at the level of the matrix, reinforcement and reinforcement/matrix interface needs to be considered.

Moving away from the analytical design of FRCM systems, their behaviour in practice as a seismic strengthening system is quite complex. Several types of failure are possible. According to Ceroni and Salzano [58] the largest concern when using FRCM systems in masonry structures is the tensile rupture of fibres. This conclusion was derived from an extensive literature review of more than five hundred experimental tests. Carozzi et al. [59] came to a similar conclusion in their experimental investigation. The most common failure mode is the cracking of the mortar which was associated with textile rupture. In some cases, slippage of the textile was also observed. It is important to state that everything concluded in [58] and [59] was verified by Carozzi et al. [60] by the use of an analytical-numerical approach that is based on a 3D model using a robust Sequential Quadratic Programming routine. Pelin et al. [61] describe an extensive experimental campaign in which a series of diagonal tensile tests on historical brick masonry wallets strengthened with fibre reinforced cementitious mortar were conducted. They came to a very important conclusion that the different types of fibres did not affect the results of the diagonal tests since the early cracking of plaster appeared.

Another major problem that may occur is the debonding failure. Mandor and El Rafai [62] developed a model for the prediction of FRCM debonding and concluded that the tensile strength of the mortar used practically had no impact on the debonding. Grande and Milani [63] presented a numerical modelling approach that is able to simulate both the cracking of the matrix and the debonding problem that occurs between the reinforcement and the matrix. The

stress transfer mechanism in FRCC systems was studied in detail by Colombi and D'Antino [64]. They studied the bond behaviour of FRCC composites using an analytical approach that is based on a bond-slip law that accounts for the possible presence of friction stresses. When comparing the results of the analytical approach and the experimental campaign, it is concluded that the methodology proposed is a fast and easy tool to estimate the bond behaviour of FRCC composites. Bellini et al. [65] showed that the application of load cycles did not remarkably affect the performance of FRCC systems and the behaviour of the bond between composites, proving their reliability under seismic forces. Unfortunately, this study was conducted on very small samples, so a verification on larger samples is needed.

The problem of debonding and delamination of the entire system were identified quite early by FRCC developers introducing the use of different types of anchors or connectors. A great number of studies were conducted on this subject. Triller et al. [66] conducted an experimental study involving a three storey building and single piers that went through a seismic strengthening process. In the analysis of the test results, they realised that the resistance and displacement capacity of URM structures can be significantly improved if delamination and separation of the coating is prevented. On a smaller scale, the effect of connectors in multi-leaf masonry walls was investigated by Cascardi et al. [67]. The main purpose of this investigation was to see the effect different types of connectors have on the failure modes of the multi-leaf masonry walls. It was concluded that the rupture of connectors was not observed in any of the specimens. The same group of authors studied the in plane and out of plane behaviour of the multi-leaf walls connected with different types of connectors in [68]. Same conclusions were reached as in [67] and additionally it was concluded that the use of connectors improves the in plane and out of plane behaviour of multi-leaf masonry walls. The need for connectors was also studied by Donnini et al. [69]. They concluded that connectors need to have high axial stiffness and that they need to be properly fixed within the masonry (chemical anchoring or inorganic matrices). Incerti et al. [70] studied the influence of the masonry texture on the shear strength of FRCC reinforced panel including the use of transversal connectors. They concluded that no substantial differences in the results can be found between different types of masonry textures thanks to the very good quality of transversal connections. Guadagnuolo et al. [71] studied the use of GFRP anchors in masonry and concrete substrates. The main idea of the investigation was to compare the experimental results of the pull-out tests and the theoretical values given by various standards. All the analysed experimental data show that the theoretical formulations underestimate the actual strength of anchors.

Another problem that occurs in masonry structures reinforced with FRCM is the delamination of the reinforcing system from the masonry substrate. Logically, with the use of transversal connections, this effect becomes less problematic. In an extensive experimental study of masonry piers Triller et al. [24] showed that with the use of a proper arrangement and number of connectors the delamination is reduced. Unfortunately, the debonding problem is not solved by using connectors, even though the ductility and the shear capacity are increased as it was reported by Gattesco et al. [45,72]. Additionally, another problem arises in the numerical part of the investigation where the connectors, their arrangement, and their effect cannot be modelled in a perfect fashion. This problem was reported by Gams et al. [73]. The use of a perfect connection between the FRCM system and the masonry substrate is usually assumed.

Besides the use of proper anchors, several things were investigated regarding the disposition of the FRCM system. Firstly, Donnini et al. [74] studied the influence that the length of the fibres overlap has on the FRCM system. Indeed, in many practical cases the FRCM meshes come in dimensions that are not able to cover the entire surface of a structural element. In that case a proper fibres overlap is needed. They concluded that, in comparison to a fibre set in continuation, a minimum overlap length of 150 mm is needed to restore the specimen's integrity and to achieve a complete transfer of tensile stresses from one fibre to another. With this overlap length, the maximum stress attained at failure is almost the same of that of specimens with continuous fibre, while the stiffness is greatly increased. Secondly, Babaeidarabad and Nanni [75] developed an experimental program where clay brick wall specimens were reinforced with two different FRCM schemes – one and four plie fibre was used. They concluded that the use of four plies of FRCM does not equate to four times the ultimate in-plane bearing capacity (not even two times). Therefore, the use of more than two layers is not needed. Finally, the use of a single-sided or double-sided strengthening system is a thoroughly discussed topic. Ferretti et al. [44] showed that the single-sided reinforced panel failed at a lower maximum load than the symmetrically reinforced panel, right after the appearance of a unique crack on the unreinforced side. On the other hand, as it was stated in the introduction, the two-sided and four-sided strengthening methods are not feasible. This was explained in detail by Giaretton et al. [76]. They also pointed out to the fact that single-sided strengthening (when subjected to in-plane loads) results in the out-of-plane bending which may lead to a lesser capacity of the wall. And even though this effect should be considered when using FRCM as a strengthening method, the out-of-plane behaviour of FRCM strengthened walls under out-of-plane loads is a much more important factor to be considered.

In his paper Bellini [77] studied the effectiveness of FRCC reinforcement applied to masonry walls that were subjected to an axial force and out-of-plane loads. The reinforcement system proved to be adequate, preventing the formation of the expected hinge at mid-height of the wall. In all cases, the identified failure mode was the tensile failure of the fibres, which occurred before the debonding of the reinforcement from the substrate. D'Ambra et al. [78] conducted an experimental campaign in which they demonstrated that the externally bonded strengthening was able to prevent a brittle failure and it was not affected by debonding at all under out-of-plane loads. Additionally, the load capacity of the retrofitted wall almost doubled with respect to the unreinforced configuration. Scacco et al. [79] even developed a new fast numerical modelling approach that shows accurate results in predicting the global behaviour and the damage pattern for both unreinforced and FRCC strengthened masonry walls under out-of-plane loading.

In conclusion, the use of new and sustainable materials, advanced production methodologies and new types and dispositions of strengthening systems are an upward trend in the civil engineering community. The use of such systems like FRCC results in a perfect combination of structural safety, compatibility, and sustainability for masonry structures [80]. With a wide variety of application fields and with all abovementioned advantages, the research on FRCC systems should be even more extensive.

The main purpose of this dissertation is the introduction of a new and improved layout of the FRCC system with innovative clamping details for seismic strengthening of masonry piers in plane. The main goal is to achieve an enhancement in ductility and force capacity in comparison to unstrengthened piers and the typical single-sided FRCC layout seen on masonry piers. The above-mentioned research will be considered, and an optimal solution will be derived. Widening of knowledge about seismic strengthening of masonry piers, with the use of the FRCC system, will be of great interest and importance for the civil engineering community and the scientific community as well.

### 3 THEORETICAL EVALUATION OF MASONRY PIERS

Before an experimental campaign was conducted, a preliminary theoretical analysis was carried out to define the proper dimensions, number, and details of testing samples. Firstly, this includes an extensive literature review that was shown in the previous two sections. Secondly, the dimensions and the details of the masonry piers were also defined by conducting on-site assessment and measurements on numerous residential and cultural URM buildings in the city of Zagreb.

The main purpose of this theoretical analysis was to get a solid estimation of the behaviour of the masonry piers before the experimental campaign. With such an analysis the idea was to get the required failure mode of the masonry piers to verify the hypothesis of the dissertation. Keeping in mind that the diagonal shear failure mode is the most common in URM walls and piers, this type of failure mode was sought to be achieved in this dissertation.

To accomplish this type of failure, three important factors were taken into consideration. First, the dimensions of the masonry pier were properly defined to obtain the desired failure mode. After that, proper material characteristics were defined. This includes the material characteristics of concrete beams used in the experimental campaign, masonry elements (bricks) and mortar used for the assembly of the masonry piers and the components used in the FRCM system that was applied. Finally, the boundary conditions were set in a proper manner.

To achieve the diagonal shear failure, the theoretical model needed to consider the possibility of all three types of failure modes. Besides the diagonal shear failure, flexural failure (rocking or toe crushing) or sliding shear failure are considered. All three types of failure modes are shown in Figure 2.2. The result of this theoretical analysis is an envelope curve in the form of an interaction diagram that considers the maximum values of all failure modes.

All the mentioned elements, factors, and the theoretical analysis itself are explained in detail in the following sections.

#### 3.1 Definition of masonry pier samples

Masonry piers can be defined as structural elements between two openings, usually windows. The dimensions of such elements vary greatly in URM structures due to different architectural preferences throughout the years. Therefore, to determine the dimensions of masonry pier samples, an extensive overview of literature and existing URM buildings was conducted as mentioned before. The most important things to consider when defining the pier samples are the desired failure mode and boundary conditions that appear in actual masonry



piers. In this research, three series of masonry piers were defined. Each series of masonry piers has three samples. All nine piers have the same dimensions, and the same materials were used for their construction.

### 3.1.1 Series 1 – URM – Unreinforced masonry piers

Series 1 represents three URM piers. The samples consist of a masonry pier and two reinforced concrete beams on the top and on the bottom of the pier. The masonry piers with dimensions  $l/h/t = 142/186,5/25$  cm were constructed from typical fire clay bricks with dimensions  $b/h/l = 12/6,5/25$  cm that are connected by vertical and horizontal mortar layers that are 1 cm thick. The mortar used is lime mortar. The mechanical properties are defined in the following sections. The bricks are placed in two orthogonal directions from one layer to the other. In the first (bottom) layer the bricks are placed perpendicular to the largest surface of the pier. In the following layer the bricks are placed parallel to the largest surface of the pier. This construction pattern continues until the pier is assembled in its full height. The last layer of brick (top layer) matches the bottom layer of the bricks. This type of detailing can be seen in Figure 3.1. This type of masonry assembly is very typical in URM structures [81].

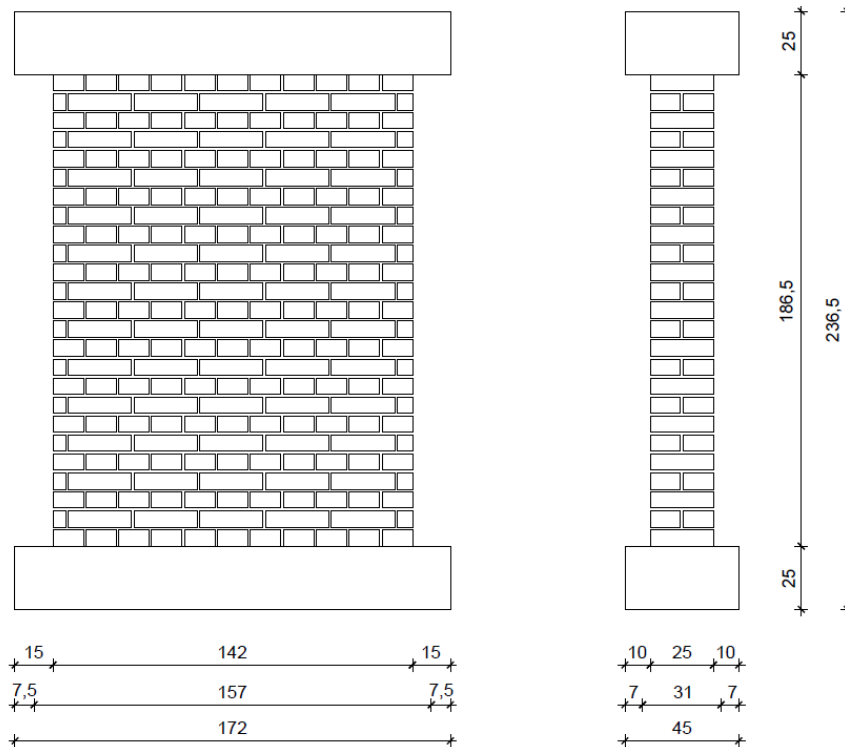


Figure 3.1 Dimensions of the masonry pier samples – Series 1 – front and side view

On the top and the bottom of the masonry piers, reinforced concrete beams were placed. The beams with the dimensions  $b/h/l = 45/25/172$  cm are used for the purposes of the experimental campaign which will be explained in section 4. All six concrete beams are

reinforced with 8  $\phi 12$  longitudinal bars and  $\phi 8$  transversal bars that are placed every 15 cm in the concrete beam. The concrete cover is 2 cm thick. The cross section of the reinforced concrete beams and the reinforcement detailing can be seen in Figure 3.2.

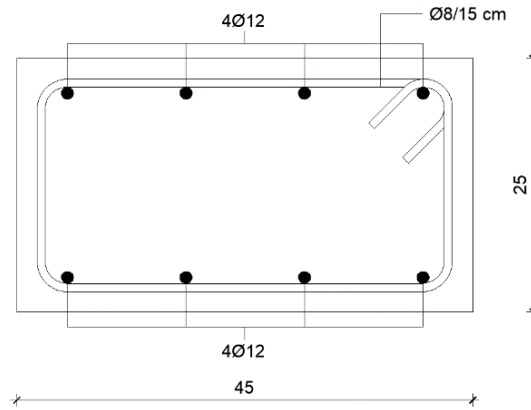


Figure 3.2 Cross section of the reinforced concrete beams

### 3.1.2 Series 2 – FRCM – Masonry piers with single sided FRCM reinforcement

Series 2 represents three masonry piers reinforced with the FRCM system on one side of the pier. The same masonry piers and reinforced concrete beams are used as for series 1. So, after the construction of URM pier samples, the FRCM system is applied. The FRCM system consists of glass fibres and a cementitious mortar. The glass fibres have the diameter of  $d = 0,6$  mm and are produced in a mesh configuration where the size of one mesh section is  $12 \text{ mm} \times 12 \text{ mm}$  (blue mesh shown in Figure 3.3). In this dissertation, only one mesh is used in the FRCM system. The thickness of the cementitious mortar matrix is 15 mm in total (green in Figure 3.3). Two layers of mortar are used. The glass fibre mesh is placed between two mortar layers. Also, transversal connectors are used to properly connect the FRCM system to the masonry sample. The connectors are shaped as glass fibre reinforced polymer (GFRP) composite bars with a diameter  $d = 10$  mm and length  $l = 150$  mm (orange dots in Figure 3.3). The transversal connectors may also be seen in Figure 3.3 in the side view. At the end of every connector, there is a bow that was impregnated at site. The bow has the diameter of 50 cm. Bows of the transversal connectors can be seen in Figure 3.3 as orange dashed circles. Besides applying the connectors at the face of the pier, the connectors are used to properly anchor the FRCM system to the reinforced concrete beams at the bottom and the top of the masonry pier. The entire application process will be explained in detail in section 4.

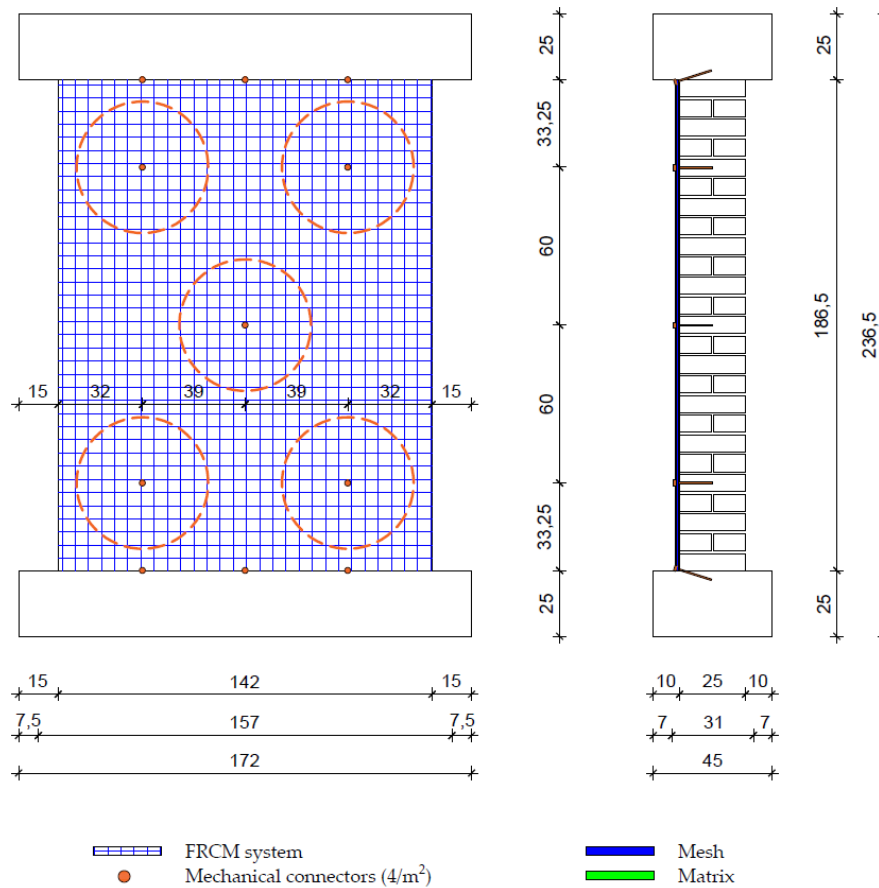


Figure 3.3 Single sided FRCM strengthening – Series 2 – front and side view

### 3.1.3 Series 3 – CFRCM – Masonry piers with new clamping details (C shaped FRCM)

Series 3 represents three masonry piers reinforced with the FRCM system on one side of the pier with added clamping details. The same masonry piers and reinforced concrete beams are used as for series 1 and series 2. So, after the construction of the URM pier samples, the FRCM system was applied. The glass fibres, cementitious mortar and the transversal connectors used are the same as they are in series 2. The only difference is that in series 3 clamping details were added on the shorter sides of the pier making a C shaped FRCM reinforcement pattern. The clamping details on the sides also consist of the same glass fibre mesh, cementitious mortar, and transversal connectors. It is important to state that the clamping details stretch to the half thickness of the pier. The C shaped FRCM system and the elements that it contains are shown in Figure 3.4.

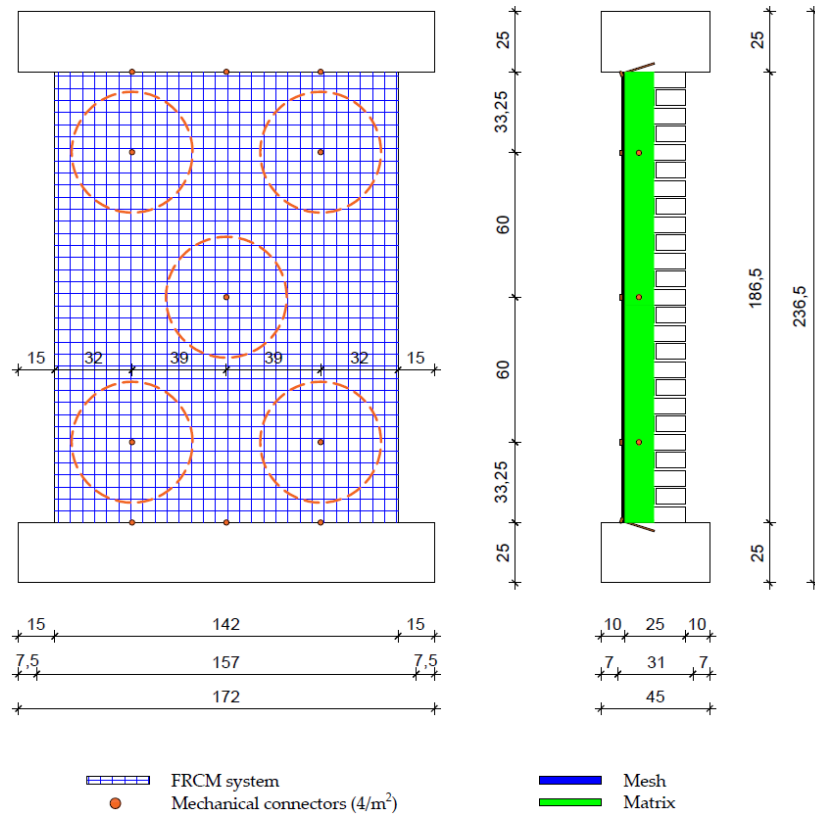


Figure 3.4 Single sided FRCM strengthening with clamping details (CFRCM) – Series 3 – front and side view

## 3.2 Mechanical properties of materials

For the purposes of a preliminary theoretical analysis, mechanical properties of different materials used need to be taken into account. It is important to state that these properties and related values were taken according to literature and standards in force. The most important mechanical properties of the materials were tested in the experimental campaign and will be used later but are not a part of the preliminary study.

### 3.2.1 Mechanical properties of concrete

The foundation and the top reinforced concrete beams that were used in the experimental campaign do not have a load bearing purpose per se. The foundation beam was used to connect the masonry pier to the laboratory floor and to achieve an adequate distribution of stress. The top beam was used for the application of the vertical distributed force and horizontal displacement. In this way, the masonry pier is unaffected by local stresses that would appear if no beams were used. Since reinforcement was used, the tensile strength of concrete is not important in this case, only the compressive strength. Therefore, the most typical strength class of concrete is chosen: C25/30. The strength and deformation characteristics of the concrete are shown in Table 3.1 and are taken according to EN 1992-1-1 [82]. The aggregate size used in this concrete is 16 mm wide (D16).

Table 3.1 Strength class of concrete C25/30

| $f_{ck}$<br>(MPa)      | $f_{ck, cube}$<br>(MPa) | $f_{cm}$<br>(MPa)      | $f_{ctm}$<br>(MPa)      | $f_{ctk, 0,05}$<br>(MPa) | $f_{ctk, 0,95}$<br>(MPa) | $E_{cm}$<br>(GPa)       |
|------------------------|-------------------------|------------------------|-------------------------|--------------------------|--------------------------|-------------------------|
| 25                     | 30                      | 33                     | 2,6                     | 1,8                      | 3,3                      | 31                      |
| $\varepsilon_{c1}$ (‰) | $\varepsilon_{cu1}$ (‰) | $\varepsilon_{c2}$ (‰) | $\varepsilon_{cu2}$ (‰) | $n$ (‰)                  | $\varepsilon_{c3}$ (‰)   | $\varepsilon_{cu3}$ (‰) |
| 2,1                    | 3,5                     | 2,0                    | 3,5                     | 2,0                      | 1,75                     | 3,5                     |

### 3.2.2 Mechanical properties of steel reinforcement

To secure an acceptable behaviour of the concrete beams, steel reinforcement was added as it was described in subsection 3.1 and Figure 3.2. The reinforcing steel used is a high ductility steel B500B with the yield strength of  $f_{yk} = 500 \text{ N/mm}^2$  and the elongation at maximum force of  $\varepsilon_{uk} = 0,05$ . According to HRN 1130-3 [83] and the book by Sorić and Kišiček [84] the smallest value of yield strength should be equal to  $400 \text{ N/mm}^2$ , mean value to  $500 \text{ N/mm}^2$ , and the largest value equal to  $600 \text{ N/mm}^2$ .

### 3.2.3 Mechanical properties of masonry elements (bricks)

As it was mentioned beforehand, the masonry elements used are fire clay bricks that are usually used in residential and cultural URM structures. The typical dimensions of such bricks are  $b/h/l = 12/6,5/25 \text{ cm}$ . For this preliminary evaluation, two mechanical properties of masonry units are important. The first one is this compressive strength of masonry units. As it is defined in EN 1996-1-1 [85] the compressive strength of masonry units, to be used in the design procedures, shall be the normalised mean compressive strength,  $f_b$ . This value can be defined either by the manufacturer or it can be obtained by converting the compressive strength of masonry units after the small-scale testing has been completed. Obviously, in the preliminary phase, no small-scale testing has been conducted so the manufacturer technical data was used as it may be seen in [86]. The masonry units used have the value of  $f_b = 40 \text{ N/mm}^2$  and the weight of  $2,95 \text{ kg}$  per unit. The second mechanical property used in this evaluation is the tensile strength of masonry elements,  $f_{bt}$ . The tensile strength is taken as a 10 % fraction of  $f_b$  according to the final working draft of the new EN 1998-3-1, part 3 [87]. With this simplification  $f_{bt} = 4 \text{ N/mm}^2$ .

### 3.2.4 Mechanical properties of masonry mortar

Masonry mortar can be defined as a mixture of one or more inorganic binders, aggregates, and water with the possibility of using admixtures for bedding, jointing, and

pointing of masonry. In old URM buildings in Croatia and Europe, lime mortar was usually used. Therefore, the masonry samples were built with lime mortar. All mortars are classified by their compressive strength  $f_c$ , expressed with the letter M followed by the compressive strength in  $\text{N/mm}^2$ , for example, M10. Therefore, the mechanical property of masonry mortar that is important for this analysis is the compressive strength of mortar. This value was obtained by small-scale testing after a 28-day period of curing. Since the small-scale testing was not conducted in this phase, the value was taken according to literature. In seismically prone areas the lowest value of the compressive strength should be  $5 \text{ N/mm}^2$  (M5). With that in mind and with the idea of simulating an old URM pier, the mortar chosen for this analysis was M5,  $f_m = 5 \text{ N/mm}^2$ . According to the Croatian national annex of EN 1996-1-1 [88] this value may vary between  $5 \text{ N/mm}^2$  and  $7,5 \text{ N/mm}^2$ .

### 3.2.5 Mechanical properties of FRCM components

The Fibre Reinforced Cementitious Matrix (FRCM) system consist of a single glass grid mesh that is embedded within a cementitious matrix. Therefore, the behaviour of this strengthening system depends on the mechanical properties of the fibres and matrix used. The mesh that is used in the FRCM system is characterized by a very high tensile strength and stiffness along the fibre direction which is the main purpose of using this type of seismic strengthening system. In this dissertation a glass mesh with a weight of  $300 \text{ g/m}^2$  FB-VAR320R12 produced by FibreNet was used. The most important mechanical properties of the fibre mesh are the tensile strength of the fibre which is  $1400 \text{ N/mm}^2$  and the modulus of elasticity  $E_f = 74000 \text{ N/mm}^2$ . All the mentioned values were given in the manufacturer's technical specification [89].

On the other hand, the matrix usually exhibits a poor tensile behaviour that is characterized by crack formation. And even though the matrix does not provide tensile strength, its contribution to the system is very important. Besides protecting the entire system from environmental influence, it provides a proper connection between the fibres and the masonry substrate. Since, the effectiveness of the system is based on the interaction between its components and the interaction between the entire system and the masonry substrate, the role of the cementitious matrix is crucial. The mechanical properties of the matrix include the compressive strength of  $15 \text{ N/mm}^2$  and the modulus of elasticity  $E_m = 6000 \text{ N/mm}^2$ . The mortar matrix is a product by RÖFIX called Röfix SismaDur FRCM. Again, all the mentioned values were given in the manufacturer's technical specification [90].

As it was mentioned above, transversal connectors were also used to avoid the delamination of the entire system. The connectors are shaped as glass fibre reinforced polymer (GFRP) composite bars with a diameter  $d = 10$  mm. The GFRP bars type FB-TUP10-VAR1A are produced by FibreNet. These connectors were applied on only one side of the pier. The mean value of the composite tensile strength equals to  $800 \text{ N/mm}^2$  and the elastic modulus that was determined on the bare fibre is  $68500 \text{ N/mm}^2$ . These values were provided by the manufacturer [91].

### 3.3 Mechanical properties of masonry piers

The first value that was considered is the characteristic compressive strength of masonry,  $f_k$ . Usually, this value is determined from test results on masonry samples. Since this is a preliminary evaluation, the following equation was used:

$$f_k = K f_b^\alpha \cdot f_m^\beta \quad (3.1)$$

|        |                 |   |
|--------|-----------------|---|
| where: | $K$             | a constant given in Table 3.3 of EN 1996-1-1 [85]                   |
|        | $\alpha, \beta$ | constants   |
|        | $f_b$           | normalised compressive strength of masonry units in $\text{N/mm}^2$ |
|        | $f_m$           | compressive strength of mortar in $\text{N/mm}^2$                   |

The value of  $K$  is a constant that is dependent on the type of mortar being used for the construction of the wall (general purpose mortar, thin layer mortar and lightweight mortar) and the type of masonry units and their group. Since general purpose mortar and clay masonry units (Group 1) were used the value of  $K$  is 0,55. This can be seen in Table 3.3 of EN 1996-1-1 [85]. Constants  $\alpha, \beta$  are defined according to EN 1996-1-1 [85]. For general purpose mortar and lightweight mortar these values are  $\alpha = 0,7$  and  $\beta = 0,3$ . The normalised compressive strength of masonry units was defined in subsection 3.2.3 according to the manufacturer with  $f_b = 40 \text{ N/mm}^2$ . The compressive strength of mortar was defined in subsection 3.2.4 with  $f_m = 5 \text{ N/mm}^2$ .

With these values, the characteristic compressive strength of masonry equals:

$$f_k = K f_b^\alpha \cdot f_m^\beta = 0,55 \cdot 40^{0,7} \cdot 5^{0,3} = 11,79 \text{ N/mm}^2$$

The second value that was considered is the characteristic shear strength of masonry,  $f_{vk}$ . This value is usually determined from the results of tests on masonry. Since this is a preliminary analysis, an equation will be used from EN 1996-1-1 [85].

When general purpose mortar is used, the following equation may be used for the determination of  $f_{vk}$ :

$$f_{vk} = f_{vk0} + 0,4 \sigma_d \quad (3.2)$$

but not greater than  $0,065 f_b$  or  $f_{vlt}$

|        |            |   |
|--------|------------|---|
| where: | $f_{vk0}$  | characteristic initial shear strength   |
|        | $f_{vlt}$  | limit value of $f_{vk}$   |
|        | 0,4        | tangent of the friction angle ( $\phi = 21,8^\circ$ ) – 0,5 for existing masonry  |
|        | $\sigma_d$ | design compressive stress perpendicular to the shear in the member at the level under consideration, using the appropriate load combination based on the mean vertical stress over the compressed part of the wall ( $d$ ) that is providing shear resistance |
|        | $f_b$      | normalised compressive strength of masonry units for the direction of application of the load on the test specimens being perpendicular to the bed face   |

The characteristic initial shear strength,  $f_{k0}$ , is the shear strength of masonry under zero compressive stress. This value is determined either from the evaluation of a database on the results of test on the initial shear strength of masonry or from the values given in table 3.4 in EN 1996-1-1 [85]. Since clay bricks and general purpose M5 mortar were used,  $f_{k0} = 0,2 \text{ N/mm}^2$ . The limit value  $f_{vlt} = 2,6 \text{ N/mm}^2$  is calculated according to the Croatian national annex of EN 1996-1-1 [92]. If  $f_b = 40 \text{ N/mm}^2$ , then the limit value equals  $f_{vlt} = 0,065 f_b = 2,60 \text{ N/mm}^2$ .

The value of  $\sigma_d$  was calculated using the following equation:

$$\sigma_d = \gamma_{G, inf} \cdot N_G / (t \cdot l_c) \quad (3.3)$$

|        |                   |                                      |
|--------|-------------------|--------------------------------------|
| where: | $\gamma_{G, inf}$ | coefficient equal to 1,0             |
|        | $N_G$             | vertical load with a positive effect |
|        | $t$               | thickness of the wall                |
|        | $l_c$             | compressed part of the wall          |

Since the value of the vertical load was varied in the preliminary analysis, the calculation of  $\sigma_d$  and  $f_{vk}$  is going to be calculated in the following sections.

The final value that was considered is the characteristic tensile strength of masonry,  $f_{tk}$ . This is the value of the tensile strength when the tensile failure appears with walls that are



simultaneously under the influence of vertical and in-plane horizontal loads. The value of  $f_{tk}$  can be determined by two types of laboratory testing. The first method includes a wall with a constant a vertical load applied that is gradually pushed with a horizontal load applied at the top of the wall. The second method is the diagonal compression test. Both methodologies are explained in the Croatian national annex of EN 1996-1-1 [92]. In the preliminary analysis, a simplification was used according final working draft of the new EN 1998-3-1 [87]. This simplification is based on the fact that the cohesion between masonry components is quite low in old masonry elements. The value of  $f_{tk}$  was simply taken as the value of characteristic initial shear strength,  $f_{vk0}$ , divided by 1,5. Therefore, for this analysis, the characteristic tensile strength of masonry,  $f_{tk} = 0,2/1,5 = 0,133 \text{ N/mm}^2$ . Such a simplification is acceptable since the values given in the final working draft of the new EN 1998-3-1 [87] for existing masonry buildings equal  $f_{vk0} = 0,16 \text{ N/mm}^2$  and  $f_{tk} = 0,16/1,5 = 0,11 \text{ N/mm}^2$ .

### 3.4 In-plane shear resistance of masonry piers

The maximum shear force that can develop in an URM pier should be taken as the minimum value amongst those defined by considering three possible failure modes: flexure  $V_f$ , shear sliding  $V_s$  and diagonal cracking  $V_d$ . All failure modes are described in section 2 and illustrated in Figure 2.2. Additionally, more information is given in the final working draft of the new EN 1998-3-1 [87]. The shear resistance of elements in reinforced masonry buildings should be calculated by adding the contribution of the shear reinforcement to the element considered that is made as URM. The calculation of the shear resistance is different for different failure modes. All failure modes were calculated with the assumption that they are under constant vertical axial load.

#### 3.4.1 Elements failing in flexure

The shear force corresponding to flexural failure of an URM pier is the minimum between those evaluated at the two end sections of the pier and can be taken as:

$$V_f = \frac{l \cdot N}{2 \cdot h_0} \cdot (1 - 1,15 \cdot v) \quad (3.4)$$

|        |       |  |
|--------|-------|--|
| where: | $l$   | in-plane horizontal dimension of the wall  |
|        | $h_0$ | distance between the section where the flexural resistance is attained and the contraflexure point |
|        | $N$   | is the axial load at the end section   |
|        | $v$   | normalised axial load  |

The in-plane dimension of the wall  $l$  is the length in case of piers. The value of  $h_0$  depends on the boundary conditions of the masonry pier. In this dissertation it was considered that the pier is fixed at the top and at the bottom so the value of  $h_0 = 0,5h$  was taken since the pier will not show a cantilever behaviour.

The normalised axial load was calculated by the following equation:

$$v = \frac{N}{l \cdot t \cdot f_k} \quad (3.5)$$

where:  $f_k$  characteristic compressive strength of masonry  
 $t$  wall thickness

The value of the compressive strength of masonry should be taken as the mean compressive strength of masonry obtained from in-situ tests. Since there are no in-situ tests carried out and that this is a preliminary study, the characteristic value was considered.

### 3.4.2 Elements failing by shear sliding

The shear force corresponding to shear sliding of an URM pier should be the minimum between those calculated at the two end sections of the pier and can be taken as:

$$V_s = l' \cdot t \cdot \left( f_{vk0} + \frac{\mu N}{l' \cdot t} \right) \leq V_{s, \text{units}} \quad (3.6)$$

where:  $l'$  depth of the compressed area at the end section of the pier  
 $t$  wall thickness  
 $f_{vk0}$  shear strength in the absence of vertical load  
 $\mu$  masonry friction coefficient, 0,5 for existing masonry  
 $V_{s, \text{units}}$  limitation of  $V_s$  due to the failure of masonry units  
 $f_b$  normalised compressive strength of masonry units

The depth of the compressed area  $l'$  is equal to the value of  $l_c$  shown in equation 3.3. The value of  $\mu = 0,5$  was calculated from the characteristic value equal to 0,4 as it is defined in EN 1996-1-1 [85] and divided by 0,8 in order to obtain the mean value, according to EN 1052-3:2002 [93] that deals with the determination of the initial shear strength of masonry.

The limitation value  $V_{s, \text{units}}$  can be taken as:

$$V_{s, \text{units}} = 0,065 \cdot f_b \cdot l' \cdot t \quad (3.7)$$

The problem that appears when calculating shear resistance  $V_s$  is that it appears to be a function of the horizontal load applied which is counterintuitive. The reason for this phenomenon is that equation 3.6 for shear resistance is a function of the compressed length which is itself a function of the horizontal load. In [94] Jäger and Gams provided a detailed

analysis of these equations. The result of the analysis is the rewriting of the equations in such a manner that the shear resistance is no longer a function of the horizontal load.

A typical design verification case of a wall of thickness  $t$ , length  $l$ , height  $h$ , loaded with vertical (normal force)  $N$  and horizontal action  $H$  with known characteristic initial shear strength  $f_{vk0}$  and maximum shear strength  $f_{vlt}$  was considered. To check if the design resistance  $V_{Rd}$  is larger than the action effect  $V_{Ed}$ , the compressed length was evaluated. The compressed length is defined and thoroughly explained in EN 1996-1-1 [85] and calculated using the following equation:

$$l_c = 3 \cdot \left( \frac{l}{2} - \frac{M}{N} \right) = 3 \cdot \left( \frac{l}{2} - \frac{H h_0 + N e_n}{N} \right) \leq l \quad (3.8)$$

|        |       |   |
|--------|-------|---|
| where: | $l$   | length of the pier  |
|        | $N$   | vertical force  |
|        | $H$   | horizontal force at the top of the pier   |
|        | $M$   | moment produced by horizontal action $H$ acting on top of the wall and in-plane eccentricity of vertical force $N$  |
|        | $h_0$ | distance between the section where the flexural resistance is attained and the contraflexure point ( $h_0 = 0,5h$ since fixed-fixed boundary conditions are used) |
|        | $e_n$ | in-plane eccentricity of vertical force $N$   |

Since both the shear resistance and the compressed length of the wall are functions of the horizontal load, an iterative approach was used. The iterative approach is defined in a manner that load  $H$  is sought so that  $V_{Ed}/V_{Rd} = 1$  holds. Another problem of this approach is that it can result in a potentially negative value of the compressed length for high values of  $V$ . In such a case, the standard EN 1996-1-1 procedure does not give (a physically feasible) a result because the wall would sooner overturn. To tackle this problem, the horizontal load needs to be reduced to obtain a solution at all. Jäger and Gams [94] designed an alternative procedure to calculate maximum shear resistance without the iterative approach. The method is based on the observation, that to obtain the actual resistance,  $V_{Rd}$  the following should hold:

$$V_{Rd} = \frac{f_{vk}}{\gamma_m} \cdot t \cdot l_c(V) = V \quad (3.9)$$

|        |            |   |
|--------|------------|---|
| where: | $t$        | thickness of the wall   |
|        | $\gamma_m$ | material partial factor   |
|        | $f_{vk}$   | characteristic shear strength of masonry ( $=\sqrt{f_0} + 0,5\sigma$ ) which is explained in equation 3.2 |

The solution for  $V_{Rd}$  can be easily expressed from equation 3.9, but different cases must be considered to account for entire or only partially compressed wall and other criteria. This also eliminates the undesired and confusing situation of the shear resistance being a function of the horizontal load. This approach can be adopted for any shear model based on the compressed part of the cross-section.

Four different cases were considered:

a) Case 1A: large eccentricity  $e_n$ ,  $f_{vk} < f_{vlt}$

According to the definition of large eccentricity, only a part of the wall is in compression:

$$0 < l_c < l$$

In that case the shear resistance of the wall is equal to:

$$V_{Rd, 1A} = \frac{\frac{3}{2} \cdot \frac{f_{vk0}}{\gamma_m} \cdot t \cdot l \cdot (1 - 2 \cdot \frac{e_n}{l}) + 0, 4 \cdot \frac{N}{\gamma_m}}{1 + 3 \cdot \frac{f_{vk0}}{\gamma_m} \cdot \frac{h_0 \cdot t}{N}} \quad (3.10)$$

b) Case 1B: large eccentricity  $e_n$ ,  $f_{vk} = f_{vlt}$

When the shear strength is limited by the allowed value  $f_{vlt}$ , equation 3.10 is reduced to:

$$V_{Rd, 1B} = \frac{\frac{3}{2} \cdot \frac{f_{vlt}}{\gamma_m} \cdot t \cdot l \cdot (1 - 2 \cdot \frac{e_n}{l})}{1 + 3 \cdot \frac{f_{vlt}}{\gamma_m} \cdot \frac{h_0 \cdot t}{N}} \quad (3.11)$$

c) Case 2A: small eccentricity  $e_n$ ,  $f_{vk} < f_{vlt}$

In this case the entire wall is in compression:

$$l_c = l$$

In that case the shear resistance of the wall is equal to:

$$V_{Rd, 2A} = (f_{vk0} + 0, 4 \cdot \frac{N}{t \cdot l}) \cdot \frac{t \cdot l}{\gamma_m} \quad (3.12)$$

d) Case 2B: small eccentricity  $e_n$ ,  $f_{vk} = f_{vlt}$

In this case the shear resistance of the wall is equal to:

$$V_{Rd, 2B} = f_{vlt} \cdot \frac{t \cdot l}{\gamma_m} \quad (3.13)$$

### 3.4.3 Elements failing due to diagonal cracking

The shear strength of masonry piers controlled by diagonal cracking is related to the formation of stair-stepped cracks and should be calculated as:

$$V_d = \frac{l \cdot t}{b} \cdot (f_{v0} + \mu \sigma_0) = \frac{l \cdot t}{b} \cdot \left( \frac{f_{v0}}{1 + \mu \cdot \phi} + \frac{\mu}{1 + \mu \cdot \phi} \cdot \sigma_0 \right) \leq V_{d, \text{lim}} \quad (3.14)$$

where:

- $l$  in-plane pier depth (length in piers)
- $t$  wall thickness
- $b$  is a correction coefficient accounting for the shear stress distribution in the middle section of the panel and related to the aspect ratio of the panel; it should be taken as  $b = h/l$ , but in any case, not greater than 1,5 and not lower than 1, where  $h$  is the height of the panel

$f_{v0}$  and  $\mu$  the equivalent shear strength, in the absence of axial loads, and the equivalent friction coefficient, related to the local mechanical properties of the mortar joint ( $f_{v0}$  and  $\mu_j$ ) and the interlocking coefficient  $\phi$ , defined as the ratio between the height of the unit and the length of overlapping between units (this parameter represents the tangent of the mean inclination of the stair-stepped crack)

$\sigma_0$  mean vertical stress in the transverse section of the panel

In the absence of accurate evaluations, the local friction coefficient  $\mu_j$  may be assumed equal to 0,6. The value of  $\sigma_0$  is calculated according to the following equation:

$$\sigma_0 = \frac{N}{l \cdot t} \quad (3.15)$$

where:  $N$  axial force at the centre of the panel

Value  $V_{d, \text{lim}}$  is the limit value of shear strength that is related to the failure of units and may be calculated as a function of the tensile strength of units  $f_{bt}$  and of the geometry of the panel. The following equation is used:

$$V_{d, \text{lim}} = \frac{l \cdot t}{b} \cdot \frac{f_{bt}}{2,3} \cdot \sqrt{1 + \frac{\sigma_0}{f_{bt}}} \quad (3.16)$$

The tensile strength of units  $f_{bt}$  may be obtained from available data or direct tests in laboratory, on specimens taken in-situ, or by the correlation with the compressive strength of units  $f_{bt} = 0,1 f_b$  as described in subsection 3.2.3.

### 3.5 In-plane shear resistance of the FRCM system

The high strength-to-weight ratio of FRCM systems makes it possible to enhance the mechanical performance of strengthened structural masonry elements, essentially being able to withstand the tensile stresses without increasing its mass or significantly changing its stiffness. The tensile stresses are taken on by the glass fibre mesh used in the FRCM system. The contribution of the FRCM system in strengthened masonry piers can be considered using the following equation from CNR-DT 215/2018 guide [53]:

$$V_{t,f} = \frac{1}{\gamma_{Rd}} \cdot n_f \cdot t_{vf} \cdot l_f \cdot \alpha \cdot \varepsilon_{fd} \cdot E_f \quad (3.17)$$

|        |                    |  |
|--------|--------------------|--|
| where: | $\gamma_{Rd}$      | partial safety factor equal to 2,0   |
|        | $n_f$              | total number of reinforcement layers arranged on the sides of the wall   |
|        | $t_{vf}$           | equivalent thickness of a layer of the fibres arranged in the direction parallel to the shear force  |
|        | $l_f$              | is the design dimension of the reinforcement measured orthogonally to the shear force, and in any case, it cannot be assumed as longer than the height of the pier   |
|        | $\alpha$           | coefficient that takes into account the reduced tensile strength of the fibres when stressed in shear (without experimental results, it can be assumed equal to 0,8) |
|        | $\varepsilon_{fd}$ | allowable design strain of FRCM  |
|        | $E_f$              | modulus of elasticity of glass fibres used in the FRCM system  |

The allowable design strain is defined by the following equation [53]:

$$\varepsilon_{fd} = \eta \frac{\varepsilon_{fk}}{\gamma_m} \quad (3.18)$$

|        |                    |   |
|--------|--------------------|---|
| where: | $\varepsilon_{fk}$ | characteristic strain at failure according to manufacturer  |
|        | $\eta$             | environmental conversion factor dependent on exposure conditions (for internal conditions it is equal to 0,9) |
|        | $\gamma_m$         | partial safety factor equal to 1,5  |

The shear capacity of the strengthened wall ( $V_{tr}$ ) is calculated as the sum of the contribution of URM ( $V_f$ ,  $V_s$  or  $V_{Rd}$ ) and the contribution of the FRCM reinforcement ( $V_{t,f}$ ).

### 3.6 Compression-shear interaction diagrams and envelope curves for URM piers

In the preliminary analysis masonry piers with dimensions  $l/h/t = 142/186,5/25$  cm were used as it was defined in section 3.1. In previous sections, mechanical properties of individual concrete and masonry materials, FRCM components and masonry piers were defined. Additionally, the in-plane behaviour of the URM piers and the FRCM system were explained. This data is necessary to calculate the compression-shear interaction diagrams for URM piers for each type of failure mode. From numerous interaction diagrams an envelope curve was derived that considers the maximum values of all failure modes of URM that were considered. The interaction diagrams and the envelope curves were developed by Jäger and Gams [94]. From these envelope curves one can directly see how shear resistance and failure mechanism are influenced by material properties, wall geometry and vertical load. The contribution of the FRCM reinforcement will be added later as a numerical value. The contribution of the concrete beams was only considered in this analysis as additional weight on the URM pier. The main purpose of this analysis was to define a proper experimental full scale test setup and forces/displacements that are applied in the laboratory.

#### 3.6.1 Compression-shear interaction diagrams for different failure modes

The compression-shear interaction diagrams were defined for each failure mode. The values of the vertical compressive force  $N$  [kN] are shown on the x-axis and the values of the horizontal in-plane force  $V$  [kN] are shown on the y-axis. Seven different failure mechanisms of URM piers and shear forces were defined in section 3.4.1 to 3.4.3. The shear forces of these failure mechanisms were used in this analysis.

To summarize:

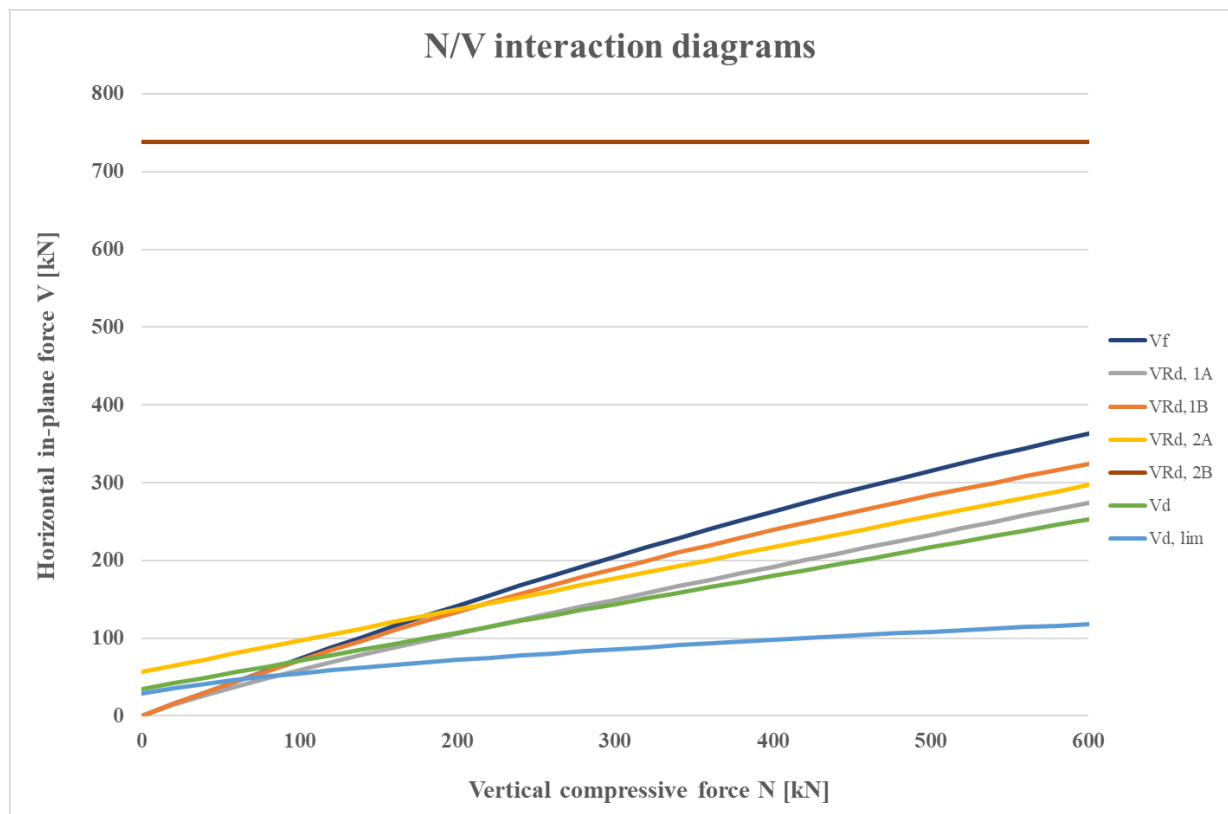
- 1) shear force corresponding to flexural failure  $V_f$
- 2) shear force corresponding to shear sliding (large eccentricity  $e_n$ ,  $f_{vk} < f_{vlt}$ )  $V_{Rd,1A}$
- 3) shear force corresponding to shear sliding (large eccentricity  $e_n$ ,  $f_{vk} = f_{vlt}$ )  $V_{Rd,1B}$
- 4) shear force corresponding to shear sliding (small eccentricity  $e_n$ ,  $f_{vk} < f_{vlt}$ )  $V_{Rd,2A}$
- 5) shear force corresponding to shear sliding (small eccentricity  $e_n$ ,  $f_{vk} = f_{vlt}$ )  $V_{Rd,2B}$
- 6) shear force corresponding to diagonal cracking  $V_d$
- 7) limit value of the shear force corresponding to diagonal cracking  $V_{d, lim}$

All failure mechanisms were explained in detail in previous sections. Also, the mechanical properties of materials and elements needed to calculate the shear forces were explained and defined. In Table 3.2 all the needed data is summarized.

Table 3.2 Properties of masonry units, mortar and masonry piers

| Masonry units and mortar   |                               |                                |                                |                               |            |            |
|----------------------------|-------------------------------|--------------------------------|--------------------------------|-------------------------------|------------|------------|
| $f_b$ (N/mm <sup>2</sup> ) | $f_{bt}$ (N/mm <sup>2</sup> ) | $f_m$ (N/mm <sup>2</sup> )     |                                |                               |            |            |
| 40                         | 4,0                           | 5                              |                                |                               |            |            |
| Masonry piers              |                               |                                |                                |                               |            |            |
| $f_k$ (N/mm <sup>2</sup> ) | $\mu=\tan(\phi)$              | $f_{vk0}$ (N/mm <sup>2</sup> ) | $f_{vlt}$ (N/mm <sup>2</sup> ) | $f_{tk}$ (N/mm <sup>2</sup> ) | $h_0$ (cm) | $\gamma_m$ |
| 11,79                      | 0,5                           | 0,2                            | 2,6                            | 0,133                         | 93,25      | 1,0        |

The interaction diagrams for the URM piers defined by seven different failure modes are shown in Figure 3.5.


 Figure 3.5 Interaction diagrams  $N/V$  for seven different failure modes



### 3.6.2 Envelope curve for data used in subsection 3.6.1

Envelope curves are very illustrative as they graphically tell the level of exploitation of the wall, as well as the collapse mechanism. Both parameters are of great value as they give insight into the expected response of a masonry pier and enable safe and optimal design. In [94] Jäger and Gams defined three different envelope curves for different ratios of height to length of the wall. The envelope curves are shown in Figure 3.6.

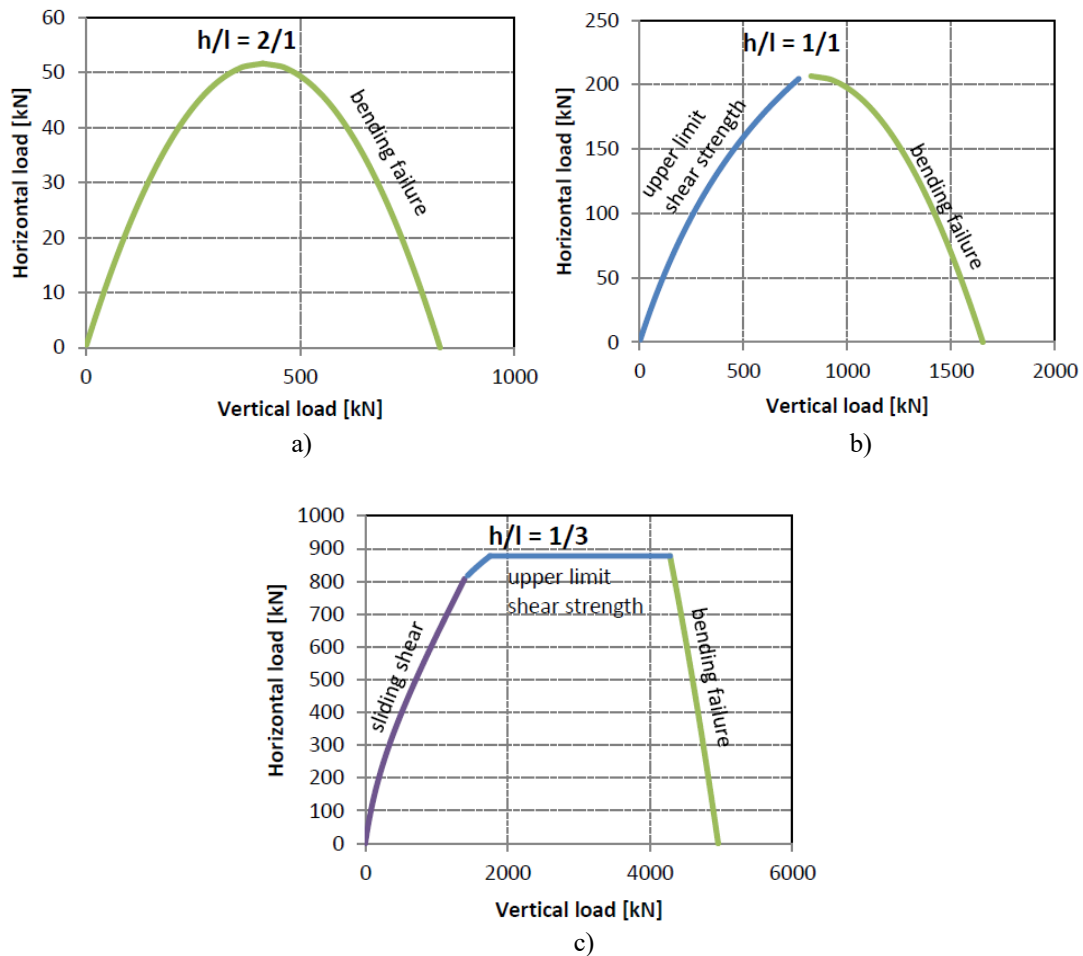


Figure 3.6 Envelope curves for a) walls with  $h/l = 2/1$  b) walls with  $h/l = 1/1$  c) walls with  $h/l = 1/3$  (sliding shear – purple, diagonal shear – blue, bending – green) [94]

For the short wall with  $h/l$  ratio of  $2/1$  bending failure governs the response over the whole range of vertical loads. For the wall with  $h/l$  ratio of  $1/1$ ,  $V_{Rd,1B}$  and  $V_{Rd,2B}$  diagonal shear is critical. For higher vertical loads, again bending failure is decisive. For the long wall with  $h/l = 1/3$ , at low vertical loads sliding shear appears. For medium vertical loads the diagonal shear takes over while the wall fails in bending for high vertical loads. Comparing the maximum horizontal load for the three walls shows that the absolute and relative shear resistance increases with decreasing  $h/l$  ratio, i.e. long walls have higher shear resistance, as is expected.

In this dissertation, a pier with  $h/l = 186,5/142 = 1,3134$  was analysed. The envelope curve for the URM pier is shown in Figure 3.7.

The values of the in-plane horizontal force  $V$  were varied between 0 and 350 kN. The values of the vertical compressive force  $N$  were varied between 0 and 600 kN. From the diagram it can be deduced that up until the point marked with A in Figure 3.7 the URM pier would fail by sliding. After that point and until the value of  $N = 600$  kN the masonry pier exhibited a diagonal shear failure. For very high values of the vertical load, a bending failure would appear. Since these values are too high to achieve in the selected laboratory, they were not considered. A similar behaviour can be seen in Figure 3.6 c).

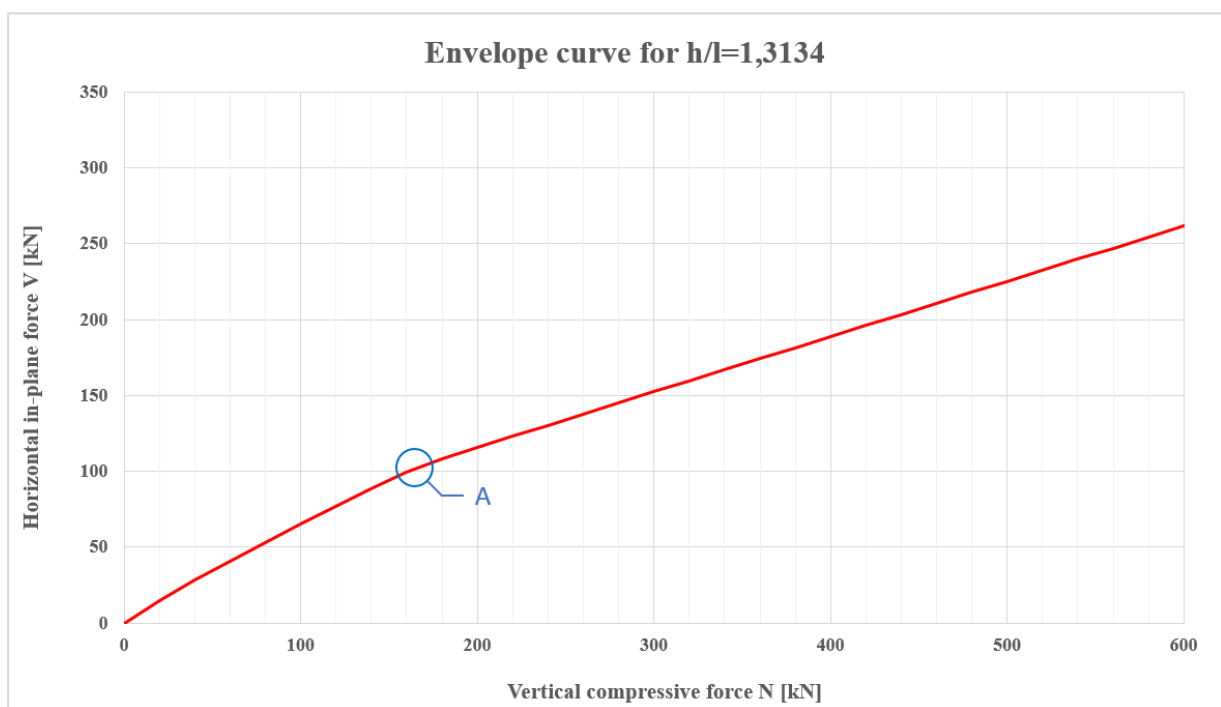


Figure 3.7 Envelope curve for the analysed URM pier

As it was mentioned, the idea of the dissertation is to achieve a diagonal shear failure in all masonry pier samples. With that in mind, after point A shown in Figure 3.7, all values of the vertical compressive force  $N$  and the corresponding horizontal in-plane shear force  $V$  may be considered. Unfortunately, these values are limited due to the possibilities of the laboratory where the experimental campaign took place. Also, the variability of certain values in Table 3.2 need to be considered. In the following section these problems will be addressed.

### 3.6.3 Parametric analysis and discussion

The envelope curve shown in Figure 3.7 considered the values chosen in subsection 3.6.1. Some of these values were taken with their characteristic value, which is not a common practice. Usually, mean values should be used that are obtained with small-scale testing. As it was explained earlier, no experiments were conducted at this phase. To bypass this problem, all characteristic values from Table 3.2 were divided by 0,8 to obtain the mean values. This simplification may be used for characteristic values according to EN 1052-3:2002 [93] that deals with the determination of the initial shear strength of masonry. Additionally, characteristic values from Table 3.2 were divided by 1,25 to see what would happen if characteristic values were underestimated. The same procedure was conducted for all values given by manufacturers to consider their variability. This way, a parametric analysis could be conducted where three types of values are used, and three different envelope curves were developed. With such an analysis the values of the vertical compressive force  $N$  and the corresponding horizontal in-plane shear force  $V$  may be considered in a wider span and with more safety. The values for the parametric analysis are shown in Table 3.3. “Version 1” values correspond to values from Table 3.2 divided by 1,25, “Version 2” to values from Table 3.2 and “Version 3” to values from Table 3.2 divide by 0,8. Of course, values  $h_0 = 93,25$  cm and  $\gamma_m = 1,0$  do not change. The result of the analysis were three envelope curves shown in Figure 3.8.

Table 3.3 Values of properties for the parametric analysis

|                                | Version 1 | Version 2 | Version 3 |
|--------------------------------|-----------|-----------|-----------|
| $f_b$ (N/mm <sup>2</sup> )     | 32        | 40        | 50        |
| $f_{bt}$ (N/mm <sup>2</sup> )  | 3,2       | 4,0       | 5,0       |
| $f_m$ (N/mm <sup>2</sup> )     | 4,0       | 5,0       | 6,25      |
| $f_k$ (N/mm <sup>2</sup> )     | 9,43      | 11,79     | 14,74     |
| $\mu = \tan(\phi)$             | 0,4       | 0,5       | 0,625     |
| $f_{vk0}$ (N/mm <sup>2</sup> ) | 0,16      | 0,2       | 0,25      |
| $f_{vlt}$ (N/mm <sup>2</sup> ) | 2,08      | 2,6       | 3,25      |
| $f_{tk}$ (N/mm <sup>2</sup> )  | 0,106     | 0,133     | 0,166     |

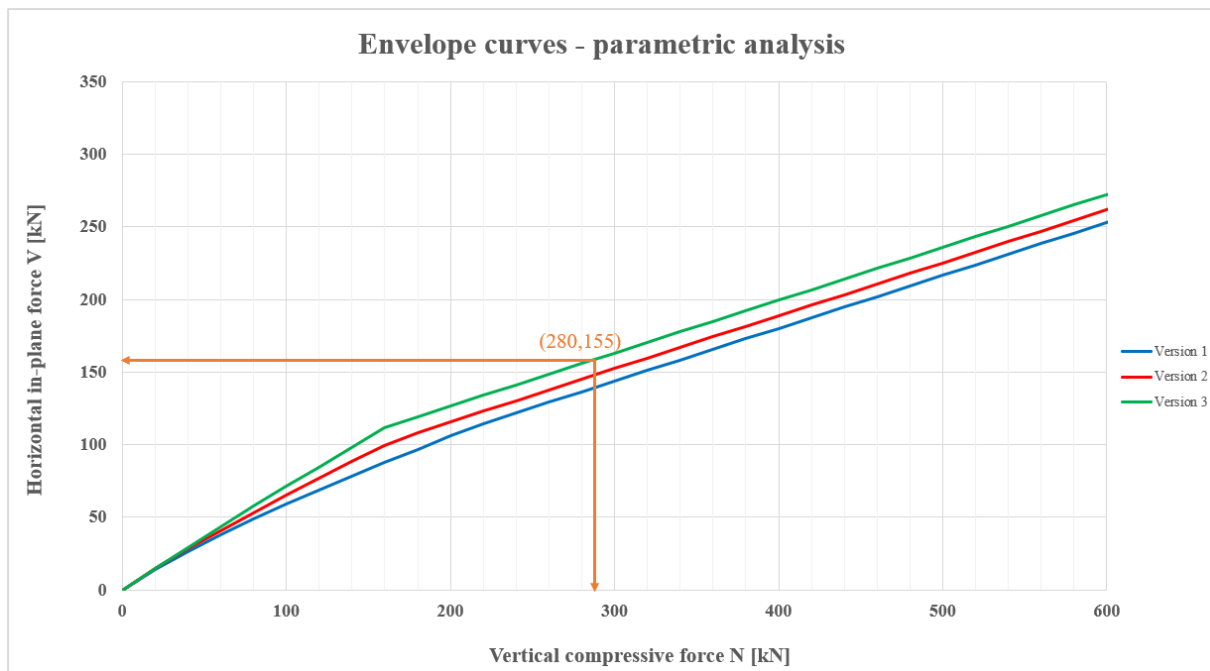


Figure 3.8 Envelope curves for the parametric analysis

The blue (Version 1), red (Version 2) and green (Version 3) envelope curves are similar in shape and corresponding values. The point in which the type of failure transforms from the sliding shear into the diagonal shear failure (explained in Figure 3.7 as point A) was practically the same for Version 2 and Version 3 envelope curves (around  $N = 160$  kN). In Version 1 envelope curve, this point comes at a later stage, around  $N = 220$  kN. What was also deduced is that for smaller values of properties (Version 1), the value of the achieved horizontal in-plane force (capacity) of the pier was also smaller. Consequently, the laboratory test setup was defined. Besides the dimensions of the wall and the boundary conditions, the forces were defined. The maximum vertical compressive force that can be achieved in the laboratory is equal to 300 kN. Since the weight of the pier with reinforced concrete beams is approximately 30 kN, the vertical compressive force of 250 kN was chosen. With the summed value of 280 kN of vertical force, all three versions observed in the parametric analysis should exhibit a diagonal shear failure. Since the laboratory experiment was conducted by displacement control, the horizontal in-plane force (capacity)  $H$  was obtained as a result. The expected values of capacity  $H$  when  $N = 280$  kN for different versions are given in Table 3.4. In the end, it can be concluded that the value of the horizontal in-plane shear capacity of the URM pier should come in the range of 136 to 155 kN with 155 kN being the highest value expected (Figure 3.8).

 Table 3.4 Values of  $H$  for  $N = 280$  kN in URM piers (Series 1)

|          | Version 1 | Version 2 | Version 3 |
|----------|-----------|-----------|-----------|
| $H$ (kN) | 136,42    | 145,04    | 155,41    |

### 3.7 Contribution of the FRCM reinforcement

After the theoretical analysis of the URM pier has been conducted, the contribution of the FRCM system was considered for the strengthened masonry piers. The in-plane shear resistance of the FRCM system was defined in subsection 3.5 and equation 3.17. The FRCM system used in this dissertation was applied in two series of samples. In series 2, the FRCM system was applied on one longer face of the masonry piers. In series 3 the FRCM system was applied in a C-shaped pattern. Both series were defined and dissected in subsection 3.1. In both cases only one mesh made from glass fibres was used. Therefore, the number of layers of the FRCM system is  $n_f = 1$ . The thickness of this layer is  $t_{vf} = 0,06$  mm. Since the FRCM system is applied on the entire face of the wall, the design dimension of the reinforcement measured orthogonally to the shear force is equal to the height of the pier  $l_f = h = 1865$  mm. The mechanical properties of the materials used in the FRCM system are summarized in Table 3.5. For the purposes of this theoretical analysis, the partial safety factors  $\gamma_d$  and  $\gamma_m$  are not considered.

Table 3.5 Mechanical properties of the FRCM system

| FRCM system |                    |        |                    |                            |
|-------------|--------------------|--------|--------------------|----------------------------|
| $\alpha_t$  | $\varepsilon_{fk}$ | $\eta$ | $\varepsilon_{fd}$ | $E_f$ (N/mm <sup>2</sup> ) |
| 0,8         | 0,02               | 0,9    | 0,018              | 74000                      |

With everything stated above, the contribution of the FRCM system in strengthened masonry piers can be seen as an increase of the in-plane shear capacity. This contribution was calculated from equation 3.17:

$$V_{t,f} = \frac{1}{\gamma_{kd}} \cdot n_f \cdot t_{vf} \cdot l_f \cdot \alpha \cdot \varepsilon_{fd} \cdot E_f = n_f \cdot t_{vf} \cdot l_f \cdot \alpha \cdot \varepsilon_{fd} \cdot E$$

$$= 1 \cdot 0,06 \cdot 1865 \cdot 0,8 \cdot 0,018 \cdot 74000 = 119 \text{ kN}$$

With the addition of this value to the values in Table 3.4, the in-plane shear resistance of the strengthened masonry piers was gained. The values are given in Table 3.6. In the end, it can be concluded that the value of the horizontal in-plane shear capacity of the strengthened pier should come in the range of 255 to 274 kN with 274 kN being the highest value expected.

Table 3.6 Values of  $H$  for  $N = 280$  kN in strengthened masonry piers (Series 2)

|          | Version 1 | Version 2 | Version 3 |
|----------|-----------|-----------|-----------|
| $H$ (kN) | 255,42    | 264,04    | 274,41    |

It is noteworthy to mention that this increase is only valid for series 2 where the FRCM system is applied on the longer face of the pier. The contribution of the clamping details in series 3 could not be considered with the current version of the CNR-DT 215/2018 standards. Therefore, in terms of the available analytical procedures, no increase in the in-plane shear force capacity should come from the usage of new clamping details. After the results of the experimental and numerical campaign are explained in the following sections, the potential contribution of the clamping details will be dissected and defined.

## 4 EXPERIMENTAL CAMPAIGN

The experimental campaign was conducted at the structural testing laboratory at the Faculty of Civil Engineering and Architecture, University of Osijek. The experimental campaign involved the testing of nine masonry piers with reinforced concrete beams. Besides that, the mechanical properties of materials were also obtained. The testing included the compressive strength of masonry elements (clay bricks) and the characteristic initial shear strength of masonry piers. Additionally, the compressive strength of concrete and mortar used in the assembly of the pier were also gathered in the construction process of the piers.

### 4.1 Construction of pier samples

The masonry piers were constructed in a construction company “Massa d.o.o.” in April and May of 2023. The first elements to be constructed were the reinforced concrete beams. In total, 18 elements were constructed. For that purpose, three mixtures of concrete were used. The reinforcement cages were the same for all beams and can be seen in Figure 4.1.



Figure 4.1 Construction of reinforcement cages

The concrete was placed using a vibrating poker and formwork vibrators immediately after being mixed. Simultaneously, three beams were cast and left in the formwork for 24 hours. After 24 hours, the beams were removed from the formwork, and the next group was cast. After the concrete was placed, the remaining concrete mix was shaped into cubes with compaction on a vibrating table. The upper (exposed) surfaces of beams and cubes were additionally

smoothed by hand tools. In Figure 4.2 the reinforcement cage inside of the formwork is shown and fully casted beams may be seen.



Figure 4.2 Formwork of the reinforced concrete beams

After 28 days, the beams were ready to be used in the construction of masonry piers. Upon the bottom beams a masonry pier was constructed. The bricks used were manufactured by Wienerberger Croatia. As it was explained in subsection 3.1.1 the bricks were laid in two orthogonal directions from one layer to the other. In the first (bottom) layer the bricks were placed perpendicular to the largest surface of the pier. The brick laying pattern is shown in Figure 4.3. After an entire pier was constructed, the top beam was added. A three-day period was usually taken before the top beam was placed, so that the pier can stiffen. The masonry pier and the concrete beams were connected by the same mortar used for the pier construction. When the pier was assembled, the samples for the testing of the compressive strength of mortar were also made. The same series of mortar was used for the construction of three piers. Therefore, three series of mortar were mixed in total. After the piers were constructed, the curing period of 28 days needed to pass before six of the nine piers could be strengthened or the URM piers could be tested. Fully constructed URM piers can be seen in Figure 4.4. In the same figure, a wooden safety structure is shown. The purpose of this structure was to keep the piers fastened during the transportation phase since they are very slender and could overturn very easily. Besides the safety structure, the piers were also tied to the transportation vehicle to ensure safety.





Figure 4.3 Construction process of the masonry piers



Figure 4.4 URM piers

The application of the FRCM system in six masonry piers was also done by “Massa d.o.o.”. The components used for the FRCM system were provided by a company named RÖFIX HR. The application of the system was done in several steps. First, the holes for transversal connectors were drilled and cleaned by blowing air into them. A piece of paper was placed in these holes so that they could be located at later stages. At this step, the superficial grouts were removed. After that, the first layer of mortar was applied. This layer is 5 to 7 mm thick. The mortar matrix is a product called Röfix SismaDur FRCM. After the mortar hardens, an IPN primer was applied to the mortar matrix. The primer is a product called FB-IPN01 and is usually applied with a brush or a roller. At this stage, half of the previously prepared fresh mix of primer was used. In the following step, the fibreglass reinforcement was placed on the fresh layer of primer using an anti-bubble impregnation roller. After the reinforcement was placed on the entire surface of the pier (and on the sides in the case of Series 3), the second layer of FB-IPN01 was applied. The applied mesh can be seen in Figure 4.5. To achieve a better connection of the mesh to the masonry substrate, transversal connectors were installed. In the predrilled holes the bonding agent was applied first. After that the transversal connectors were installed in the shape of GFRP bars type FB-TUP10-VAR1A produced by FibreNet. The installation of transversal connectors is shown in Figure 4.6. In the final step of the process the second layer of the mortar was applied which can also be seen in Figure 4.6. The same thickness of 5 to 7 mm was used as in the first layer. Strengthened masonry piers (Series 2 and 3) can be seen in Figure 4.7.



Figure 4.5 Application of the glass fibre mesh



Figure 4.6 Installation of transversal connectors and application of the final layer of the mortar matrix



Figure 4.7 Strengthened masonry piers

## 4.2 Testing of mechanical properties of materials

### 4.2.1 Compressive strength of concrete

Concrete cubes with a side length of 15 cm were tested for compression strength at the age of 28 days to enable the classification of concrete. The testing was conducted in the laboratory of a company called “Betonekspert” in Osijek using a device with a maximum force of 3000 kN. The samples were tested at the age of 28 days, in May of 2023. Figure 4.8 shows a sample cube just before the compression strength test. Three samples were taken in total in the process of casting the reinforced concrete beams.



Figure 4.8 Compression strength testing of concrete cubes

The tests were conducted in accordance with the HRN EN 12390-1 [95] and HRN EN 12390-3 [96] standards. All samples were dried and cleaned before testing, and all measuring devices were appropriately calibrated. The dimensions of all tested cubes were satisfactory. Table 4.1 shows the test results for all groups of cubes. It was estimated that an acceptable mode of failure was achieved for all samples. All results were accepted and processed.

Table 4.1 Results of the compressive strength testing of concrete cubes.

| Sample              | Density [kg/m <sup>3</sup> ] | Compressive strength $f$ [N/mm <sup>2</sup> ] |
|---------------------|------------------------------|---|
| Series 1 – sample 1 | 2330                         | 38,10   |
| Series 1 – sample 2 | 2340                         | 41,70   |
| Series 1 – sample 3 | 2330                         | 36,80   |

In Table 4.2, the values required for the classification of concrete are presented. The classification was carried out in accordance with the identity control procedure outlined in the HRN EN 206-1 standard annex B [97]. The mean value of the concrete strength  $f_{cm}$  is shown in the second column of the table. In the third column, a 15 % deviation from the mean value is indicated. All samples must fall within these values, which is satisfied by comparing the values from Table 4.1 with the values in the third column of Table 4.2. The mean value must be greater by  $1 \text{ N/mm}^2$  than the nominal characteristic value of the concrete grade, which is why the fourth column of Table 4.2 shows  $f_{cm} - 1$ . The concrete grade for three samples is shown in the fifth column. The grade selected is C30/37. The next higher concrete grade is C35/45, and the value in the fourth column should be greater than 45 for that grade. Each individual sample must have a strength of at least  $f_{ck} - 4$ , as shown in the last column of Table 4.2. By comparing the results from Table 4.1 with these values, it is evident that all samples met the requirements, and the classification from Table 4.2 was accepted.

Table 4.2 Classification of concrete based on the results of cube testing

| Series | $f_{cm}$ [ $\text{N/mm}^2$ ] | 15 % deviation | $f_{cm} - 1$ | Concrete grade | $f_{ck} - 4$ |
|--------|------------------------------|----------------|--------------|----------------|--------------|
| 1      | 38,87                        | 33,04 – 44,70  | 37,87        | <b>C30/37</b>  | 33,00        |

#### 4.2.2 Compressive strength of masonry units

Masonry units, that were tested for the determination of the compressive strength, were taken during the construction of masonry piers. All masonry units were sampled from the same consignment using the random sampling method according to HRN EN 771-1:2011 standard [98]. In total 9 test specimens were defined using 18 clay bricks. The minimum number of test specimens is six. Before connecting the two bricks into one sample, the surfaces of bricks were properly prepared by grinding. The test specimens were defined by connecting two bricks with mortar. Additionally, at the surfaces of the bricks mortar was applied. This process is called capping. Usually, a cement based capping mortar is used. The declared dimensions of the larger face of the masonry units are  $250 \times 120 \text{ mm}$ . The mean values of the same dimensions measured on the 9 samples are  $251 \times 120 \text{ mm}$ . This is satisfactory. The test specimens can be seen in Figure 4.9. Before the testing campaign was conducted, the specimens were conditioned. The air-dry condition was chosen. The specimens were stored in the laboratory for 14 days under the temperature of  $15 \text{ }^\circ\text{C}$  and under the relative humidity of 65 %. The number of samples, the curating process and the testing procedure were all defined according to HRN EN 772-1:2011 standard [99].



Figure 4.9 Test specimens for the determination of the compressive strength of masonry units

The testing was conducted in the structural testing laboratory at the Faculty of Civil Engineering and Architecture, University of Osijek. The samples were tested in October of 2023 after the curating period. Table 4.3 shows the test results for all samples. It was estimated that an acceptable mode of failure was achieved for all samples. All results were accepted and processed. The test specimens before and after the testing procedure can be seen in Figure 4.10.

Table 4.3 Results of the compressive strength testing of masonry units

| Sample   | Force at failure [kN] | Compressive strength $f$ [N/mm <sup>2</sup> ] |
|----------|-----------------------|---|
| Sample 1 | 821,50                | 27,38   |
| Sample 2 | 1003,70               | 33,46   |
| Sample 3 | 857,20                | 28,57   |
| Sample 4 | 1053,30               | 35,11   |
| Sample 5 | 994,60                | 33,15   |
| Sample 6 | 1051,20               | 35,04   |
| Sample 7 | 1004,10               | 33,47   |
| Sample 8 | 965,30                | 32,18   |
| Sample 9 | 939,80                | 31,33   |



Figure 4.10 Test specimens before and after the testing

In Table 4.4, the values required for the classification of masonry units are presented. Firstly, the mean value of the force at failure  $F_{avg}$  is shown in the second column. In the third column, the coefficient of variation is calculated for the force at failure. The variation is satisfactory since it is under 10 %. The mean value of the compressive strength of masonry units,  $f_{avg}$  is shown in the fourth column of the table. In the fifth column, the coefficient of variation is calculated for  $f_{avg}$ . The variation is satisfactory since it is under 10 %.

Table 4.4 Mean values and variation coefficients for the compressive strength of masonry units

| Series | $F_{avg}$ [kN] | $\sigma_F$ [kN] | $f_{avg}$ [N/mm <sup>2</sup> ] | $\sigma_f$ [N/mm <sup>2</sup> ] |
|--------|----------------|-----------------|--------------------------------|---------------------------------|
| 1      | 965,60         | 76,00           | 32,19                          | 2,53                            |

In order to obtain the normalised compressive strength used in design procedures, the air-dry compressive strength of masonry units was multiplied by a shape factor,  $\delta$ , given in Table A.1 of HRN EN 772-1:2011 standard [99]. The width and height of the test specimens that are needed for the definition of factor  $\delta$  were determined in accordance with HRN EN 772-16:2011 standard [100]. For the tested specimens the value  $\delta = 1,15$  was derived from Table A.1. Therefore, the normalised mean compressive strength,  $f_b = 37,02$  N/mm<sup>2</sup> was calculated by multiplying  $f_{avg}$  by 1,15. This value will be used in the numerical campaign in the following paragraphs.

### 4.2.3 Compressive strength of hardened mortar

Samples for the determination of the compressive strength of hardened mortar were taken during the construction of masonry piers. The sampling was conducted according to HRN EN 1015-2:2019 standard [101] and the testing was conducted according to HRN EN 1015-11:2019 standard [102]. The test specimens had the dimensions of 160 mm × 40 mm × 40 mm. Three specimens were provided per batch of mortar used. For the compressive strength test, the specimens were broken into two halves to provide six half specimens. The mould for forming test specimens with three samples taken during the construction of masonry piers are shown in Figure 4.11. The compartment walls of the mould were at least 8 mm thick and rigid enough to prevent distortion or damage to specimens on removal. The assembled mould frame was firmly attached to a rigid base plate by means of a fixing screw arrangement. In this case, 12 samples of mortar in total were taken during the construction.



Figure 4.11 Three samples for the compressive strength test of hardened mortar

The testing was also conducted in the laboratory of a company called “Betonekspert” in Osijek. The samples were tested at the age of 28 days, in June of 2023. The loading rate of the device was 200 N/s as it is suggested in HRN EN 1015-11:2019 [102] for mortar class M5 that was used. The dimensions of all samples were satisfactory. Table 4.5 shows the test results for all groups of samples. It was estimated that an acceptable mode of failure was achieved for all samples. All results were accepted and processed.

Table 4.5 Results of the compressive strength testing of hardened mortar samples

| Sample               | Density [kg/m <sup>3</sup> ] | Compressive strength $f$ [N/mm <sup>2</sup> ] | Mean $f$ [N/mm <sup>2</sup> ] |
|----------------------|------------------------------|---|-------------------------------|
| Series 1 – sample 1  | 2067                         | 6,40  | 6,33                          |
| Series 1 – sample 2  | 2073                         | 6,50  |                               |
| Series 1 – sample 3  | 2057                         | 6,10  |                               |
| Series 2 – sample 4  | 2010                         | 6,10  | 6,10                          |
| Series 2 – sample 5  | 2022                         | 6,30  |                               |
| Series 2 – sample 6  | 2008                         | 5,90  |                               |
| Series 3 – sample 7  | 1905                         | 5,70  | 5,73                          |
| Series 3 – sample 8  | 1912                         | 5,50  |                               |
| Series 3 – sample 9  | 1897                         | 6,00  |                               |
| Series 4 – sample 10 | 1946                         | 6,30  | 6,30                          |
| Series 4 – sample 11 | 1940                         | 5,90  |                               |
| Series 4 – sample 12 | 1962                         | 6,70  |                               |

Specifications of mortar for masonry are provided in the HRN EN 998-2:2016 standard [88]. According to [88] when masonry mortar is sampled and tested the compressive strength shall not be less than the declared compressive strength or the declared compressive strength class. Therefore, the results shown in Table 4.5 are all valid for mortar M5. At the end of the table, mean values for each series are shown. The mean value of the compressive strength for all samples equals  $f_m = 6,12 \text{ N/mm}^2$  and will be considered during the numerical modelling campaign.



#### 4.2.4 Initial shear strength of masonry

The test specimens were tested in the structural testing laboratory at the Faculty of Civil Engineering and Architecture, University of Osijek. In total, 9 samples were prepared. The samples were prepared according to HRN EN 1052-3 standard [93]. The test specimens consisted of bricks and mortar that were used during the construction of the masonry piers. For each test specimen, three clay bricks were connected with 1 cm thick mortar as it can be seen in Figure 4.12. Before the masonry units were connected, the bearing surfaces were cleaned. After the assembly, the masonry units were checked for linear alignment and level using a set-square and spirit level. Excess mortar was then removed using a trowel.



Figure 4.12 Nine test specimens for the initial shear strength test of masonry

The samples were tested in September of 2023 after the curing period at the age of 28 days. The testing procedure was conducted according to HRN EN 1052-3 standard [93]. Firstly, the test setup was defined, and the test specimens were placed into the testing machine. When placing the test specimens in the testing machine, the ends of the specimen were properly supported. For this purpose, 12 mm thick steel plates were used. The test setup is shown in Figure 4.13.



Figure 4.13 Test setup for the initial shear strength test of masonry

Before the application of the shear stress, the precompression loads were applied. For each of the three precompression loads, three test specimens were used. The precompression loads are equal to  $0,2 \text{ N/mm}^2$ ,  $0,6 \text{ N/mm}^2$ , and  $1,0 \text{ N/mm}^2$ . The precompression loads were kept within 2 % of the initial value. For each precompression load, a shear stress was applied until failure. In Figure 4.14, the test specimens after testing are shown.



Figure 4.14 Test specimens after the testing

For each test specimen, the shear strength was calculated according to the following equation:

$$f_{vk0i} = \frac{F_{i, \max}}{2 \cdot A_i} \quad (4.1)$$

where:  $f_{vk0i}$  shear strength of the test specimen  
 $F_{i, \max}$  shear force at failure  
 $A_i$  loaded area

The loaded area  $A_i$  for all samples was the same and equal to 30000 mm<sup>2</sup>. The results of the testing campaign can be seen in Table 4.6. In the second column the values of precompressions are shown. The shear force at failure,  $F_{i, \max}$  for each test are shown in the third column. By dividing the shear force with the loaded area, the shear strength was obtained and shown in the fourth column. The mean values of the shear strength for each precompression phase were calculated and are shown in the fifth column.

With the values from the second and the fifth column a graph is plotted. On the horizontal axis the values of the mean shear strengths were placed and on the vertical axis the related precompression values were placed. Therefore, three points were defined. After that, a line was plotted using the linear regression methodology of the defined points. The shear strength to precompression diagram can be seen in Figure 4.15. The initial shear strength of masonry was obtained by intercepting the line (dotted blue line in Figure 4.15) with the vertical axis. The value of  $f_{vk0i} = 0,23 \text{ N/mm}^2$  was achieved. This value was taken as the second value in the formula of the diagram seen in Figure 4.15. The first value in the diagram, next to x, is the slope of the line and representative of the angle of internal friction.

Table 4.6 Results of the initial shear strength testing of masonry test specimens

| Sample | Precompression [N/mm <sup>2</sup> ] | Shear force [kN] | Shear strength, $f_{vk0i}$ [N/mm <sup>2</sup> ] | Mean $f_{vk0i}$ [N/mm <sup>2</sup> ] |
|--------|-------------------------------------|------------------|---|--------------------------------------|
| 1-1    | 0,2                                 | 12,50            | 0,21  | 0,37                                 |
| 1-2    | 0,2                                 | 36,56            | 0,61  |                                      |
| 1-3    | 0,2                                 | 18,38            | 0,31  |                                      |
| 2-1    | 0,6                                 | 53,24            | 0,89  | 0,99                                 |
| 2-2    | 0,6                                 | 71,25            | 1,19  |                                      |
| 2-3    | 0,6                                 | 53,53            | 0,89  |                                      |
| 3-1    | 1,0                                 | 85,12            | 1,42  | 1,20                                 |
| 3-2    | 1,0                                 | 80,80            | 1,35  |                                      |
| 3-3    | 1,0                                 | 50,88            | 0,85  |                                      |

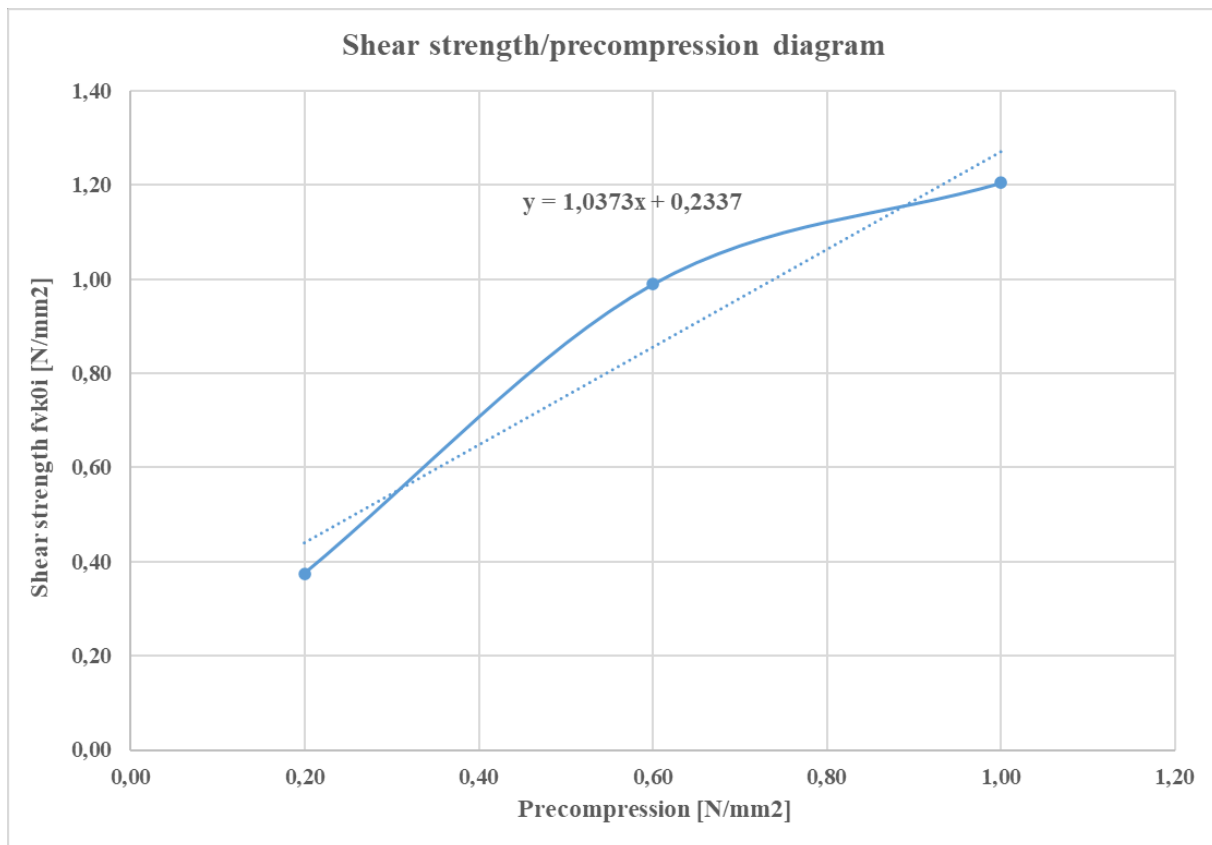


Figure 4.15 Shear strength/precompression diagram for masonry

### 4.3 Quasi-static cyclic displacement-controlled testing of masonry piers – Preparation and testing protocol

The quasi-static cyclic testing of masonry piers was conducted at the structural testing laboratory at the Faculty of Civil Engineering and Architecture, University of Osijek in three phases. In each phase, one series of masonry piers was tested. The URM piers (Series 1 – URM) were tested in June of 2023, the FRCM strengthened piers (Series 2 – FRCM) in June and July of 2023 and the masonry piers with new FRCM clamping details (Series 3 – CFRCM) were tested in September of 2023. The specimens were tested under constant vertical load and quasi-static cyclic lateral displacements.

#### 4.3.1 Transportation and placement of samples

Due to the slenderness, size and weight of masonry piers, the transportation had to be organized and executed carefully. The transportation from the construction site at “Massa d.o.o.” to the structural testing laboratory was done in three phases. In each phase, three masonry piers were transported. The transportation of the piers can be seen in Figure 4.16. Two types of safety measures were implemented during transport. First, the masonry piers were adequately fastened to the vehicle using buckles, so they do not overturn during transportation.

The second safety measure that was taken included a wooden safety structure that was constructed around the masonry piers. Both measures can be seen in Figure 4.16.



Figure 4.16 Transportation of masonry piers to the laboratory

After the masonry samples were transported to the laboratory, they were placed inside the test setup. This transportation was conducted by a laboratory track crane. For the purposes of this transport, special steel hooks were added at the foundation reinforced concrete beams. The steel chains that were connected to the crane were connected also to these hooks providing a safe way of transporting the masonry piers. The transportation inside the laboratory can be seen in Figure 4.17. In the end, all masonry piers were placed at the experiment setup site inside the laboratory.



Figure 4.17 Transportation of masonry piers inside the laboratory

### 4.3.2 The experiment setup and the testing equipment

In Figure 4.18, a schematic display of the experimental setup for testing the shear capacity by applying cyclic loading is shown. During construction, a reinforced concrete beam was placed at the top and bottom of the pier. The role of the top beam was to distribute vertical loads evenly and transmit horizontal forces from the hydraulic jacks. At the top of the reinforced concrete beam, vertical loading was applied by two hydraulic jacks, each with a capacity of 500 kN. All hydraulic jacks were supported by a rigid reference steel frame that was anchored to a rigid reactive base and, at the same time, was supported by a rigid vertical reactive wall. A roller support with a teflon coating and steel rollers was inserted between the reinforced concrete beam and the steel plates placed under the vertical hydraulic jacks to ensure a smooth horizontal surface and prevent shear deformations of the jacks caused by friction during the application of horizontal loads to the masonry pier. The role of the bottom reinforced concrete beam was to properly connect the masonry pier to the laboratory floor. For this purpose, four steel threaded rods were used with related nuts. This way the masonry pier was fixed to the floor and by adding the defined values of vertical forces, no overturning of the pier was possible.

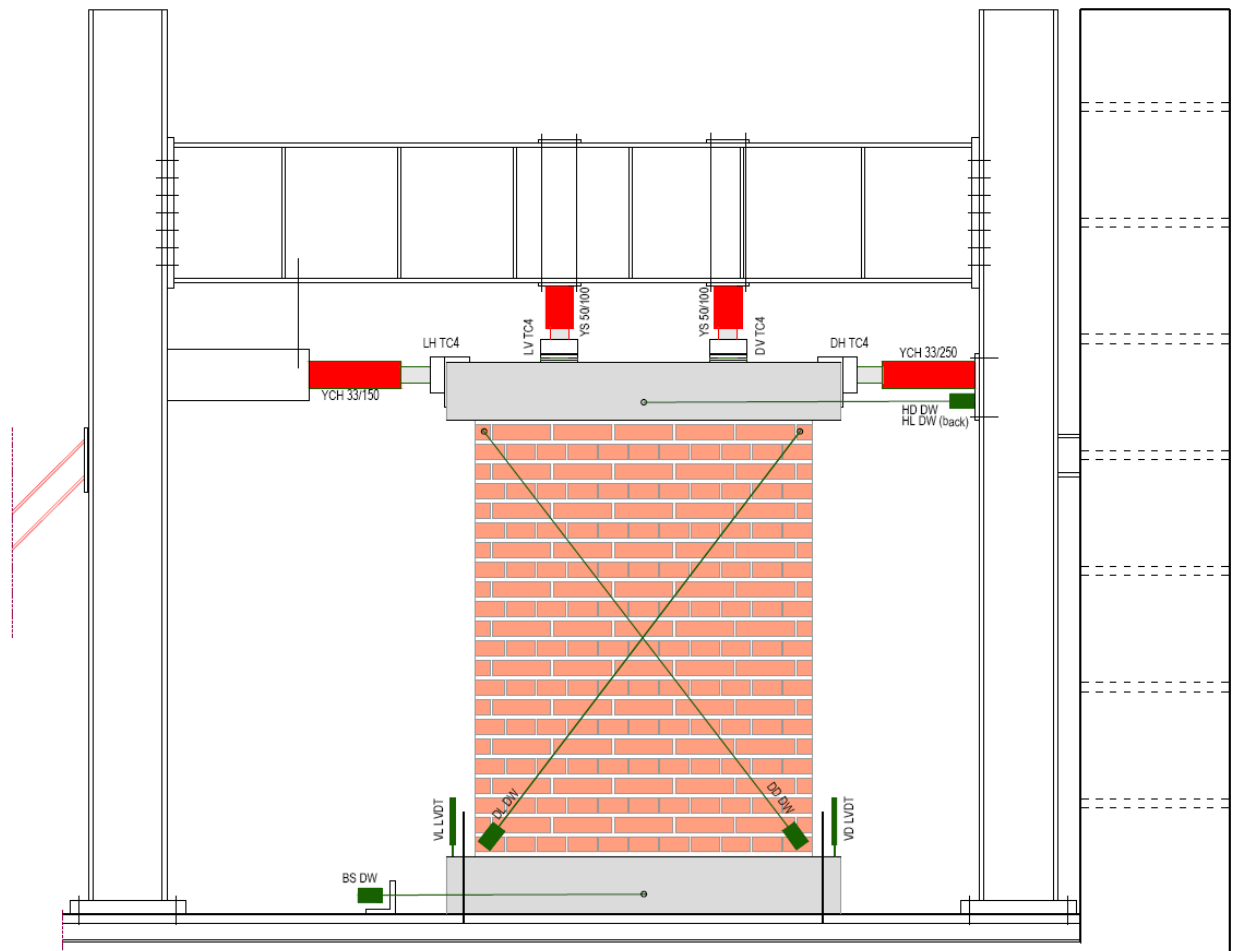


Figure 4.18 Schematic display of the experimental setup

The cyclic testing of the shear capacity was conducted in two steps. First, a gradual vertical force,  $F_v$ , was applied until reaching a total value of 250 kN. Two jacks were used each applying a vertical force equal to 125 kN (marked YS 50/100 in Figure 4.18). The valves on the jacks were closed when the designed compressive stress was achieved. The compressive stress was taken as  $\sigma = 0,7$  MPa, which may be slightly higher than the usual vertical load for a constructed building but was chosen with the specific goal of achieving diagonal shear failure.

In the second step, two horizontal jacks were used. The horizontal jack on the left (marked YCH 33/150 in Figure 4.18) has a maximum displacement range of 150 mm. The horizontal jack on the right (marked YCH 33/250 in Figure 4.18) has a maximum displacement range of 250 mm. Both horizontal jacks have a force capacity of 335 kN. With the jack valves closed, further vertical movement of the pier at the level of the top reinforced concrete beam and its rotation were prevented. As a consequence of using such a testing method, there was an increase in vertical load along with an increase in horizontal load due to the forcibly imposed controlled displacements.

To achieve the best possible results, a combination of testing equipment was set up on the masonry piers. To capture the in-plane response of masonry piers in the most precise manner, a total of five wire sensors (draw-wire), two linear variable differential transformer (LVDTs), and four pressure gauges were installed. The labels and properties of all instruments for measuring displacements, deformations, and forces and of the hydraulic jacks used in the testing procedure are shown in Figure 4.18 and are explained as follows:

Instruments:

1) Horizontal displacements at the top of the sample:

HD DW ( $d_{h1}$ ) – Draw wire SX50, range: 100 mm

HL DW ( $d_{h2}$ ) – Draw wire SX50, range: 100 mm

2) Horizontal displacement at the bottom of the sample (sliding):

BS DW ( $d_{h3}$ ) – Draw wire SX50, range: 100 mm

3) Vertical displacements of the bottom of the sample:

VL LVDT ( $d_{v1}$ ) – RDP DC TH 500A, range:  $\pm 12,5$ mm

VD LVDT ( $d_{v2}$ ) – RDP DC TH 500A, range:  $\pm 12,5$ mm

4) Diagonal deformations of the sample:

DL DW1 ( $d_{d1}$ ) – Draw wire SX50, range: 100 mm

DD DW ( $d_{d2}$ ) – Draw wire SX50, range: 100 mm

Hydraulic jacks:

1) Horizontal forces at the top of the sample:

YALE YCH 33/250 ( $F_{h1}$ ), range: 335 kN / 250 mm

AEP DH TC4 force transducer 500 kN

YALE YCH 33/150 ( $F_{h2}$ ), range 335 kN / 150 mm

AEP LH TC4 force transducer 500 kN

2) Vertical forces at the top of the sample:

YALE YS 50/100 ( $F_v$ ), range: 500 kN / 100 mm

AEP DV TC4 force transducer 500 kN

AEP LV TC4 force transducer 500 kN

The positions where the values of the displacements ( $d_{h1}$ ,  $d_{h2}$ ,  $d_{h3}$ ,  $d_{v1}$ ,  $d_{v2}$ ) deformations ( $d_{d1}$ ,  $d_{d2}$ ), and forces ( $F_{h1}$ ,  $F_{h2}$ ,  $F_v$ ) were measured are shown in Figure 4.19.

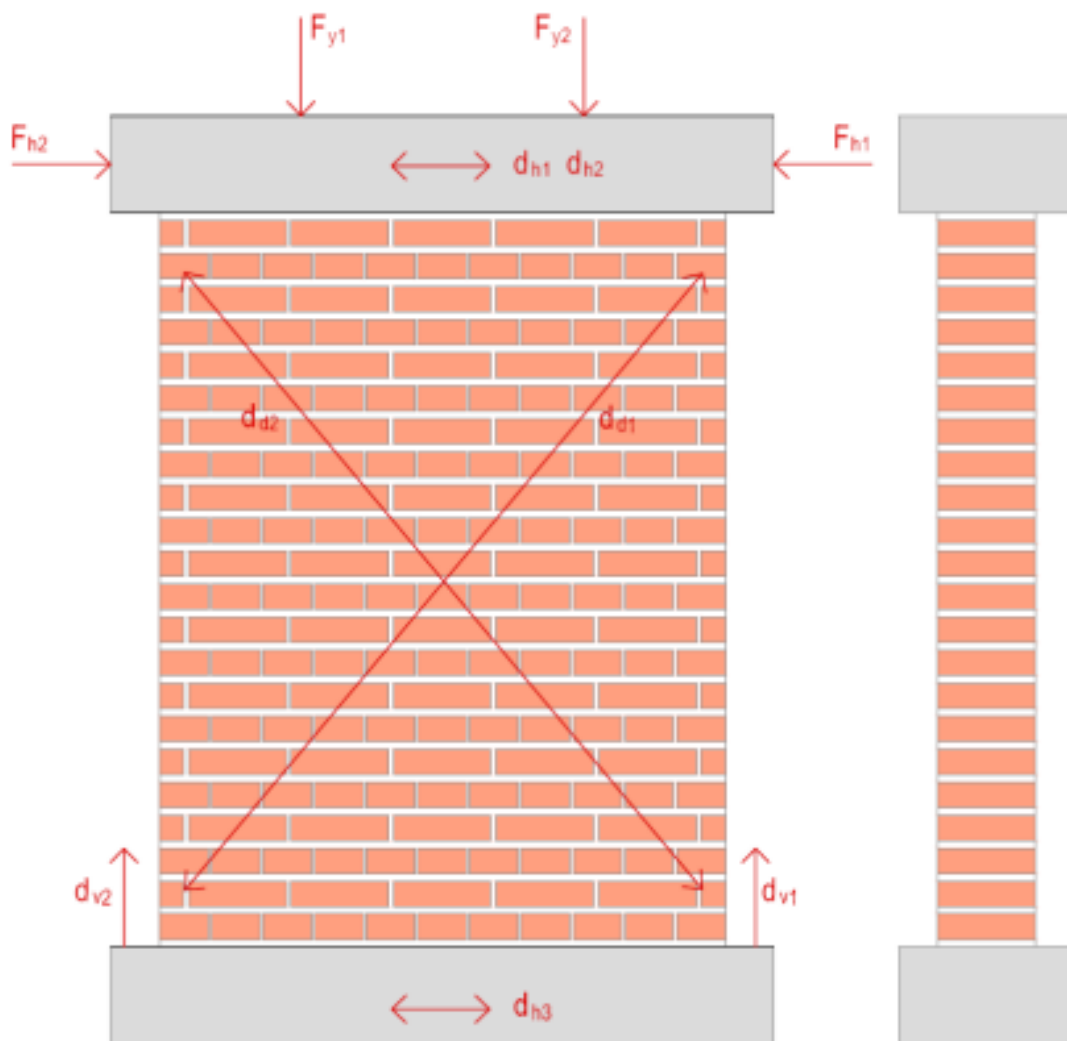


Figure 4.19 Overview of measured values



### 4.3.3 The quasi-static cyclic testing protocol

The quasi-static cyclic testing protocol replicated the seismic effects by the slow application of cyclic displacements. The adopted approach aimed to identify and capture accumulated damage, to enable the detection of the failure mechanism and to determine the force–displacement properties. The loading history consisted of stepwise increasing deformation amplitudes. In a complete cycle the target displacement was imposed in the positive and negative loading direction, returning to the original position of the pier. The first step was 1 mm in both directions. In each next step the displacement is increased 1 mm in comparison to the previous step. The loading history adopted for all masonry piers in the quasi-static cyclic testing is shown in Figure 4.20. The loading protocol included 13 to 22 displacement amplitude steps.

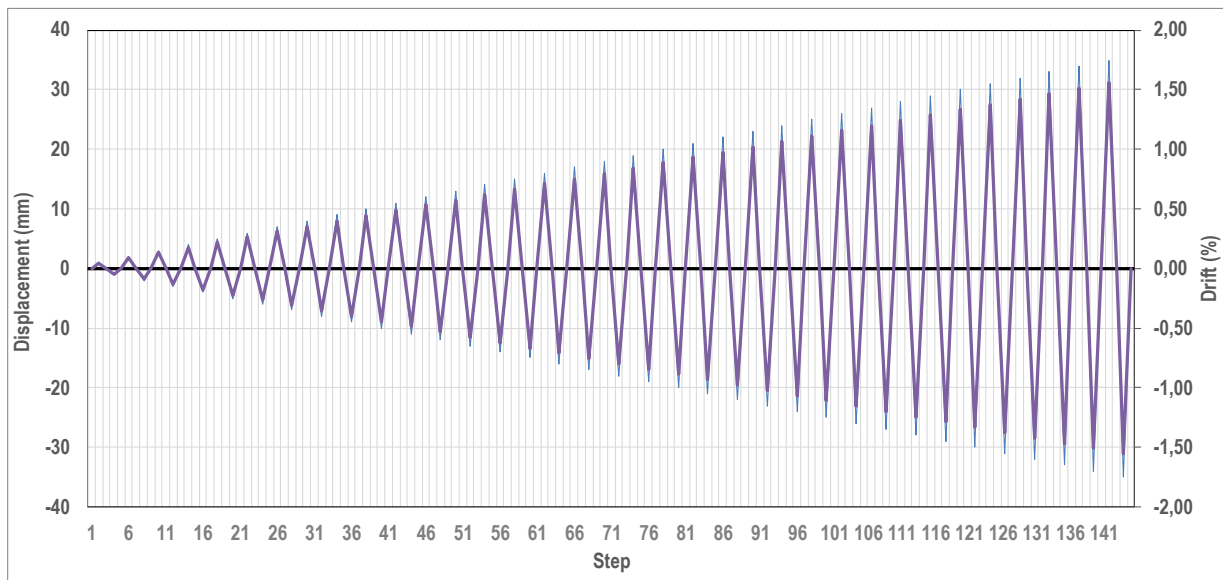


Figure 4.20 Loading history in the testing protocol

## 4.4 Quasi-static cyclic displacement-controlled testing of masonry piers – Results

In the following pages, the results of the tests for each series of piers are presented separately. The results are presented in the order in which the tests were conducted, with notes related to the recorded behaviour. The results for all piers are graphically and numerically presented. The graphical representation of results is shown in form of hysteresis curves (experimental response curves) and resistance envelope curves that were derived from them. The resistance envelope curves were formed by connecting the peak points in the loading cycles under increasing deformations. In these diagrams, on the horizontal axis the horizontal displacement of the pier is shown in millimetres (mm). On the vertical axis the horizontal in-

plane force is shown in kilonewtons (kN). The most important values of each curve are shown in tables. After that, the results for all series of piers are shown, and comparisons are made.

#### 4.4.1 Series 1 – URM – Unreinforced masonry piers

After the pier was placed at the testing position and all the instrumentation was set, the first step was to check the dimensions of the pier. The dimensions of all three URM piers with the related testing dates are shown in Table 4.7. At the testing dates the measurements were taken and the piers were tested. An URM pier placed at the testing position in the laboratory can be seen in Figure 4.21.

Table 4.7 Dimension and testing dates of URM piers

|                                    | URM 1                         | URM 2                         | URM 3                         |
|------------------------------------|-------------------------------|-------------------------------|-------------------------------|
| <b>Dimensions <math>l/h</math></b> | 145/188                       | 145/188                       | 145/188                       |
| <b>Testing date</b>                | 19 <sup>th</sup> of June 2023 | 21 <sup>st</sup> of June 2023 | 21 <sup>st</sup> of June 2023 |



Figure 4.21 Testing of an URM pier

The first pier tested was the URM 1 pier. After it was placed at the testing location and the equipment was properly set, the experiment was conducted. First, the vertical compressive load was applied. After that the quasi-static cyclic displacement-controlled testing begun. The aim of the laboratory crew was to check for crack formation at the pier surface at each step of the testing protocol. The first cracks that should appear would be at the corners of the pier or at the very middle. In case of URM 1 the first crack appeared at the bottom right corner as it may be seen in Figure 4.22. Basically, at the next step the second crack appeared at the very middle of the pier. It can also be seen in Figure 4.22. This type of crack formation is very typical for piers and walls that should have a diagonal shear failure mechanism when the shear resistance is completely dissipated.



Figure 4.22 First and second crack of URM 1 pier

After the crack would be accounted for, the testing procedure would proceed. In each step the new cracks would appear, and the old ones would widen. The crack propagation and crack formation in different steps of the testing protocol can be seen in Figure 4.23. In Figure 4.23 a) the crack propagation in step 7 may be seen. At the horizontal displacement of 7 mm the masonry pier exhibited cracks at the bottom corner and in the middle. In Figure 4.23 b) the stair stepped crack pattern is now quite visible and it is clear that the pier would fail due to diagonal shear failure. In the final part of the figure, Figure 4.23 c) the final crack propagation

of URM 1 pier can be seen. The cracks spread through both the mortar joints and the middle of the bricks. At this point the shear resistance of the pier was spent entirely, and the testing procedure was stopped. The failure of the URM 1 pier was brittle and sudden. The final failure mechanism of URM 1 pier can also be seen in Figure 4.24. The maximum value of the crack width that was measured for the URM 1 pier was 7,0 mm.

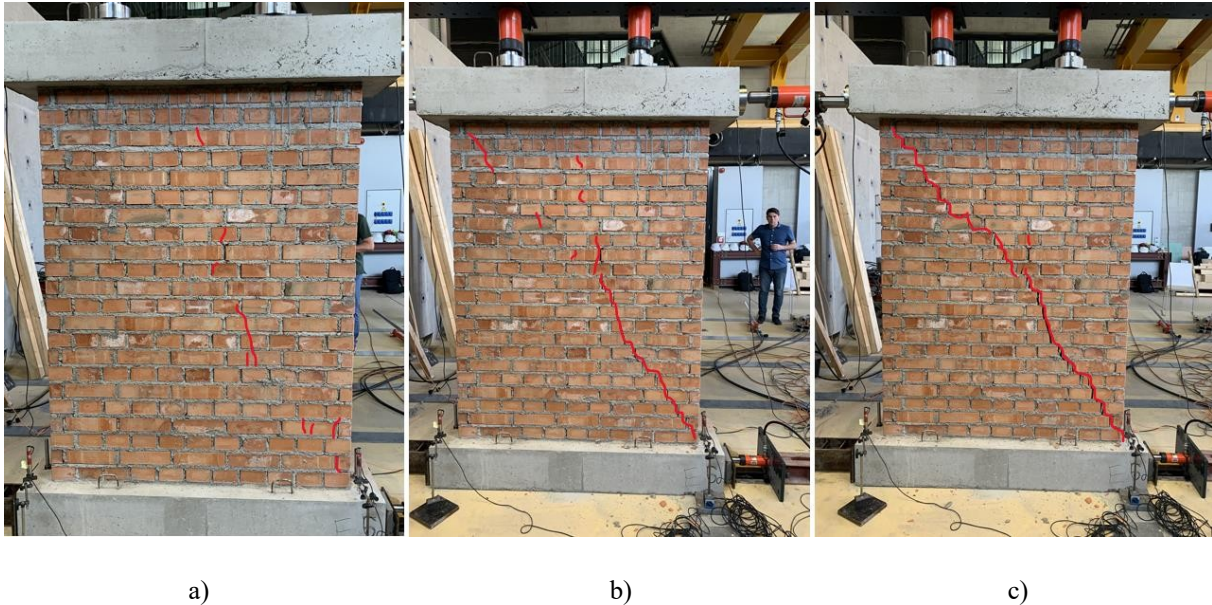


Figure 4.23 URM 1 a) Crack propagation - step 7 b) Crack propagation step - 10 c) Crack propagation - failure



Figure 4.24 Final failure mechanism of URM 1 pier

The results of the testing campaign are shown in the form of a hysteresis curve and a resistance envelope curve. Both may be seen in Figure 4.25 where the hysteresis curve is plotted in red, and the corresponding envelope curve is given in a black solid line.

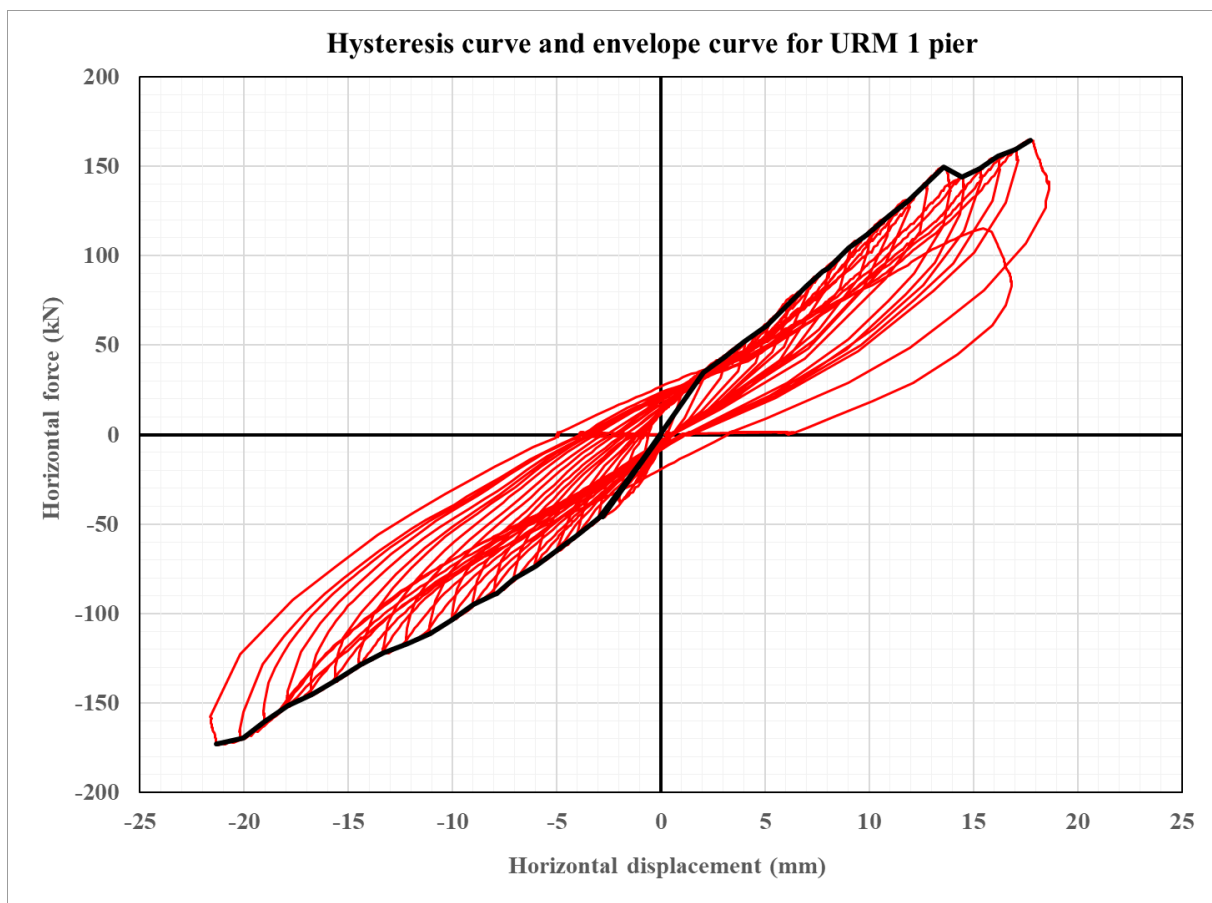


Figure 4.25 Hysteresis curve and envelope curve for URM 1 pier

Since the envelope curve has no apparent yielding point and the ductility cannot be properly calculated, a trilinearization of the envelope curve was carried out. The trilinear curve of the URM 1 pier can be seen in Figure 4.26. The first part of the trilinear curve is defined by the point in which the first crack appeared. After that the second part of the curve is plotted between the point of the first crack and the yielding point. The yielding point is defined by the second part of the trilinear curve intersecting the envelope curve at 70 % of the horizontal force. At the same time, the final part of the curve is plotted between the yielding point and the point of failure in such a manner so that the area under the trilinear curve and the envelope curve become the same. The same procedure was applied in the positive and negative direction. The ductility is calculated by dividing the maximum displacement with the displacement at yielding point. The values of ductility in both directions and the rest of the results gathered from the trilinear curve can be seen in Table 4.8 under URM 1 pier. From these results and the crack pattern shown in Figure 4.23 c) the behaviour of the URM 1 pier was considered satisfactory.

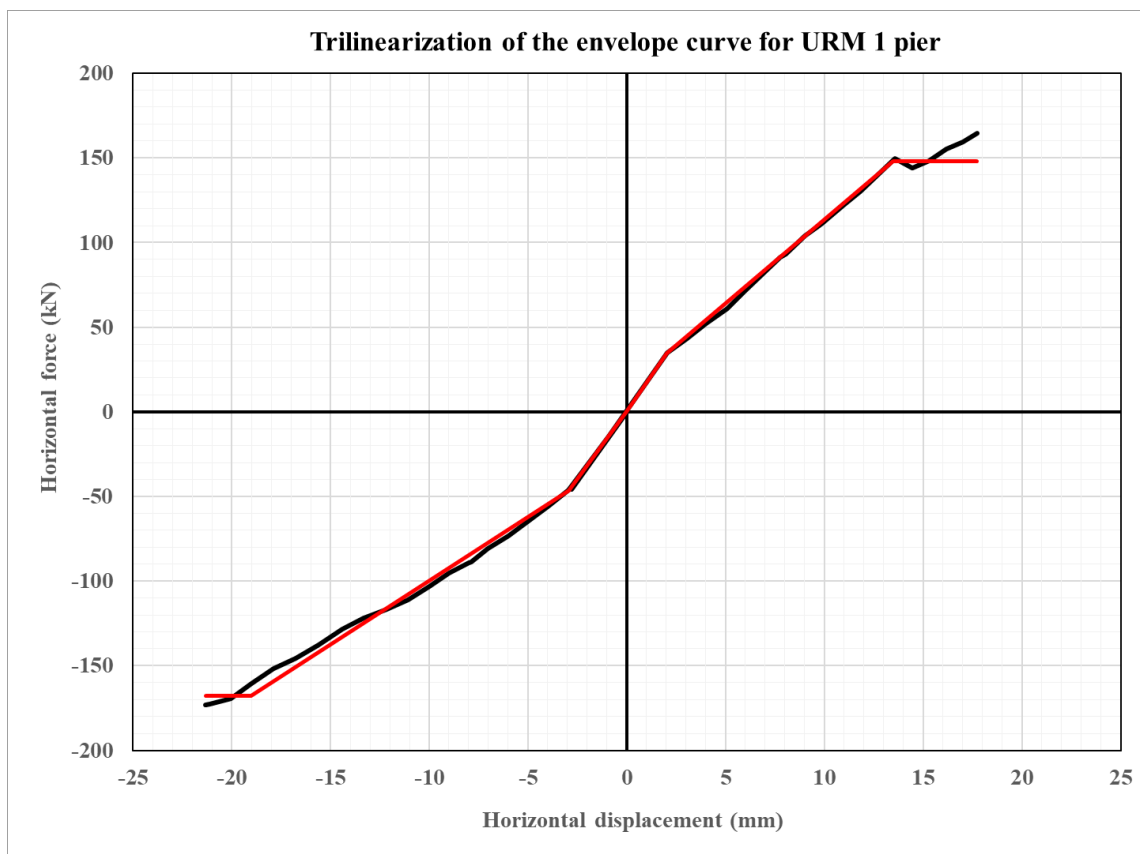


Figure 4.26 Trilinearization of the envelope curve for URM 1 pier

Table 4.8 Results of the experimental campaign for URM piers

| Value  | URM 1  | URM 2  | URM 3  | mean   |
|--|--------|--------|--------|--------|
| Maximum horizontal force – positive direction [kN]       | 148,24 | 164,34 | 147,65 | 153,39 |
| Maximum displacement – positive direction [mm]           | 17,71  | 14,10  | 10,95  | 14,25  |
| Displacement at yielding point – positive direction [mm] | 13,46  | 9,38   | 8,31   | 10,38  |
| Ductility – positive direction                           | 1,32   | 1,50   | 1,32   | 1,38   |
| Initial stiffness – positive direction [kN/mm]           | 16,70  | 20,90  | 21,21  | 19,60  |
| Maximum horizontal force – negative direction [kN]       | 167,71 | 167,06 | 146,57 | 160,45 |
| Maximum displacement – negative direction [mm]           | 21,32  | 13,68  | 14,06  | 16,35  |
| Displacement at yielding point – negative direction [mm] | 19,03  | 11,88  | 11,61  | 14,17  |
| Ductility – negative direction                           | 1,12   | 1,15   | 1,21   | 1,16   |
| Initial stiffness – negative direction [kN/mm]           | 15,72  | 20,17  | 17,91  | 17,93  |

On the 21<sup>st</sup> of June the second URM pier, URM 2 was tested. In case of URM 2 pier, the first crack appeared at the middle of the pier as it may be seen in Figure 4.27. At the same time a crack appeared at the bottom left corner of the pier. It can also be seen in Figure 4.27. Yet again, this type of crack formation is very typical for piers and walls that should have a diagonal shear failure mechanism when the shear resistance is completely dissipated.

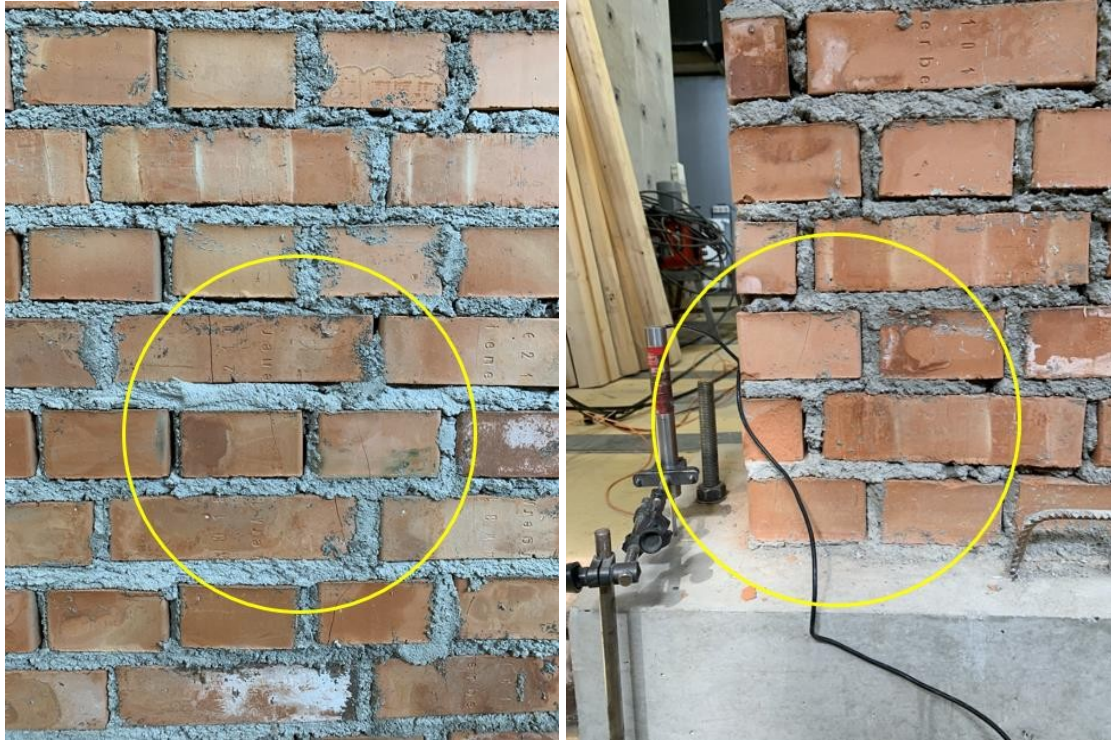
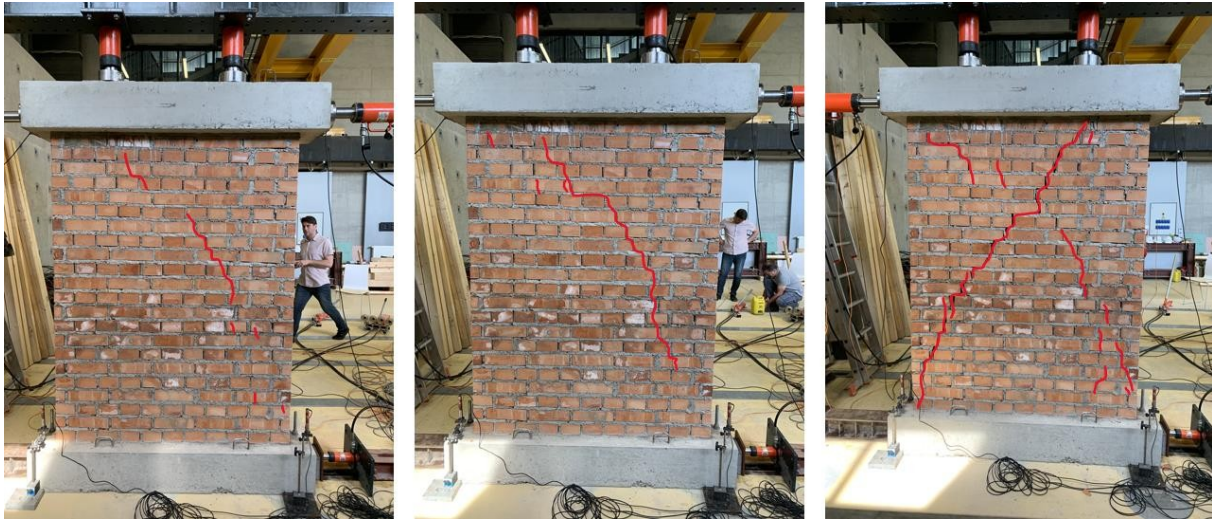


Figure 4.27 First and second crack of URM 2 pier

The crack propagation and crack formation in different steps of the testing protocol can be seen in Figure 4.28. In Figure 4.28 a) the crack propagation in step 7 may be seen. At the horizontal displacement of 7 mm the masonry pier exhibited cracks that form mostly in the middle of the pier. In Figure 4.28 b) the stair stepped crack pattern is now quite visible and the pier should fail due to diagonal shear failure. In the final part of the figure, Figure 4.28 c) the final crack propagation of URM 2 pier can be seen. In the case of URM 2 pier everything in the testing procedure was indicative of a diagonal shear failure through the first diagonal (from the top left to the bottom right corner). However, a very brittle and sudden failure of the pier happened at the final step through the second diagonal (from bottom left to top right corner). At this point the shear resistance of the pier was spent entirely, and the testing procedure was stopped. The failure pattern of the URM 2 pier in the end looks like an X pattern where both diagonals of the walls were opened completely, but in reality, only the second diagonal was utilized in full capacity. The final failure mechanism of URM 2 pier can also be seen in Figure

4.29. The maximum value of the crack width that was measured for the URM 2 pier was 10,0 mm.



a)

b)

c)

Figure 4.28 URM 2 a) Crack propagation – step 7 b) Crack propagation step – 10 c) Crack propagation – failure



Figure 4.29 Final failure mechanism of URM 2 pier

The results of the testing campaign are shown in the form of a hysteresis curve and a resistance envelope curve. Both may be seen in Figure 4.30 where the hysteresis curve is plotted in red, and the corresponding envelope curve is given in a black dotted line.



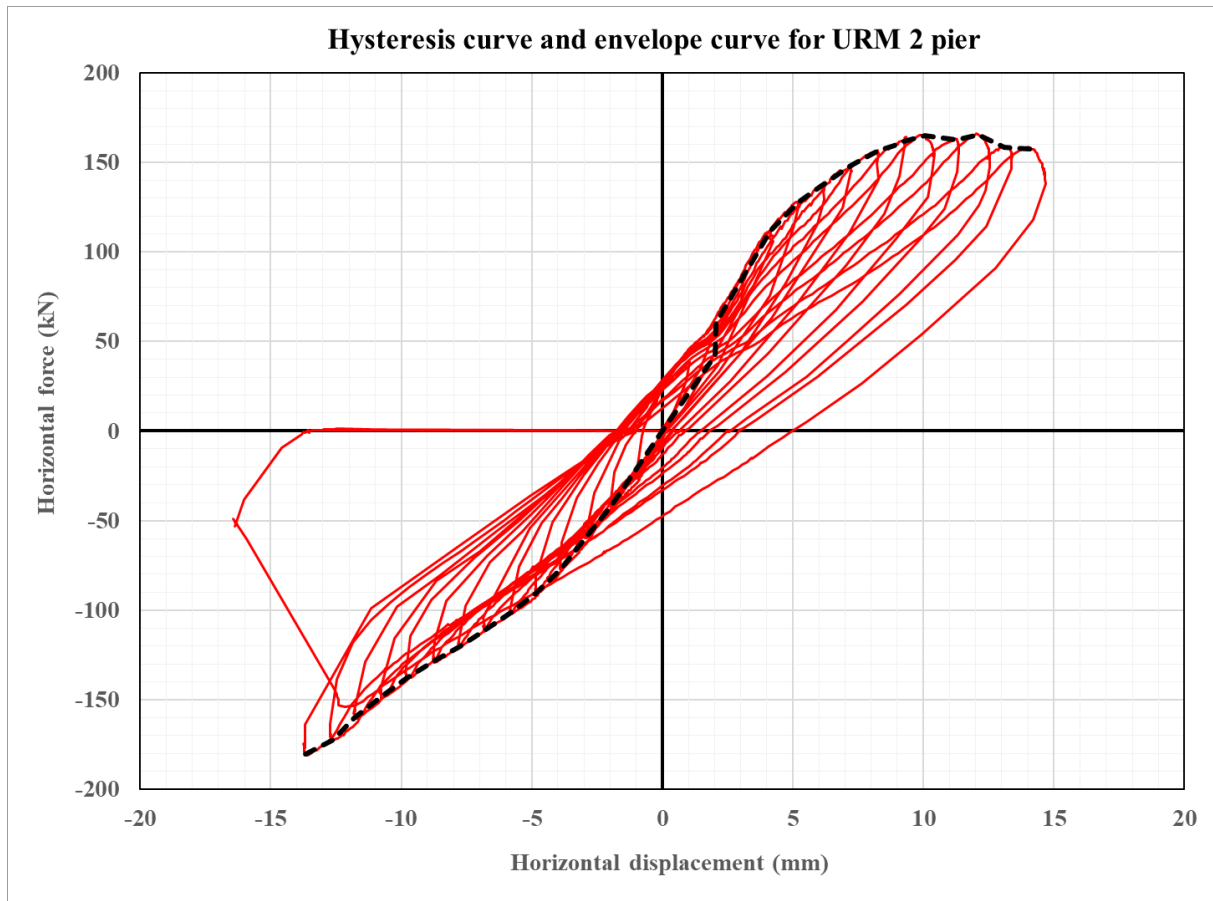


Figure 4.30 Hysteresis curve and envelope curve for URM 2 pier

The corresponding trilinear curve of the URM 2 pier can be seen in Figure 4.31. The most important results can be seen in Table 4.8 under URM 2 pier. From these results and the crack pattern shown in Figure 4.28 c) it is clear that the behaviour of the URM 2 pier was satisfactory. The maximum forces, maximum displacements, and initial stiffness for the positive and negative direction were very similar for URM 2 pier. The ductility differed in the positive and negative direction as is the case for all URM piers. It may be concluded that the results for the URM 2 pier are satisfactory in total.

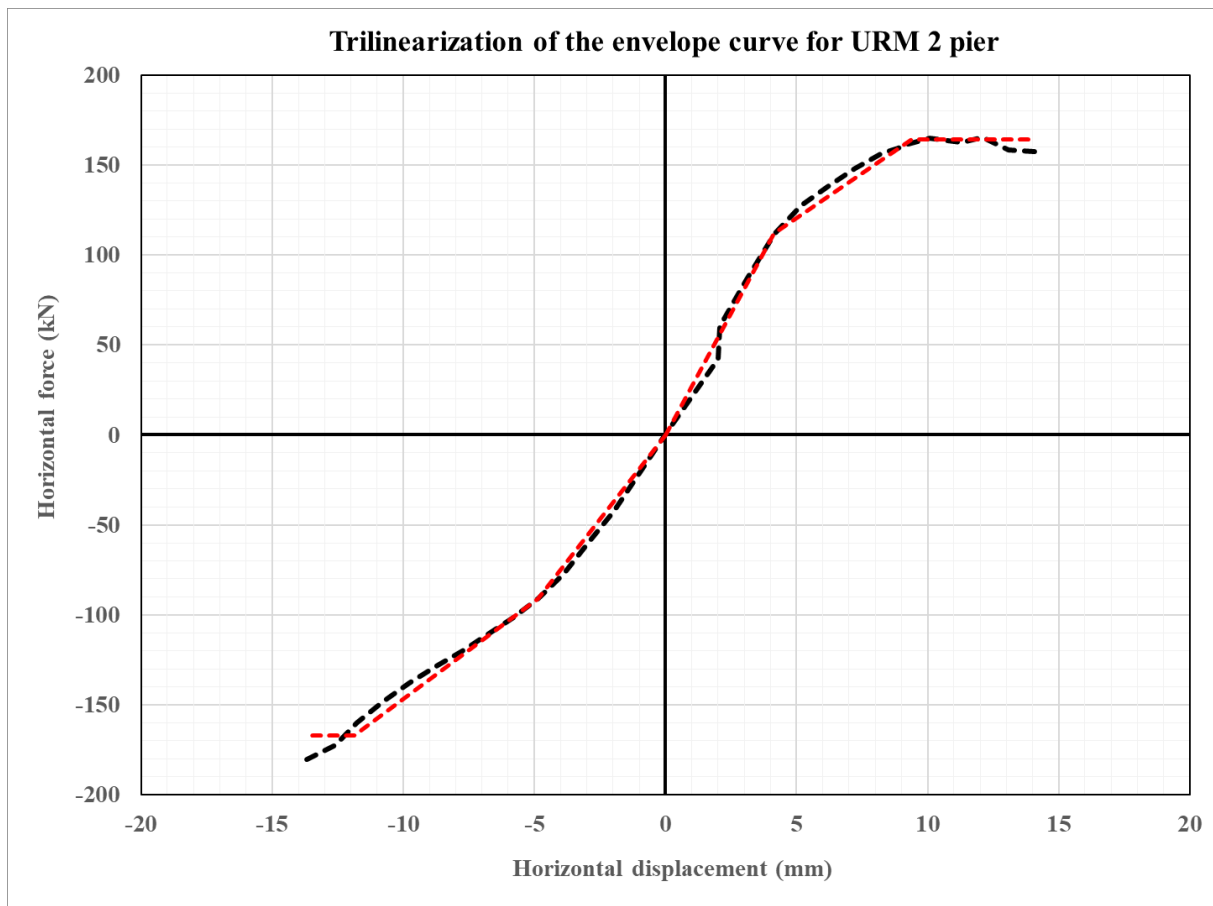


Figure 4.31 Trilinearization of the envelope curve for URM 2 pier

On the same day, the third URM pier, URM 3 was tested. The same loading and experimental protocol were used, and the crack propagation was once again monitored. In case of URM 3 pier, the first crack appeared at the middle of the pier as it may be seen in Figure 4.32. Since this type of crack formation is very typical for piers and walls that should have a diagonal shear failure mechanism and has been in seen in previous URM samples, it was concluded that the experiment was going as planned. The crack propagation and crack formation in different steps of the testing protocol can be seen in Figure 4.33. In Figure 4.33 a) the crack propagation in step 5 may be seen. At the horizontal displacement of 5 mm the masonry pier exhibits cracks that form mostly in the middle of the pier and the bottom right corner. In Figure 4.33 b) the final crack propagation of URM 3 pier can be seen. In the case of URM 3 pier a diagonal shear failure appeared from the bottom right corner to the middle of the pier on the left side. This type of diagonal failure is not as textbook as for the first two URM piers but considered acceptable. Additionally, the failure was very sudden and brittle. At this point the shear resistance of the pier was spent entirely, and the testing procedure was stopped. The final failure mechanism of URM 3 pier can also be seen in Figure 4.34. The maximum value of the crack width that was measured for the URM 3 pier was 3,0 mm.

The results of the testing campaign for the third URM pier are shown in the form of a hysteresis curve and a resistance envelope curve. Both may be seen in Figure 4.35 where the hysteresis curve is plotted in red, and the corresponding envelope curve is given in a black long dash – dot line.



Figure 4.32 First crack of URM 3 pier

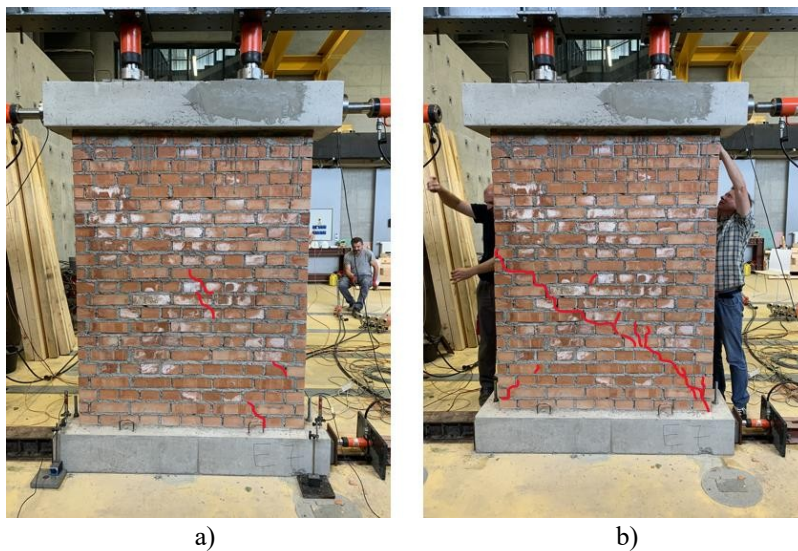


Figure 4.33 URM 3 a) Crack propagation – step 5 b) Crack propagation – failure

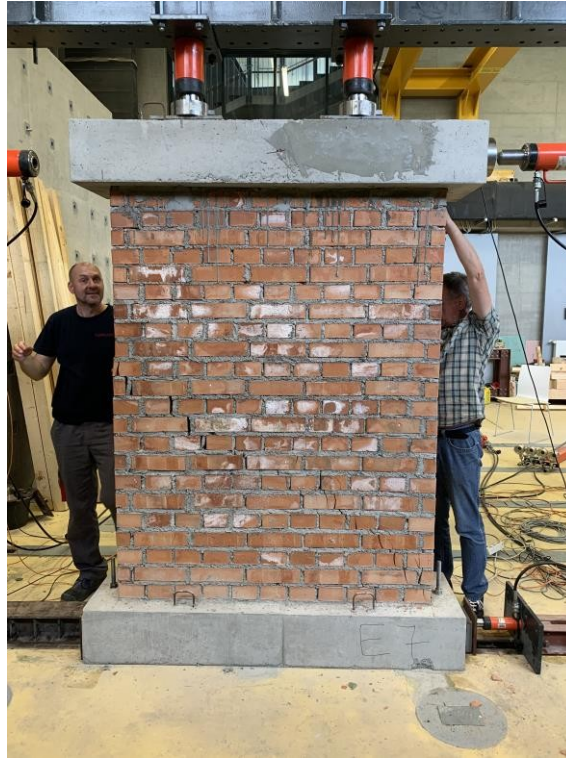


Figure 4.34 Final failure mechanism of URM 3 pier

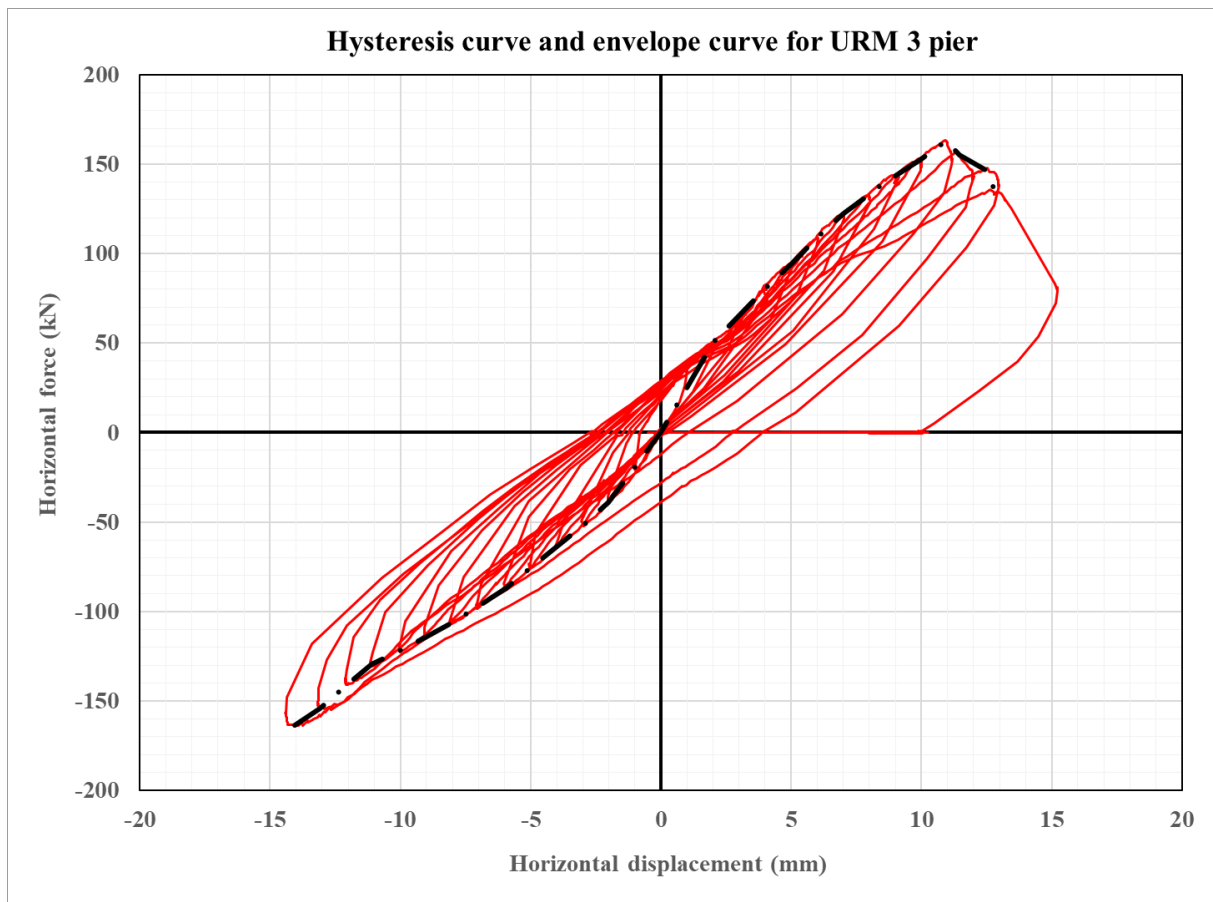


Figure 4.35 Hysteresis curve and envelope curve for URM 3 pier

The corresponding trilinear curve of the URM 3 pier can be seen in Figure 4.36. The most important results can be seen in Table 4.8 under URM 3 pier. From these results and the crack pattern shown in Figure 4.33 b) it is clear that the behaviour of the URM 3 pier was satisfactory. The maximum forces and ductility for the positive and negative direction were very similar for URM 3 pier. On the other hand, the maximum displacements, and initial stiffness differed greatly in the two directions. The maximum displacement in the negative direction was 28 % larger than the one in the positive direction. In contrast, the initial stiffness of the pier in the positive direction was 18 % larger than the one in the negative direction. This is a sign of non-symmetrical behaviour of the masonry pier due to geometrical imperfections that are very common in the building process. This is also considered to be the reason for such a brittle failure and an untypical diagonal shear failure mode. It may be concluded that the results for the URM 3 pier may be considered satisfactory in total but the differences in the measured values should be considered and properly addressed.

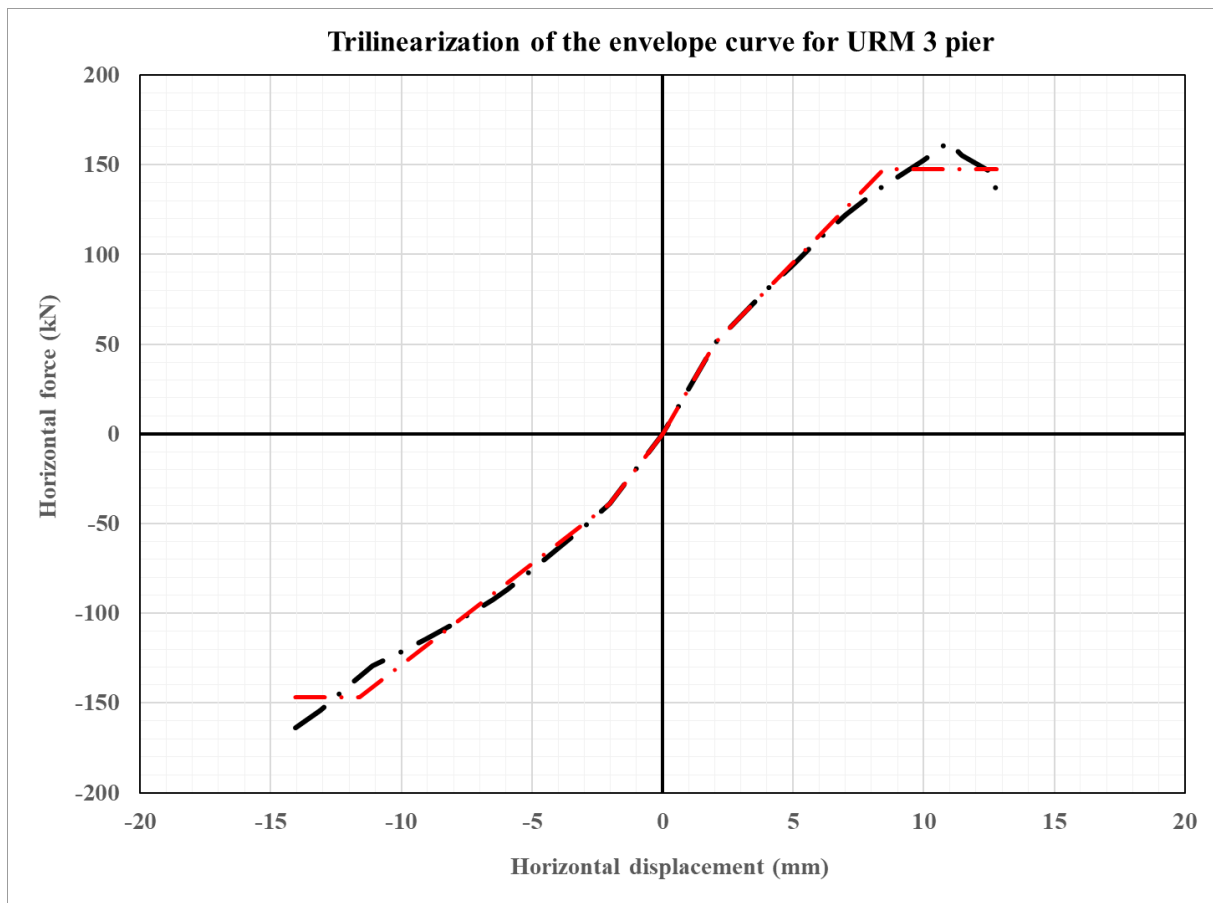


Figure 4.36 Trilinearization of the envelope curve for URM 3 pier

As it was already explained, the most important measured values for all three URM piers are given in Table 4.8. When comparing the three URM piers some similarities can be seen. The maximum horizontal force in all three URM piers was practically the same. The

maximum displacement in the two directions differed greatly. The main reason for this is the heterogeneity of masonry piers but as it is clear, the testing protocol itself. As for the initial stiffness and the ductility, they were greater in the positive direction in all three cases. The mean values are given in the final column of Table 4.8. In Figure 4.37 the envelope curves for all three URM piers can be seen and compared. The maximum horizontal forces for all three URM piers are similar. In the positive direction, which is also evident from Table 4.8, the forces are practically the same. In the negative direction they differ a bit but can be considered comparable. The maximum displacements are very similar for piers URM 2 and URM 3. For these two URM piers, the initial stiffness is also considered comparable. The URM 1 pier differs greatly from the other URM piers, especially in maximum displacement that is much greater in both directions. The initial stiffness is smaller in comparison to URM 2 and URM 3. It is evident that the URM 1 pier showed a more flexible behaviour than the other URM piers. The ductility in both directions is very comparable as it is clear from Table 4.8. Even though these differences cannot be ignored, all URM piers and their corresponding values will be considered in the comparison to the reinforced masonry piers (Series 2 and 3).

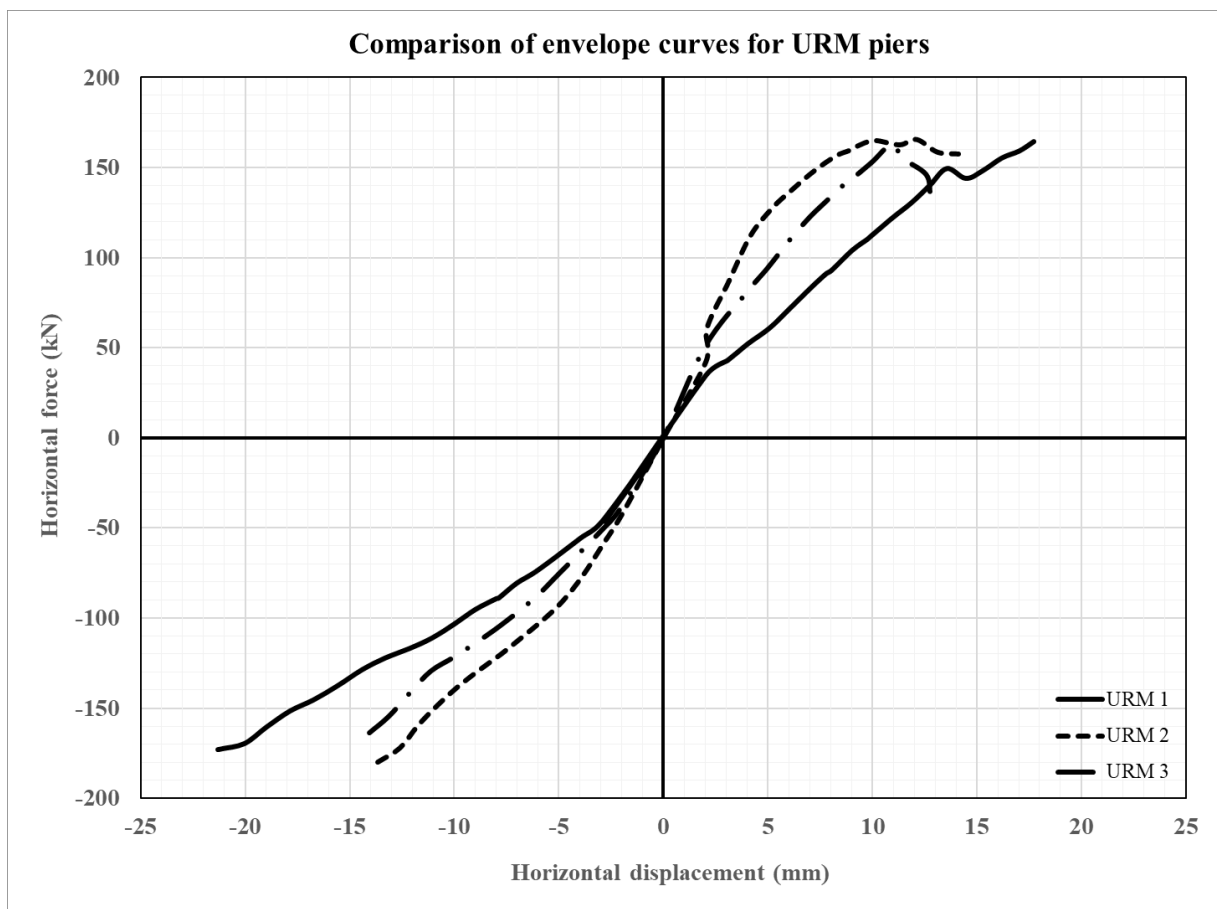


Figure 4.37 Envelope curves for all three URM piers

#### 4.4.2 Series 2 – FRCM – Masonry piers with single sided FRCM reinforcement

The dimensions of all three FRCM piers with the related testing dates are shown in Table 4.9. At the testing dates the measurements were taken and the piers were tested. Additionally, all FRCM piers were checked for initial cracks in the coating to see if any irregularities existed. Only small cracks were found in the coating of FRCM 3 pier that were considered irrelevant. FRCM pier placed at the testing position in the laboratory can be seen in Figure 4.38.

Table 4.9 Dimension and testing dates of FRCM piers

|                                    | <b>FRCM 1</b>                 | <b>FRCM 2</b>                 | <b>FRCM 3</b>                 |
|------------------------------------|-------------------------------|-------------------------------|-------------------------------|
| <b>Dimensions <math>l/h</math></b> | 145/188                       | 145/188                       | 145/186                       |
| <b>Testing date</b>                | 18 <sup>th</sup> of July 2023 | 18 <sup>th</sup> of July 2023 | 19 <sup>th</sup> of July 2023 |



Figure 4.38 Testing of a FRCM pier

The first strengthened pier tested on 18<sup>th</sup> of July was the FRCM 1 pier. After it was placed at the testing location and the equipment was properly set, the experiment was conducted. In case of FRCM 1 pier the first crack appeared at the bottom right corner as it may be seen in Figure 4.39. This type of crack formation is very typical for piers and walls strengthened with the FRCM system. Because of the stiffness of the coating the strengthened pier in general acts in a stiffer manner and the first cracks usually appear at the top or bottom of the FRCM strengthened pier, at the connection with the foundation beam.

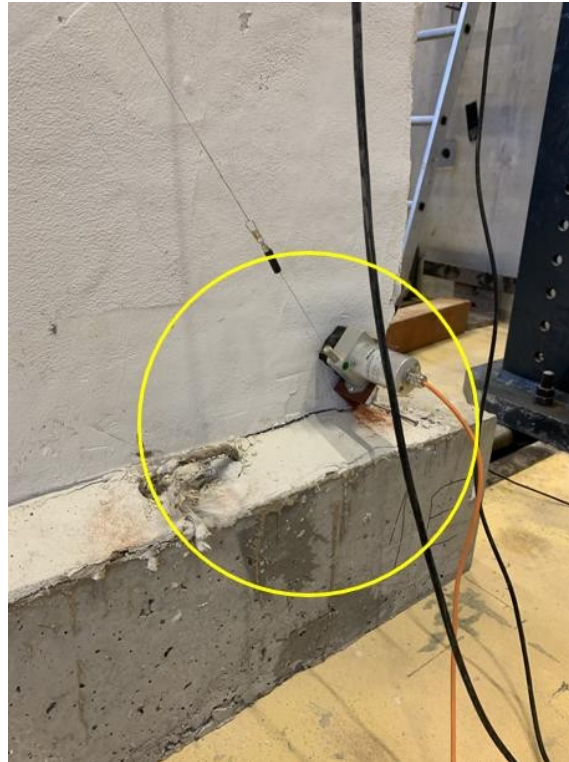


Figure 4.39 First crack of FRCM 1 pier

After the cracks would be accounted for in each step, the testing procedure would proceed. Since the cracks mostly appeared (or are more visible) on the strengthened side of the FRCM pier, it was very easy to highlight them with a simple marker. The crack propagation and crack formation in different steps of the testing protocol can be seen in Figure 4.40. In Figure 4.40 a) the crack propagation in step 10 may be seen. At the horizontal displacement of 10 mm the FRCM strengthened masonry pier exhibited initial cracks mostly in the middle of the pier. In Figure 4.40 b) the stair stepped crack x-pattern is now quite visible and it is clear that the pier should fail due to diagonal shear failure. In the final part of the figure, Figure 4.40 c) the final crack propagation of FRCM 1 pier can be seen. Even though the cracks spread through both diagonals of the pier, making an x-pattern, the pier failed through only one diagonal (from the bottom left corner to the upper right corner). At this point the shear resistance



of the pier was spent entirely, and the testing procedure was stopped. The failure of the FRCM 1 pier was very gradual which can be attributed to the one-sided FRCM strengthening. The final failure mechanism of FRCM 1 pier can also be seen in Figure 4.41. The maximum value of the crack width that was measured for the FRCM 1 pier was 5,0 mm.

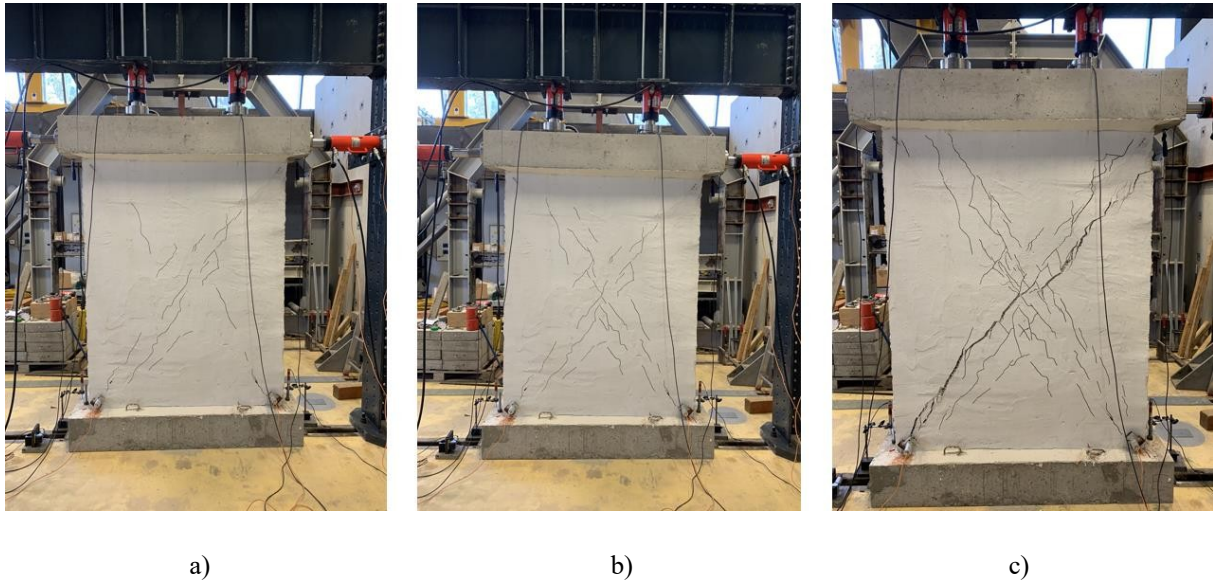


Figure 4.40 FRCM 1 a) Crack propagation – step 10 b) Crack propagation step – 15 c) Crack propagation – failure

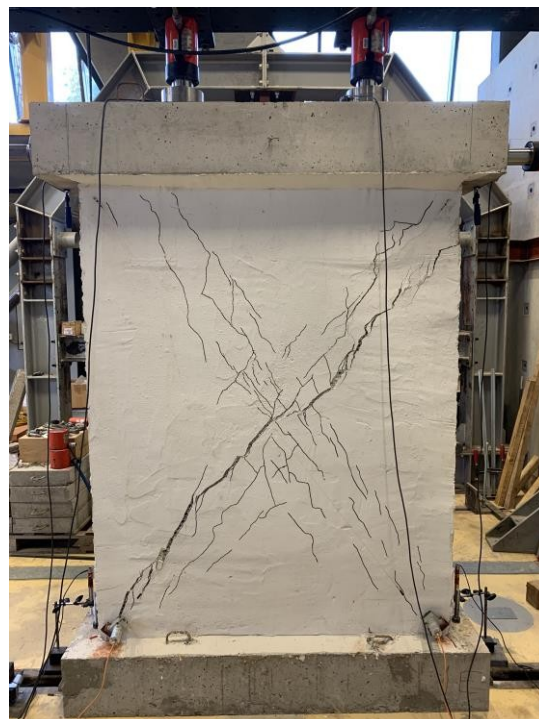


Figure 4.41 Final failure mechanism of FRCM 1 pier

The results of the testing campaign are shown in the form of a hysteresis curve (blue) and a resistance envelope curve (orange solid line) that can be seen in Figure 4.42.

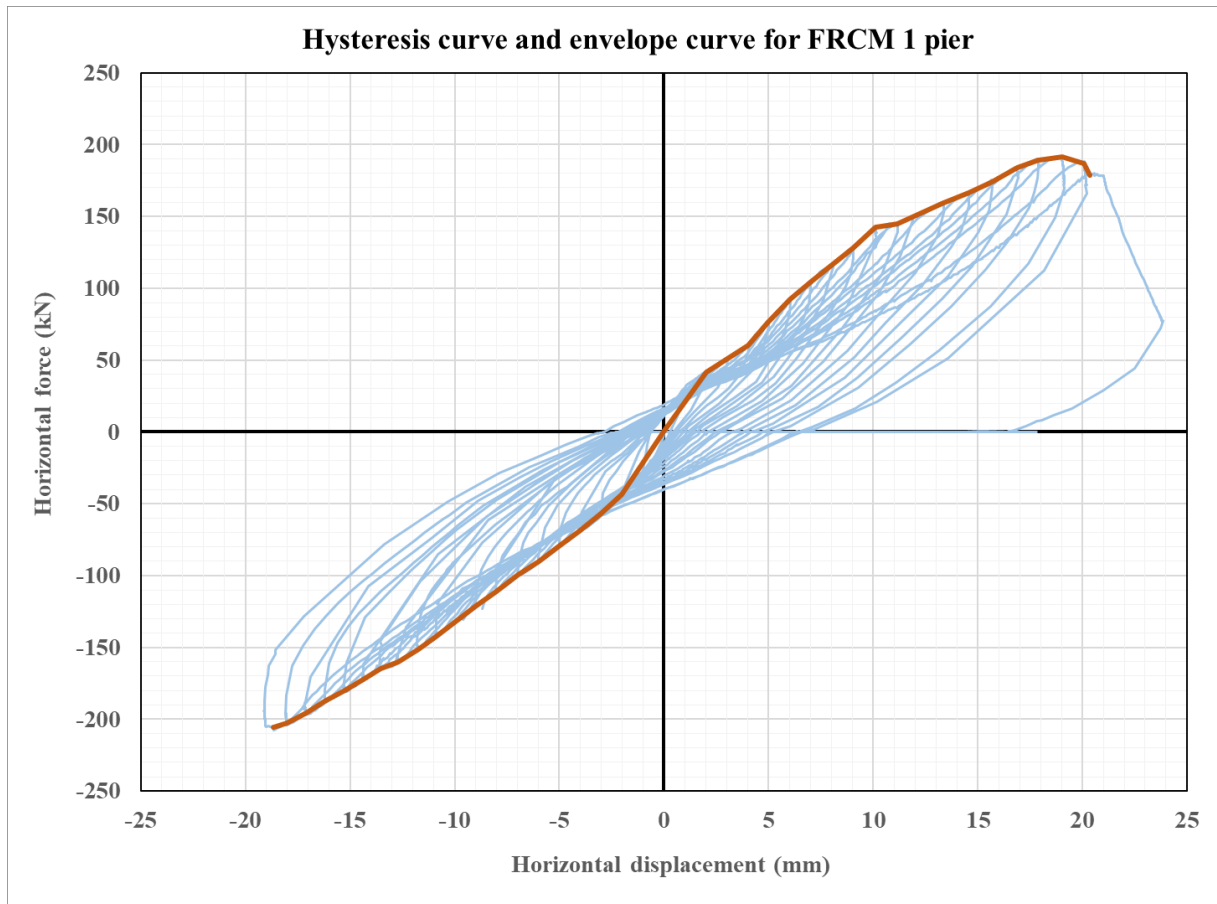


Figure 4.42 Hysteresis curve and envelope curve for FRCM 1 pier

The trilinear curve of the FRCM 1 pier can be seen in Figure 4.43. The most important results from the trilinear curve can be seen in Table 4.10 under FRCM 1 pier. From these results and the crack pattern shown in Figure 4.40 c) it is clear that the behaviour of the FRCM 1 pier was satisfactory. The maximum forces, maximum displacements, ductility and initial stiffness for the positive and negative direction were similar for FRCM 1 pier. It may be concluded that the results for the FRCM 1 pier may be considered satisfactory in total.

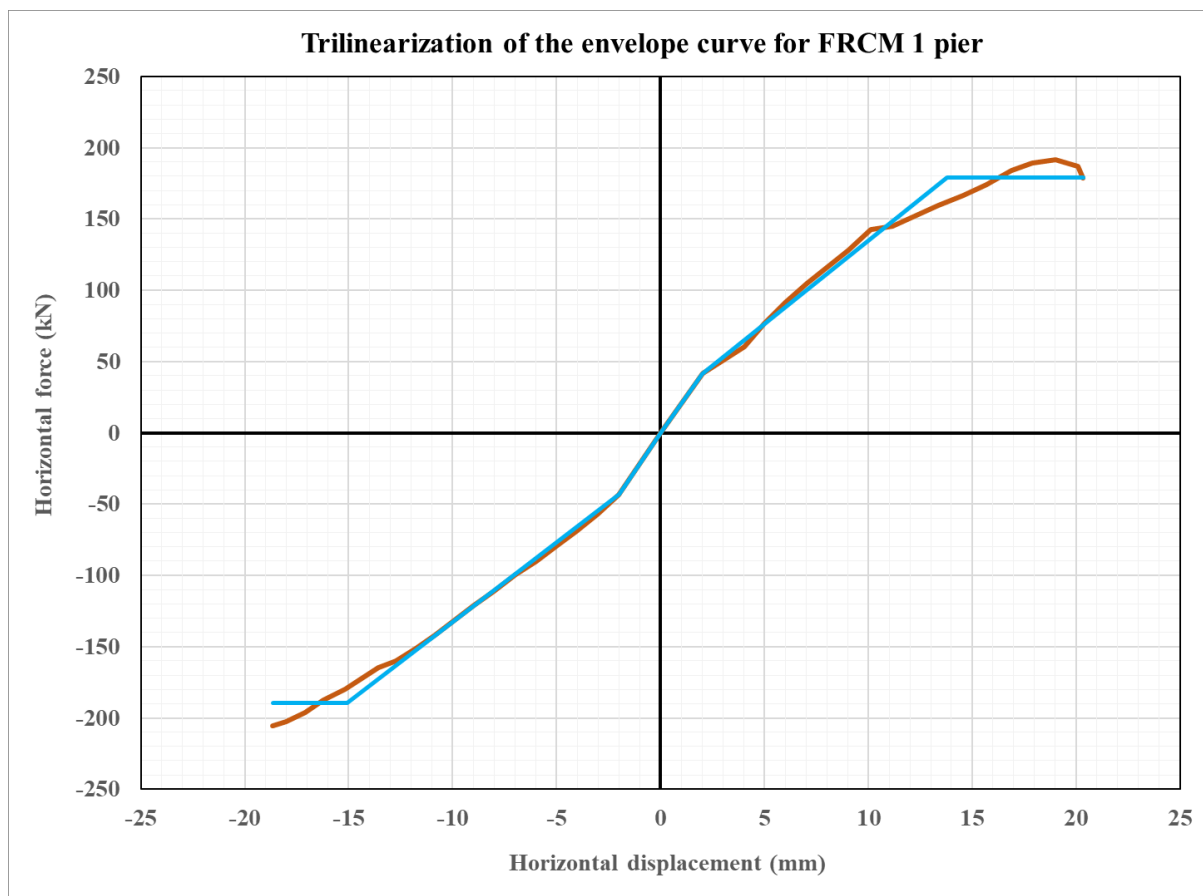


Figure 4.43 Trilinearization of the envelope curve for FRCM 1 pier

Table 4.10 Results of the experimental campaign for FRCM piers

| Value   | FRCM 1 | FRCM 2 | FRCM 3 | mean   |
|---|--------|--------|--------|--------|
| <b>Maximum horizontal force – positive direction [kN]</b>       | 179,20 | 250,68 | 183,67 | 204,52 |
| <b>Maximum displacement – positive direction [mm]</b>           | 20,34  | 21,60  | 20,36  | 20,77  |
| <b>Displacement at yielding point – positive direction [mm]</b> | 13,79  | 17,62  | 15,37  | 15,59  |
| <b>Ductility – positive direction</b>                           | 1,47   | 1,23   | 1,32   | 1,34   |
| <b>Initial stiffness – positive direction [kN/mm]</b>           | 20,52  | 14,85  | 17,29  | 17,55  |
| <b>Maximum horizontal force – negative direction [kN]</b>       | 189,63 | 204,21 | 225,36 | 206,40 |
| <b>Maximum displacement – negative direction [mm]</b>           | 18,65  | 19,77  | 19,44  | 19,29  |
| <b>Displacement at yielding point – negative direction [mm]</b> | 15,09  | 17,90  | 17,57  | 16,85  |
| <b>Ductility – negative direction</b>                           | 1,24   | 1,10   | 1,11   | 1,15   |
| <b>Initial stiffness – negative direction [kN/mm]</b>           | 21,68  | 17,87  | 24,92  | 21,49  |

The second pier tested was the FRCM 2 pier. In case of FRCM 2 the first crack appeared at the bottom left corner as it may be seen in Figure 4.44. This type of crack formation is very typical for piers and walls strengthened with the FRCM system.

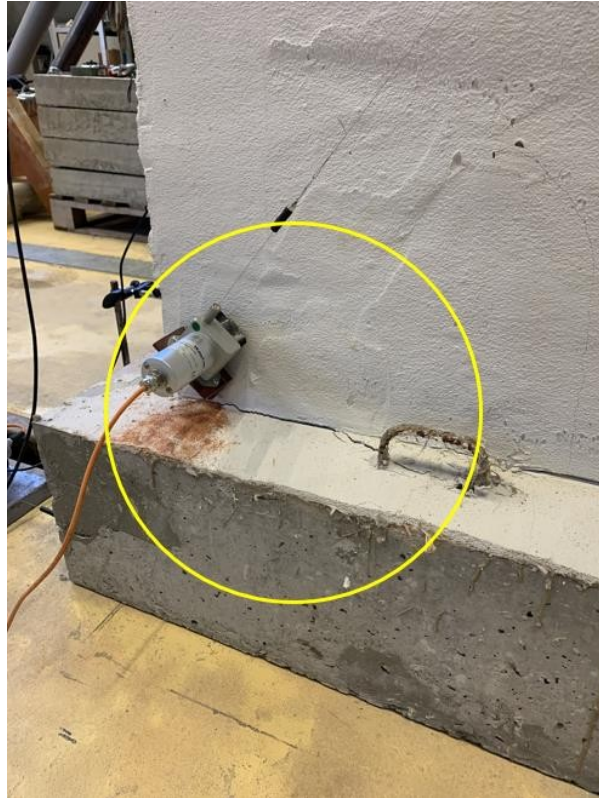


Figure 4.44 First crack of FRCM 2 pier

The crack propagation and crack formation in different steps of the testing protocol can be seen in Figure 4.45. In Figure 4.45 a) the crack propagation in step 12 may be seen. At the horizontal displacement of 12 mm the FRCM strengthened masonry pier exhibited initial cracks mostly in the middle of the pier. In Figure 4.45 b) the number of cracks increased, again mostly in the middle of the pier. In the final part of the figure, Figure 4.45 c) the final crack propagation of FRCM 2 pier can be seen. Even though, the cracks appeared in both diagonals of the pier, making a resemblance of an x-pattern, the pier failed through only one diagonal (from the bottom left corner to the upper right corner). The final failure mechanism of FRCM 2 pier can also be seen in Figure 4.46 where the unstrengthened side of the pier is shown. The maximum value of the crack width that was measured for the FRCM 2 pier was 6,0 mm.

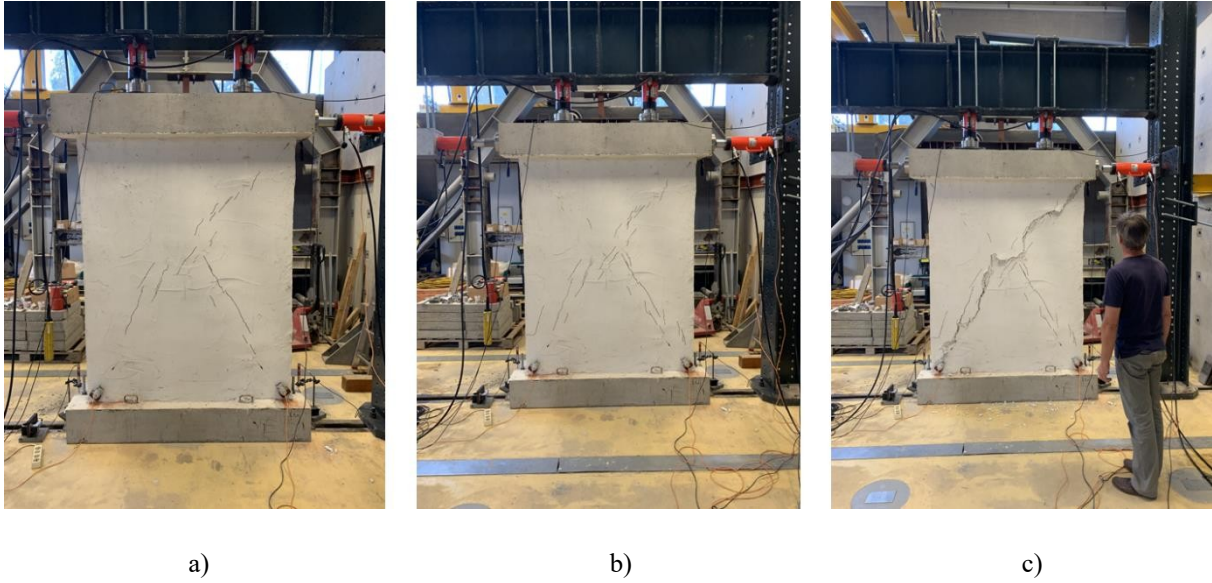


Figure 4.45 FRCM 2 a) Crack propagation – step 12 b) Crack propagation step – 15 c) Crack propagation – failure



Figure 4.46 Final failure mechanism of FRCM 2 pier

The results of the testing campaign are shown in the form of a hysteresis curve and a resistance envelope curve. Both may be seen in Figure 4.47 where the hysteresis curve is plotted in blue, and the corresponding envelope curve is given in an orange dotted line. The trilinear curve of the FRCM 2 pier can be seen in Figure 4.48. The most important results from the trilinear curve can be seen in Table 4.10 under FRCM 1 pier. From these results and the crack pattern shown in Figure 4.45 c) it is clear that the behaviour of the FRCM 2 pier was satisfactory.

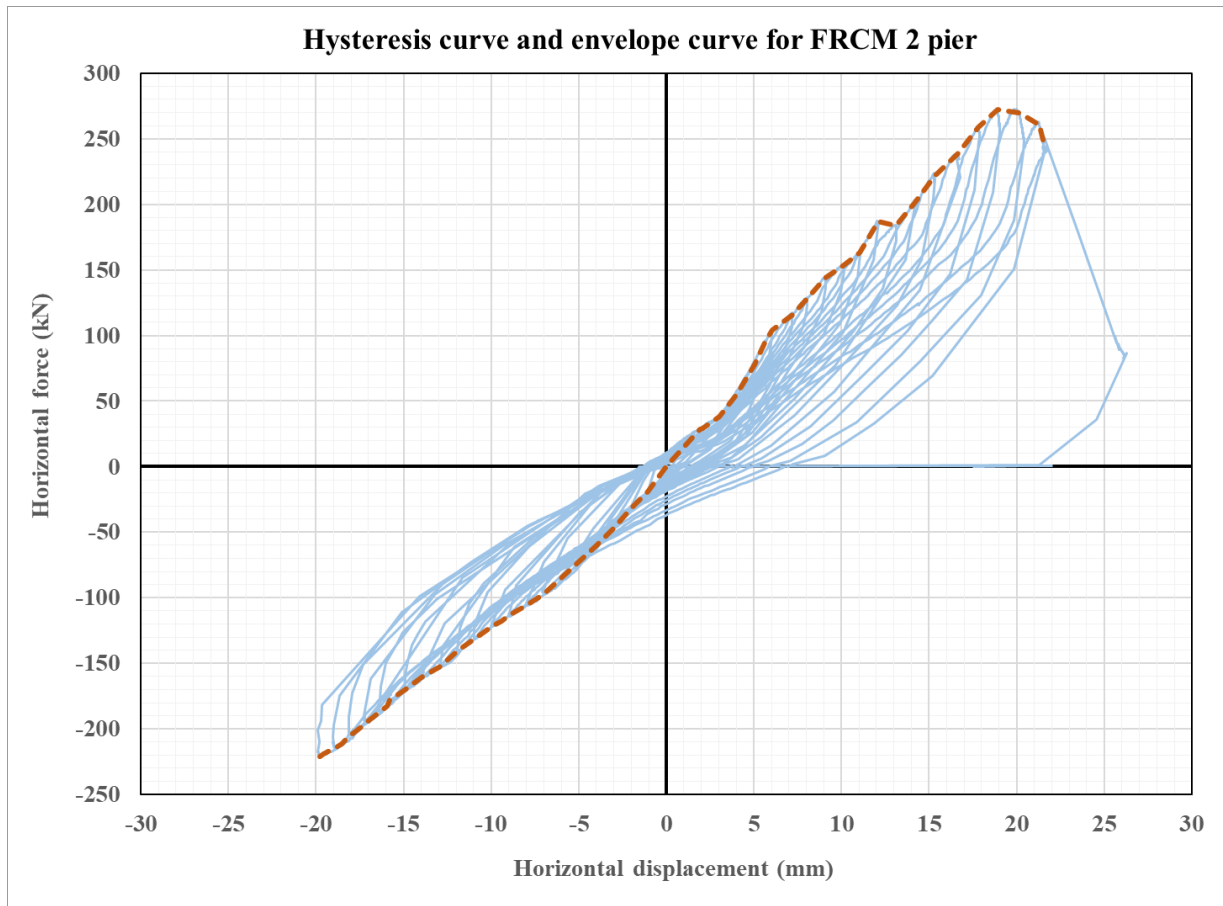


Figure 4.47 Hysteresis curve and envelope curve for FRCM 2 pier

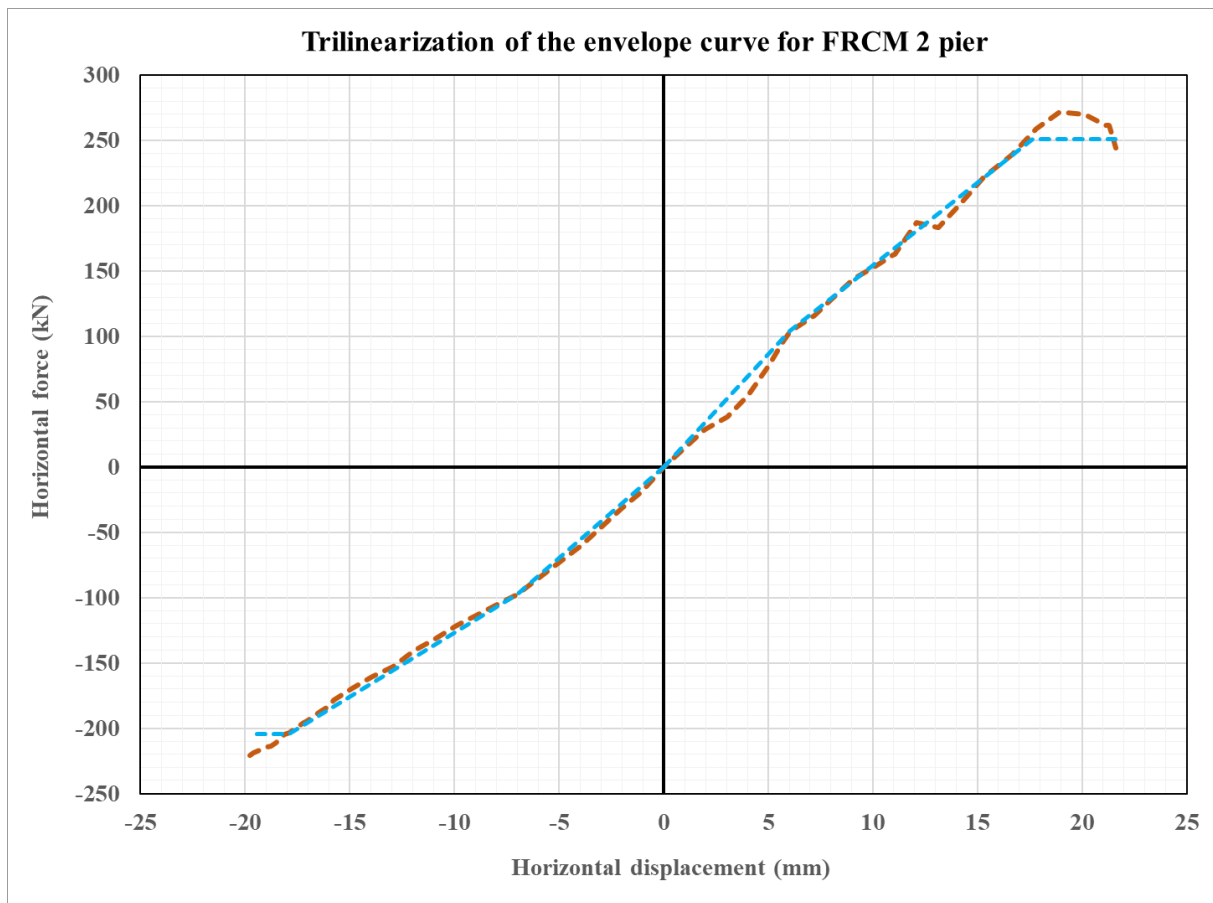


Figure 4.48 Trilinearization of the envelope curve for FRCM 2 pier

The following day the FRCM 3 pier was tested. After it was placed at the testing location and the equipment was properly set, the experiment was conducted. In case of FRCM 3 pier the first crack appeared at the bottom left corner as it was the case in FRCM 2 pier. This type of crack formation is very typical for piers and walls strengthened with the FRCM system. The failure of FRCM 3 pier was more sudden than in the case of the first two FRCM piers. The FRCM 3 pier failed through only one diagonal (from the bottom left corner to the upper right corner). The other diagonal was not activated. The final failure mechanism of FRCM 3 pier can be seen in Figure 4.49. The maximum value of the crack width that was measured for the FRCM 3 pier was 4,0 mm. The results of the testing campaign are shown in Figure 4.50 where the hysteresis curve is plotted in blue, and the corresponding envelope curve is given in an orange long dash - dot line. The most important results can be seen in Table 4.10 under FRCM 3 pier. From these results and the crack pattern shown in Figure 4.49 the behaviour of the FRCM 3 pier was satisfactory.



Figure 4.49 Final failure mechanism of FRCM 3 pier

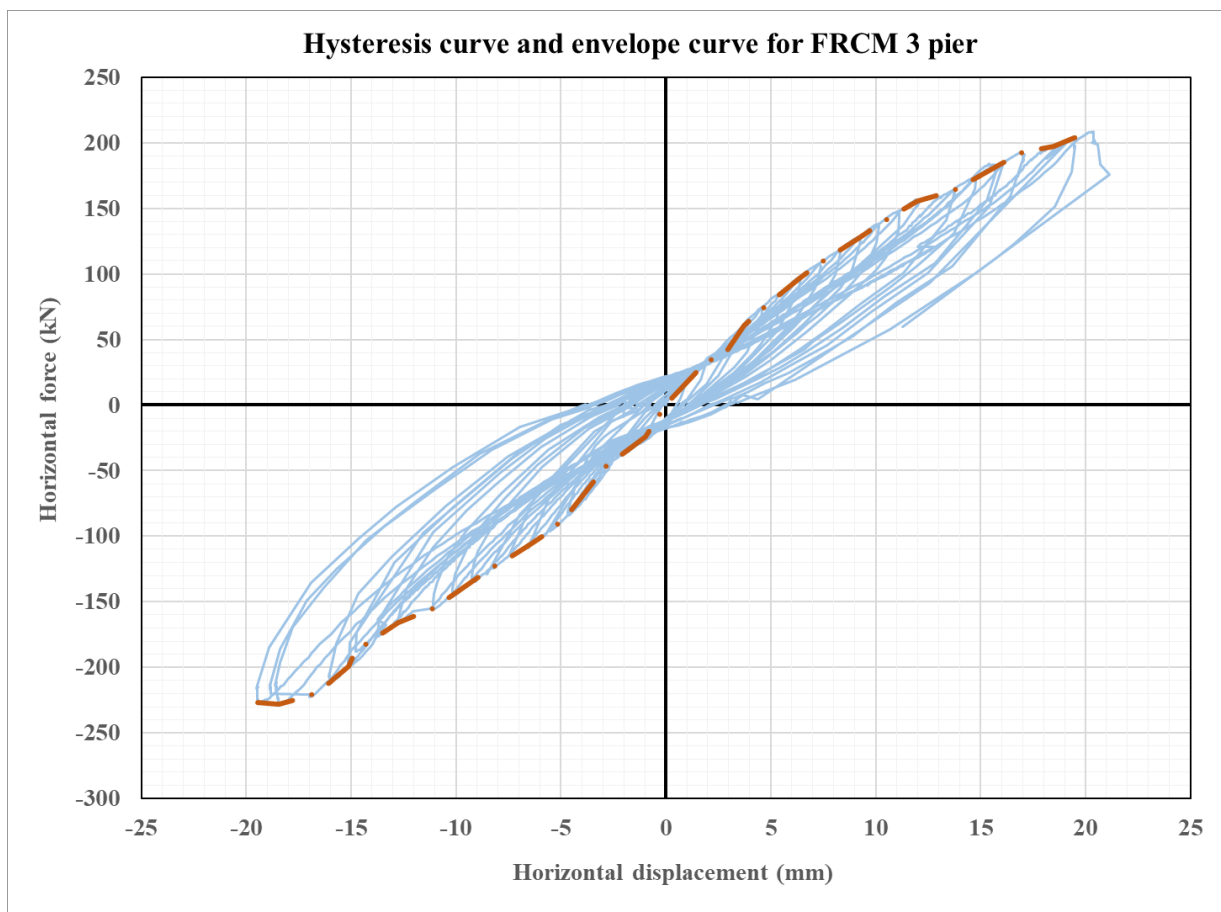


Figure 4.50 Hysteresis curve and envelope curve for FRCM 3 pier



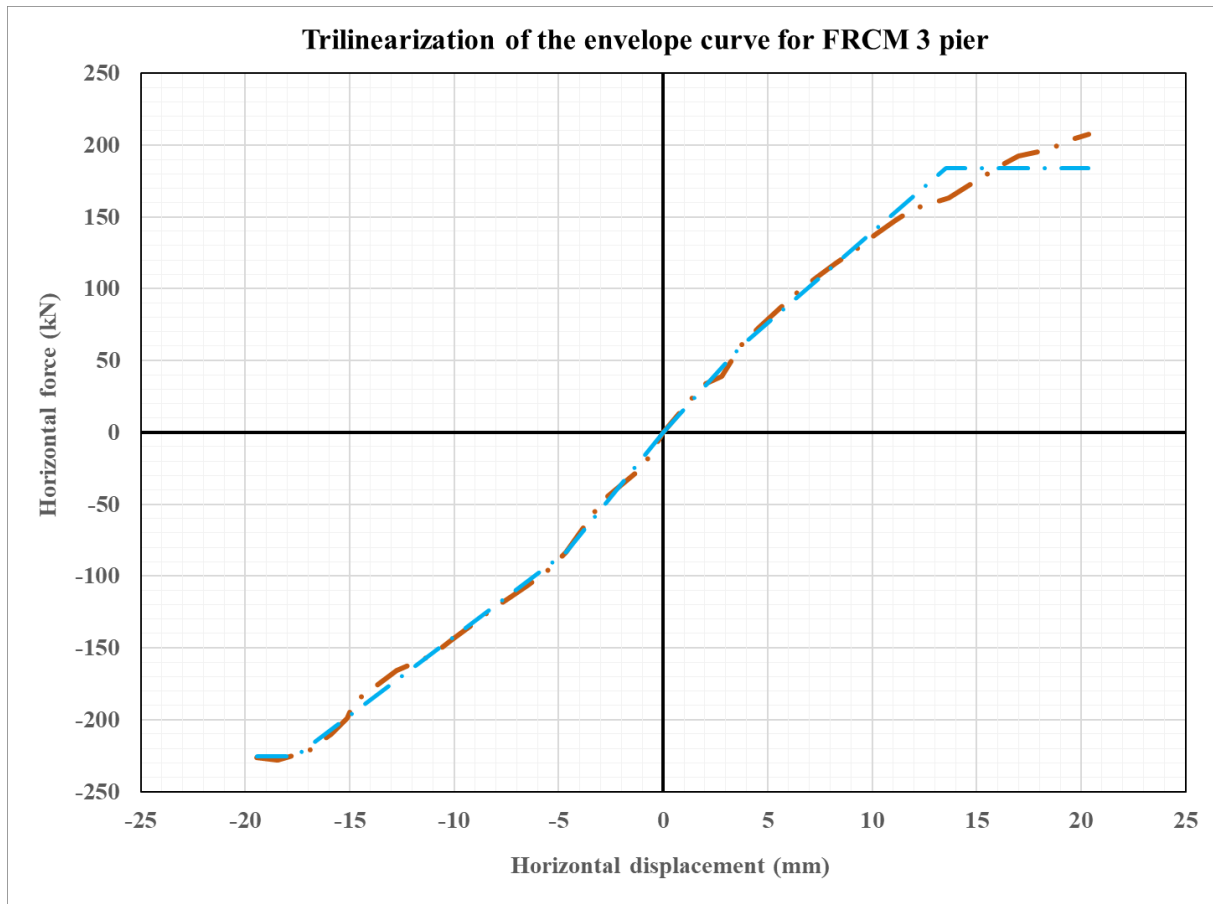


Figure 4.51 Trilinearization of the envelope curve for FRCM 3 pier

When comparing the three FRCM piers, three different behaviours were observed. Even though all three piers suffered a diagonal shear failure through only one diagonal, all of them acted differently leading up to the failure. In FRCM 1 pier, both diagonals were activated resembling a X pattern failure until the very failure. In FRCM 2 pier the second diagonal was mildly activated and in FRCM 3 pier, the second diagonal was not activated at all. As it was already explained, the most important measured values for all three FRCM piers are given in Table 4.10. Not many similarities may be seen. The maximum horizontal forces in the positive and negative direction vary from one FRCM pier to the other. In the case of maximum displacements, for all three FRCM piers the values are very similar in the positive and negative direction. As for the initial stiffness, no apparent pattern may be seen between the three FRCM piers. The main reasons for these differences are attributed to the heterogeneity of masonry piers. The ductility is higher in the positive direction for all three FRCM piers, as was the case with URM piers. The mean values are given in the final column of Table 4.10.

In Figure 4.52 the envelope curves for all three FRCM piers are compared. The maximum horizontal forces for all three FRCM piers are very similar in the negative direction. In the positive direction, the maximum forces are quite similar for FRCM 1 and FRCM 3 pier,

whereas the positive part of the envelope curve for FRCM 2 pier differs greatly. The same pattern may be seen the maximum displacements which are very similar for piers FRCM 1 and FRCM 3 especially in the negative direction. The initial stiffness in both directions differs between all three FRCM piers. The FRCM 2 pier differs greatly from the other two FRCM piers, especially in the maximum force and maximum displacement in the positive direction. Even though these differences cannot be ignored, all FRCM piers failed in a satisfying fashion. The diagonal patters were very clear and dominant on the side where the FRCM strengthening technique was applied. No apparent delamination was observed until the maximum shear force was reached. It should be noted that the failures were sudden and brittle and that the piers did not exhibit a flexible behaviour. It may be concluded that all three FRCM piers and their corresponding values will be considered in the comparison to the URM piers (Series 1) and the masonry piers strengthened with the FRCM system using new clamping details (Series 3).

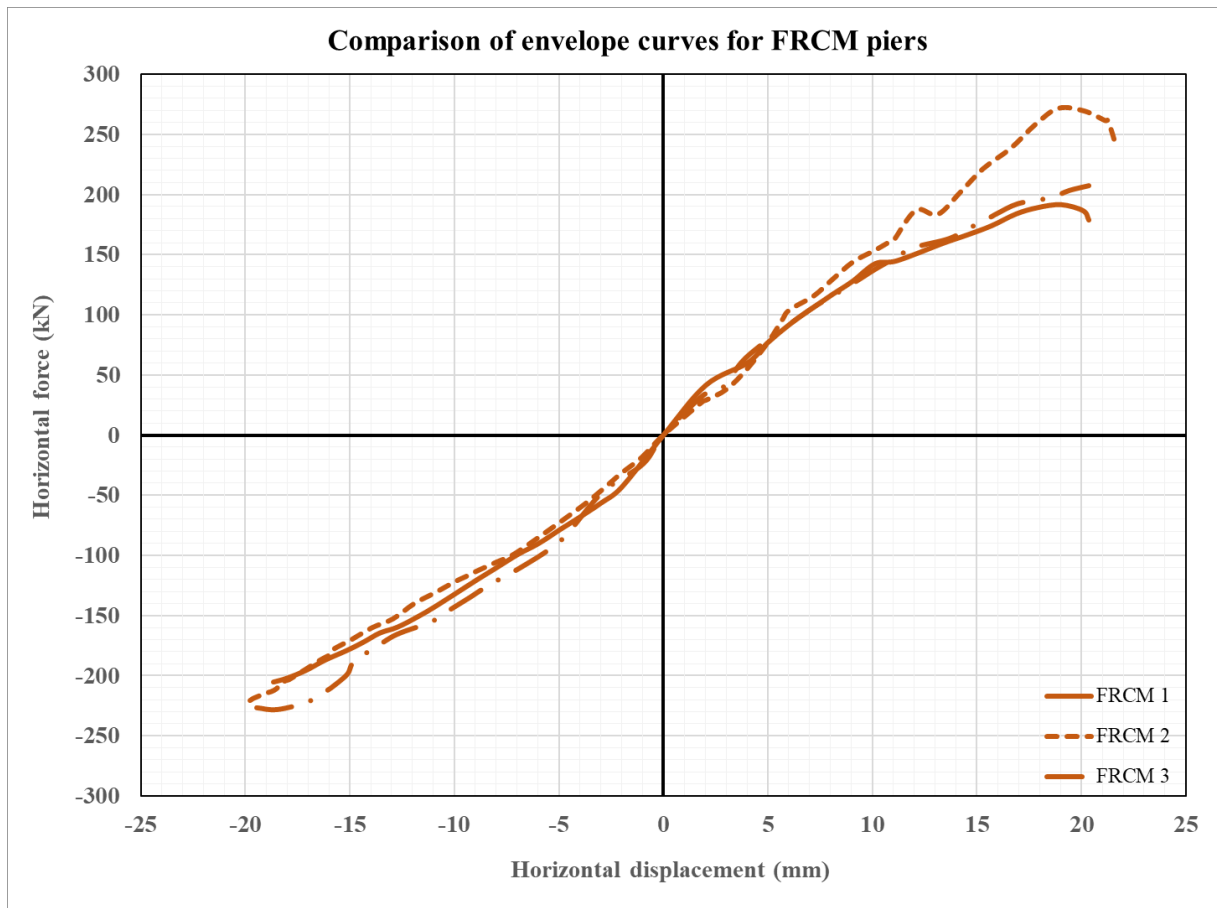


Figure 4.52 Envelope curves for all three FRCM piers

#### 4.4.3 Series 3 – CFRCM – Masonry piers with new clamping details (C shaped FRCM)

The dimensions of all three CFRCM piers with the related testing dates are shown in Table 4.11. At the testing dates the measurements were taken and the piers were tested. Additionally, all CFRCM piers were checked for initial cracks in the coating to see if any irregularities existed. Only small cracks were found in the coating of CFRCM 2 pier that are considered irrelevant. CFRCM pier placed at the testing position in the laboratory can be seen in Figure 4.53.

Table 4.11 Dimension and testing dates of CFRCM piers

|                                    | CFRCM 1                         | CFRCM 2                          | CFRCM 3                          |
|------------------------------------|---------------------------------|----------------------------------|----------------------------------|
| <b>Dimensions <math>l/h</math></b> | 145/188                         | 145/188                          | 145/186                          |
| <b>Testing date</b>                | 9 <sup>th</sup> of October 2023 | 19 <sup>th</sup> of October 2023 | 19 <sup>th</sup> of October 2023 |



Figure 4.53 Testing of a CFRCM pier

The first pier from the Series 3 tested on 9<sup>th</sup> of October was the CFRCM 1 pier. The crack propagation and crack formation in different steps of the testing protocol can be seen in Figure 4.54. In Figure 4.54 a) the crack propagation at 10 mm may be seen where the CFRCM pier 1 exhibited initial cracks in the middle of the pier. In Figure 4.54 b) the number of cracks increases, mostly in the middle of the pier. In the final part of the figure, Figure 4.54 c) the final crack propagation can be seen. Even though, the cracks appeared in both diagonals of the pier, the pier failed through only one diagonal (from the bottom left corner to the upper right corner). The final failure mechanism of CFRCM 1 pier can also be seen in Figure 4.55 where the unstrengthened side of the pier is shown. The maximum value of the crack width that was measured for the CFRCM 1 pier was 13,0 mm. The results of the testing campaign are shown in the form of a hysteresis curve (green) and a resistance envelope curve (purple solid line) that can be seen in Figure 4.56.

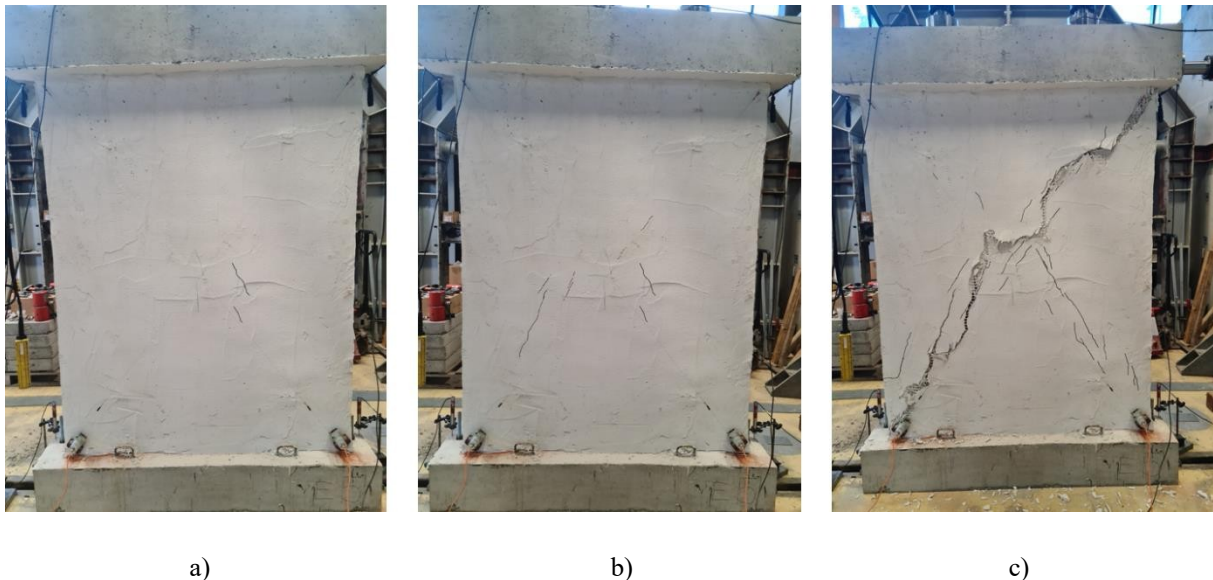


Figure 4.54 CFRCM 1 a) Crack propagation – step 10 b) Crack propagation – step 15 c) Crack propagation – failure



Figure 4.55 Final failure mechanism of CFRCM 1 pier

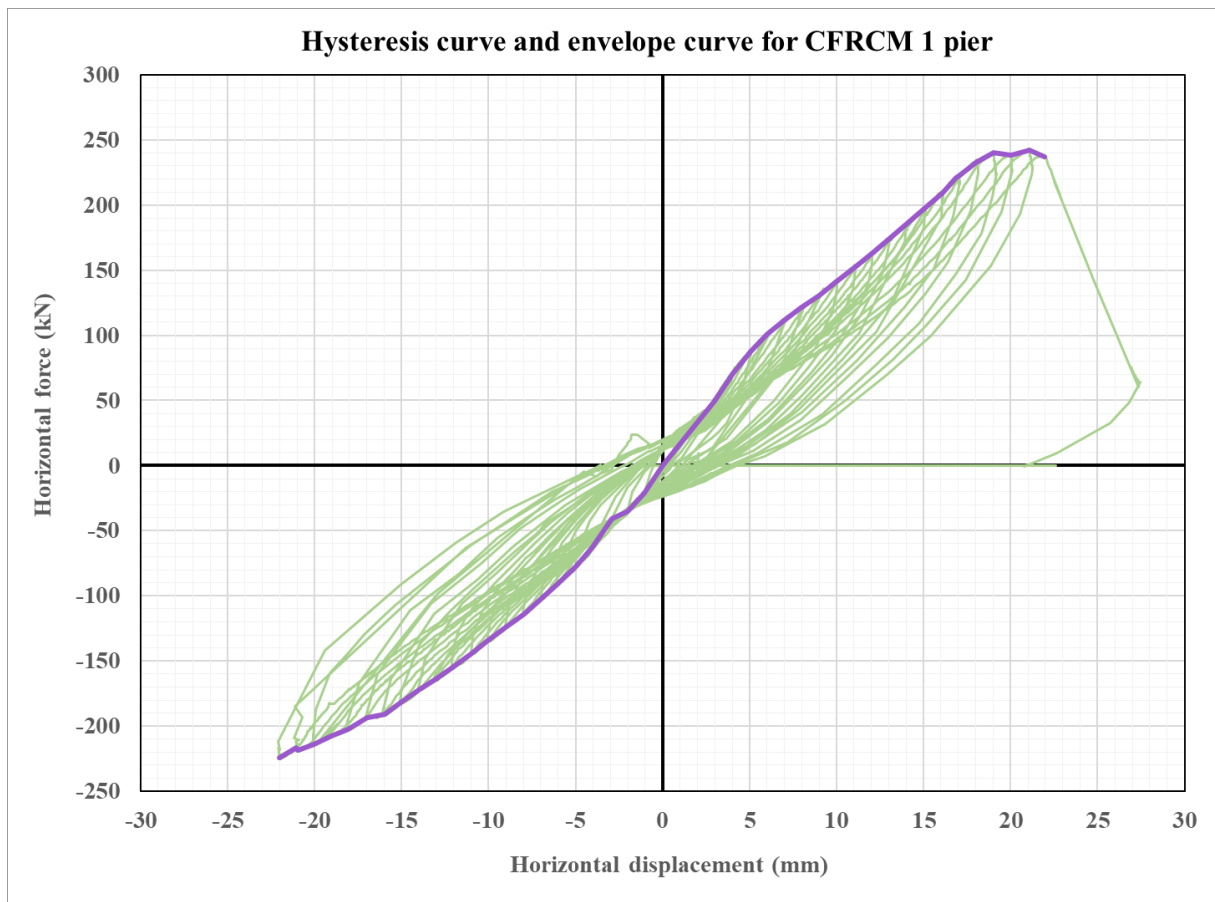


Figure 4.56 Hysteresis curve and envelope curve for CFRCM 1 pier

The trilinear curve of the CFRCM 1 pier can be seen in Figure 4.57. The most important results from the trilinear curve can be seen in Table 4.12 under CFRCM 1 pier. From these results and the crack pattern shown in Figure 4.54 c) the behaviour of the CFRCM 1 pier was considered satisfactory. The maximum forces, maximum displacements, ductility, and initial stiffness for the positive and negative direction were very similar for CFRCM 1 pier. It is concluded that the results for the CFRCM 1 pier may be considered satisfactory.

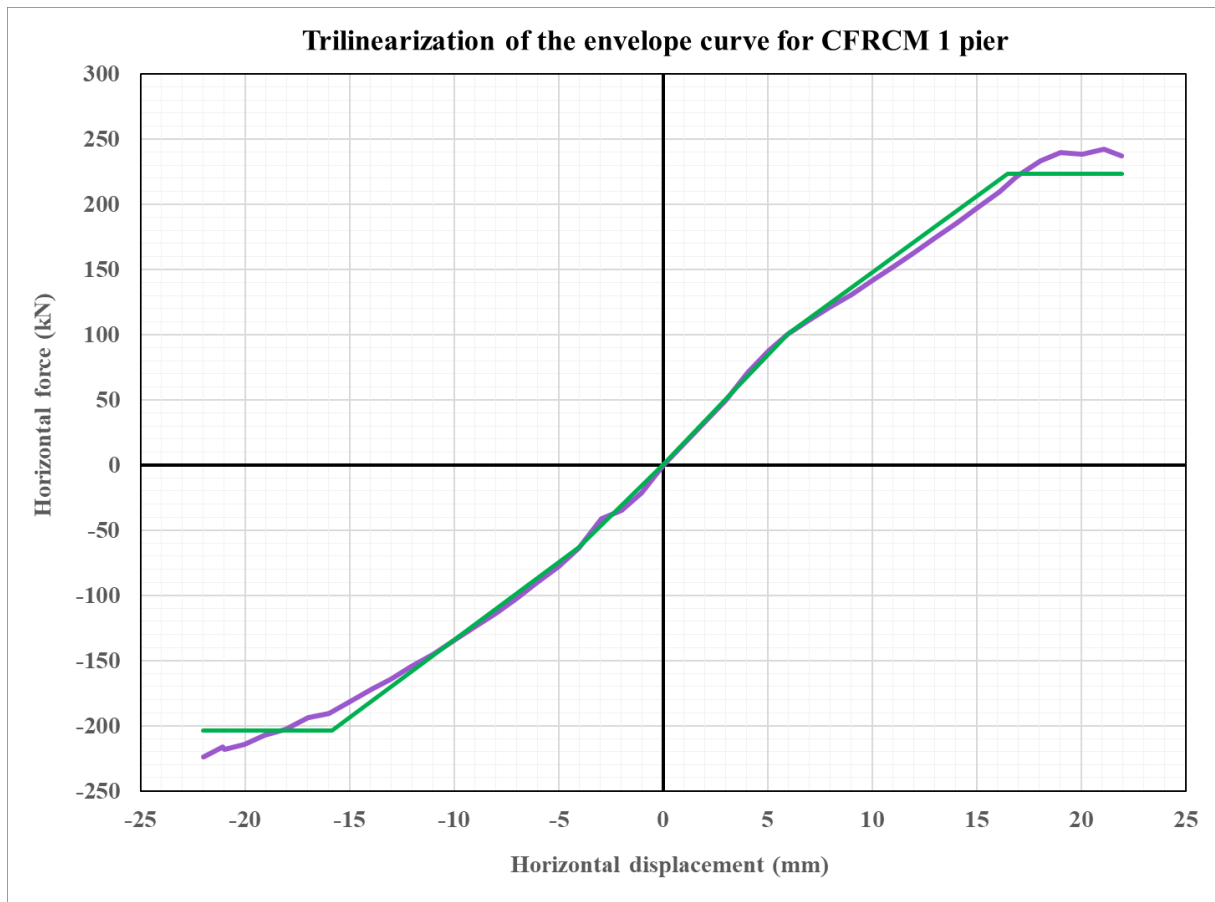


Figure 4.57 Trilinearization of the envelope curve for CFRCM 1 pier

Table 4.12 Results of the experimental campaign for CFRCM piers

| Value  | CFRCM 1 | CFRCM 3 | mean   |
|--|---------|---------|--------|
| Maximum horizontal force – positive direction [kN]       | 223,32  | 208,05  | 215,69 |
| Maximum displacement – positive direction [mm]           | 21,94   | 20,09   | 21,02  |
| Displacement at yielding point – positive direction [mm] | 16,08   | 14,28   | 15,18  |
| Ductility – positive direction                           | 1,36    | 1,41    | 1,39   |
| Initial stiffness – positive direction [kN/mm]           | 16,70   | 15,65   | 16,18  |

|   |        |        |        |
|---|--------|--------|--------|
| <b>Maximum horizontal force – negative direction [kN]</b>       | 203,54 | 160,13 | 206,40 |
| <b>Maximum displacement – negative direction [mm]</b>           | 22,01  | 15,59  | 18,80  |
| <b>Displacement at yielding point – negative direction [mm]</b> | 15,05  | 11,05  | 13,05  |
| <b>Ductility – negative direction</b>                           | 1,46   | 1,42   | 1,44   |
| <b>Initial stiffness – negative direction [kN/mm]</b>           | 20,56  | 22,09  | 21,33  |

The second CFRCM pier was tested on 19<sup>th</sup> of October. In case of CFRCM 2 pier the first crack appeared at the bottom right corner. The crack propagation and crack formation in different steps of the testing protocol can be seen in Figure 4.58. In Figure 4.58 a) the crack propagation in step 7 may be seen. At the horizontal displacement of 7 mm the FRCM strengthened masonry pier exhibited cracks in the middle of the pier. In Figure 4.58 b) the final crack propagation of the pier can be seen. The pier failed through only one diagonal (from the bottom left corner to the upper right corner). This type of failure is similar to CFRCM 1 pier where the same failure mechanism appeared even though the second diagonal was activated a bit more. The final failure mechanism of CFRCM 2 pier can also be seen in Figure 4.59. The maximum value of the crack width that was measured for the CFRCM 2 pier was 5,0 mm. The results of the testing campaign are shown in the form of a hysteresis curve (green) and a resistance envelope curve (purple dotted line) that can be seen in Figure 4.60.

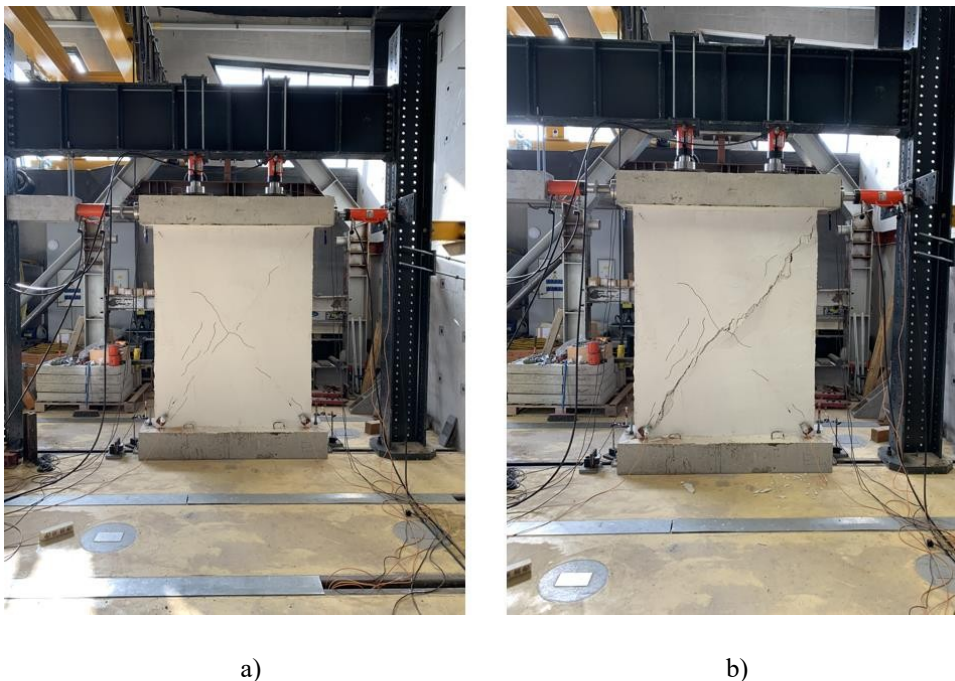


Figure 4.58 CFRCM 2 a) Crack propagation – step 7 b) Crack propagation – failure



Figure 4.59 Final failure mechanism of CFRCM 2 pier

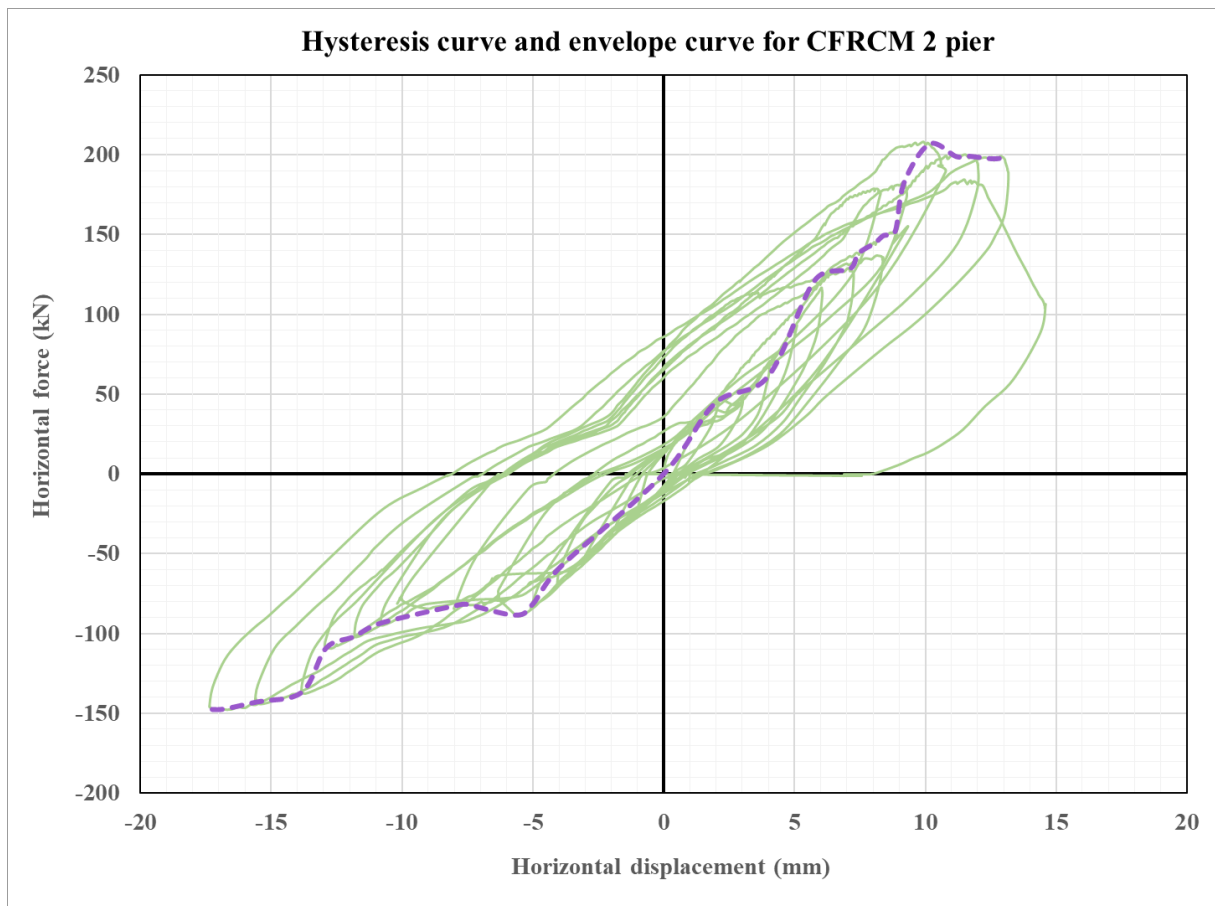


Figure 4.60 Hysteresis curve and envelope curve for CFRCM 2 pier



The most important results can be seen in Table 4.12 under CFRCM 2 pier. Even though the crack pattern shown in Figure 4.58 b) is satisfactory, the quality of results of the experiment are deficient. First, the hysteresis and the corresponding envelope curves show interference and scattering of results. Secondly, the maximum forces and the maximum displacements in the positive and negative direction differ greatly in the two directions. The maximum force in the positive direction is 40 % larger than the one in the negative direction. The maximum displacement in the positive direction is 70 % larger than the one in the negative direction. The reason for such inadequate behaviour is attributed to the pronounced initial curvature of the pier section, especially in the upper third of the pier height. Just before the examination, the bottom of the pier was rotated slightly to avoid eccentricity of the vertical load. This type of adjustment impacted the piers behaviour greatly. Therefore, the results gathered from the CFRCM 2 pier will not be considered in the further analysis.

The final CFRCM pier was also tested on 19<sup>th</sup> of October. In case of CFRCM 3 pier the first crack appeared at the bottom right corner. In Figure 4.61 a) the crack propagation in step 10 may be seen where the CFRCM pier 3 exhibited cracks mostly in the middle of the pier. In Figure 4.61 b) the final crack propagation of CFRCM 3 pier can be seen. The pier failed through only one diagonal (from the bottom left corner to the upper right corner). The failure mechanism and the crack pattern differed a bit from CFRCM 1 and CFRCM 2 piers since the second diagonal was not activated. The final failure mechanism of CFRCM 3 pier can also be seen in Figure 4.62 where the unstrengthen side of the pier is shown. The maximum value of the crack width that was measured for the CFRCM 3 pier was 4,0 mm. The results of the testing campaign are shown in the form of a hysteresis curve and a resistance envelope curve in Figure 4.63 where the hysteresis curve is plotted in green, and the envelope curve is given in a purple long dash - dot line.



a)

b)

Figure 4.61 CFRCM 3 a) Crack propagation – step 10 b) Crack propagation – failure



Figure 4.62 Final failure mechanism of CFRCM 3 pier

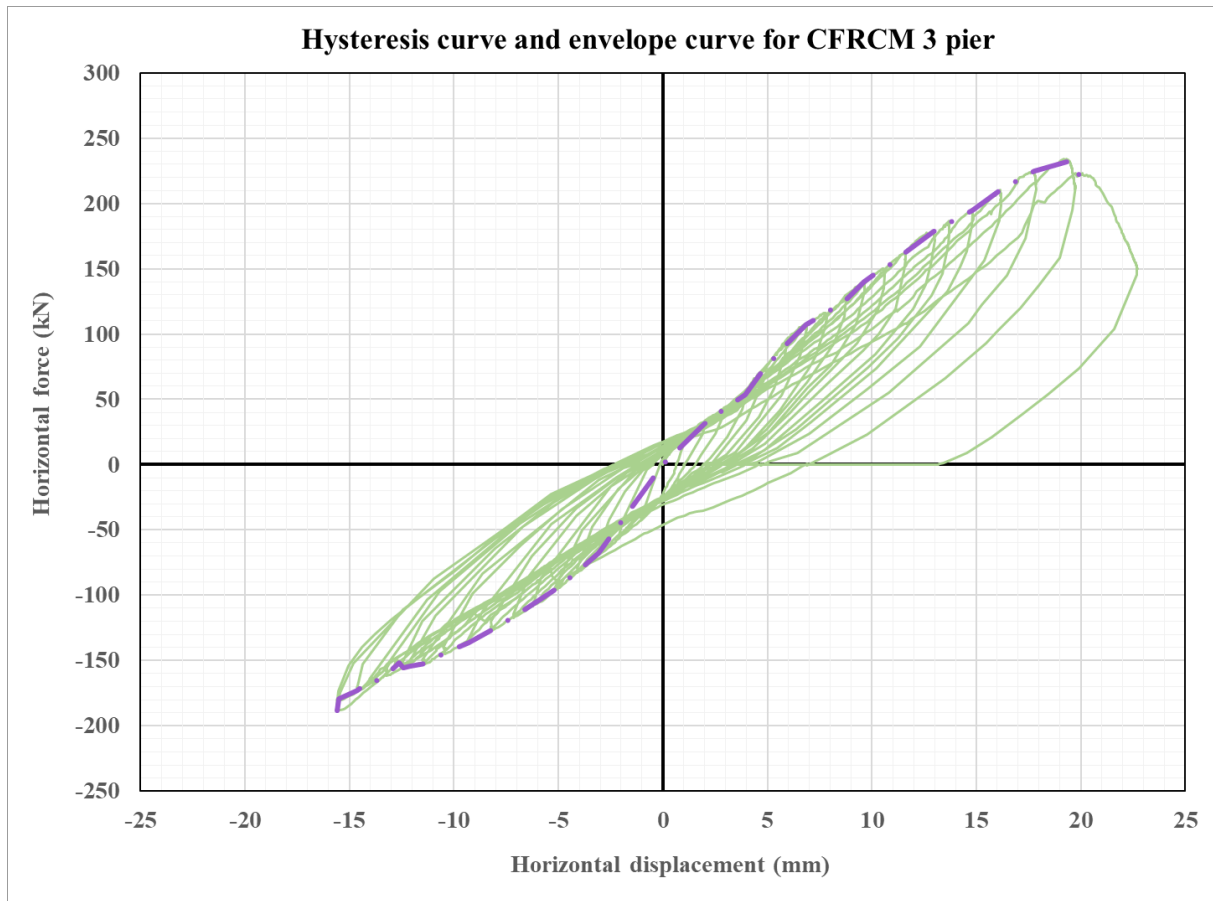


Figure 4.63 Hysteresis curve and envelope curve for CFRCM 3 pier

The trilinear curve of the CFRCM 3 pier can be seen in Figure 4.64. The most important results from the trilinear curve can be seen in Table 4.12 under CFRCM 3 pier. From the crack pattern shown in Figure 4.61 b) it can be concluded that the behaviour of the CFRCM 3 pier was satisfactory. On the other hand, the values of the maximum forces, maximum displacements, and initial stiffness differ quite a bit while the ductility has the same value in the positive and negative direction. The maximum force in the positive direction is 30 % larger than the maximum force in the negative direction. The same pattern may be seen in the difference in the maximum displacements where the one in the positive direction is larger by 29 % than the one in the negative direction. In the initial stiffness, the one in the negative direction is larger by 40 %. These differences are attributed to the heterogeneity of masonry piers. With everything stated above, the results gathered from CFRCM 3 pier will be considered in the analysis.

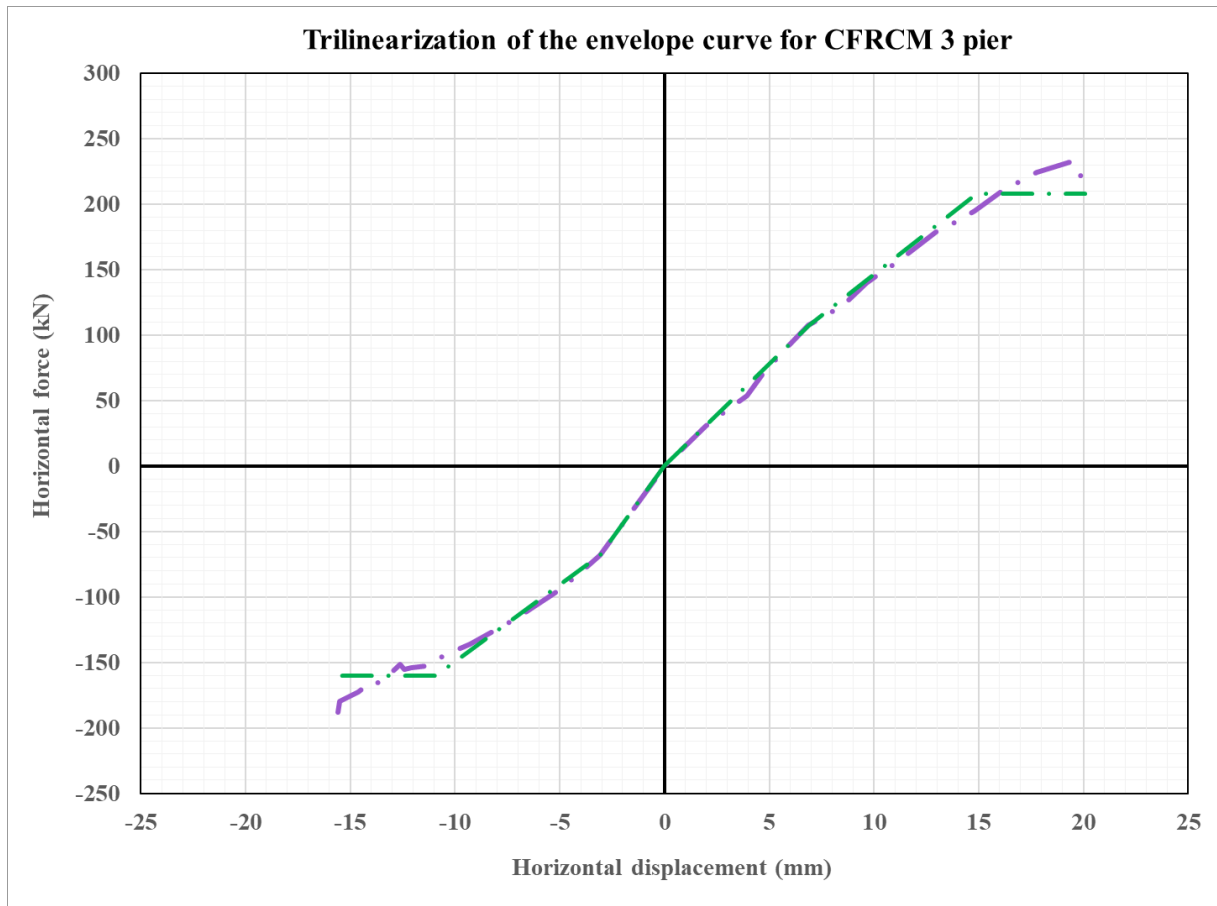


Figure 4.64 Trilinearization of the envelope curve for CFRCM 3 pier

When comparing CFRCM 1 and CFRCM 3 piers, similar behaviours were observed. As it was already explained, the most important measured values for CFRCM piers are given in Table 4.12. In both cases the maximum horizontal force was larger in the positive direction. In the negative direction though, the values differed quite a bit. The same pattern may be seen in the maximum displacement. In the positive direction, the maximum displacements were practically the same for both piers, whereas the values in the negative direction cannot be considered equivalent at all. In case of CFRCM 3 pier, these values were quite different showing a unsymmetrical behaviour. The same conclusion was derived for the initial stiffness. In case of CFRCM 1 pier, the initial stiffness was very similar in both directions. In CFRCM 3 pier these values differed greatly. The ductility for both piers in both directions were similar. The mean values are given in the final column of Table 4.12.

In Figure 4.65 the envelope curves for all CFRCM 1 and 3 piers can be seen and compared. Considering the differences mentioned above, the behaviour of the two CFRCM piers are very similar. And even though these differences cannot be ignored, both piers failed in a satisfying fashion. The diagonal patters were very clear and dominant on the side where

the FRCM strengthening technique was applied. No apparent delamination was observed until the maximum shear force was reached. It should be noted that the behaviour of the CFRCM piers was more flexible than in the case of URM and FRCM piers. Additionally, the envelope curves are practically overlapping each other which was not the case in URM or FRCM piers. CFRCM 1 and 3 piers and their corresponding values will be considered in the comparison to the URM piers (Series 1) and FRCM piers (Series 2). CFRCM 2 pier will not be considered.

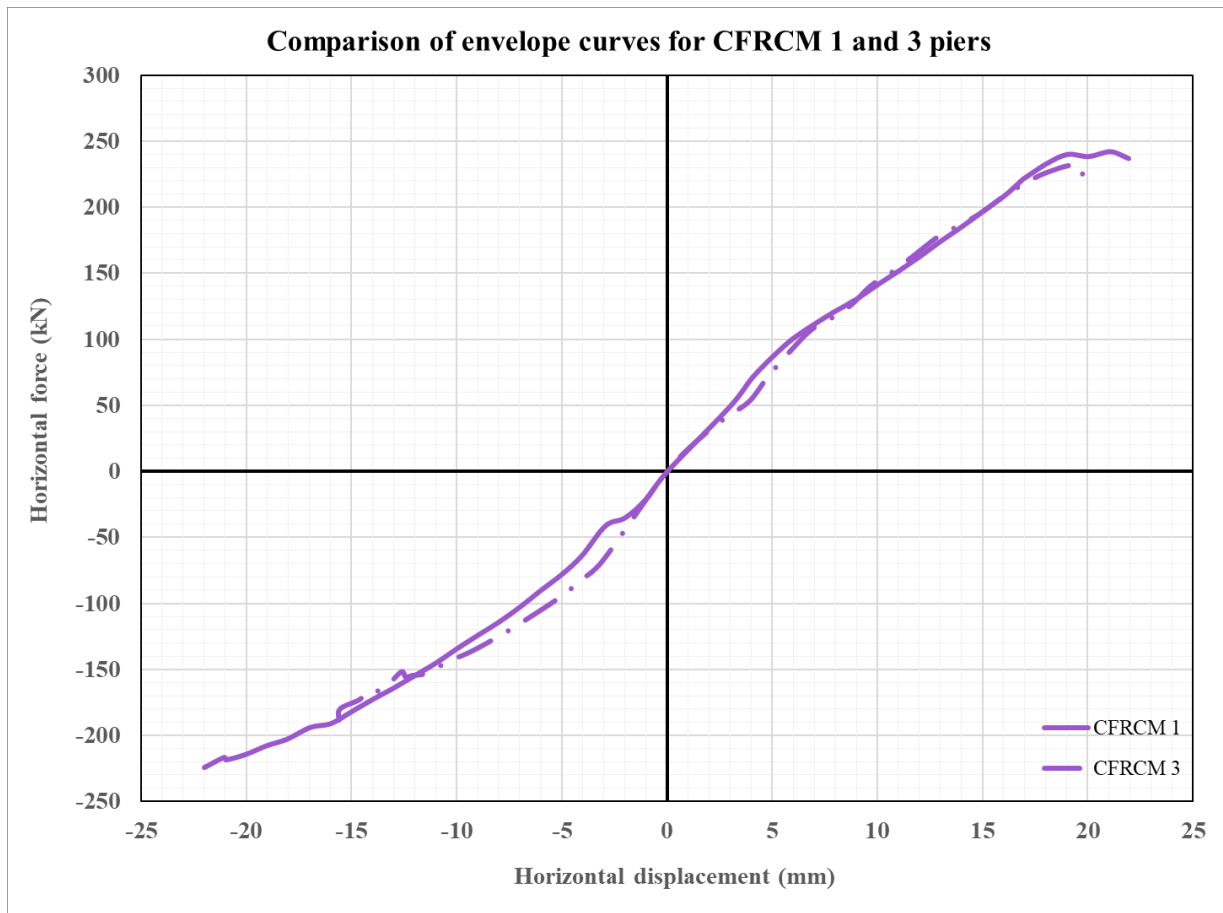


Figure 4.65 Envelope curves for CFRCM 1 and 3 piers

#### 4.4.4 Comparison of the experimental results

After the experimental campaign was conducted, comparisons between different series are drawn. Firstly, the crack patterns of the piers are discussed. The aim of the experimental campaign was to achieve a diagonal shear failure since that is the most common type of failure in masonry piers.

In Series 1, the URM piers failed in three different patterns. The crack pattern of the URM 1 pier was a very clean diagonal shear failure through only one diagonal (Figure 4.24). The second diagonal was not activated. In the case of URM 2 pier, an x-pattern failure appeared through both diagonals (Figure 4.29). The URM 3 pier also failed through one diagonal, but the

diagonal spread from the bottom corner on one side to the half of the pier's height on the other side (Figure 4.34). Until failure, the piers exhibited a flexible behaviour after which the failure itself was very sudden and brittle.

In Series 2, all three FRCM piers exhibited a diagonal shear failure through one diagonal, but in different manners. In case of the FRCM 1 pier, the second diagonal was very active, resembling an x-pattern failure till the very end when the pier failed through only one diagonal (Figure 4.41). The FRCM 2 pier failed through the same diagonal, but the second diagonal was mildly activated (Figure 4.46). Finally, in case of the FRCM 3 pier, the second diagonal was not activated at all, making the failure very clean through only one diagonal (Figure 4.49). The behaviour of the FRCM piers until failure was very flexible, while the failure itself was sudden.

The CFRCM piers that were a part of Series 3 were tested last. All three CFRCM piers exhibited a diagonal shear failure through one diagonal, practically in the same manner. CFRCM 1 pier failed through only one diagonal with the second diagonal barely being activated (Figure 4.55). The same crack patterns can be seen in Figure 4.59 and Figure 4.65 representing CFRCM 2 and CFRCM 3 piers respectively. The behaviour of CFRCM piers in comparison to URM and FRCM piers was much more stable which is clear from the matching crack patterns and failure mechanisms. The behaviour was very flexible, and the failure appeared much more gradually.

Besides the crack patterns that were observed throughout the testing campaign, numerous important values were measured to illustrate the piers behaviour. The mean values for all three series are shown in Table 4.13. It is important to remember that the values for CFRCM 2 pier were not taken into consideration because of the poor construction quality of the pier which had a pronounced initial curvature, especially in the upper third of the pier height. In Figure 4.66 envelope curves of all 8 considered piers are presented.

Table 4.13 Comparison of results for all masonry piers

| Value   | URM    | FRCM   | CFRCM  |
|---|--------|--------|--------|
| <b>Maximum horizontal force – positive direction [kN]</b>       | 153,39 | 204,52 | 215,69 |
| <b>Maximum displacement – positive direction [mm]</b>           | 14,25  | 20,77  | 21,02  |
| <b>Displacement at yielding point – positive direction [mm]</b> | 10,38  | 15,59  | 15,18  |
| <b>Ductility – positive direction</b>                           | 1,38   | 1,34   | 1,39   |
| <b>Initial stiffness – positive direction [kN/mm]</b>           | 19,60  | 17,55  | 16,18  |

|   |        |        |        |
|---|--------|--------|--------|
| <b>Maximum horizontal force – negative direction [kN]</b>       | 160,45 | 206,40 | 206,40 |
| <b>Maximum displacement – negative direction [mm]</b>           | 16,35  | 19,29  | 18,80  |
| <b>Displacement at yielding point – negative direction [mm]</b> | 14,17  | 16,85  | 13,05  |
| <b>Ductility – negative direction</b>                           | 1,16   | 1,15   | 1,44   |
| <b>Initial stiffness – negative direction [kN/mm]</b>           | 17,93  | 21,49  | 21,33  |

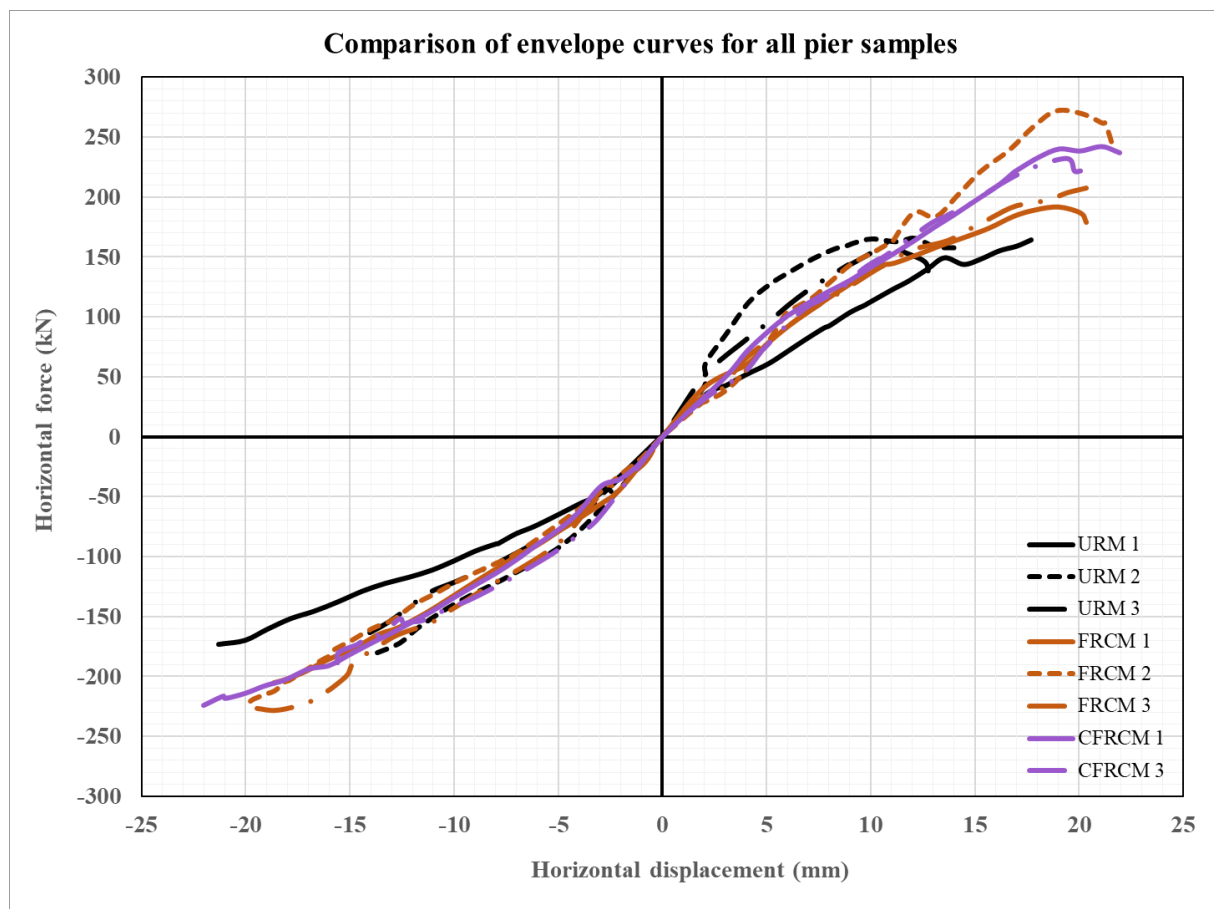


Figure 4.66 Envelope curves for all considered piers

From these results several conclusions may be drawn. The first parameter that was analysed is the maximum horizontal force achieved during the experimental campaign. As it was explained earlier, the maximum horizontal force is correspondent to the shear strength of the pier. The horizontal force was measured in two directions. From Table 4.13 it is obvious that the values differ slightly in the two directions for all series which is normal due to the heterogeneity of masonry piers in general. When comparing the values of the maximum horizontal forces between different series, a vast improvement was reported when using the

FRCM strengthening method. In the positive direction the, the mean value of the maximum horizontal force increased by almost 51 kN or 33 % when using the single sided FRCM strengthening system (Series 2). By adding clamping details, the improvement was even greater rising to 62 kN or 41 %. In the negative direction, the maximum horizontal force also increased by adding FRCM strengthening. By adding FRCM strengthening on one side, the mean value of the maximum horizontal force increased by 46 kN or 29 %. When clamping details were added, the increase was also 46 kN or 29 %. These improvements in shear strength may also be seen in Figure 4.66 where the envelope curves of all 8 considered piers are presented. When comparing the FRCM to the CFRCM piers, no apparent improvement in the horizontal in-plane strength may be observed by adding clamping details. As it is clear from Table 4.13 the CFRCM piers have a higher horizontal force in the positive direction and the same horizontal force in the negative direction in regards to the FRCM piers. The same may be concluded from Figure 4.66. In the positive direction, CFRCM 1 and CFRCM 3 piers had higher values of the horizontal force than FRCM 1 and FRCM 3 piers. On the other hand, FRCM 2 pier had a higher value than both CFRCM piers. In the negative direction, FRCM piers showed higher values and better behaviour. Therefore, it was concluded that the clamping details had no impact on the in-plane horizontal strength when diagonal shear failure occurred.

The second value to be considered was the maximum displacement of masonry piers in the positive and negative direction. The maximum displacement can be defined as the displacement under which the pier fails. As it was the case with the horizontal forces, by looking in Table 4.13, it is obvious that the displacements differed in the two directions for all series which is normal due to the heterogeneity of masonry piers. Additionally, it is evident that by adding FRCM reinforcement the displacement under which the pier fails increased. In the positive direction, the mean value of the maximum displacement increased by almost 6,52 mm or 46 % when the single sided FRCM strengthening system (Series 2) was applied. By adding clamping details, the improvement was even greater rising to 6,77 mm or 48 %. In the negative direction, the improvement was also visible but in a smaller manner. By adding FRCM strengthening on one side, the mean value of the maximum displacement increased by 2,94 mm and 2,45 mm when clamping details were added on the pier's sides. These improvements in the displacement capacity of the piers may also be seen in Figure 4.66.

The more important factor to be considered was the ductility of masonry pier in both directions. The value of ductility was gathered by dividing the maximum displacement with the displacement at the yielding point in the positive and negative direction. These values are shown in the trilinearization process for each pier. Mean values of the ductility in both directions for



all piers are shown in Table 4.13. In the positive direction, the mean value of ductility has not increased when the single sided FRCM strengthening system (Series 2) was applied. By adding clamping details, the improvement was very small equalling under 1 %. In the negative direction, the improvement was very visible. By adding FRCM strengthening on one side, the mean value of ductility stayed practically the same. When clamping details were added the ductility increased by 24 % in regards to FRCM and URM piers. These facts led to the conclusion that adding clamping details had a positive impact on the ductility of masonry piers, but a more extensive experimental campaign with primarily more samples needs to be conducted.

The final value that was measured was the initial stiffness of the masonry piers in the positive and negative direction. From values reported in Table 4.13 it is self-evident that by using single sided FRCM strengthening with or without clamping details had no effect on the initial stiffness of the piers. In the positive direction, the mean value of the initial stiffness for the URM piers was higher than the mean value for FRCM piers by 2,05 kN/mm or 12 %. When clamping details were added, this difference was even higher in favour of URM piers equalling to 3,42 kN/mm or 21 %. In the negative direction, the initial stiffness was higher in FRCM and CFRCM piers than in the URM piers. No apparent improvement in initial stiffness can be reported by using FRCM reinforcement or clamping details which was contradictory to earlier findings in the literature review. To address this issue and for a more precise numerical modelling campaign, an analysis was conducted. The main purpose of the analysis was to check the test setup to see why the initial stiffness did not increase in both directions when FRCM and CFRCM piers were tested. The main goal was to check if the double clamped boundary conditions were achieved. The analysis is displayed in the following subsection.

Overall, by using FRCM reinforcement the behaviour of the masonry piers improved drastically especially considering the maximum force and displacement. By adding clamping details, it is concluded that no improvement on the maximum horizontal force is achieved. On the other hand, the ductility of unstrengthened masonry piers and masonry piers strengthened with a FRCM coating on one side of the pier can be improved by using clamping details.

#### **4.4.5 Analysis of the boundary conditions in the test setup**

To achieve a diagonal failure and a proper behaviour of masonry piers, the double clamped boundary conditions needed to be achieved. At the bottom of all masonry piers, the reinforced concrete foundation beams were properly fixed to the laboratory floor. Therefore, the fixed boundary condition was achieved at the bottom. At the top of the samples the fixed conditions

are achieved through the forces and displacements in two vertical and two horizontal hydraulic jacks. To achieve a double clamped system, the bending moment in the middle of the pier needs to be equal to zero. The bending moment in the middle is calculated by summing the bending moments of the two vertical forces applied at the top of the pier and the bending moment achieved by the horizontal force in regards to the middle point of the pier. Through this analysis it was concluded that in case of all 8 considered piers, a bending moment appeared in the middle of the pier. The hysteresis and envelope curves of the bending moments for all piers are given from Figure 4.67 to Figure 4.74. These bending moments are defined by the differences in the vertical compressive forces throughout the experiment. Since all piers exhibited a diagonal shear failure but bending moments in the middle appeared, it can be concluded that all 8 piers exhibited a behaviour that is somewhere between a cantilever system and a double clamped system. This is the main reason behind the problem of initial stiffnesses in all masonry piers. The values of bending moments were different for all piers in the negative and positive direction. Additionally, the values are different for different piers. Through the envelope curves of these bending moments the atypical behaviour of masonry piers will be considered in the numerical modelling analysis so that the most accurate results are achieved for each pier.

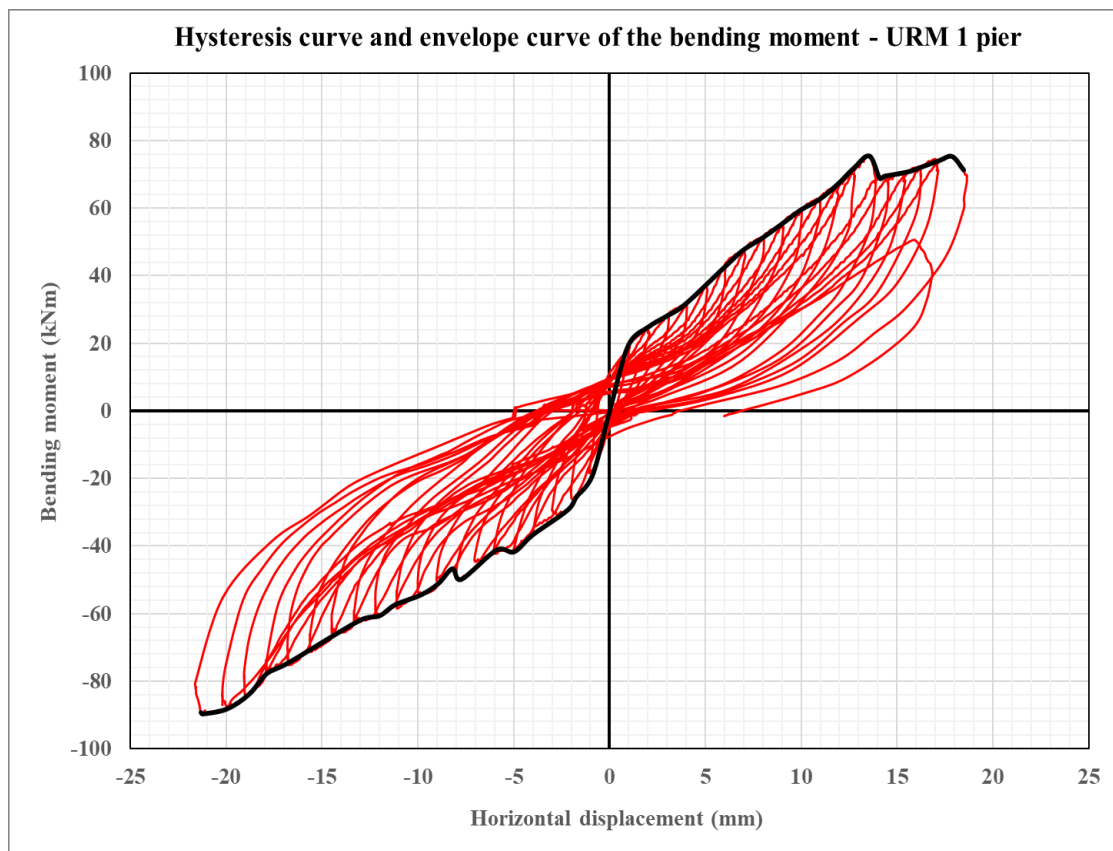


Figure 4.67 Hysteresis curve and envelope curve of the bending moment – URM 1 pier

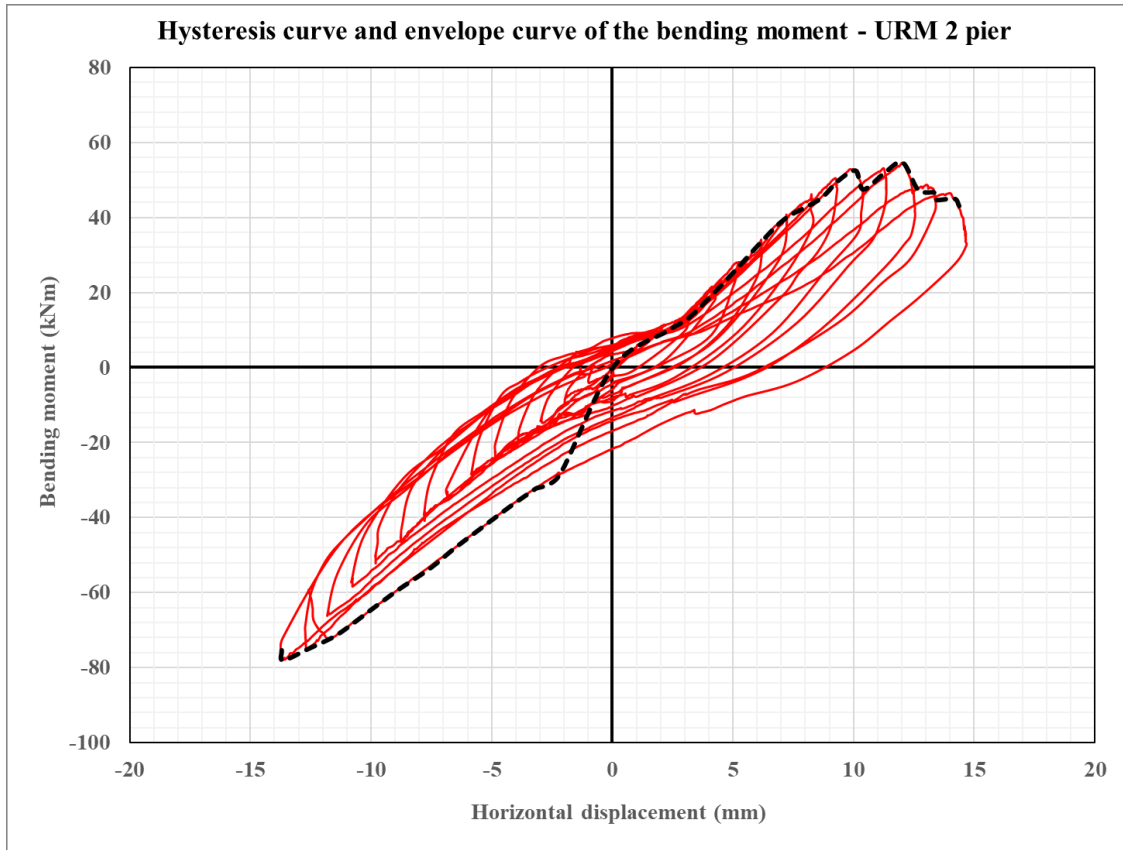


Figure 4.68 Hysteresis curve and envelope curve of the bending moment – URM 2 pier

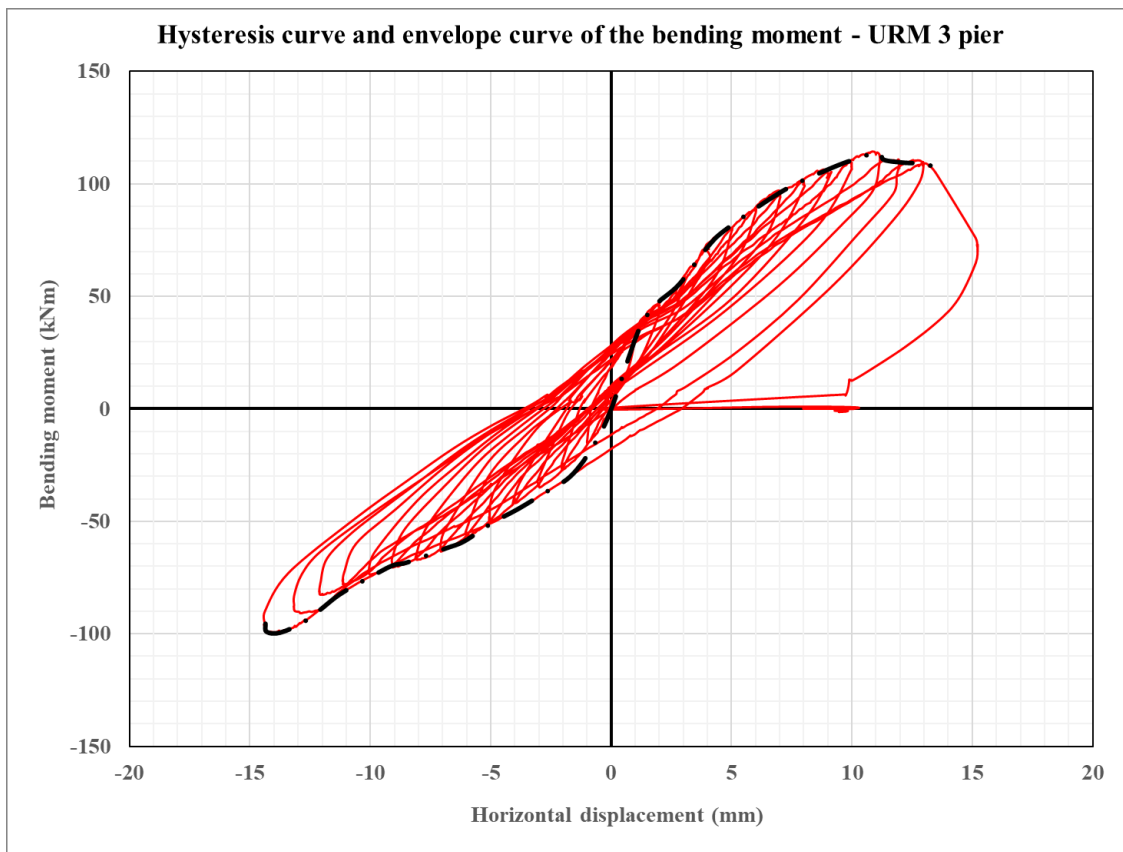


Figure 4.69 Hysteresis curve and envelope curve of the bending moment – URM 3 pier

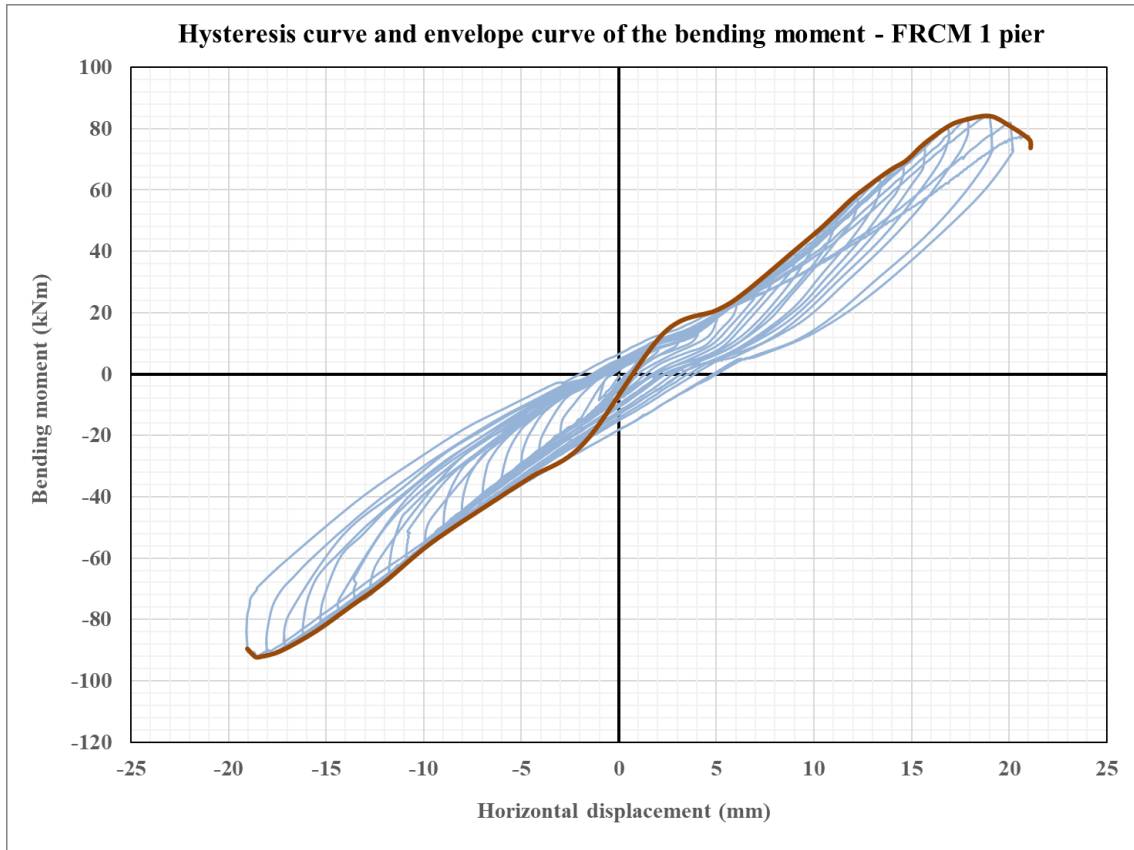


Figure 4.70 Hysteresis curve and envelope curve of the bending moment – FRCM 1 pier

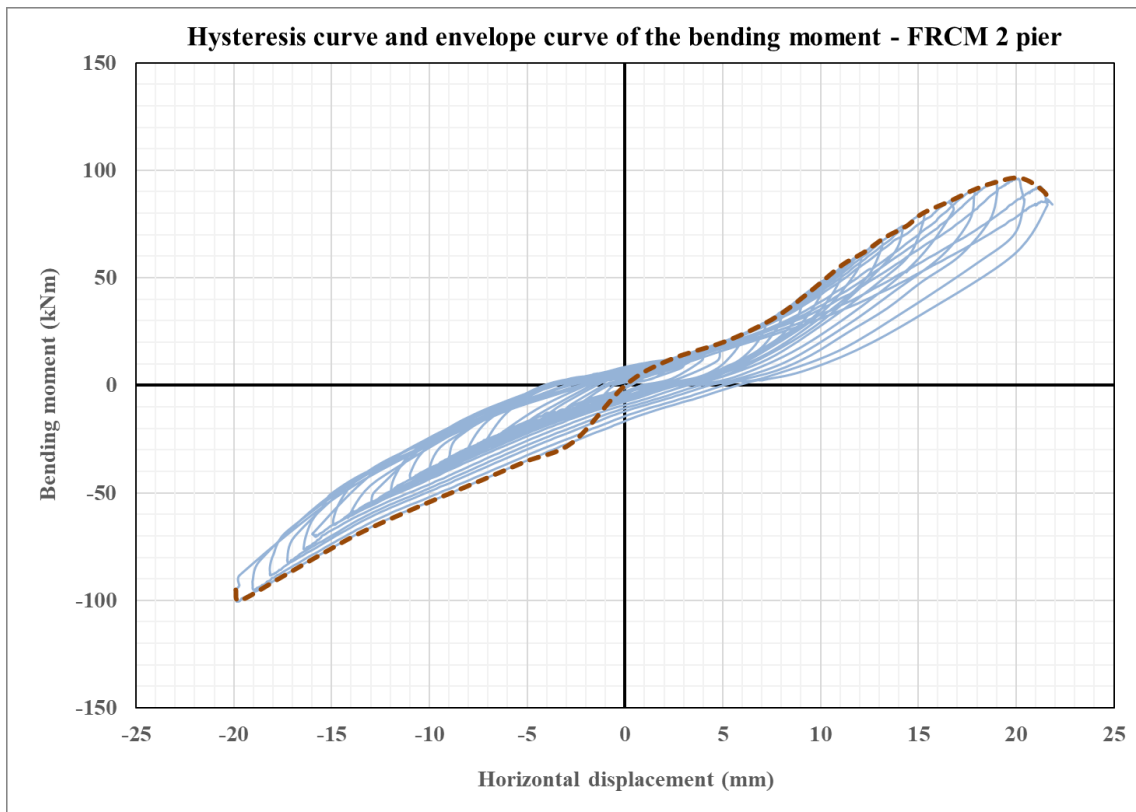


Figure 4.71 Hysteresis curve and envelope curve of the bending moment – FRCM 2 pier

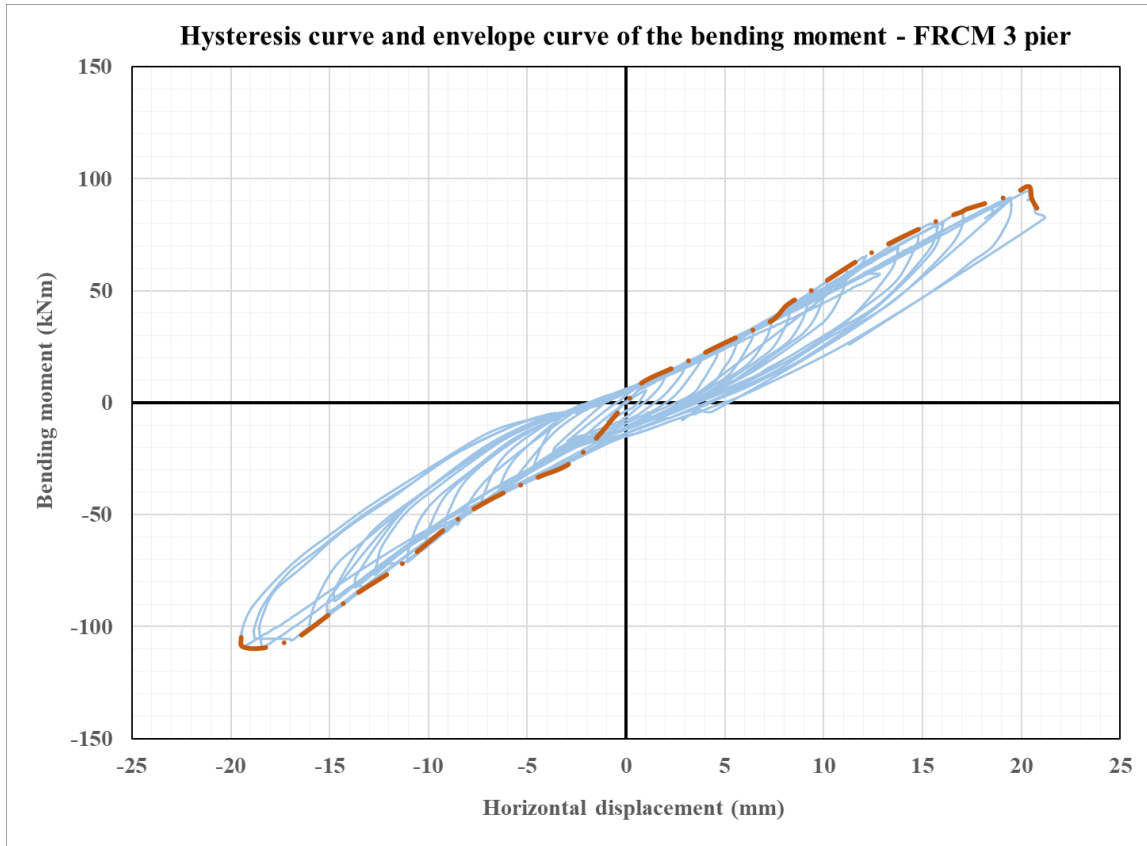


Figure 4.72 Hysteresis curve and envelope curve of the bending moment – FRCM 3 pier

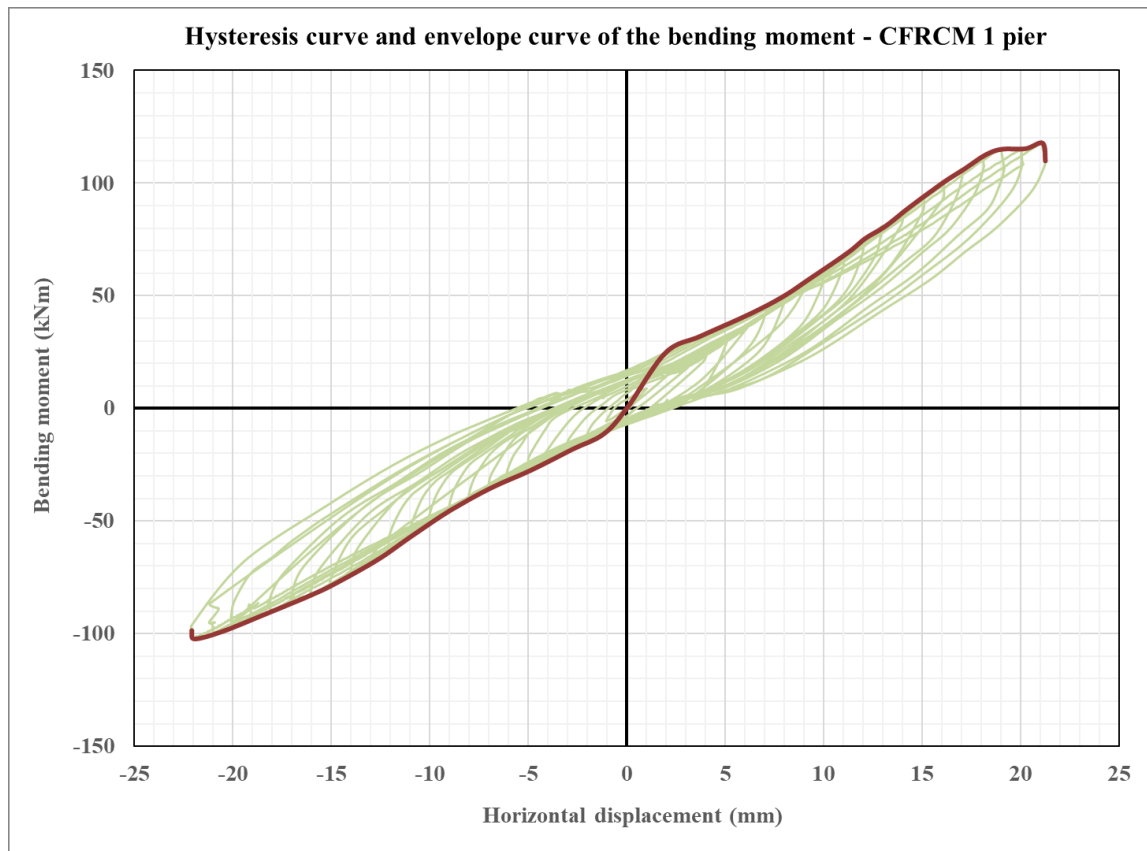


Figure 4.73 Hysteresis curve and envelope curve of the bending moment – CFRCM 1 pier

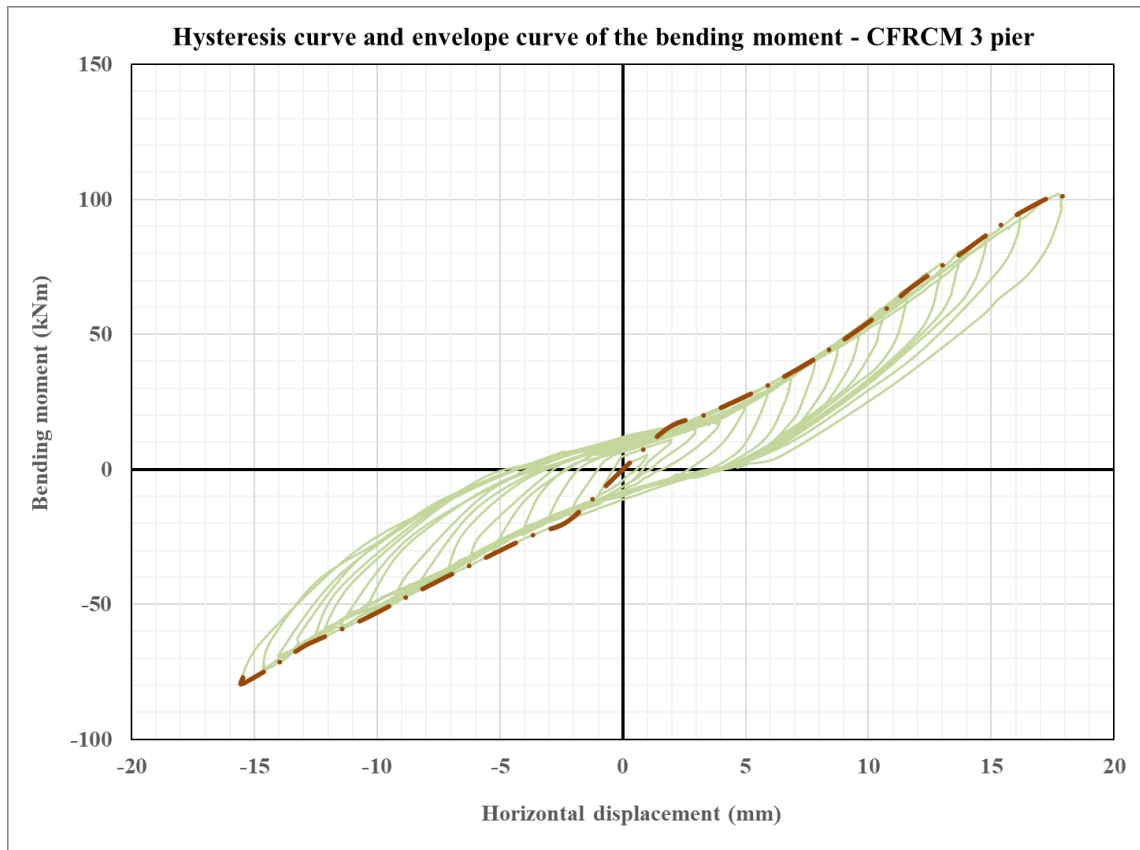


Figure 4.74 Hysteresis curve and envelope curve of the bending moment – CFRCM 3 pier

## 5 NUMERICAL MODELLING

In the previous section the experimental campaign was explained in detail. The results of the experimental campaign were satisfactory, with all nine piers failing in diagonal shear. And even though the results seem legitimate, they need to be confirmed and cross examined. For these purposes numerical modelling was used. In this dissertation the DIANA FEA 10.4 software was used. Numerous research on this software indicates it is a powerful tool for the numerical modelling of masonry [103] as it was reported by Asikoglu et al. It was also widely reported that the software was successful in simulations of experiments done on FRM-strengthened elements. The numerical modelling of both strengthened masonry walls as it was concluded by Murgo et al. [104] and by Lignola et. al [105] and strengthened masonry arches as it was reported by Ricci et al. [106] is feasible with DIANA FEA software. For the purposes of this dissertation, the micro-modelling approach was chosen for the most detailed analysis of the pier's behaviour.

### 5.1 Introduction

In this subsection, a classification of the numerical strategies for masonry structures is shown. This classification is based on how masonry structures (in this case piers) are conceived and modelled. Several different numerical strategies exist and are used for scientific and design needs. Each numerical approach has some specific attractive characteristics, which are optimal for a specific field of utilization. Additionally, different scales of material testing can be utilized to define the mechanical properties of elements used in the model, depending on the scale of representation considered in the modelling approach.

Detailed numerical modelling can be divided into four groups: block-based models (BBMs), continuum models (CMs), macro element models (MMs), and geometry-based models (GBMs) as it was defined by D'Altri et al. [107].

The block-based model or BBMs are based on a block-by-block definition of the masonry structure in the numerical model. Therefore, the actual texture of masonry could be accounted for. Each block can be treated as a rigid or deformable body, while the mechanical interaction between blocks is modelled through various formulations. The continuum model (CMs) on the other hand conceive masonry as a continuum deformable body, without any differentiation between the bricks and mortar layers. The masonry material constitutive law can be described using one of two approaches. The direct approach is based on tuning the constitutive laws through experimental tests. The second approach is based on homogenization

procedures and multiscale approaches. In macro element models or MMs, the panel-scale structural components or macroelements that have phenomenological or mechanical-based responses are defined and connected to idealize the masonry structure. Basically, two macroelements (i.e., piers and spandrels) can be recognized. The distinction of macroelements in a masonry structure must be carried out based on the interpretation of the structural arrangement. This approach is used mostly in structures, not in individual structural elements. Finally, the geometry-based models (GBMs) are represented by a rigid body that is employed to model the structure. The only input data needed in these modelling approaches is represented by the geometry of the structure. Therefore, no block-by-block description of masonry is conceived in this approach [107].

In this dissertation a block-based model was used. The BBMs are the most detailed approach in which material characteristics and heterogeneity of masonry are considered in the most detailed manner. As it was already mentioned, these models can account for the actual texture of masonry, which governs the failure mode of the material and its mechanical properties. The pioneering work developed by Page [108] was one of the first examples of a nonlinear BBM. In this case, the bricks were modelled as elastic blocks linked together by mortar joint elements that have restricted shear strength depending on the bond strength and the normal stress state. From there on, the block-based models can be categorized into various subclasses depending on the manner the interaction between blocks is conceived. They include the interface element-based approaches, contact-based approaches, textured continuum-based approaches, block-based limit analysis approaches and extended finite element (FE) approaches [107]. In this dissertation, the interface element-based approach was used. This interface element-based approach was developed by Lofti and Shing [109]. In this study, the mortar layers were defined as zero-thickness interface elements between blocks. The idea was to expand the blocks dimensions to simulate such a zero thickness. Also, the study conducted by Lourenco and Rots [110] was used. In this paper, a significant enhancement was introduced through the development of a multi-surface interface model where all nonlinearities were concentrated in the zero-thickness interfaces, in the context of softening plasticity. With this enhancement, the effectiveness of the model increased. The final upgrade of the interface model was developed by Oliveira and Lourenco [111] for the simulation of the cyclic response of masonry panels. The main advantages of such a micro modelling approach are the most accurate description of the masonry texture and details, detailed characterization of mechanical properties and explicit crack patterns [107]. Additionally, the possible failure modes and the accompanying crack patterns can only be fully obtained by a micro modelling strategy as it was



reported by Plassiard et al. [112], Nerilli et al. [113] and Rots [114]. The macro modelling approach usually has numerous issues in this area as it was discussed by Betti et al. [115]. The main downsides of the micro modelling approach were reported by Bertolesi et al. [116]. They concluded that the massive computational effort and the time-consuming work of assembling the model block by block are the main issues. This is why only a few full-size structures were modelled using the block-based approach. Another problem that occurred is that too many material properties need to be known. In the end, the quality of results is the most important part of the numerical modelling campaign, so the micro modelling approach was employed.

## 5.2 Numerical modelling of Series 1 – URM piers

### 5.2.1 Geometry

In the finite element micro-modelling approach, masonry is subdivided into solid elements (elastic blocks) with different properties connected by nonlinear interface elements. The same methodology was used in this dissertation to assess the quality of results gathered in the experimental campaign. Therefore, the same URM pier with dimensions  $l/h/t = 142/186,5/25$  cm was examined. The masonry pier was placed upon a concrete foundation beam, which is used to fix the specimen to the floor. On top of the pier a concrete beam was modelled for the distribution of loads and for imposing proper boundary conditions. The isometric view of the URM masonry pier modelled in DIANA FEA 10.4 can be seen in Figure 5.1 a) and the front view of the same pier can be seen in Figure 5.1 b).

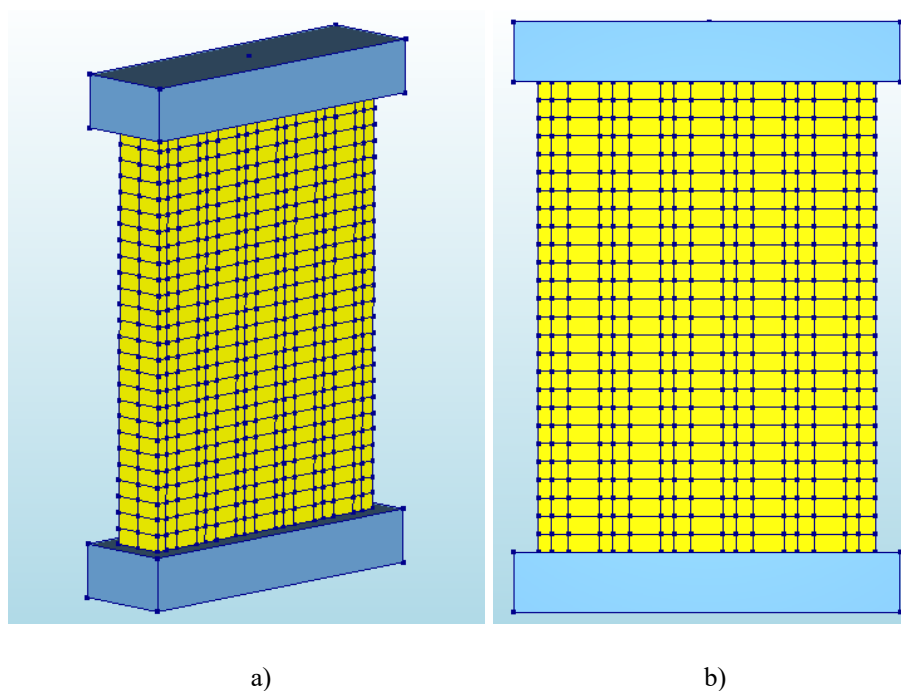


Figure 5.1 URM pier (Series 1) in DIANA FEA 10.4 software a) Isometric view 7 b) Front view

Upon examination, it is clear that the concrete beams (light blue in Figure 5.1) were defined by one element each. Each of these elements were defined as 3D solid shapes. On the other hand, the bricks (yellow in Figure 5.1) were defined by 884 solid 3D shapes that were used to model the masonry pier. The dimensions of the bricks were slightly increased in the model so that the mortar joints could be modelled with zero thickness. The actual dimensions of the bricks were  $b/h/l = 12/6,5/25$  cm, whereas the dimensions in the model were  $b/h/l = 13/7,5/26$  cm. An approach with zero-thickness joints was used to save computational time and to have a clearer crack pattern between the bricks as it was reported by Balkema [117]. Also, it was stated that such an approach has little impact on the overall results, but it makes the modelling process much easier. The second simplification was to divide the bricks into parts to achieve a proper connection in the vertical and horizontal directions. The simplification is shown in Figure 5.2, where the detail between brick elements is shown – the walls are constructed in English bond. The vertical mortar joints between bricks are drawn in green, and the horizontal bed joints in red. The blue denotes a fixed connection between two pieces of the same brick. The reason for this simplification is that the DIANA FEA 10.4 software cannot connect two 3D shapes of different sizes. The same problem occurred at the connection between the masonry pier and the RC beams at the top and bottom. To properly connect the bricks to a much larger concrete element, the outlines of bricks were projected/imprinted on to the foundation beam and the top beam with a proper function in the software. This adaptation can be seen in Figure 5.3 where the lowest row of bricks is projected to the surface of the foundation beam. The same adaptation was used between the highest row of bricks and the top beam.

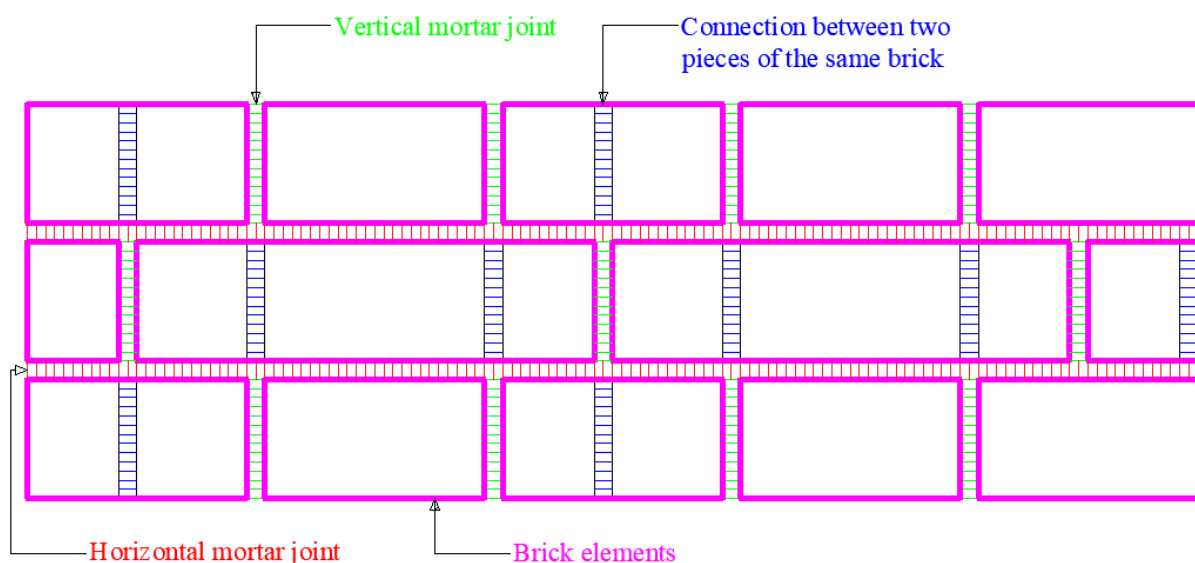


Figure 5.2 Interfaces between brick elements – green (vertical joints), red (horizontal joints), blue (connection between two pieces of the same brick) and magenta (brick elements)

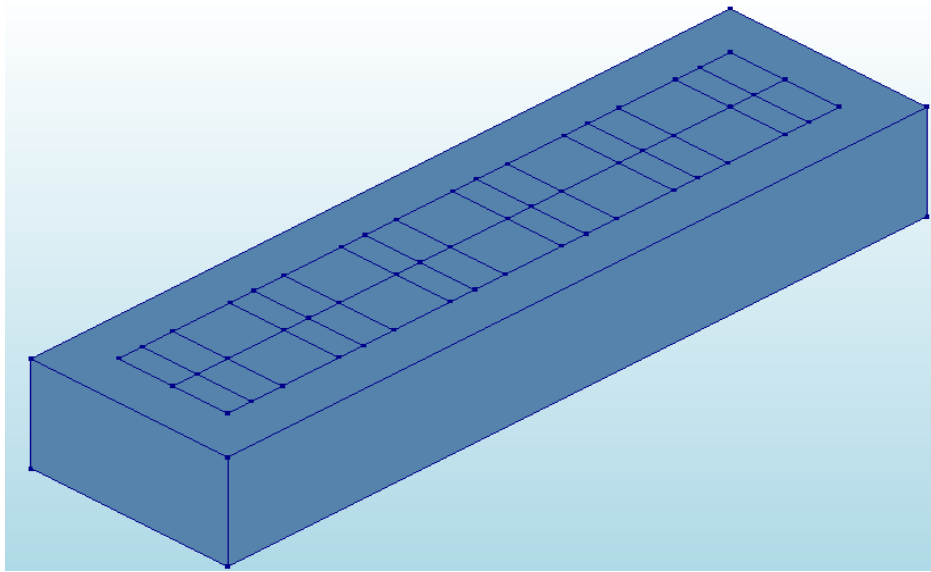


Figure 5.3 Detail of the imprint between the lowest row of bricks and the concrete foundation

### 5.2.2 Mechanical properties of materials

In case of URM piers, three different materials were used. The concrete beams at the top and at the bottom of the masonry pier, elongated bricks and vertical and horizontal interfaces representing mortar joints. The concrete beams and masonry bricks were defined as solid elements with linear elastic properties. The linear elastic properties of concrete and masonry bricks are shown in Table 5.1 and include the modulus of elasticity ( $E$ ), Poisson's ratio ( $\nu$ ) and mass density. The values for concrete were defined for grade C30/37 obtained by testing the compressive strength of concrete in subsection 4.2.1. The values for masonry were obtained according to literature. According to the New Zealand Society for Earthquake Engineering (NZSEE) explained by Ghiassi et al. [118] the value of the modulus of elasticity can be estimated using the compressive strength of the masonry unit,  $f_b$ . It was proposed that the modulus of elasticity can be taken in the range of  $125-1400 f_b$  with a mean value of  $350 \cdot f_b$ . Therefore, the modulus of elasticity was calculated as  $E = 350 \cdot 37,02 \text{ N/mm}^2 = 12957 \text{ N/mm}^2$ . The Poisson's ratio was taken according to the same literature as 0,2 for common stiff bricks. The mass density was given by the manufacturer. The variability of mechanical properties of masonry was one of the largest factors influencing the results of the numerical modelling [119].

Table 5.1 Linear elastic properties of concrete and masonry

| Element        | $E$ (N/mm <sup>2</sup> ) | $\nu$ | Mass density (kg/m <sup>3</sup> ) |
|----------------|--------------------------|-------|-----------------------------------|
| Concrete beams | 33000                    | 0,2   | 2500                              |
| Masonry bricks | 12957                    | 0,2   | 1500                              |

On the other hand, the vertical and horizontal interfaces representing mortar joints were modelled as 3D surface interfaces. These interfaces were defined by linear material properties (normal and shear stiffness moduli) and a nonlinear combined cracking-shearing-crushing material model. This model considered all basic types of failure modes that may appear in masonry: cracking of the joints, sliding along joints at low values of normal stress, cracking of the bricks in direct tension, brick diagonal tensile cracking and masonry crushing as it was explained by Lourenco and Rots [110]. The material properties of all interface elements representing mortar joints are shown in Table 5.2. It is obvious that many parameters need to be defined to get a clear and adequate behaviour of the interfaces and the piers in general. The variability of these parameters may also greatly influence the numerical model as it was reported by D'Ambra et al. [120]. The same properties were used for the horizontal and vertical interfaces, but different local interface axes were defined to captivate the actual behaviour of the mortar joints.

The first parameters that need to be defined are the linear material properties that include the normal stiffness  $k_n$  in the local z-axis and shear stiffness  $k_s$  that was taken with the same value in the x-axis and the y-axis. The following equations were used for their calculation that were defined by Lourenco and Rots [110]:

$$k_n = E_b \cdot E_m / h_m \cdot (E_b - E_m) \quad (5.1)$$

$$k_s = G_b G_m / h_m \cdot (G_b - G_m) \quad (5.2)$$

|        |       |   |
|--------|-------|---|
| where: | $E_b$ | modulus of elasticity for bricks (Table 5.1)      |
|        | $E_m$ | modulus of elasticity for mortar                  |
|        | $h_m$ | thickness of the mortar layer equal to 10 mm      |
|        | $G_b$ | shear modulus for bricks equal to $0,4 \cdot E_b$ |
|        | $G_m$ | shear modulus for mortar equal to $0,4 \cdot E_m$ |

The mortar that was used in this model is a M5 general purpose mortar which was tested and explained in subsection 4.2.3. The value of  $E_m = 3000 \text{ kN/mm}^2$  was assumed, as can be found in old masonry buildings according to Murgo et al. [104]. According to equations 5.1 and 5.2, the normal and shear stiffness are calculated and can be seen in Table 5.2.

After that, the values needed for the nonlinear combined cracking-shearing crushing model were defined. The values can be split into four categories.

The first category consisted of two values that are important in the cracking phase of the model (tensile behaviour), tensile strength  $f_t$  and the bond fracture energy  $G_f^I$ . According to EN

1996-1-1 the tensile strength was calculated as  $f_t = f_{vk0}/1,5$  where  $f_{vk0} = 0,23 \text{ N/mm}^2$  is the initial shear strength of masonry that was obtained in subsection 4.2.4. According to Heffler [121], the bond fracture energy,  $G_f^I$  is defined as a function of the tensile strength  $f_t$ :

$$G_f^I = 0,01571 \cdot f_t + 0,0004882 \quad (5.3)$$

The values for both,  $f_t$  and  $G_f^I$  were calculated and shown in Table 5.2.

The second category consisted of values needed for the interpretation of the shear behavior of the pier. The cohesion or bond strength was calculated as  $c = 1,5 \cdot a_f$  it was explained by Petersen [122]. The tangent friction angle should be taken as 0,75 independent of the type of unit or mortar according to Ghiassi et al. [118]. EN 1996-1-1 [85], on the other hand recommends the value of 0,4 so in conclusion the tangent friction angle should be taken in the range of 0,4 to 0,75. The residual friction angle was assumed equal to the friction angle. The dilatancy angle can be assumed equal to zero as it diminishes with increasing axial stresses and slip at the interface. The confining normal stress  $\sigma_n$  and the exponential degradation coefficient were taken according to Murgo et al. [104]. Finally, the mode II fracture energy  $G_f^{II}$  was dependent on the normal stress level and can be taken according to Ghiassi et al. [118] as  $G_f^{II} = 0,1 \cdot c$ .

In the third category, the factors for the crushing phase of the masonry were introduced. The compressive strength of masonry was taken according to equation 3.1 in subsection 3.3. With the value of the normalized compressive strength of masonry units being equal to  $f_b = 37,02 \text{ N/mm}^2$  (subsection 4.2.2.) the compressive strength of masonry is equal to:

$$f_k = K f_b^\alpha \cdot f_m^\beta = 0,55 \cdot 37^{0,7} \cdot 5^{0,3} = 11,16 \text{ N/mm}^2 \quad (5.4)$$

An additional factor was introduced in this phase called  $C_s$ . The factor of  $C_s = 9$  was taken according to Murgo et al. [104].

The final part of the nonlinear combined cracking-shearing-crushing material model consisted of two parameters representing the compressive inelastic law. The compressive fracture energy, proposed in Model code 90 for concrete [123], may be used for masonry. The following equation was used:

$$G_f^c = 15 + 0,43 f_b - 0,0036 \cdot f_b^2 \quad (5.5)$$

The value of the compressive fracture energy was calculated and shown in Table 5.2. The equivalent plastic relative displacement was taken with 50 mm as it was presented in Murgo et al. [104]. After all of the parameters were defined and explained, the boundary conditions needed to be defined to approximate the behavior of the piers during the experimental

campaign. Also, the vertical compression load and the horizontal displacement need to be defined and added to the numerical models.

Table 5.2 Mechanical properties of mortar joints

|   |  |   |
|---|--|---|
| <b>Normal stiffness <math>k_n</math> (N/mm<sup>3</sup>)</b> | <b>Shear stiffness <math>k_s</math> (N/mm<sup>3</sup>)</b> | <b>Tensile strength <math>f_t</math> (N/mm<sup>2</sup>)</b>     |
| 390   | 156  | 0,15  |
| <b>Fracture energy <math>G_f^I</math> (N/mm)</b>            | <b>Cohesion <math>c</math> (N/mm<sup>2</sup>)</b>          | <b>Friction angle (rad)</b>                                     |
| 0,003   | 0,23   | 0,75  |
| <b>Dilatancy angle (rad)</b>                                | <b>Residual friction angle (rad)</b>                       | <b>Confining normal stress (N/mm<sup>2</sup>)</b>               |
| 0   | 0,75   | -0,7  |
| <b>Exponential degradation coefficient (mm)</b>             | <b>Fracture energy <math>G_f^{II}</math> (N/mm)</b>        | <b>Compressive strength <math>f_k</math> (N/mm<sup>2</sup>)</b> |
| 5   | 0,023  | 11  |
| <b>Factor <math>C_s</math></b>                              | <b>Compressive fracture energy (N/mm<sup>2</sup>)</b>      | <b>Equivalent plastic relative displacement (mm)</b>            |
| 9   | 26   | 50  |

### 5.2.3 Boundary conditions and applied loads

After the geometry of the pier was defined and the mechanical properties were set for elements used in the model, the boundary conditions (supports) and applied loads were defined. As for the boundary conditions, the idea was to simulate the experimental campaign. At the bottom of the reinforced concrete foundation beam, a fixed support was added. By adding such a support, the pier should be fixed in place and no translatory movement should appear. Therefore, translations in three global directions (x,y,z) were fixed. To avoid adding supports in all available nodes at the bottom of the foundation beam, a tying option was used. With this option, all nodes at the bottom of the foundation beam were connected. The fixed supports were then added at only one corner of the bottom face of the foundation beam and were prescribed to the entire bottom face. The fixed support can be seen in Figure 5.4.

Till this point, the numerical model for all three URM piers was the same since the geometry, mechanical properties of materials and boundary conditions needed to be correspondent. The differences observed between the URM piers during the experimental campaign were considered via the applied loads. In all three cases the loads were applied at the top reinforced concrete beam. In the vertical direction, the vertical compressive force was applied. With the value of 250 kN the force was applied at the central node of the top face of the top beam for all three URM piers. The central node was connected to the other nodes at the

top face of the top beam using the tying option. By using this simplification, the force was applied in one node and distributed along the entire face.

To apply the horizontal displacement, a new set of supports was defined and added. In this case the supports were added across the upper face of the top beam and had a fixed translation only in the in-plane direction of the pier (y-direction). The supports at the top beam can be seen in Figure 5.5. The displacement was applied in the horizontal y-direction with the total value of 21,50 mm for all three URM piers. This value was chosen according to Table 4.8 where the maximum displacement of all URM piers was 21,32 mm for URM 1 pier in the negative direction.

The final load that was applied for each URM pier was the bending moment around the x-axis. The reason for applying these bending moments were the differences in the vertical compressive forces in the two vertical hydraulic jacks throughout the experiment that were reported in subsection 4.4.5 for all three URM piers. As it is clear from Figure 4.67, Figure 4.68 and Figure 4.69 that are correspondent to URM 1, URM 2 and URM 3 piers, the values of these bending moments are different for each pier. Therefore, three separate numerical models were needed to display the proper behaviour of each pier. As it was explained in subsection 4.4.5 for each URM pier a hysteresis curve of the bending moment was gathered. For each hysteresis curve an envelope curve was derived with values in the negative and positive directions. Since the numerical model was based on the pushover analysis, the values of the bending moments were considered in the numerical model with either a pushover curve that was achieved in the positive direction or a pushover curve that was achieved in the negative direction. From Figure 4.67, Figure 4.68 and Figure 4.69 the pushover curve with the highest absolute value of the bending moment was chosen for each URM pier. Therefore, for the URM 1 and URM 2 piers the pushover curve in the negative direction was chosen as the representative curve. The maximum values of the bending moments for the URM 1 and URM 2 pier were equal to 89,33 kNm and 78,00 kNm respectively. In case of URM 3 pier the pushover curve in the positive direction was chosen as the representative curve with the maximum value of the bending moment equal to 113,75 kNm. All pushover curves of the bending moments were added to their correspondent numerical models as positive values. A typical pushover curve of the bending moment that was applied in the numerical model can be seen in Figure 5.6. This pushover curve was defined for the URM 1 pier. The pushover curve was defined through a time dependency as it is clear from Figure 5.6. It is important to state that the same time dependency factors were used for both the horizontal displacement and the bending moment so that they are connected and applied at the same time and in the same manner.

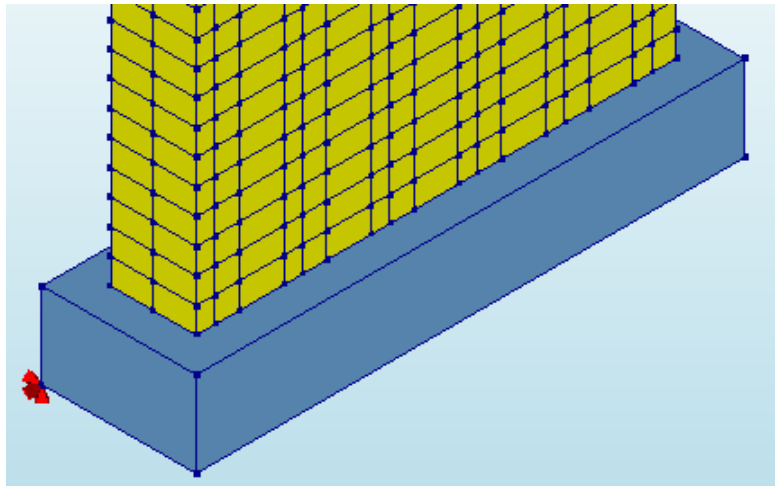


Figure 5.4 Fixed support at the bottom face of the foundation beam (red colour)

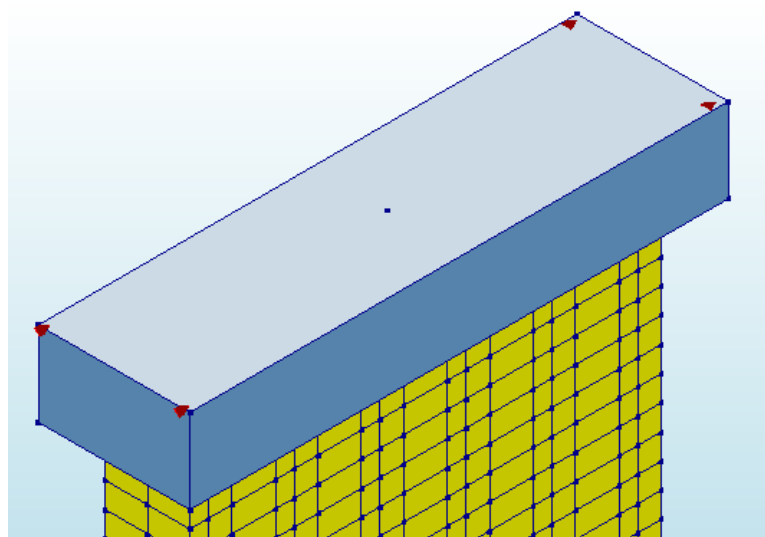


Figure 5.5 Support at the upper face of the top beam (red colour)

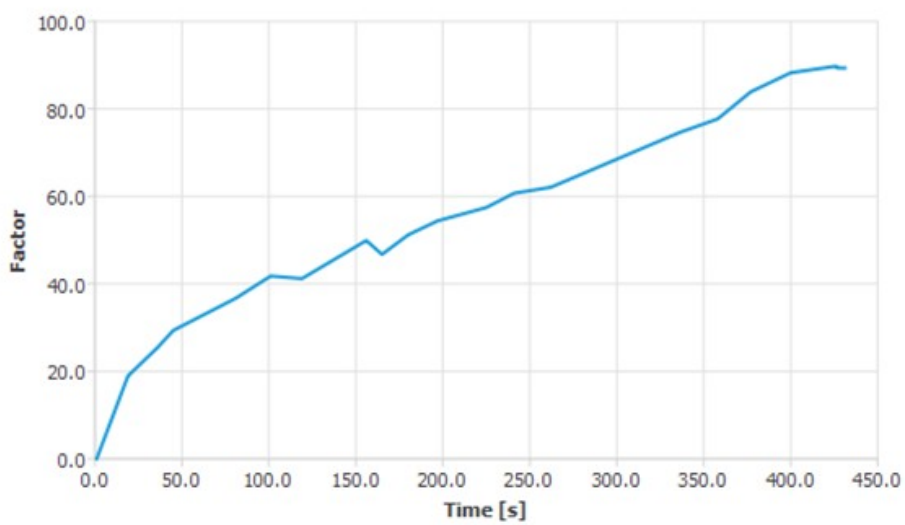


Figure 5.6 Pushover curve of the bending moment for URM 1 pier – numerical model



### 5.2.4 Mesh settings and the nonlinear analysis

In the previous subsections, the geometry, the mechanical properties of materials and the boundary conditions were defined. After that, the vertical compressive force, horizontal in-plane displacement, and the bending moment were applied to each URM pier model. The next step was to define proper the mesh settings for the nonlinear analysis. The basic principle is that the smaller the mesh size, the more detailed the analysis. In this dissertation, the mesh size was chosen so that even the smallest elements in the model can be meshed. Since the smallest 3D element used in the model was a half brick element with dimensions  $b/h/l = 6/6,5/12$  cm, a mesh size of 50 mm or 5 cm was chosen. Since the meshing targets were 3D shapes, a hexa/quad meshing type was defined. The mesh configuration can be seen in Figure 5.7.

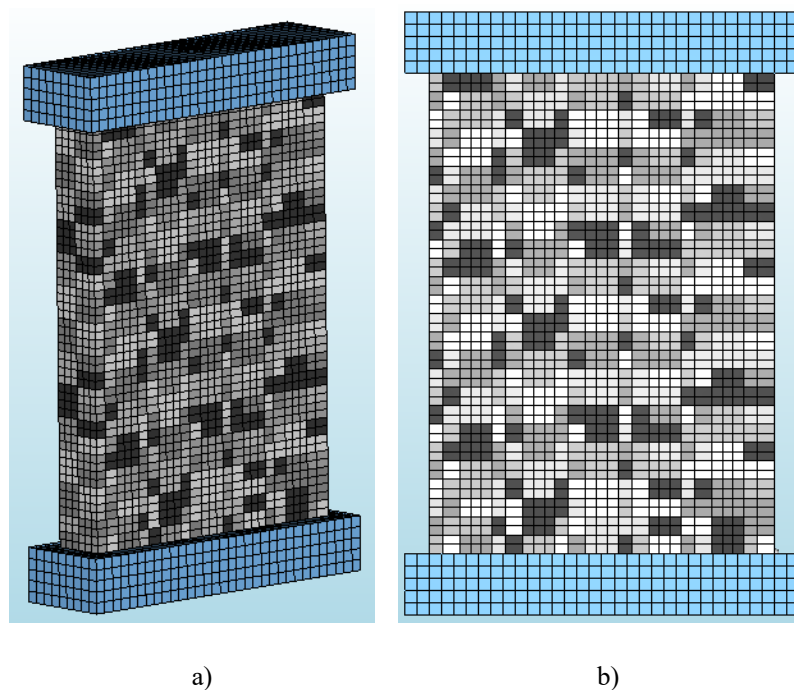


Figure 5.7 Meshing configuration for URM pier: a) isometric view b) front view

After the model was meshed, a nonlinear pushover analysis was defined for each URM pier. The pushover analysis was divided into two phases. In the first phase the vertical loads were defined. First, the weight load was applied in 10 equal steps. As an iteration procedure, the Secant (Quasi-Newton) was chosen. The maximum number of iterations is 100. In each step, convergence norms needed to be satisfied for the model to function. For the weight load, all three convergence norms needed to be satisfied (energy, displacement, and force norm). In the following step, the vertical load of 250 kN is applied in 10 equal steps. The same iteration procedure and maximum number of iterations were chosen. The same convergence norms needed to be satisfied.

In the second phase, the horizontal in-plane displacement and the bending moments were applied. The total displacement of 21,50 mm was divided into 430 steps that were 0,05 mm long each. The bending moments were applied simultaneously through the time dependency defined in the previous section. As an iteration procedure, the Secant (Quasi-Newton) was chosen. The maximum number of iterations was 50 in this case to save computational time. In each step, the same convergence norms needed to be satisfied for the model to function (energy, displacement, and force norms). After the analysis was defined and conducted for each URM pier, a broad spectrum of results was retrieved.

### 5.2.5 Results of the nonlinear pushover analysis

The results of the nonlinear pushover analysis for URM piers were divided into three categories. The categories included element results, nodal results, and cracking patterns.

The first element result that was checked were the total stresses in the URM piers in the vertical direction. The reason for this was to check that no compressive failure of the piers occurred at the end of the first phase where the weight and the vertical compressive force were applied. Additionally, it was important to determine if the vertical load was adequately transferred from the top reinforced concrete beam to the URM piers. The vertical compressive stress was calculated according to equation 3.15 in section 3 as  $\sigma_0 = N/l \cdot t = 250000/1420 \cdot 250 = 0,7 \text{ N/mm}^2$ . In Figure 5.8 the total vertical stresses in the entire URM piers can be seen. Since the same vertical stress was applied in case of all three URM piers, the values seen in Figure 5.8 are correspondent to all three URM piers. The total vertical stresses in the URM pier (cyan colour in Figure 5.8) were similar to the calculated value and considered accurate. It was also observed that no cracks appeared under compression and that the URM piers can be loaded with the horizontal in-plane displacement and the bending moments.

After the transfer of the vertical load was checked, displacements and reaction forces were processed. Of course, the most important displacement and reaction force to extract were the ones in the in-plane direction of the URM piers (global y-axis). The URM piers at the final step (step 430) of the shear load in the nonlinear analysis can be seen in Figure 5.9, Figure 5.10 and Figure 5.11 that are correspondent to the URM 1, URM 2 and URM 3 piers respectively. The most important thing to check were the boundary conditions. In this case, all three URM piers subjected to a vertical compressive force and an in-plane horizontal displacement had no in-plane displacements at the bottom and the assigned displacement of 21,50 mm at the top as it is clear from Figure 5.9, Figure 5.10 and Figure 5.11. Additionally, no overturning or bending appeared. All the mentioned results were satisfactory and correspondent to the experimental

campaign test setup. What can also be observed, is the cracking patterns of the URM piers. A typical diagonal shear failure appeared in all three cases. The diagonal crack extends from the top left corner where the horizontal displacement and the bending moment were applied, all the way to the bottom right corner. The diagonal cracks spread through the vertical and horizontal mortar joints of the piers. The cracking patterns are very similar for all three URM piers.

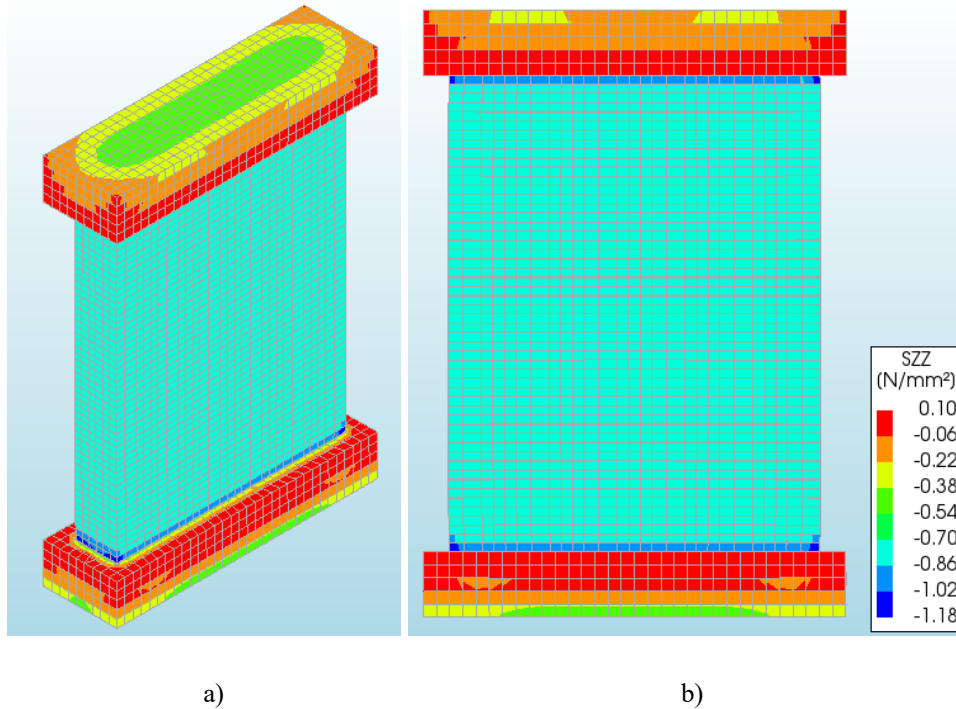


Figure 5.8 Total vertical stresses of the URM piers: a) isometric view b) front view

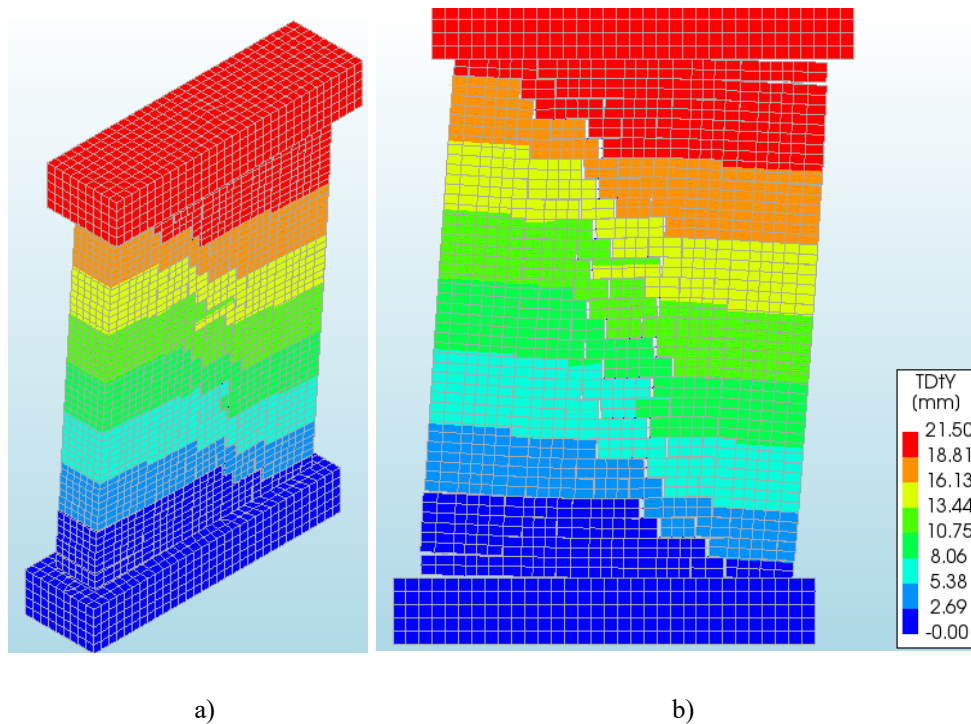


Figure 5.9 Deformed shape of the URM 1 pier at 21,50 mm: a) isometric view b) front view

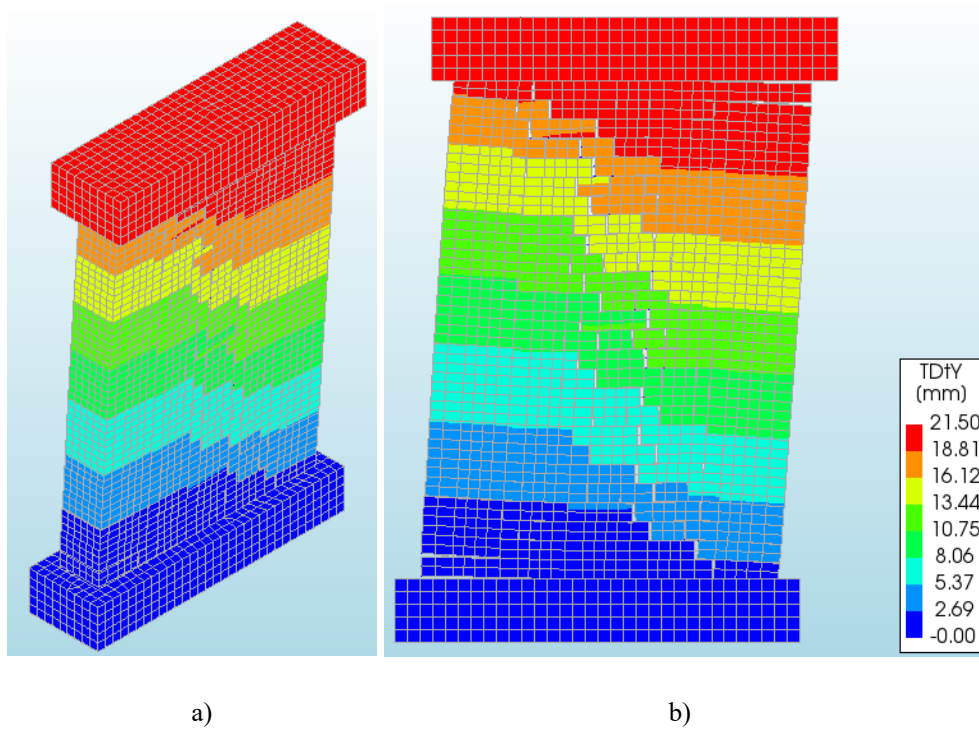


Figure 5.10 Deformed shape of the URM 2 pier at 21,50 mm: a) isometric view b) front view

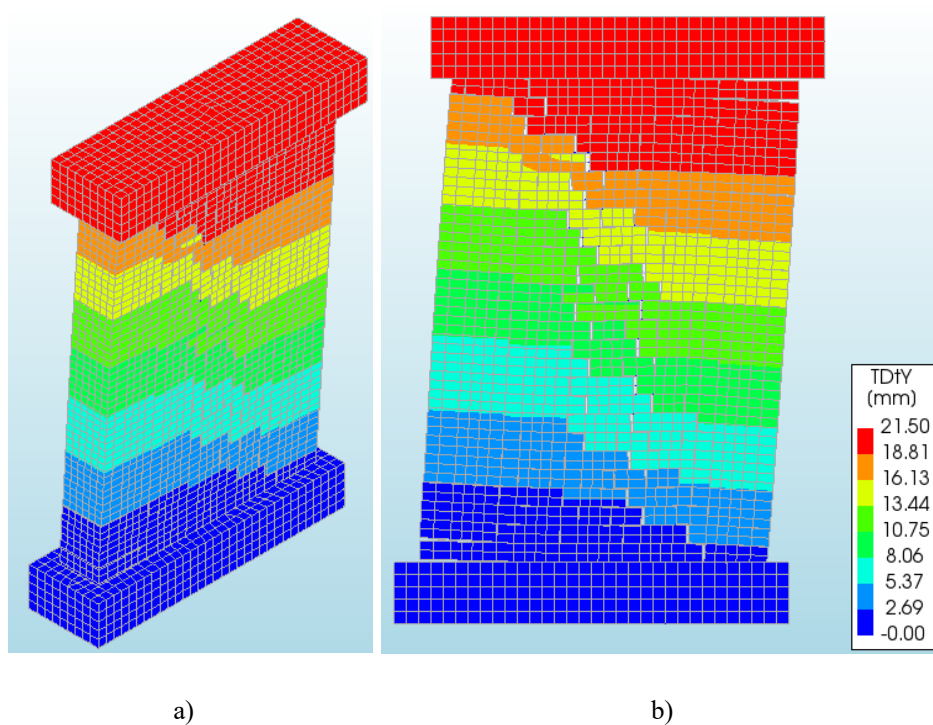


Figure 5.11 Deformed shape of the URM 3 pier at 21,50 mm: a) isometric view b) front view

After the displacements were analysed, the reaction forces in the in-plane direction were observed for each URM pier. As it was already explained, all nodes at the bottom of the foundation beam were connected by a tying option. Therefore, the fixed supports were located at only one corner of the bottom face of the foundation beam. Consequently, the values of the reaction forces were observed at the same corner of each pier as a vector value. Additionally,

as a result a pushover curve in the positive direction was obtained at the final step of the shear load in the nonlinear analysis for each pier. The pushover curve in the negative direction is the mirrored version of the pushover curve in the positive direction using negative values for displacement and force. With this simplification an envelope curve is achieved for each URM pier. The pushover curves for all three URM piers in both directions can be seen in Figure 5.12. The most important values that were gathered from the pushover curves are displayed in Table 5.3. Since the curves in the positive and negative direction are the same, in Table 5.3 only the values gathered in the positive direction are displayed. In case of the curves gathered from the numerical modelling campaign for URM piers, there was no need for the trilinearization of the curves. The point in which the yielding appeared is obvious as it is clear from Figure 5.12 for all three URM piers. Therefore, the ductility was calculated by dividing the maximum displacement and the displacement at the yielding point given in Table 5.3 for each URM pier.

The resulting pushover curves were very flexible with a brittle failure at the end. The nonlinear pushover analysis was continued till the assigned horizontal displacement of 21,50 mm was reached in all three cases, but the value of the horizontal in-plane force did not change after the brittle failure. Consequently, the cracking patterns seen in Figure 5.9, Figure 5.10 and Figure 5.11 did not change after the failure till the assigned displacement of 21,50 mm.

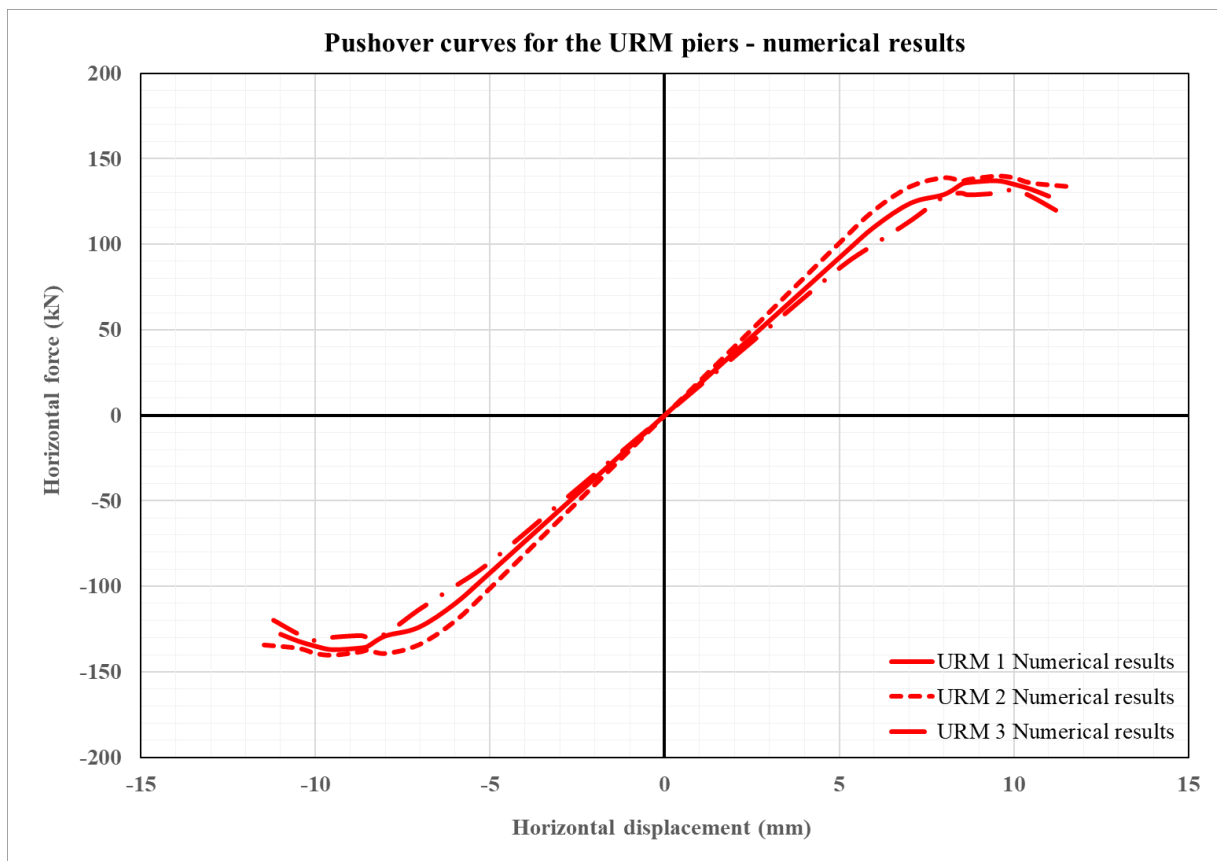


Figure 5.12 Pushover curves for the URM piers from the numerical modelling

Table 5.3 Results of the numerical modelling for URM piers

| Value                               | URM 1  | URM 2  | URM 3  | mean   |
|-------------------------------------|--------|--------|--------|--------|
| Maximum horizontal force [kN]       | 137,00 | 140,00 | 130,00 | 135,67 |
| Maximum displacement [mm]           | 11,00  | 11,50  | 11,20  | 11,23  |
| Displacement at yielding point [mm] | 8,00   | 7,85   | 8,05   | 7,97   |
| Ductility                           | 1,38   | 1,47   | 1,39   | 1,41   |

Finally, to confirm that the cracking appeared in the mortar joints, the interface relative displacements were checked in the in-plane direction for each URM pier. All displacements in the mortar joint interfaces are shown in Figure 5.13. It is concluded that the maximum crack width was equal to 3,11 mm in the URM 1 pier, 2,85 mm in the URM 2 pier and 2,89 mm in the URM 3 pier. The maximum crack widths for all three URM piers were practically the same. This relative displacement appeared mostly in the horizontal mortar joints which seem more affected than the vertical mortar joints.

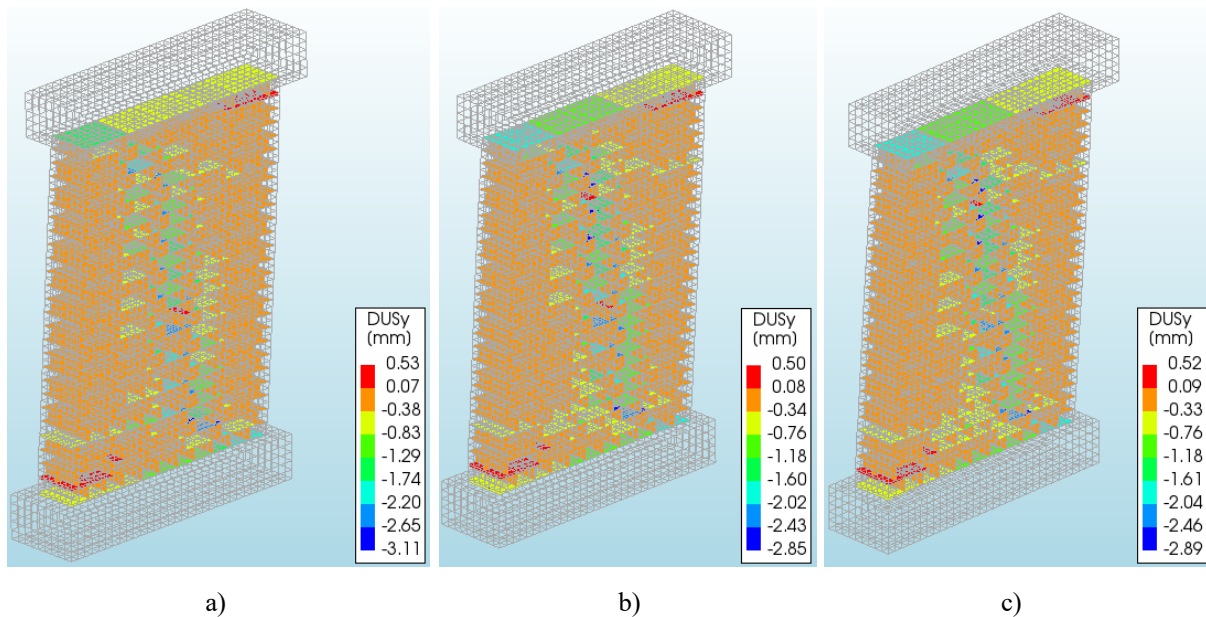


Figure 5.13 Interface relative displacements of mortar joints: a) URM 1 pier b) URM 2 pier c) URM 3 pier

## 5.3 Numerical modelling of Series 2 – FRCM piers

### 5.3.1 Geometry

After the modelling of the URM piers, the FRCM strengthening was modelled. The FRCM strengthening consisted of two types of elements. First, the matrix (mortar) of the FRCM system is modelled. In case of Series 2, FRCM piers, the matrix was added via 442 2D shapes that were assigned on one side of the masonry piers. These 2D shapes were modelled as regular

curved shells with a thickness of 15 mm. The pattern of the matrix elements corresponded to the pattern in which the 3D solid shapes of the URM piers were modelled. The FRCM strengthened pier and the matrix elements pattern can be seen in Figure 5.14. The most important part of the modelling procedure was the proper definition of the interface elements. In this case, two connections were defined. Firstly, the brick-to-matrix interfaces were defined as 3D surface elements with perfect bond. These 3D surface elements were modelled as structural plane interfaces. The reason for the assumed perfect bond is the lack of literature on failure modes/models where the problem stemmed from the connection between the mortar matrix and the bricks. Additionally, since mechanical connectors were used, a perfect bond must be considered. Therefore, the system usually fails at the matrix-to-fibres interface. After that, another interface was defined. The matrix-to-matrix interfaces, which connect the smaller parts of the matrix elements, were defined as 3D line elements. These line elements were modelled as structural shell interfaces with a thickness of 15 mm. The idea was to create a possibility of cracking in the matrix. Of course, for the interfaces that connect two parts of the matrix in the vertical direction and for the interfaces that connect two parts of the matrix in the horizontal direction, different local axes were assigned.

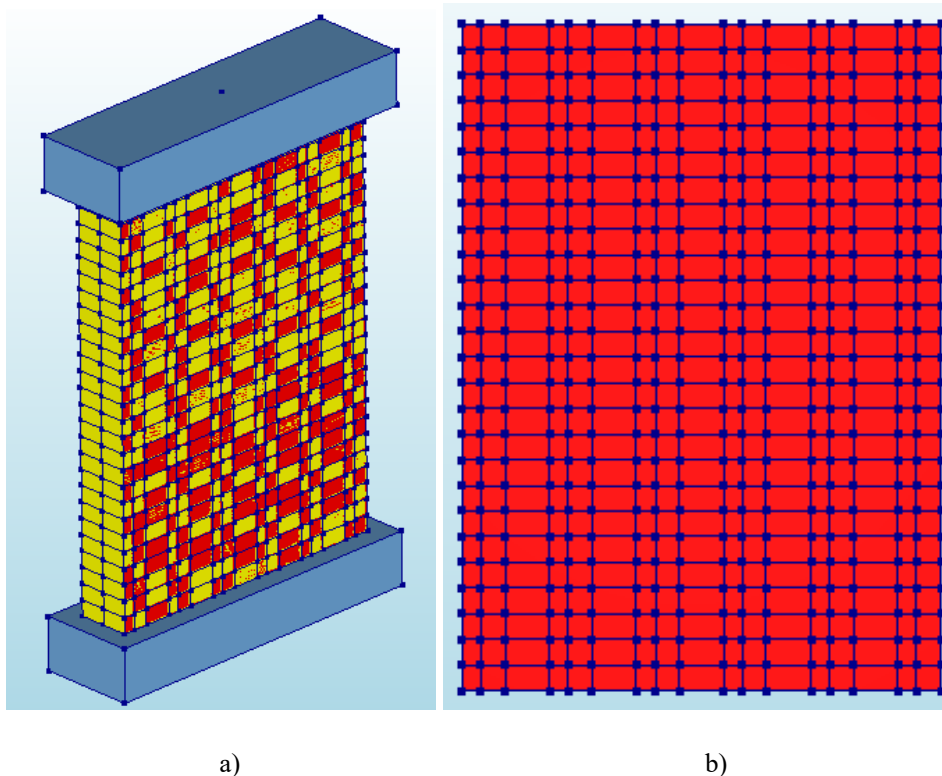


Figure 5.14 FRCM pier (Series 2) in DIANA FEA 10.4 software a) Isometric view b) Front view of the FRCM matrix pattern

In the following steps, the glass fibres of the FRCM system were defined and modelled. The mesh size of the fibres equalled 12 mm in both directions. This mesh was composed from fibres defined in the horizontal and vertical direction. The fibres were modelled as 1D reinforcement elements. These 1D reinforcement elements were modelled as embedded bars with a cross section of  $0,47 \text{ mm}^2$ . The composition of the fibres and the zoomed in detail of the composition for the FRCM piers (Series 2) can be seen in Figure 5.15. The fibres in the vertical and the horizontal direction were defined separately. The reason for this is that different element geometries need to be introduced since the fibres were applied in two perpendicular directions.

After the definition of the fibres, they were then connected to the mortar matrix 2D elements using line-shell interface elements where the bond-slip law was introduced. The main reason behind the use of 1D elements for the definition of the fibre grid was the introduction of the bond-slip law. The bond-slip model adopted, within the software DIANA FEA, sets a non-linear relation between the shear stress and the shear slip. In contrast, the relation between normal traction and normal relative displacement was maintained linear. Since the bond-slip failure is a common type of failure in FRCM systems, it needed to be adequately considered.

In the following section, the mechanical properties of materials used in the modelling of the FRCM piers will be defined and explained.

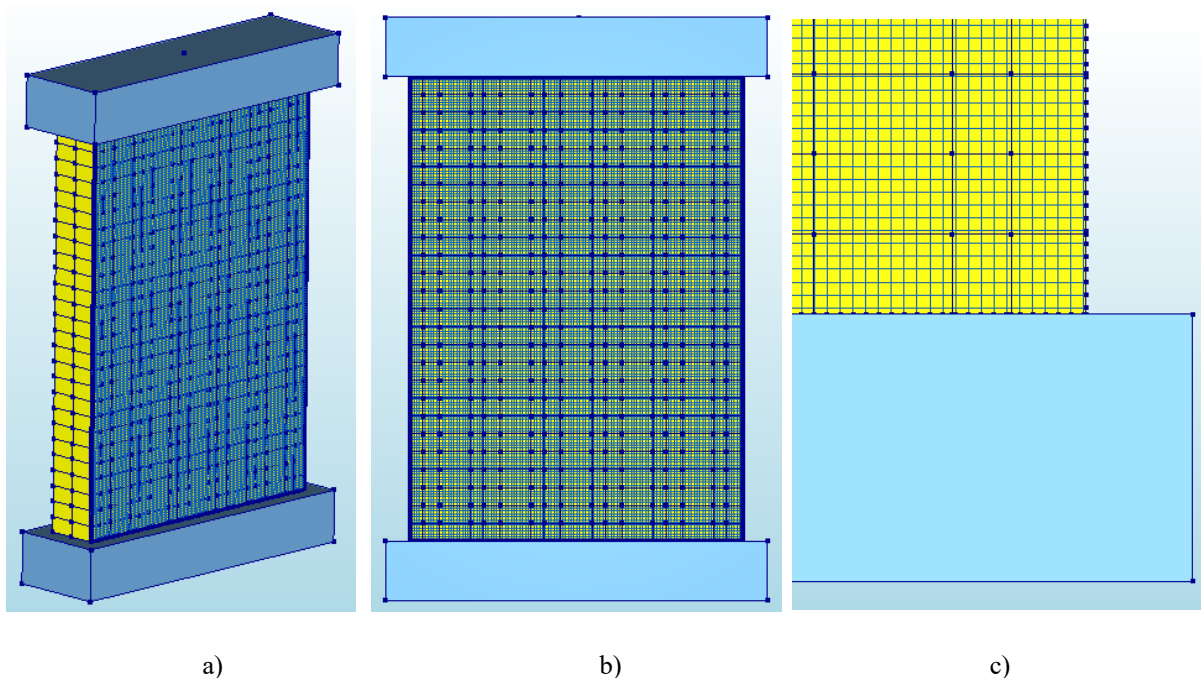


Figure 5.15 Composition of fibres for FRCM piers (Series 2) in DIANA FEA 10.4 software a) Isometric view 7 b) Front view c) Detail of the fibre composition at the bottom right corner (front view)



### 5.3.2 Mechanical properties of materials

As it was explained in subsection 5.2.2., the URM piers were defined by using three different materials. The mechanical properties of these materials are summarized in Table 5.1 and Table 5.2. The same values were used for the definition of the FRCM piers. Masonry and the concrete were defined with linear material properties. The same approach was used for the definition of the material properties of the glass fibres and the mortar matrix in the FRCM system. The corresponding values are given in Table 5.4 and were defined by the manufacturer as it was explained in subsection 3.2.5.

Table 5.4 Linear elastic properties of glass fibres and mortar matrix (FRCM system)

| Element       | $E$ (N/mm <sup>2</sup> ) | $\nu$ | Mass density (kg/m <sup>3</sup> ) |
|---------------|--------------------------|-------|-----------------------------------|
| Glass fibres  | 74000                    | 0,20  | 2650                              |
| Mortar matrix | 6000                     | 0,20  | 1500                              |

After that, material properties were assigned to different types of interfaces. First, the brick-to-matrix interface was defined as a 3D surface interface with linear material properties. Since a perfect bond was expected, the combined cracking-shearing-crushing model was not used for this interface. As was the case with the vertical and horizontal mortar joints, the linear material properties were defined with the normal stiffness  $k_n$  and shear stiffness  $k_s$  that were calculated according to equations 5.1 and 5.2. The values for bricks stayed the same and the values for the mortar used in joints were replaced by values given in Table 5.4 for the mortar matrix. The thickness of the mortar matrix  $h_m = 15$  mm. The values for the normal stiffness  $k_n$  and shear stiffness  $k_s$  are given in Table 5.5. The second interface that was considered are the matrix-to-matrix interfaces. In this case, 3D line interfaces between shells were used to define these interfaces. These interfaces were defined by linear material properties (normal and shear stiffness moduli) and a nonlinear combined cracking-shearing-crushing material model explained in 5.2.2. All mechanical properties for the matrix-to-matrix interface are given in Table 5.6. According to the manufacturer the expected value of the tensile strength was  $f_t = 0,6$  N/mm<sup>2</sup>. The compressive strength was also given by the manufacturer with the value of 15 N/mm<sup>2</sup> as it was stated in subsection 3.2.5. For the calculation of all the other parameters, the same equations were used as in 5.2.2. with the values taken from Table 5.2 and Table 5.6.

Table 5.5 Mechanical properties of the brick-to-matrix interface

| Interface       | Normal stiffness (N/mm <sup>3</sup> ) | Shear stiffness (N/mm <sup>3</sup> ) |
|-----------------|---------------------------------------|--------------------------------------|
| Brick-to-matrix | 745                                   | 298                                  |

Table 5.6 Mechanical properties of the matrix-to-matrix interface

|   |  |   |
|---|--|---|
| <b>Normal stiffness <math>k_n</math> (N/mm<sup>3</sup>)</b> | <b>Shear stiffness <math>k_s</math> (N/mm<sup>3</sup>)</b> | <b>Tensile strength <math>f_t</math> (N/mm<sup>2</sup>)</b>     |
| 400   | 160  | 0,6   |
| <b>Fracture energy <math>G_r^I</math> (N/mm)</b>            | <b>Cohesion <math>c</math> (N/mm<sup>2</sup>)</b>          | <b>Friction angle (rad)</b>                                     |
| 0,01  | 0,9  | 0,75  |
| <b>Dilatancy angle (rad)</b>                                | <b>Residual friction angle (rad)</b>                       | <b>Confining normal stress (N/mm<sup>2</sup>)</b>               |
| 0   | 0,75   | -0,7  |
| <b>Exponential degradation coefficient (mm)</b>             | <b>Fracture energy <math>G_r^{II}</math> (N/mm)</b>        | <b>Compressive strength <math>f_k</math> (N/mm<sup>2</sup>)</b> |
| 5   | 0,09   | 15  |
| <b>Factor <math>C_s</math></b>                              | <b>Compressive fracture energy (N/mm<sup>2</sup>)</b>      | <b>Equivalent plastic relative displacement (mm)</b>            |
| 9   | 26   | 50  |

Finally, the connection of the glass fibres to the mortar matrix was assigned via the bond-slip law. For the bond-slip law two values were defined first. The normal stiffness modulus of 0,01 N/mm<sup>2</sup> and shear stiffness modulus of 53 N/mm<sup>2</sup> were defined according to Murgo et al. [104]. Consequently, the bond-slip law and the values attached to it were also taken according to [104] since no additional bond-slip tests were conducted in the experimental campaign.

### 5.3.3 Boundary conditions and applied loads

After the geometry of the pier was defined and the mechanical properties were set for elements used in the model, the boundary conditions (supports) and applied loads were defined. Since the boundary conditions simulate the experimental campaign setup, they remained the same as they were for the URM piers. A thorough explanation is given in subsection 5.2.3.

Till this point, the numerical model for all three FRCM piers was the same as was the case with URM piers. In the vertical direction, the vertical compressive force stayed the same for all three FRCM piers with the value of 250 kN. In the horizontal y-direction, the displacement was applied with the total value of 23 mm for all three FRCM piers. This value was chosen according to Table 4.10 where the maximum displacement of all FRCM piers was 21,60 mm for FRCM 2 pier in the positive direction. The final load that was applied for each FRCM pier was the bending moment around the x-axis. As it is clear from Figure 4.70, Figure 4.71 and Figure 4.72 that are correspondent to FRCM 1, FRCM 2 and FRCM 3 piers, the values of these bending moments are different for each pier. Therefore, three separate numerical models were needed to display the proper behaviour of each pier. The same methodology was used as it was explained in subsection 5.2.3. for URM piers. From Figure 4.70, Figure 4.71 and

Figure 4.72 the pushover curve with the highest absolute value of the bending moment was chosen for each FRCM pier. In all three cases the pushover curve in the negative direction was chosen as the representative curve. The maximum values of the bending moments for the FRCM 1, FRCM 2 and FRCM 3 pier were equal to 92,20 kNm, 100,00 and 109,60 kNm respectively. All pushover curves of the bending moments were added to their correspondent numerical models as positive values in the same manner as it was explained in subsection 5.2.3. for URM piers.

### 5.3.4 Mesh settings and the nonlinear analysis

The next step was to define a proper mesh for the nonlinear analysis. Since the matrix elements added were the same size as the bricks, the mesh size was again chosen according to the smallest elements in the model. Since the smallest element used in the model was a half brick element with dimensions  $b/h/l = 6/6,5/12$  cm, a mesh size of 50 mm or 5 cm was chosen. Again, the hexa/quad meshing type was defined. The mesh configuration for the FRCM piers can be seen in Figure 5.16.

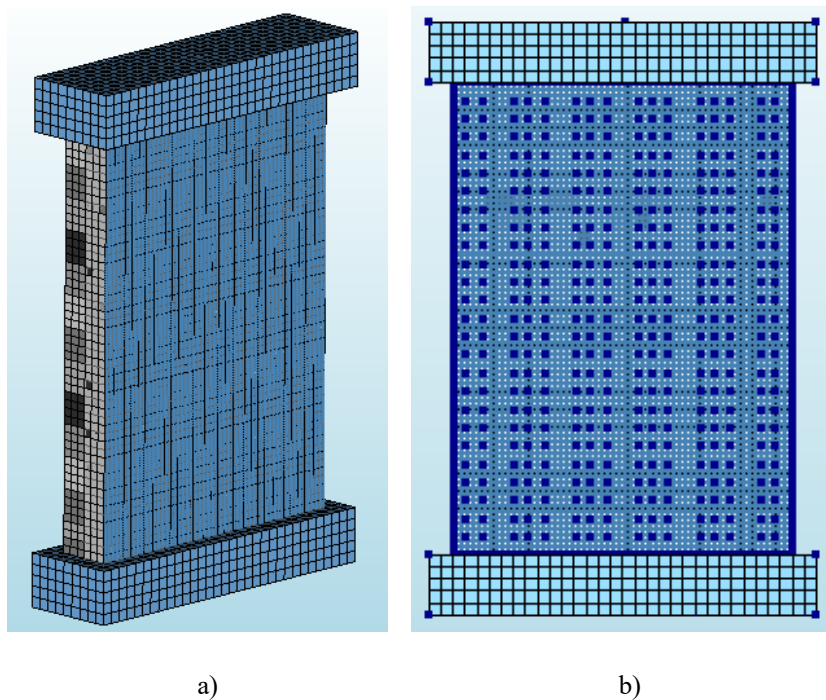


Figure 5.16 Meshing configuration for FRCM pier: a) isometric view b) front view

After the model was meshed, a nonlinear pushover analysis was defined for each FRCM pier. Everything was defined in the same manner as for the URM piers besides the horizontal in-plane displacement of 23 mm which was applied in 460 steps (0,05 mm per step). The bending moments were applied simultaneously through the time dependency. After the analysis, the same results were gathered as in subsection 5.2.5.

### 5.3.5 Results of the nonlinear pushover analysis

In this subsection, the results of the nonlinear pushover analysis for FRCM piers are obtained. In the results for the URM piers, three categories were observed. These categories included element results, nodal results, and cracking patterns. In the case of FRCM piers, an additional category was taken into consideration. Since the glass fibre reinforcement in the vertical and horizontal direction were assigned as separate elements, the reinforcement results were also obtained. Thus, different output data for the reinforcement as a separate element were gathered.

The first element result that was checked were the total stresses in the FRCM pier in the vertical direction. The vertical compressive stress was calculated according to equation 3.15 in section 3 as  $\sigma_0 = 0,7 \text{ N/mm}^2$ . In Figure 5.17 the total vertical stresses in the entire FRCM pier can be seen. Since the same vertical stress was applied in case of all piers, these values were the same for all three FRCM piers. In the isometric view the total vertical stresses in the masonry part of the FRCM pier (green colour in Figure 5.17) can be observed. It is self-evident that the results were correspondent to the calculated value. In the front view of Figure 5.17 the total vertical stresses in the mortar matrix of the FRCM pier (yellow colour in Figure 5.17) can be observed. A similar value of the vertical stress can be seen in the mortar matrix even though it was placed at the very end of the pier section. Finally, it is apparent that no visible cracks appeared under compression and that the FRCM pier can be loaded with the horizontal in-plane displacement.

As it was the case with URM piers, after the transfer of the vertical load, the displacements and reaction forces were examined. The most important displacement and reaction force extracted were the ones in the in-plane direction of the FRCM piers. The FRCM piers at the final step (step 460) of the shear load in the nonlinear analysis can be seen in Figure 5.18, Figure 5.19 and Figure 5.20 that are correspondent to the FRCM 1, FRCM 2 and FRCM 3 piers respectively. In these figures the deformed shape of the FRCM piers is shown. It was concluded that no rupture of glass fibres appeared in all three FRCM models due to the high modulus of elasticity. In Figure 5.18 b), Figure 5.19 b) and Figure 5.20 b) the deformed shapes of the FRCM piers are shown as well, but without the glass fibres in the image. It can be observed that the cracking pattern corresponded to the diagonal shear failure of the FRCM system in all three cases. The failure appeared in the mortar matrix. Practically the same cracking patterns were observed in URM piers. The diagonal cracks spread through the vertical and horizontal mortar joints of the pier and through the mortar matrix as it was expected.

Additionally, it was important to check the boundary conditions. In this case, the FRCM piers had no in-plane displacements at the bottom and the assigned displacement of 23 mm at the top in all three cases. No overturning or bending appeared in the FRCM piers. All the mentioned results were satisfactory and correspondent to the experimental campaign test setup.

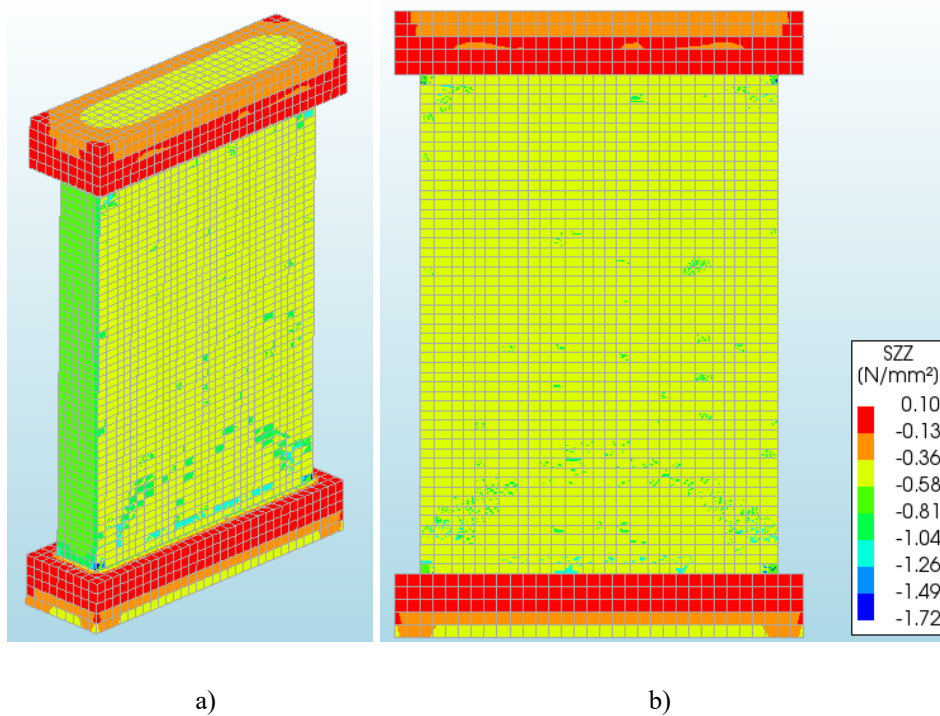


Figure 5.17 Total vertical stresses of the FRCM piers: a) isometric view b) front view

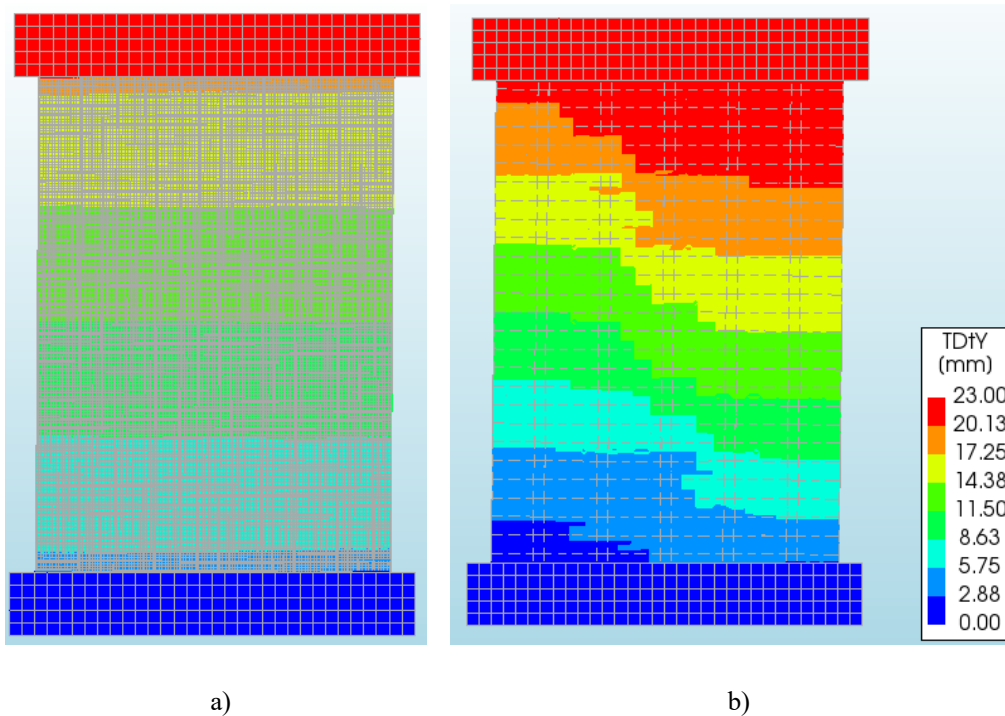
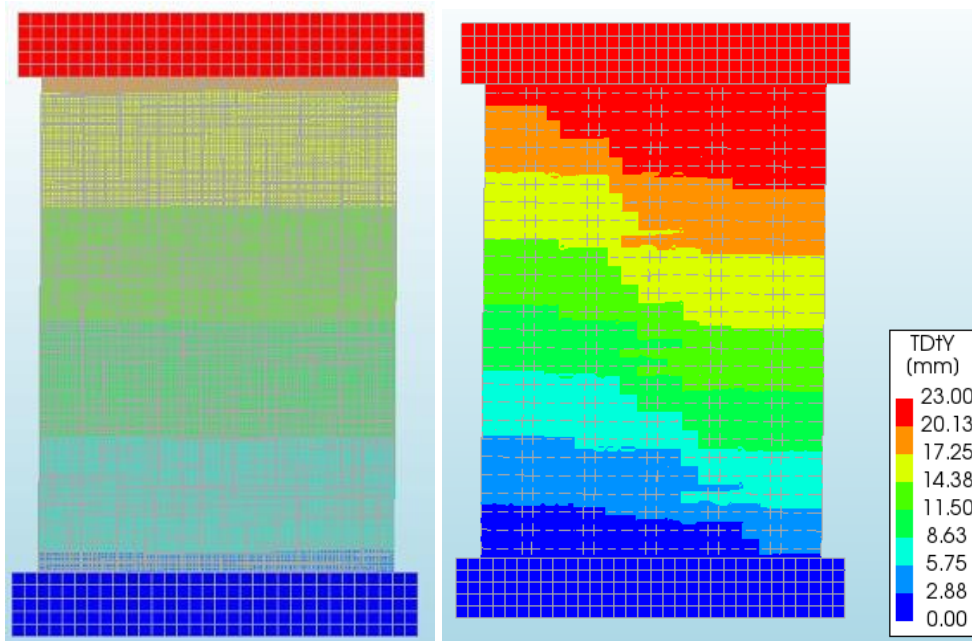


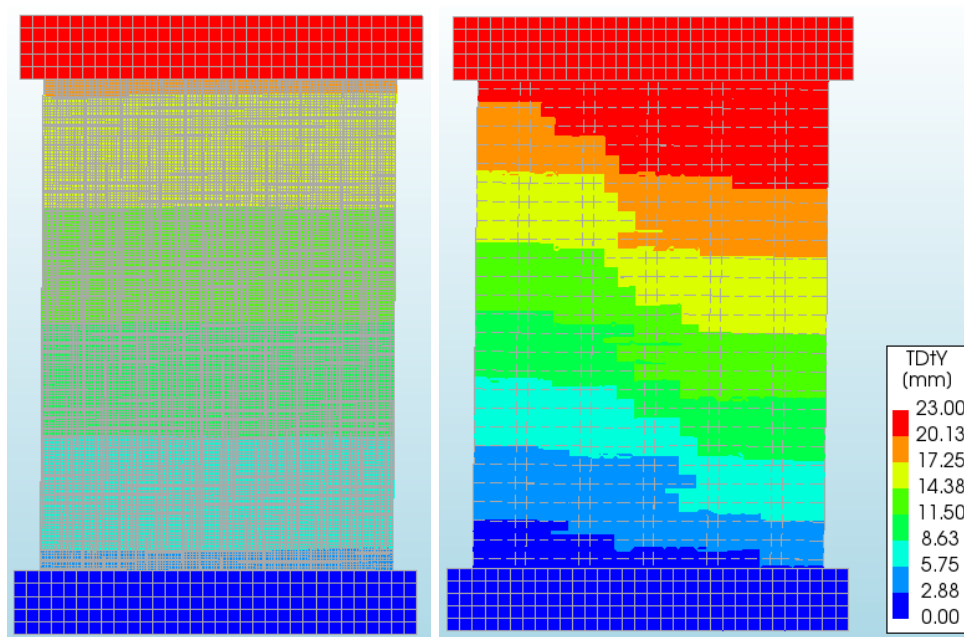
Figure 5.18 Deformed shape of the FRCM 1 pier at 23 mm: a) front view of the FRCM pier - glass fibres b) front view of the FRCM pier - mortar matrix failure



a)

b)

Figure 5.19 Deformed shape of the FRCM 2 pier at 23 mm: a) front view of the FRCM pier - glass fibres b) front view of the FRCM pier - mortar matrix failure



a)

b)

Figure 5.20 Deformed shape of the FRCM 3 pier at 23 mm: a) front view of the FRCM pier - glass fibres b) front view of the FRCM pier - mortar matrix failure

Following the analysis of displacements, the reaction forces were observed in the in-plane direction for each FRCM pier. As a result of the analysis a pushover curve in the positive direction was obtained at the final step of the shear load in the nonlinear analysis. The pushover curve in the negative direction is the mirrored version of the pushover curve in the positive

direction using negative values for displacement and force. The pushover curves for each FRCM pier in both directions can be seen in Figure 5.21. The most important values that were gathered from the pushover curves are displayed in Table 5.7. Since the curves in the positive and negative direction are the same, in Table 5.7 only the values gathered in the positive direction are displayed. In case of the curves gathered from the numerical modelling campaign for FRCM piers, there was no need for the trilinearization of the curves since the yielding point is obvious as it is clear from Figure 5.21 for all three FRCM piers. Again, the ductility was calculated by dividing the maximum displacement and the displacement at the yielding point given in Table 5.7 for each pier.

The nonlinear pushover analysis was continued till the assigned horizontal displacement of 23 mm was reached in all three cases, but the value of the horizontal in-plane force did not change after the brittle failure. Consequently, the cracking patterns seen in Figure 5.18 b), Figure 5.19 b) and Figure 5.20 b) did not change after the failure till the assigned displacement of 23 mm.

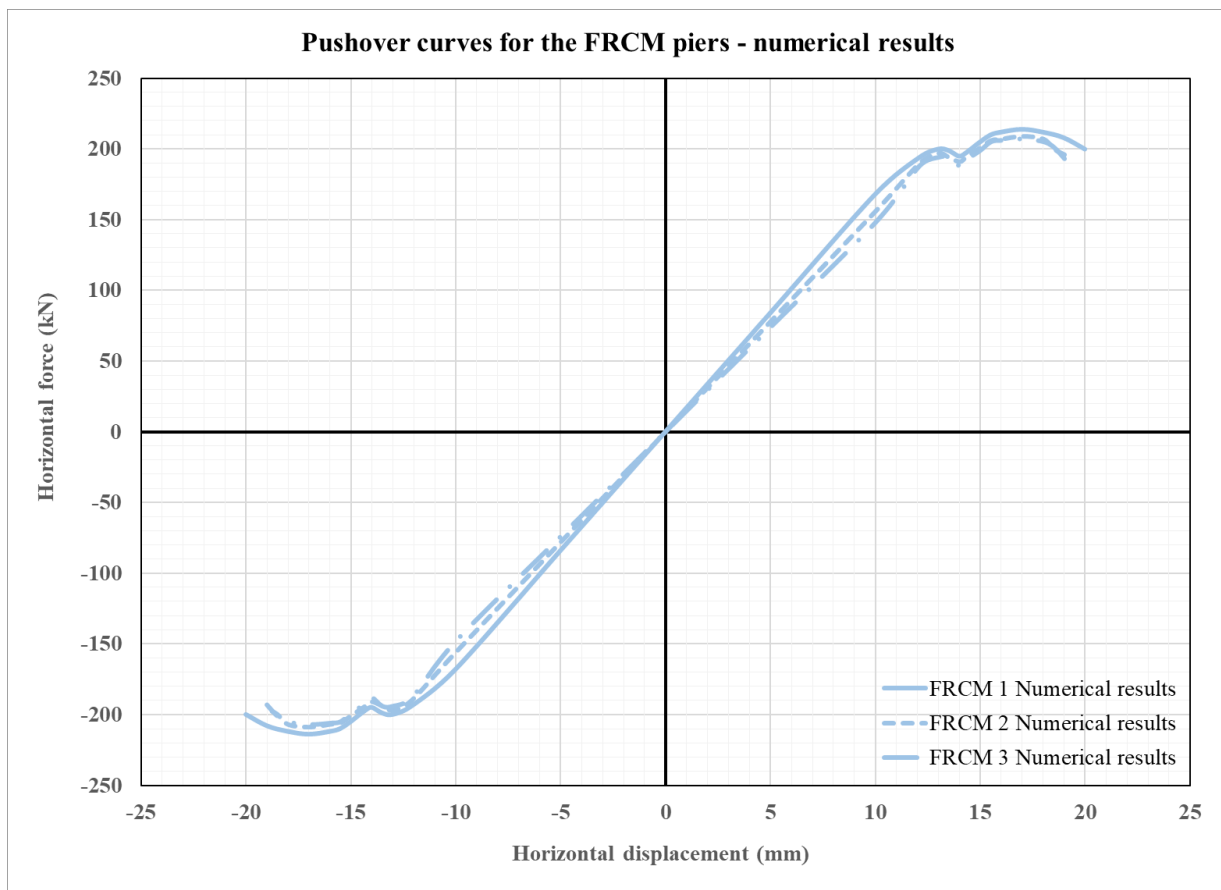


Figure 5.21 Pushover curves for the FRCM piers from the numerical modelling

Table 5.7 Results of the numerical modelling for FRCM piers

| Value                               | FRCM 1 | FRCM 2 | FRCM 3 | mean   |
|-------------------------------------|--------|--------|--------|--------|
| Maximum horizontal force [kN]       | 214,00 | 209,00 | 207,00 | 210,00 |
| Maximum displacement [mm]           | 20,10  | 19,20  | 19,10  | 19,47  |
| Displacement at yielding point [mm] | 13,80  | 13,50  | 13,40  | 13,57  |
| Ductility                           | 1,46   | 1,42   | 1,43   | 1,44   |

Two categories of cracks were checked next. For the masonry pier, to confirm that the cracking appeared in the mortar joints, the interface relative displacements were checked in the in-plane direction. All displacements in the mortar joint interfaces are shown in Figure 5.22 a), Figure 5.23 a) and Figure 5.24 a) for FRCM 1, FRCM 2 and FRCM 3 pier respectively. The maximum crack width was equal to 3,01 mm in the FRCM 1 pier and 2,98 mm for both FRCM 2 and FRCM 3 piers. For the mortar matrix, to confirm that the cracking appeared in the matrix-to-matrix interfaces, the interface relative displacements of the mortar matrix were checked in the in-plane direction. All displacements in the matrix-to-matrix interfaces are shown in Figure 5.22 b), Figure 5.23 b) and Figure 5.24 b) for FRCM 1, FRCM 2 and FRCM 3 pier respectively. The maximum crack width was equal to 3,01 mm in the FRCM 1 pier and 2,98 mm for both FRCM 2 and FRCM 3 piers. Therefore, it is concluded that the masonry pier and the mortar matrix had a corresponding diagonal shear failure and accompanying crack widths.

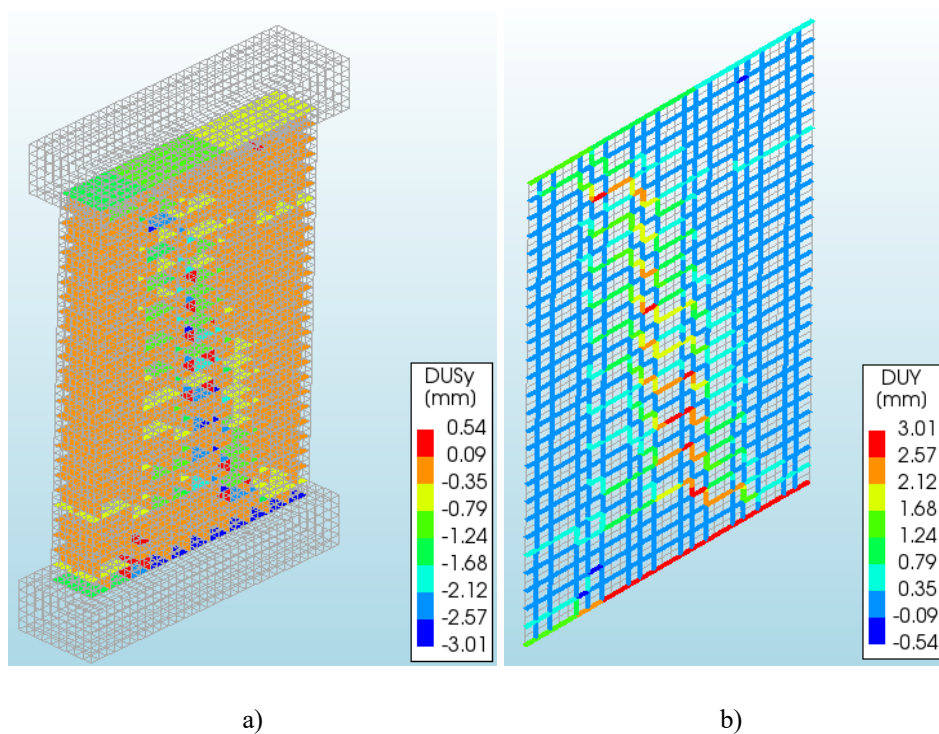


Figure 5.22 Interface relative displacements of the FRCM 1 pier a) in the mortar joints of the masonry pier b) in the mortar matrix interfaces



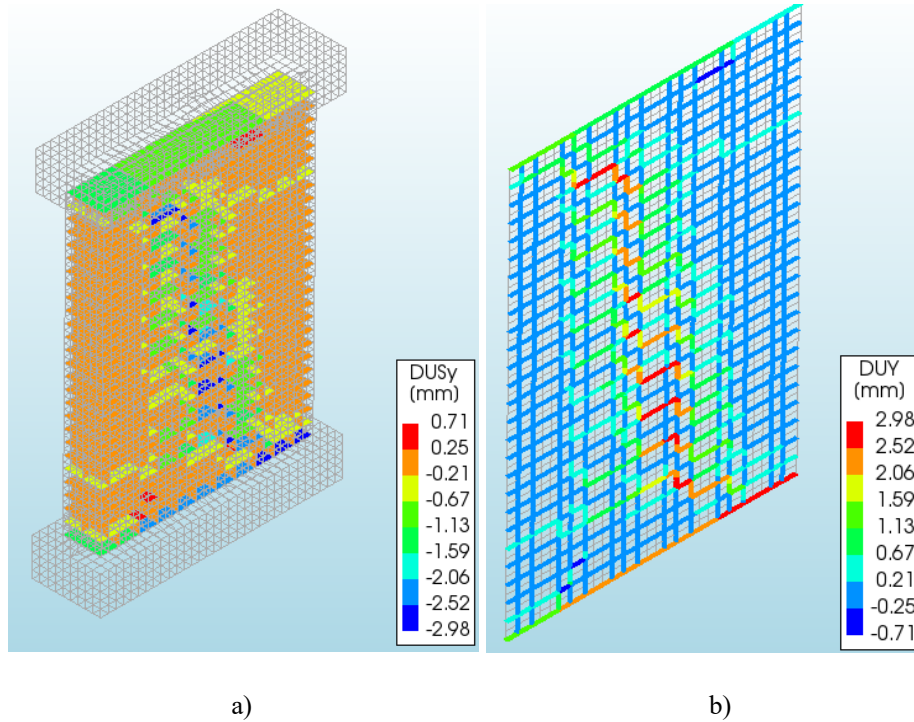


Figure 5.23 Interface relative displacements of the FRCM 2 pier a) in the mortar joints of the masonry pier b) in the mortar matrix interfaces

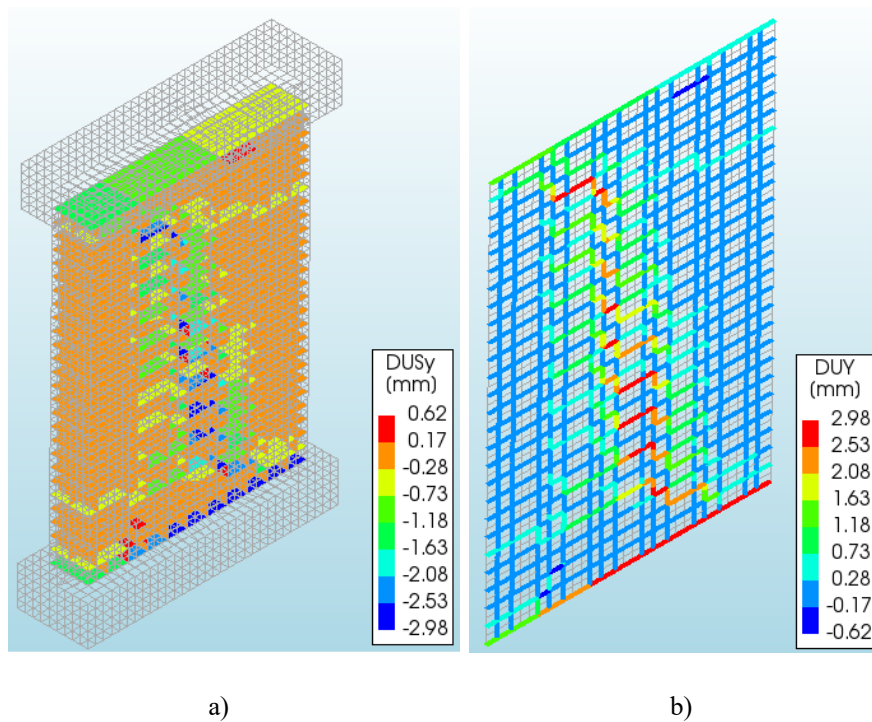


Figure 5.24 Interface relative displacements of the FRCM 3 pier a) in the mortar joints of the masonry pier b) in the mortar matrix interfaces

Finally, the reinforcement results were observed. As it can be seen in Figure 5.18 a) Figure 5.19 a) and Figure 5.20 a) no slippage, debonding or rupture of glass fibres appeared in any of the FRCM piers. To be sure that no failure of fibres appeared, the total stresses in the in-plane direction (global y-direction) were checked for each pier. From Figure 5.25 a) it was

deduced that the maximum stress of  $\sigma_f = 48,07 \text{ N/mm}^2$  in the glass fibres appeared at the corners of the FRCM 1 pier. From Figure 5.25 b) it was deduced that the maximum stress of  $\sigma_f = 45,22 \text{ N/mm}^2$  in the glass fibres appeared at the corners of the FRCM 2 pier. Finally, from Figure 5.25 c) it was deduced that the maximum stress of  $\sigma_f = 46,77 \text{ N/mm}^2$  in the glass fibres appeared at the corners of the FRCM 3 pier. The maximum value of the in-plane stress for FRCM fibres was calculated as  $\sigma_f = \varepsilon_{fd} \cdot E_f = 0,018 \cdot 74000 = 1332 \text{ N/mm}^2$ . It can be concluded that no failure of glass fibres appeared in the FRCM system.

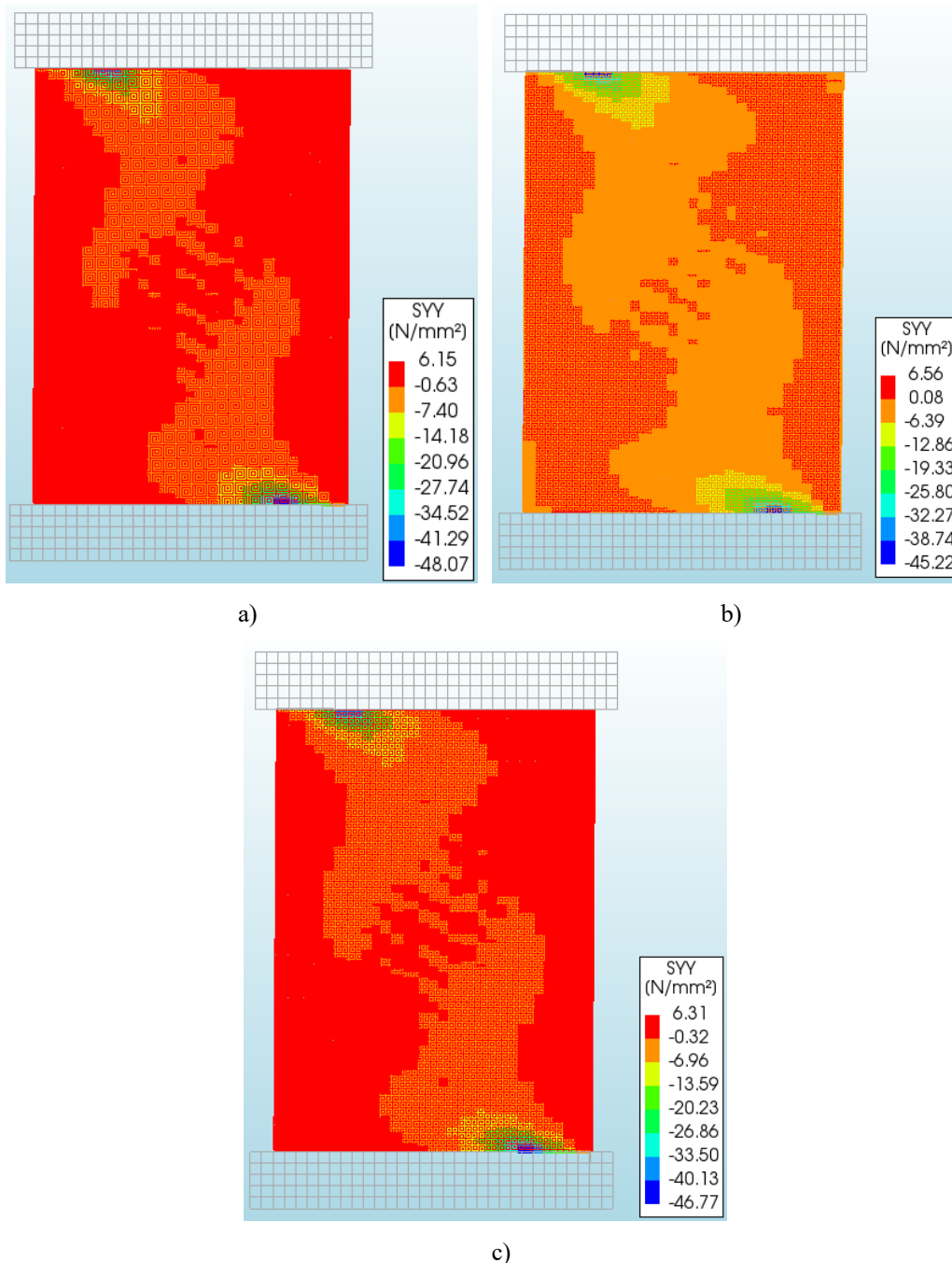


Figure 5.25 Total stresses in the glass reinforcement in the in-plane direction for a) FRCM 1 pier b) FRCM 2 pier c) FRCM 3 pier

## 5.4 Numerical modelling of Series 3 – CFRCM piers

### 5.4.1 Geometry

After the modelling of the URM the FRCM piers, the CFRCM piers were modelled. The FRCM strengthening consisted of two types of elements. First, the matrix (mortar) of the FRCM system was modelled. In case of Series 3, CFRCM piers, the matrix was defined by 2D shapes that were assigned on one front side of the piers and 2D shapes assigned on both sides of the piers. On the front side, 442 2D shapes were added as was the case with FRCM piers. After that, additional 52 2D shapes were added on the sides of the piers. All 2D shapes were modelled as regular curved shells with a thickness of 15 mm. Once again, the pattern of the matrix elements corresponded to the pattern in which the 3D solid shapes of the URM piers were modelled. The CFRCM pier and the matrix elements pattern can be seen in Figure 5.26. The matrix on the sides (green in Figure 5.26) was applied on both sides of the pier through the entire height of the pier. After that, the interface elements were modelled. The brick-to-matrix interface and the matrix-to-matrix interface were defined in the same way as for the FRCM piers. These elements were defined and explained in subsection 5.3.1.

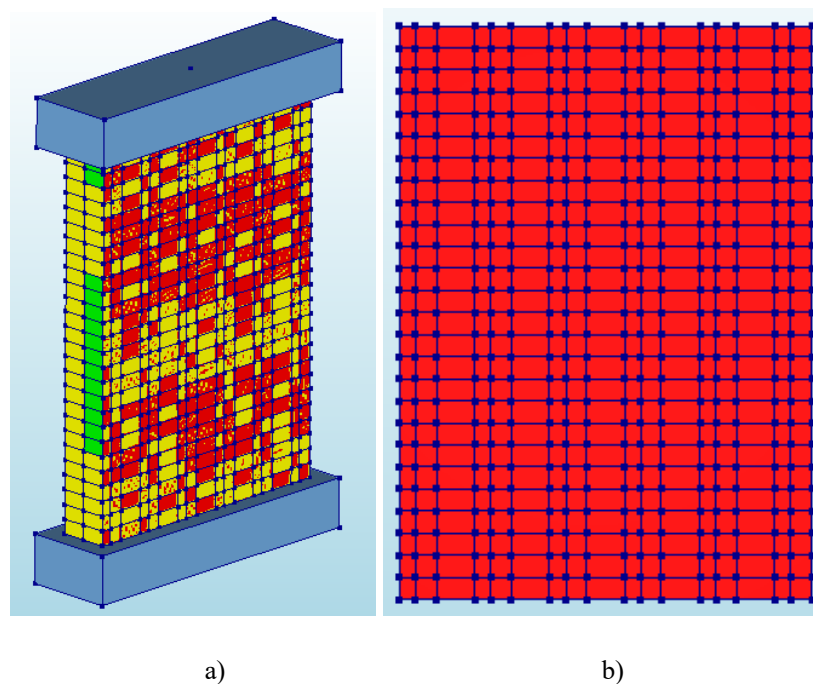


Figure 5.26 CFRCM pier (Series 3) in DIANA FEA 10.4 software a) Isometric view (front matrix in red and side matrix in green) b) Front view of the FRCM matrix pattern in CFRCM piers

In the following steps, the glass fibres of the FRCM system were defined and modelled. Again, the fibres were modelled as 1D reinforcement elements which were defined as embedded bars with a cross section of  $0,47 \text{ mm}^2$ . The composition of the fibres and the zoomed

in detail of the composition for the CFRCM piers (Series 3) can be seen in Figure 5.27. In the model, four different 1D fibre elements were defined: horizontal front fibres, vertical front fibres, horizontal fibres on the sides and vertical fibres on the sides.

After the definition of the fibres, they were then connected to the mortar matrix 2D elements in the same way as for the FRCM piers, by using line-shell interface elements where the bond-slip law was introduced.

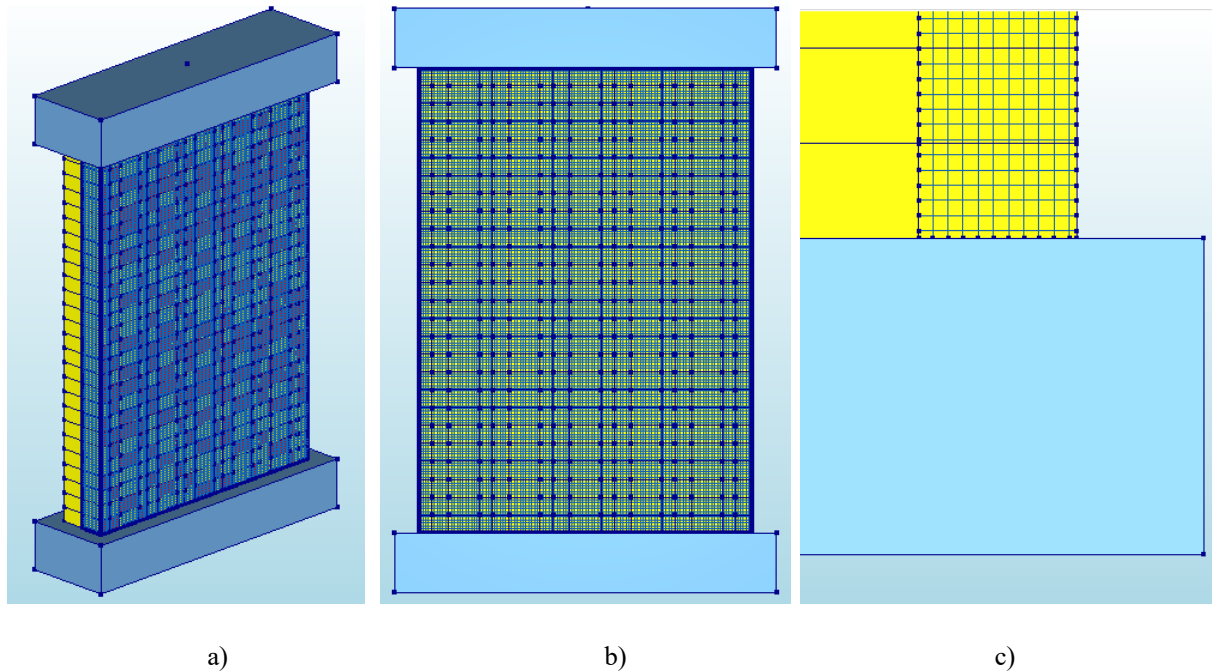


Figure 5.27 Composition of fibres for CFRCM piers (Series 3) in DIANA FEA 10.4 software a) Isometric view b) Front view c) Detail of the fibre composition at the bottom right corner (side view)

### 5.4.2 Mechanical properties of materials

The mechanical properties of materials were taken with the same values and equations as for the FRCM piers. All values are given in subsection 5.3.2. and tables Table 5.4, Table 5.5 and Table 5.6.

### 5.4.3 Boundary conditions and applied loads

After the geometry of the pier was defined and the mechanical properties were set for elements used in the model, the boundary conditions (supports) and applied loads were defined. Since the boundary conditions simulate the experimental campaign setup, they remained the same as they were for the URM and FRCM piers.

Till this point, the numerical model for both CFRCM piers that were considered was the same. In the vertical direction, the vertical compressive force stayed the same with the value of 250 kN. In the horizontal y-direction, the displacement was applied with the total value of 23

mm for both FRCM piers. This value was chosen according to Table 4.12 where the maximum displacement of all CFRCM piers was 22,01 mm for CFRCM 1 pier in the negative direction. The final load that was applied for each CFRCM pier was the bending moment around the x-axis. As it is clear from Figure 4.73 and Figure 4.74 that are correspondent to CFRCM 1 and CFRCM 3 piers, the values of these bending moments are different. From these figures, the pushover curve with the highest absolute value of the bending moment was chosen for each CFRCM pier. In both cases the pushover curve in the positive direction was chosen as the representative curve. The maximum values of the bending moments for the CFRCM 1 and CFRCM 3 pier were equal to 117,65 kNm and 102,17 kNm respectively. All pushover curves of the bending moments were added to their correspondent numerical models as positive values.

#### 5.4.4 Mesh settings and the nonlinear analysis

The next step was to define a proper mesh for the nonlinear analysis. Since the matrix elements added were the same size as the bricks, the mesh size was again chosen according to the smallest elements in the models. Since the smallest element used in the models was a half brick element with dimensions  $b/h/l = 6/6,5/12$  cm, a mesh size of 50 mm or 5 cm was chosen. Again, the hexa/quad meshing type was defined. The mesh configuration for the CFRCM piers can be seen in Figure 5.28.

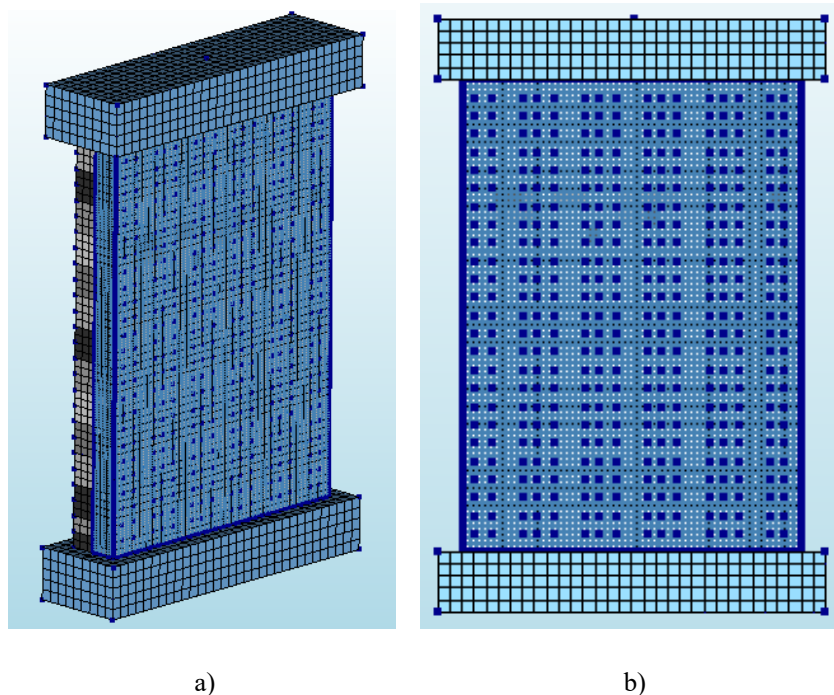


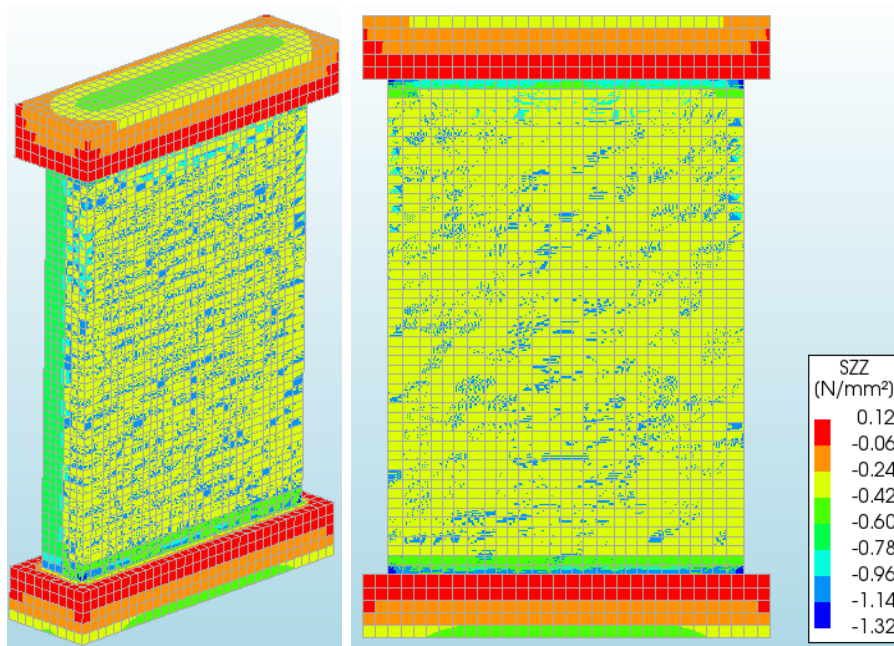
Figure 5.28 Meshing configuration for CFRCM piers: a) isometric view b) front view

After the model was meshed, a nonlinear pushover analysis was defined. The pushover analysis was defined in the same manner and with the same values as it was for FRCM piers.

#### 5.4.5 Results of the nonlinear pushover analysis

The outcomes of the nonlinear pushover analysis conducted on CFRCM piers are presented next. Similarly, to the results obtained for FRCM piers, four categories of results were examined: element results, nodal results, cracking patterns, and reinforcement results. First, the total stresses in the CFRCM piers in the vertical direction were examined. The vertical compressive stress  $\sigma_0$  was again equal to  $0,7 \text{ N/mm}^2$ . Figure 5.29 illustrates the total vertical stresses throughout the entire CFRCM pier. Since the same vertical stress was applied in case of all piers, these values were the same for both CFRCM 1 and CFRCM 3 pier that were considered. CFRCM 2 pier was not considered, the same as in the analysis of the experimental results. In the isometric view of Figure 5.29, the total vertical stresses in the masonry part of the CFRCM pier (highlighted in green) are evident, aligning with the calculated value and deemed accurate. Additionally, the total vertical stresses in the mortar matrix on the side of the CFRCM pier (highlighted in yellow) are visible. The front view of Figure 5.29 displays the total vertical stresses in the mortar matrix of the CFRCM pier (highlighted in yellow). Despite its location at the end of the pier section, a comparable value of vertical stress was observed in the mortar matrix. Notably, no visible cracks appeared.

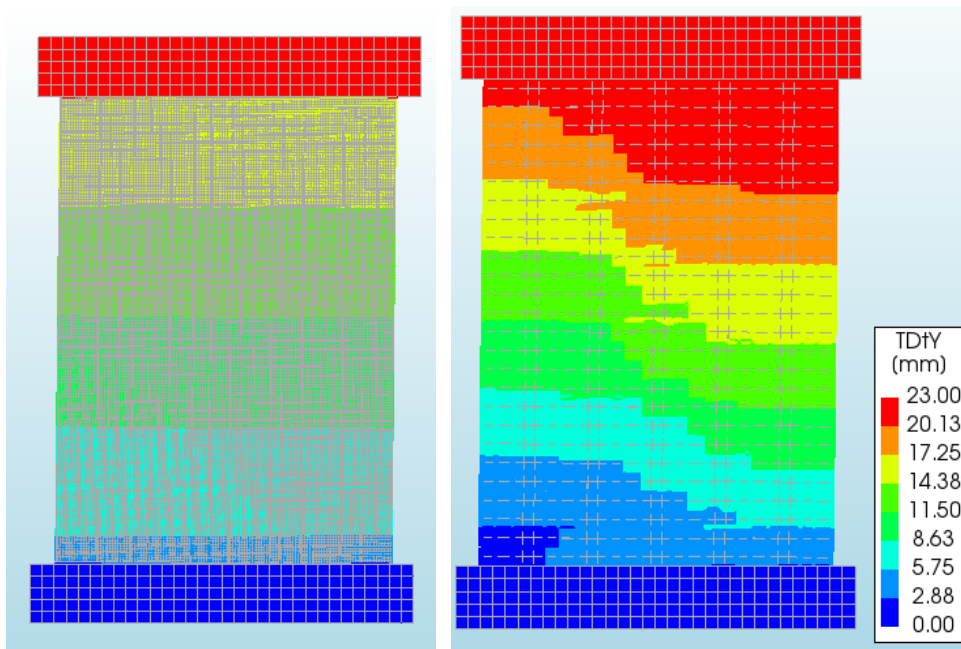
After the vertical load was transferred, the displacements and reaction forces were examined. The CFRCM piers at the final step of the shear loading phase can be seen in Figure 5.30 a) and Figure 5.31 a). In both figures the deformed shape of the CFRCM piers is presented. Due to the high modulus of elasticity of glass fibres no rupture appeared in the CFRCM piers. In Figure 5.30 b) and Figure 5.31 b) the deformed shapes CFRCM 1 and CFRCM 3 piers without the glass fibres are displayed. As it was the case in the FRCM piers, the cracking pattern corresponded to the diagonal shear failure of the mortar matrix through the same diagonal. The diagonal cracks spread through the vertical and horizontal mortar joints of the pier and through the mortar matrix as it was expected from the modelling setup. No cracks in the mortar matrix were visible on the sides of the pier. Additionally, it was important to check the boundary conditions. In this case, the CFRCM piers subjected to a vertical compressive force and an in-plane horizontal displacement had no in-plane displacements at the bottom and the assigned displacement of 23 mm at the top as it is clear from Figure 5.30 b) and Figure 5.31 b). In the end it is important to state that no overturning or bending appeared in the CFRCM piers. All the mentioned results were satisfactory and correspondent to the experimental campaign test setup.



a)

b)

Figure 5.29 Total vertical stresses of the CFRCM piers: a) isometric view b) front view



a)

b)

Figure 5.30 Deformed shape of the CFRCM 1 pier at 23 mm: a) front view of the CFRCM pier - glass fibres b) front view of the CFRCM pier - mortar matrix failure

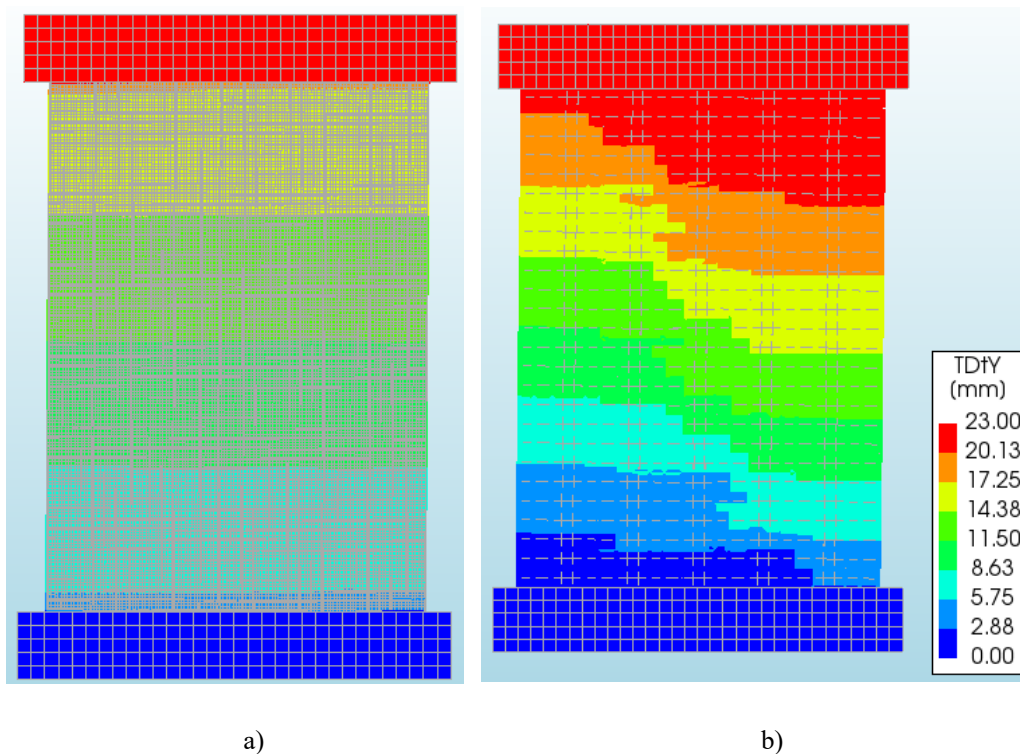


Figure 5.31 Deformed shape of the CFRCM 3 pier at 23 mm: a) front view of the CFRCM pier - glass fibres b) front view of the CFRCM pier - mortar matrix failure

The reaction forces were observed next. As a result of the analysis a pushover curve in the positive direction was obtained at the final step of the shear load in the nonlinear analysis. The pushover curve in the negative direction was mirrored again. The pushover curves for each CFRCM pier can be seen in Figure 5.32. The most important values that were gathered from the pushover curves are displayed in Table 5.8. The ductility was calculated by dividing the maximum displacement and the displacement at the yielding point given in Table 5.8.

The nonlinear pushover analysis was continued till the assigned horizontal displacement of 23 mm was reached in both cases, but the value of the horizontal in-plane force did not change after failure. Consequently, the cracking patterns seen in Figure 5.30 b) and Figure 5.31 b) did not change after the failure till the assigned displacement of 23 mm. It can also be observed that practically no cracks appeared in the mortar matrix on the sides of the pier.



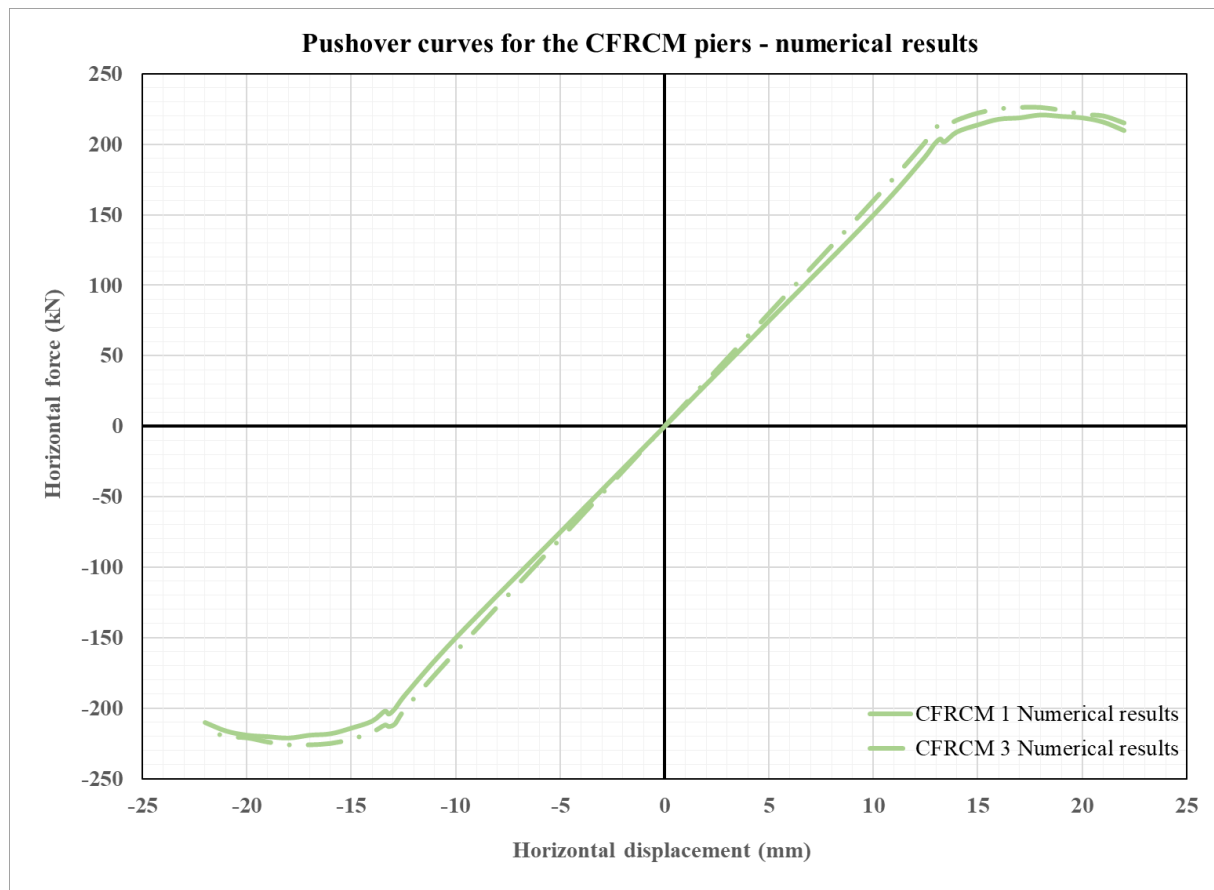


Figure 5.32 Pushover curves for the CFRCM piers from the numerical modelling

Table 5.8 Results of the numerical modelling for CFRCM piers

| Value                                      | CFRCM 1 | CFRCM 3 | mean   |
|--|---------|---------|--------|
| <b>Maximum horizontal force [kN]</b>       | 221,00  | 226,00  | 223,50 |
| <b>Maximum displacement [mm]</b>           | 22,20   | 22,10   | 22,15  |
| <b>Displacement at yielding point [mm]</b> | 13,60   | 13,40   | 13,50  |
| <b>Ductility</b>                           | 1,63    | 1,65    | 1,64   |

Two categories of cracks were checked next. For the masonry pier, the interface relative displacements were checked in the in-plane direction. All displacements in the mortar joint interfaces are shown in Figure 5.33 a) and Figure 5.34 a) for CFRCM 1 and CFRCM 3 pier respectively. The maximum crack width was equal to 3,20 mm in the CFRCM 1 pier and 3,17 mm in the CFRCM 3 pier. For the mortar matrix, the interface relative displacements of the mortar matrix were checked in the in-plane direction. The displacements in the matrix-to-matrix interfaces are shown in Figure 5.33 b) and Figure 5.34 b) for CFRCM 1 and CFRCM 3 pier respectively. The maximum crack width was equal to 3,20 mm in the CFRCM 1 pier and 3,17 mm in CFRCM 3 pier. Therefore, it is concluded that the masonry pier and the mortar matrix had a corresponding diagonal shear failure and accompanying crack widths.

To be sure that no failure of fibres appeared, the total stresses in the in-plane direction (global y-direction) were checked for each pier. From Figure 5.35 a) it was deduced that the maximum stress of  $\sigma_f = 63,10 \text{ N/mm}^2$  in the glass fibres appeared at the corners of the CFRCM 1 pier. From Figure 5.35 b) it was deduced that the maximum stress of  $\sigma_f = 48,83 \text{ N/mm}^2$  in the glass fibres appeared at the corners of the CFRCM 3 pier. The maximum value of the in-plane stress for FRCM fibres was  $\sigma_f = \varepsilon_{fd} \cdot E_f = 0,018 \cdot 74000 = 1332 \text{ N/mm}^2$ . It can be concluded that no failure of glass fibres appeared in the FRCM system.

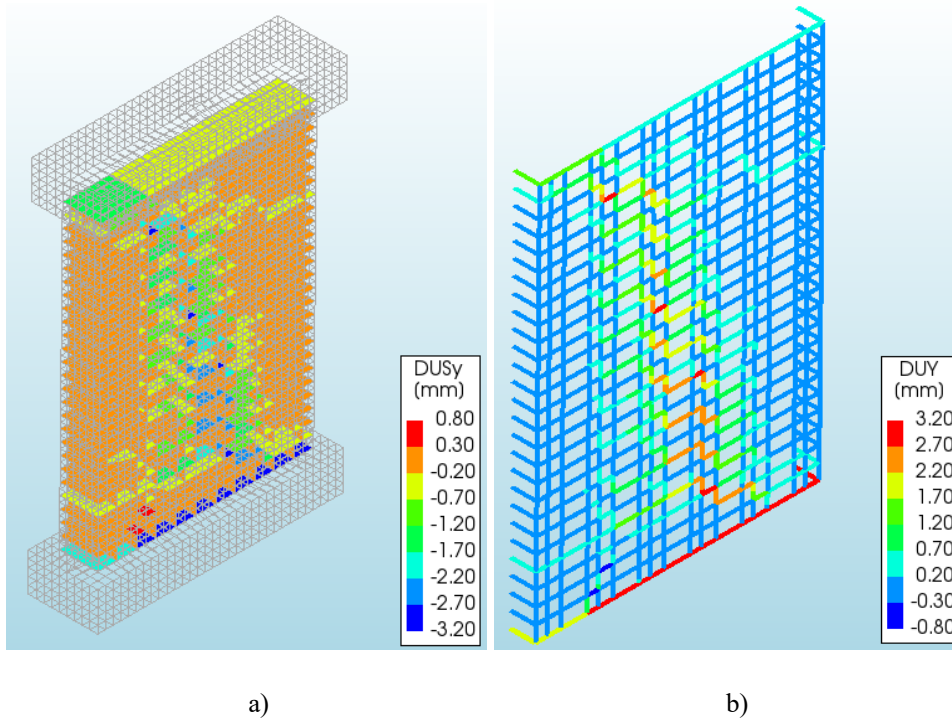
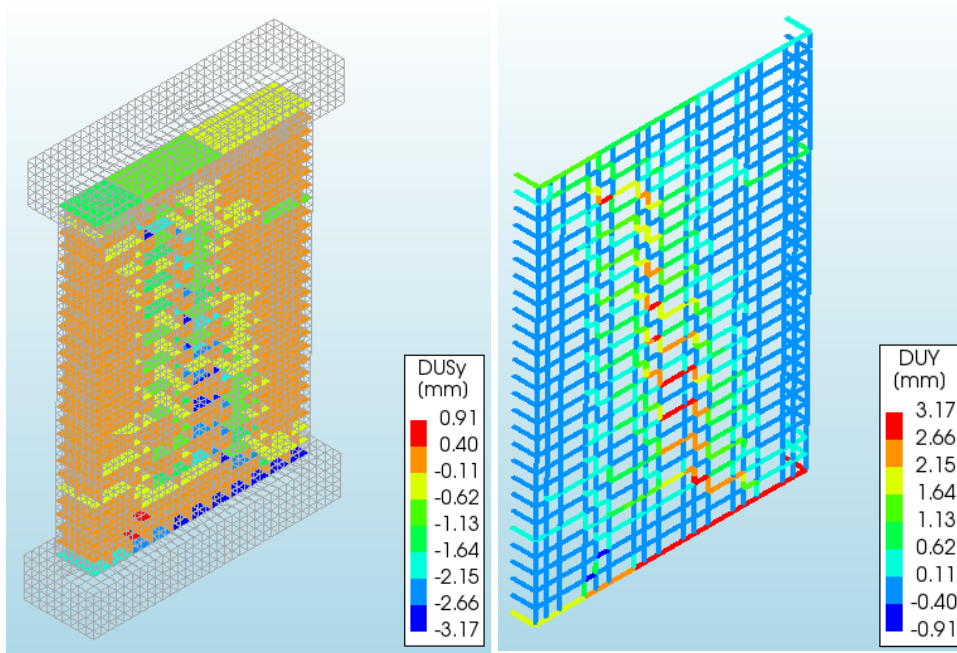


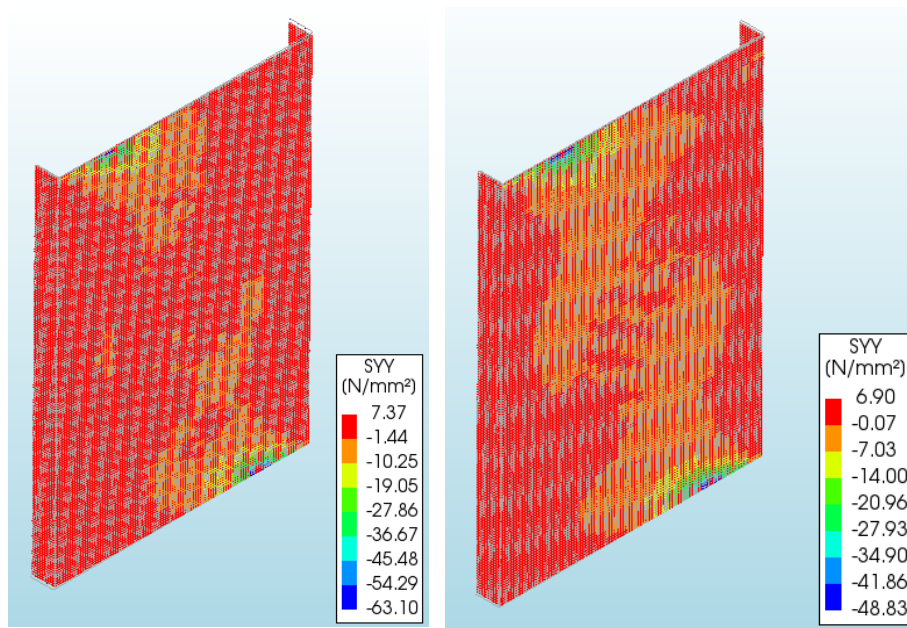
Figure 5.33 Interface relative displacements of the CFRCM 1 pier a) in the mortar joints of the masonry pier b) in the mortar matrix interfaces



a)

b)

Figure 5.34 Interface relative displacements of the CFRCM 3 pier a) in the mortar joints of the masonry pier b) in the mortar matrix interfaces



a)

b)

Figure 5.35 Total stresses in the glass reinforcement in the in-plane direction for a) CFRCM 1 pier b) CFRCM 3 pier

## 5.5 Comparison of the numerical modelling results

After the numerical modelling of three different types of masonry piers, analogies between them need to be made. Firstly, the vertical compressive force of 250 kN was successfully transferred from the top reinforced concrete beam to all three types of masonry piers as it may be seen in Figure 5.8, Figure 5.17, and Figure 5.29. Following that verification, the horizontal displacement was applied. In case of URM piers, the total displacement applied was 21,50 mm and in case of FRFCM and CFRFCM piers the total displacement equalled 23 mm. The reasoning behind this was the expected increase in the maximum displacement when the strengthening method was applied.

The first thing that was examined were the crack patterns. The correlation between crack patterns of all eight masonry piers is seen in Figure 5.36. In all cases the diagonal shear failure was hoped to be achieved and can be observed from the figure. However, several differences were noticed. The first difference was that the failure in the URM piers spread only through the vertical and horizontal mortar joints of the pier while in case of FRFCM and CFRFCM piers the cracks appeared both in mortar joints of the piers and the mortar matrix of the FRFCM system. Therefore, it can be concluded that the FRFCM system failed due to the cracking of the mortar matrix in both FRFCM and CFRFCM piers.

Secondly, the deformed shapes were very different when comparing the URM piers to the FRFCM and CFRFCM piers which is also visible from Figure 5.36. While the URM piers had a visibly deformed shape due to the translatory action in all three cases, the FRFCM and CFRFCM piers did not deform in an obvious manner. The justification for this is the glass reinforcement that was used in the strengthening system that had a high value of modulus of elasticity increasing the stiffness of the strengthened piers. Thus, the cracking pattern remained similar between the piers, while the deformation was different. The deformed shapes of FRFCM and CFRFCM piers were practically the same. In all cases, the in-plane displacements were equal to 0 at the bottom and had the assigned value at the top which means that the boundary conditions were defined properly. Also, no overturning or bending appeared in the piers.

Finally, the maximum crack widths of different piers were very similar. The crack widths in masonry piers (vertical and horizontal mortar joints) may be seen in Table 5.9. The values given are the mean values for each type of pier. The differences observed between the piers were not significant. In case of CFRFCM piers the cracks were a bit wider. When FRFCM strengthening and particularly the new clamping details are used, it allows the masonry pier to have a higher ductility and possibility to widen the cracks until failure. The crack widths in the

mortar joints of the masonry pier and the mortar matrix of the strengthening system were correspondent in case of both FRCM and CFRCM piers. The basis for this is a perfect connection between the bricks and the mortar matrix that was defined in the model.

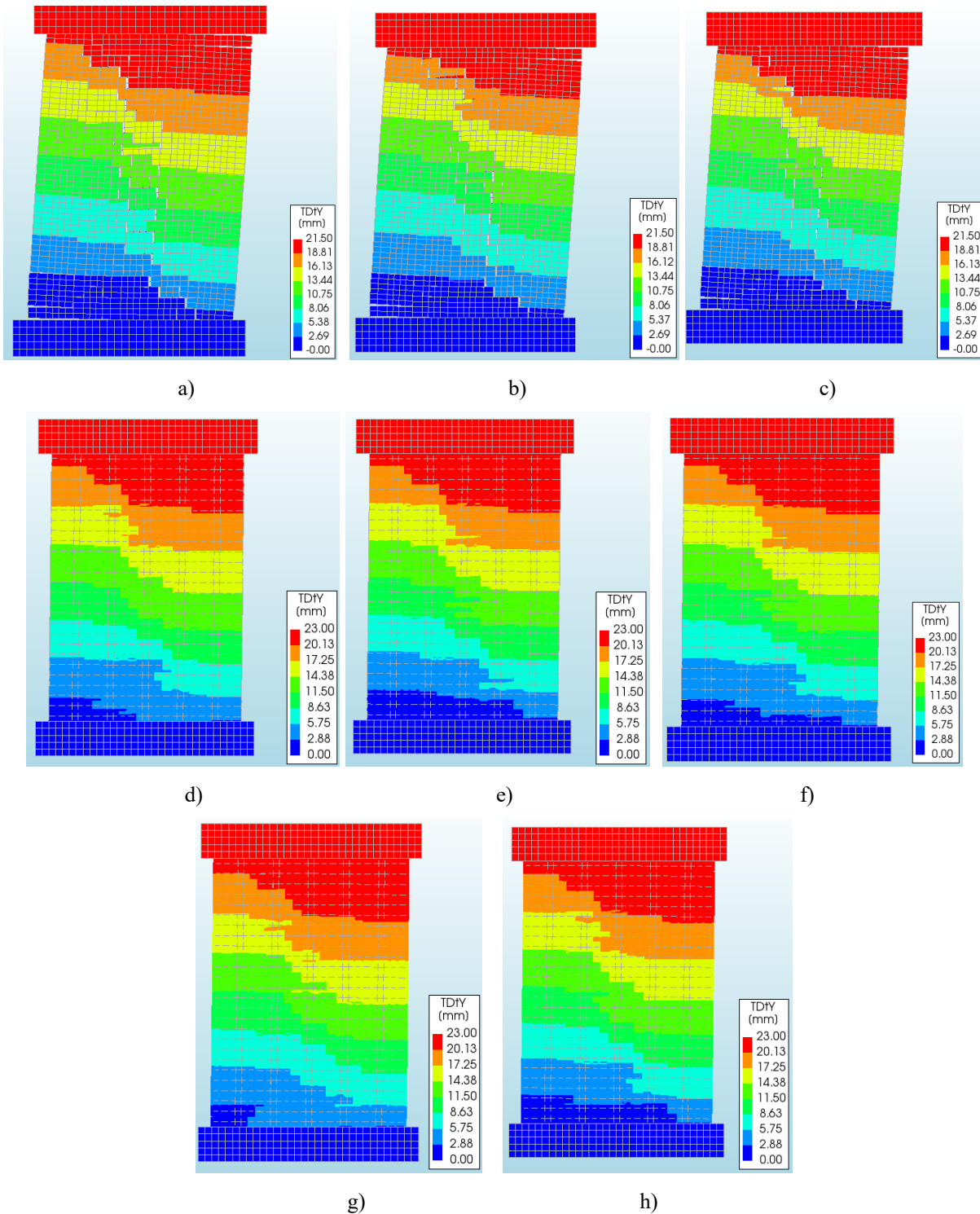


Figure 5.36 Crack patterns at the final step of the analysis a) URM 1 pier b) URM 2 pier c) URM 3 pier d) FRCM 1 pier e) FRCM 2 pier f) FRCM 3 pier g) CFRCM 1 pier h) CFRCM 3 pier

Table 5.9 Comparison of results for all masonry piers

| Value                         | URM    | FRCM   | CFRCM  |
|-------------------------------|--------|--------|--------|
| Maximum crack width [mm]      | 2,95   | 2,99   | 3,19   |
| Maximum horizontal force [kN] | 135,67 | 210,00 | 223,50 |
| Maximum displacement [mm]     | 11,23  | 19,47  | 22,15  |
| Ductility                     | 1,41   | 1,44   | 1,64   |

Following the analysis of the cracking patterns and deformations, the achieved horizontal displacements and in-plane reaction forces were observed and compared. Both parameters were derived from the pushover curves that were plotted for each pier. The comparison of pushover curves is shown in Figure 5.37. For the URM piers, the pushover curve was obtained at 21,50 mm and for the FRCM and CFRCM piers at 23 mm of the horizontal in-plane displacement.

From Figure 5.37 several conclusions can be derived. Firstly, it is obvious that the increase of the maximum horizontal force or in-plane shear capacity was significant when the FRCM strengthening was used. The same can be seen by analysing the results in Table 5.9. In case of FRCM piers, this increase equalled 74,33 kN or 55 % in regards to URM piers. In case of CFRCM piers, this increase equalled 87,83 kN or 65 % in regards to URM piers. Also, an increase of 13,50 kN or 6 % was observed when comparing CFRCM and FRCM piers. This increase is visible in Figure 5.37. It is attributed to the use of clamping details in CFRCM piers.

The same conclusions were drawn when the maximum horizontal displacements were compared. The significant enhancement of the maximum displacement was evident when employing FRCM strengthening, as indicated by the pushover curves in Figure 5.37 and the results in Table 5.9. Specifically, for FRCM piers, this increase amounted to 8,24 mm or 73 % compared to URM piers. In the case of CFRCM piers, the increase was even more pronounced at 10,92 mm, corresponding to a 97 % rise in comparison to URM piers. Additionally, a noticeable increase of 2,68 mm or 14 % was observed when comparing CFRCM and FRCM piers, as illustrated in Figure 5.37. This increment was yet again attributed to the implementation of clamping details in CFRCM piers.

When ductility is observed, similar patterns can be seen. Specifically, for FRCM piers, this ductility increased by 0,03 or 2 % compared to URM piers. This increase is considered insignificant. In the case of CFRCM piers, the increase was more pronounced at 0,23, corresponding to a 16 % rise in comparison to URM piers. Additionally, a noticeable increase

of 0,20 or 14 % was observed when comparing CFRCM and FRCM piers, as illustrated in Figure 5.37. This increment was again attributed to the implementation of clamping details.

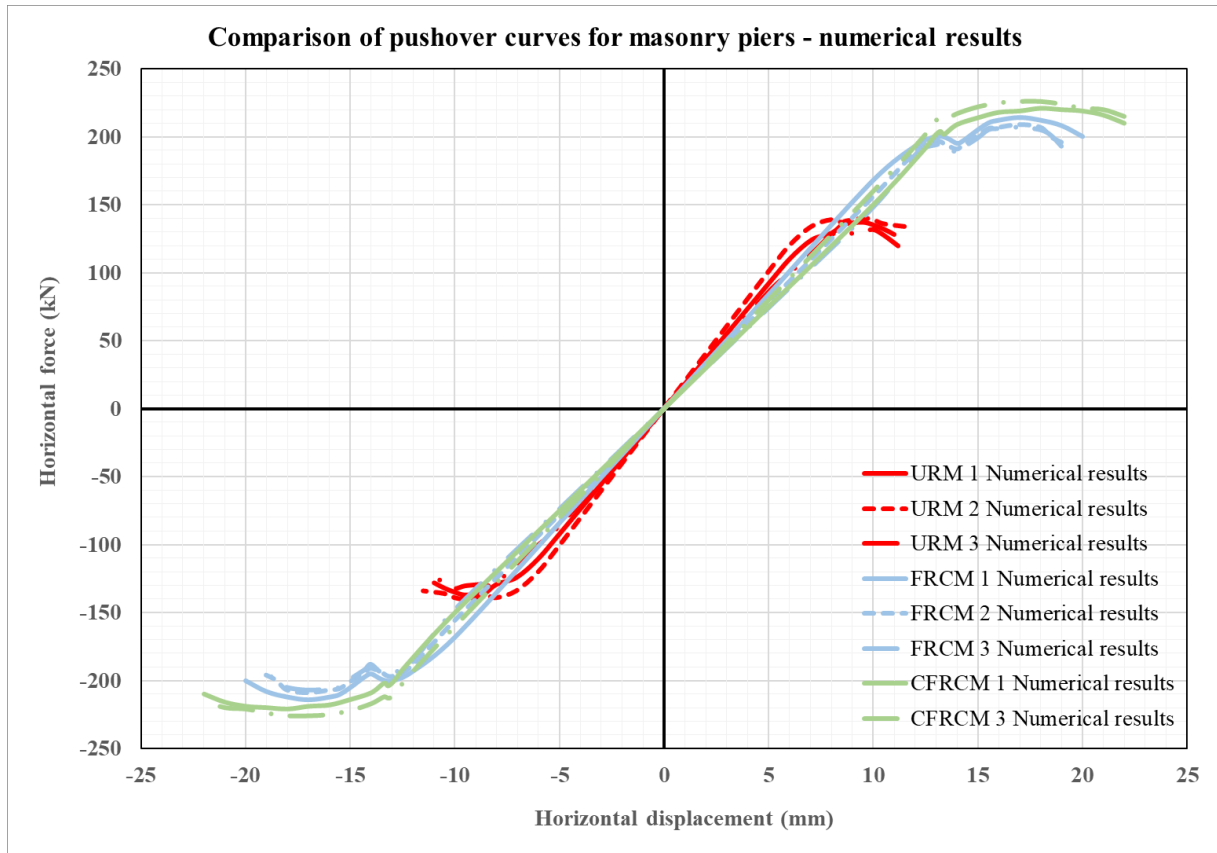


Figure 5.37 Comparison of pushover curves for masonry piers – numerical results

## 6 COMPARISON OF RESULTS

In the previous sections the theoretical evaluation, experimental campaign and the numerical modelling of URM piers and masonry piers strengthened with FRCM coating in two different compositions were explained. First, the theoretical analysis was conducted to define the parameters of the experimental campaign. With these results, the experimental campaign and the accompanying test setup were defined and carried out. Finally, the numerical modelling campaign was conducted to check the results of the experimental campaign. In this section, the gathered results will be examined and compared.

### 6.1 The update of the theoretical evaluation results

To have a proper comparison, the results of the preliminary theoretical evaluation need to be updated first. The input data considered in the preliminary analysis was taken from various literature since at that point no experiments were conducted to obtain the mechanical properties of materials. As it was mentioned before, a part of the experimental campaign included small-scale testing. The parameters that were collected include the compressive strength of concrete, compressive strength of masonry units, compressive strength of hardened mortar and the initial shear strength of masonry. Therefore, the compression-shear interaction diagrams and envelope curves that were used for the assessment of URM piers (Series 1) need to be updated. As outlined in subsection 3.6.1 the compression-shear interaction diagrams were defined for seven different failure modes. The values of the vertical compressive force  $N$  [kN] are shown on the x-axis and the values of the horizontal in-plane force  $V$  [kN] are shown on the y-axis. The data presented in Table 3.2 is updated with the results gathered in the testing of the mechanical properties of materials and displayed in Table 6.1.

Table 6.1 Updated properties of masonry units, mortar and masonry piers

| Masonry units and mortar   |                               |                                |                                |                               |            |            |
|----------------------------|-------------------------------|--------------------------------|--------------------------------|-------------------------------|------------|------------|
| $f_b$ (N/mm <sup>2</sup> ) | $f_{bt}$ (N/mm <sup>2</sup> ) | $f_m$ (N/mm <sup>2</sup> )     |                                |                               |            |            |
| 37                         | 3,7                           | 6,12                           |                                |                               |            |            |
| Masonry piers              |                               |                                |                                |                               |            |            |
| $f_k$ (N/mm <sup>2</sup> ) | $\mu=\tan(\phi)$              | $f_{vk0}$ (N/mm <sup>2</sup> ) | $f_{vlt}$ (N/mm <sup>2</sup> ) | $f_{tk}$ (N/mm <sup>2</sup> ) | $h_0$ (cm) | $\gamma_m$ |
| 11,16                      | 0,5                           | 0,23                           | 2,4                            | 0,15                          | 93,25      | 1,0        |

The updated interaction diagrams for the URM piers defined by seven different failure modes are shown in Figure 6.1. From these seven interaction diagrams, an envelope curve was



derived. The updated envelope curve can be seen in Figure 6.2. In Figure 6.2 it is clear that, with the summed value of 280 kN of vertical force, the value of the horizontal in-plane shear capacity of the URM pier is equal to 149 kN.

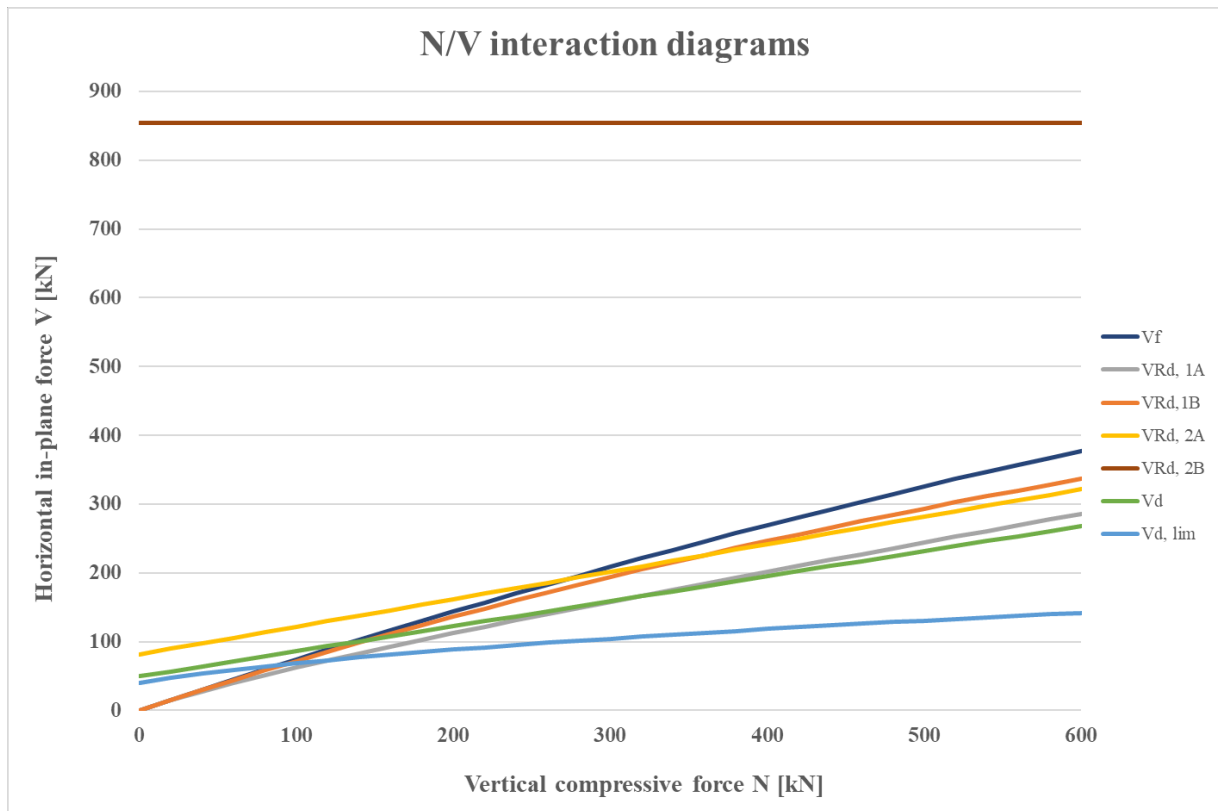


Figure 6.1 Updated interaction diagrams  $N/V$  for seven different failure modes

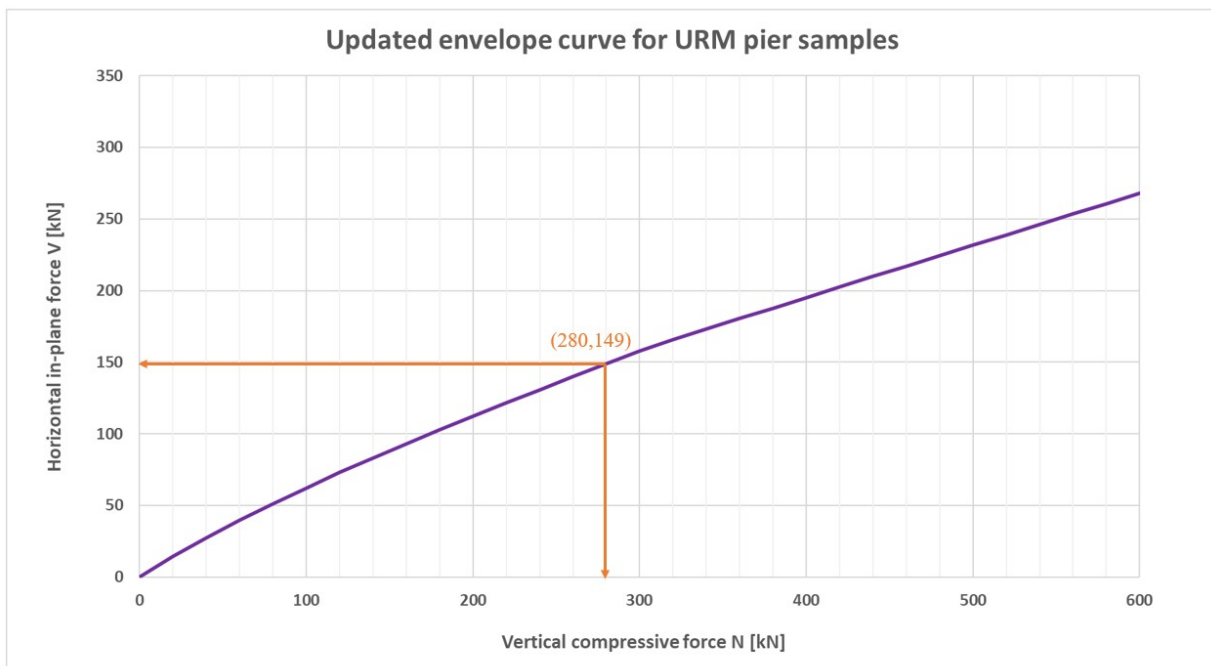


Figure 6.2 Updated envelope curve for the analysed URM pier

The contribution of the FRCM reinforcement for single sided FRCM strengthening did not change in value since no testing of mechanical properties of FRCM components was conducted. Therefore, the contribution of the FRCM reinforcement to the in-plane shear capacity was taken with the same value  $V_{t,f} = 119$  kN. With the addition of this value to the value of 149 kN for URM piers the in-plane shear resistance of the single-sided strengthened masonry piers (Series 2) was achieved. The value of the in-plane shear capacity of the Series 2 piers is therefore equal to 268 kN. The contribution of the clamping details in Series 3 cannot be considered with the current version of the CNR-DT 215/2018 standards. Therefore, in terms of the available analytical procedures, no increase in the in-plane shear force capacity should come from the usage of new clamping details.

## 6.2 Comparison of theoretical, experimental, and numerical results

The first results that were evaluated are the ones from the URM piers (Series 1). In the preliminary analysis described and carried out in subsection 3.6, the compression-shear interaction diagrams and the corresponding envelope curve were defined. Since the input data was taken from literature this analysis can only be considered as preliminary and used for the definition of the parameters in the experimental campaign. After the testing of mechanical properties, the compression-shear interaction diagrams and the envelope curve were updated in subsection 6.1. The most important value to be derived from the envelope curve is the horizontal in-plane shear capacity of the URM pier. The value is shown in Table 6.2 under maximum horizontal force – positive direction (theoretical results). Since the horizontal in-plane shear capacity in the theoretical evaluation was gathered in only one direction, the same value was considered for the maximum horizontal force – negative direction.

After the theoretical evaluation, the experimental results were compared. In subsection 4.4.1 the results of the quasi-static cyclic displacement-controlled testing of three URM piers were gathered and explained. The most important values that were derived are the maximum horizontal force, maximum displacement, ductility and the initial stiffness in the positive and negative directions. The mean values for each parameter were calculated and shown in Table 6.2. When compared to the theoretical results for the maximum horizontal force, a higher value was achieved in the experimental campaign. The difference amounted to 4,39 kN or 3 % in the positive direction and 11,45 kN or 8 % in the negative direction. These differences are considered insignificant. The quantitative results of the experimental campaign were gathered and calculated using the envelope curves for each URM pier. The envelope curves from the experimental campaign are shown in Figure 6.3 under URM 1, URM 2 and URM 3 piers.

To check the validity of the results gathered from the experiment, a numerical modelling campaign was conducted. The micro-modelling approach was chosen for the most detailed analysis of the pier's behaviour. After the models were meshed, a nonlinear pushover analysis was defined and carried out for each URM pier. The result of the analysis was a pushover curve in the positive direction for each pier. The pushover curves in the negative direction were defined as the mirrored version of the pushover curves in the positive direction using negative values for displacement and force. The pushover curves from the numerical campaign are plotted in red in Figure 6.3 under URM 1 Numerical results, URM 2 Numerical results and URM 3 Numerical results. When compared to the results of the experimental campaign, the first thing that was obvious are the discrepancies in the maximum horizontal force and maximum displacement. The same was concluded when the mean values of the numerical results and the mean values of the experimental results were compared in Table 6.2. When the maximum horizontal force was considered, the experimental results had higher values than the numerical modelling results. The difference amounted to 17,72 kN or 13 % in the positive direction and 24,78 kN or 18 % in the negative direction. Furthermore, when maximum displacements were compared, the experimental results had higher values than the numerical modelling results. The difference amounted to 3,02 mm or 27 % in the positive direction and 5,12 mm or 46 % in the negative direction. The reason for this underestimation in the numerical modelling campaign was the conservative nature of the numerical modelling process. This fact was proved by the difference in the maximum horizontal force when theoretical and numerical results are compared. In the theoretical evaluation a higher value was achieved with the difference amounting to 13,33 kN or 10 %. Therefore, if the maximum horizontal force has a higher value when conservative analytical procedures given in standards were used, then the numerical results must be considered conservative as well. On the other hand, the ductility was higher for URM piers in the numerical modelling campaign than in the experiment. In the positive direction the ductility was higher by 0,03 or 2 % in comparison to the experimental results. In the negative direction the ductility was higher by 0,25 or 22 %. Finally, the initial stiffness in the positive and negative direction are considered correspondent when numerical and experimental results are compared in Figure 6.3 for all three URM piers. It is therefore concluded that this type of numerical modelling campaign is an adequate tool in obtaining the experimental results of URM piers.

Table 6.2 Theoretical, experimental, and numerical results for URM piers

| Value  | Theoretical results | Experimental results (mean) | Numerical results (mean) |
|--|---------------------|-----------------------------|--------------------------|
| Maximum horizontal force – positive direction [kN] | 149,00              | 153,39                      | 135,67                   |
| Maximum displacement – positive direction [mm]     | -                   | 14,25                       | 11,23                    |
| Ductility – positive direction                     | -                   | 1,38                        | 1,41                     |
| Initial stiffness – positive direction [kN/mm]     | -                   | 19,60                       | -                        |
| Maximum horizontal force – negative direction [kN] | 149,00              | 160,45                      | 135,67                   |
| Maximum displacement – negative direction [mm]     | -                   | 16,35                       | 11,23                    |
| Ductility – negative direction                     | -                   | 1,16                        | 1,41                     |
| Initial stiffness – negative direction [kN/mm]     | -                   | 17,93                       | -                        |

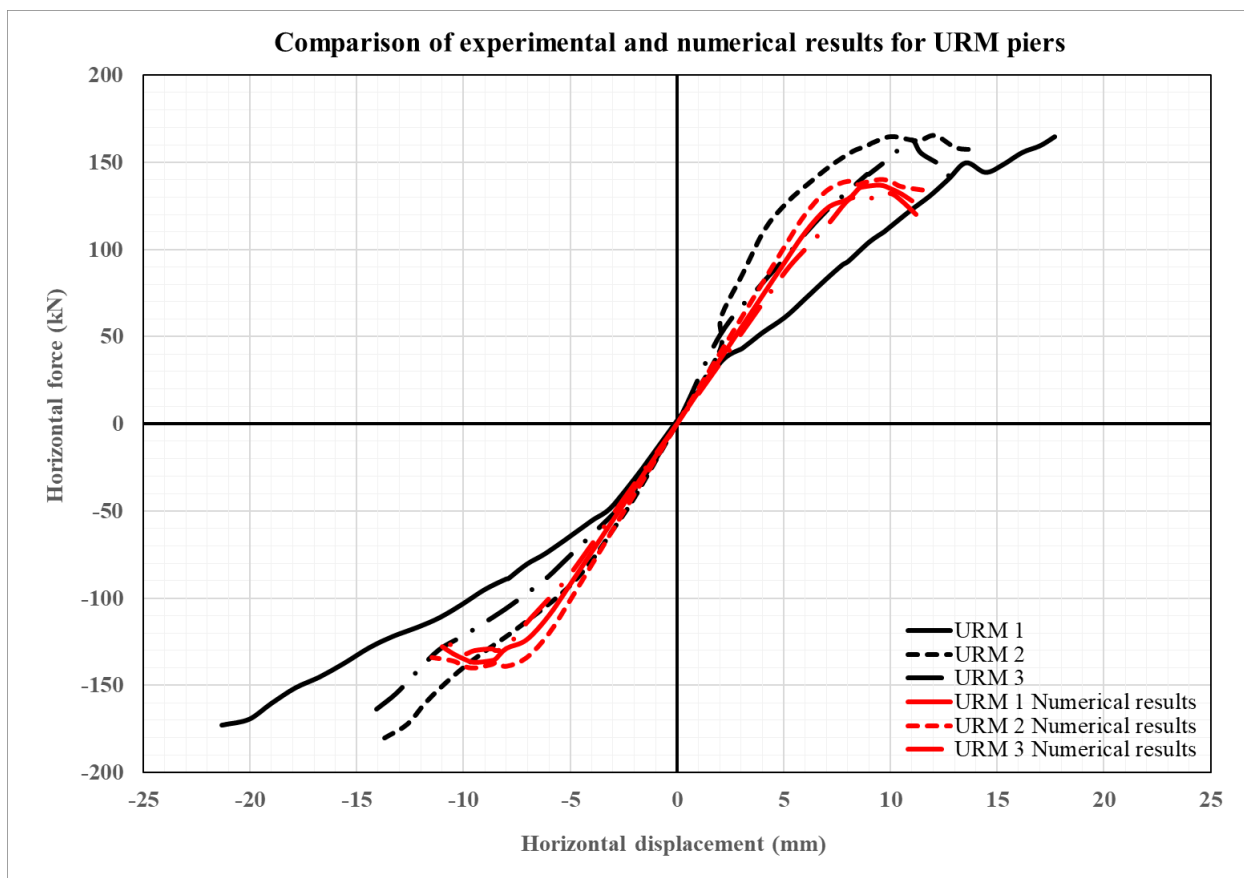


Figure 6.3 Comparison of envelope and pushover curves for URM piers – experimental and numerical results

The results that were evaluated next are the results from the FRCCM piers (Series 2). In the preliminary analysis described and carried out in subsection 3.6, the compression-shear interaction diagrams and the corresponding envelope curve were obtained for the URM pier. The compression-shear interaction diagrams, and the envelope curve of the URM pier were updated in subsection 6.1. The most important value to be derived from the envelope curve is the horizontal in-plane shear capacity of the URM pier. After that, the contribution of the FRCCM reinforcement to the in-plane shear capacity of the pier was calculated in subsection 3.7. No update was needed since the mechanical properties of FRCCM components were not tested in the experimental campaign. By summing these two values the in-plane shear capacity of the FRCCM pier was calculated. The value is shown in Table 6.3 under maximum horizontal force – positive direction (theoretical results). Since the horizontal in-plane shear capacity in the theoretical evaluation was gathered in only one direction, the same value was considered in the negative direction.

Following the theoretical assessment, a comparison was made with the experimental results. In subsection 4.4.2, the results obtained from the quasi-static cyclic displacement-controlled tests on three FRCCM piers were presented. Key parameters derived from the tests include the maximum horizontal force, maximum displacement, and initial stiffness in both positive and negative directions. In comparison to the theoretical result for the maximum horizontal force, the experimental campaign yielded smaller values. Specifically, the difference amounted to 63,48 kN or 31 % in the positive direction and 61,60 kN or 30 % in the negative direction. This disparity is attributed to the overestimation of the contribution of the FRCCM reinforcement. The analytical procedure that was defined in the preliminary evaluation did not consider the partial safety factors  $\gamma_{Rd}$  and  $\gamma_m$  to achieve the highest possible increase in the in-plane shear capacity. Additionally, characteristic values of the mechanical properties of materials were used since no small-scale testing campaign was conducted for FRCCM components. It is concluded that the theoretical contribution of the FRCCM reinforcement should be considered using the values of the mechanical properties of materials that were tested in a small-scale testing campaign and not with the values given by the manufacturer. Since this was a preliminary analysis, the overestimation of the theoretical evaluation is considered useful. Quantitative results from the experimental campaign were compiled and computed using envelope curves for each FRCCM pier. The envelope curves from the experimental campaign are illustrated in Figure 6.4 under FRCCM 1, FRCCM 2, and FRCCM 3.

To verify the reliability of the experimentally gathered results, a numerical modelling campaign was undertaken. The pushover curves from the numerical modelling campaign, both

in the positive and negative directions, are depicted in light blue in Figure 6.4. The most important values are highlighted in Table 6.3. In terms of maximum horizontal force, the numerical modelling results shows higher values than the experimental data, with a difference of 5,48 kN or 3 % in the positive direction and 3,60 kN or 2 % in the negative direction. These differences are considered negligible. When comparing maximum displacements, the experimental values and the numerical modelling values are very similar. In the positive direction the experiment yielded a higher value of the maximum displacement equal to 1,30 mm or 7 %. On the other hand, in the negative direction the numerical model had a higher value of the maximum displacement equal to 0,18 mm or 1 %. In this case, the conservative nature of the modelling process was not evident from the values of the maximum horizontal force and maximum displacement. When ductility is compared, the numerical modelling campaign had higher values than the experimental campaign. In the positive direction the difference equalled to 0,1 or 8 % while in the negative direction the difference was 0,29 or 25 %.

The comparison of the envelope curves from the experimental campaign and the resulting pushover curves from the numerical modelling campaign are shown in Figure 6.4. The initial stiffness in both the positive and negative direction were similar for the experimental and the numerical modelling campaign. It is therefore concluded that this type of numerical modelling campaign is an adequate tool in obtaining the experimental results of FRCM piers.

Table 6.3 Theoretical, experimental, and numerical results for FRCM piers

| <b>Value</b>  | <b>Theoretical results</b> | <b>Experimental results (mean)</b> | <b>Numerical results (mean)</b> |
|---|----------------------------|------------------------------------|---------------------------------|
| <b>Maximum horizontal force – positive direction [kN]</b> | 268,00                     | 204,52                             | 210,00                          |
| <b>Maximum displacement – positive direction [mm]</b>     | -                          | 20,77                              | 19,47                           |
| <b>Ductility – positive direction</b>                     | -                          | 1,34                               | 1,44                            |
| <b>Initial stiffness – positive direction [kN/mm]</b>     | -                          | 17,55                              | -                               |
| <b>Maximum horizontal force – negative direction [kN]</b> | 268,00                     | 206,40                             | 210,00                          |
| <b>Maximum displacement – negative direction [mm]</b>     | -                          | 19,29                              | 19,47                           |
| <b>Ductility – negative direction</b>                     | -                          | 1,15                               | 1,44                            |
| <b>Initial stiffness – negative direction [kN/mm]</b>     | -                          | 21,49                              | -                               |

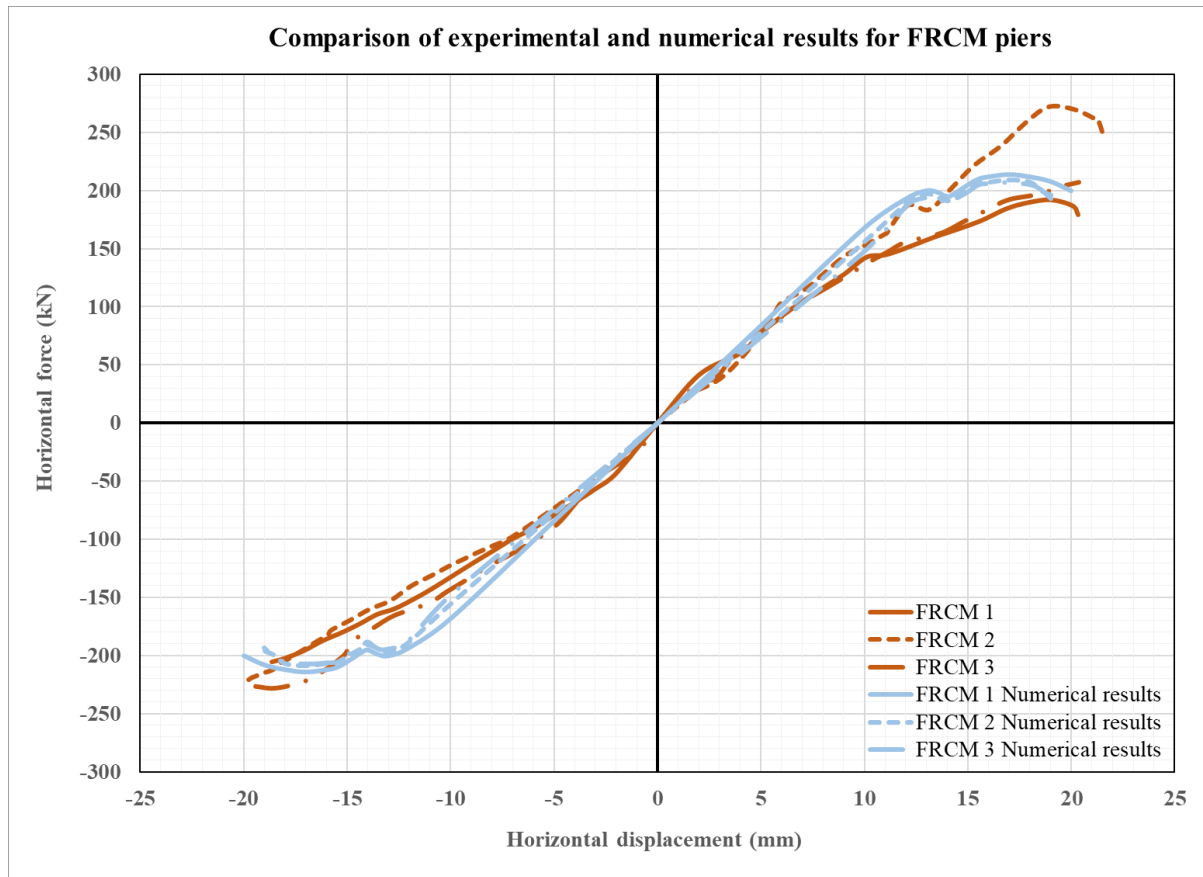


Figure 6.4 Comparison of envelope and pushover curves for FRCM piers – experimental and numerical results

The final results that were evaluated are the results from the CFRCM piers (Series 3). In the preliminary analysis the CFRCM piers were not observed. The reason for this is the lack of coefficients and parameters in the current standards which would consider the addition of clamping details and their effect on the in-plane shear capacity of masonry piers. Therefore, if an increase in the in-plane shear capacity was achieved in the experimental and numerical modelling campaign by adding clamping details, they would be considered adequately.

In subsection 4.4.3, the results obtained from the quasi-static cyclic displacement-controlled tests on three CFRCM piers were presented. Since the results of CFRCM 2 pier were unsatisfactory, they were not considered. Mean values for each parameter were calculated and presented in Table 6.4. Quantitative results from the experimental campaign were compiled and computed using envelope curves for each CFRCM pier. The envelope curves from the experimental campaign are illustrated in Figure 6.5 under CFRCM 1 and CFRCM 3.

To validate the reliability of the experimentally obtained results, a numerical modelling campaign was conducted. Pushover curves from the numerical modelling campaign are presented in light green in Figure 6.5 for each CFRCM pier. The maximum horizontal force and maximum displacement exhibited similarities, as outlined in Table 6.4. Regarding the

maximum horizontal force, the numerical data indicated a higher value than the experimental results in the positive direction, with a disparity of 7,81 kN or 4 %. In the negative direction, the maximum horizontal force had a higher value in the numerical model equalling to 17,10 kN or 8 %. Similarly, regarding the maximum displacement, the numerical data indicated a higher value than the experimental results in the positive direction, with a disparity of 1,13 mm or 5 %. In the negative direction, the maximum horizontal displacement had a higher value in the numerical model equalling to 3,35 mm or 18 %. Despite these variations, these values are considered similar. In case of the ductility, the numerical model exhibited higher values than the experiment in both directions. In the positive direction the difference in ductility was equal to 0,25 or 18 %. In the negative direction the difference in ductility was equal to 0,2 or 14 %.

Finally, the initial stiffness in both positive and negative directions were very similar in the numerical modelling campaign and in the experiments as it is clear from Figure 6.5. Once again, it is concluded that this type of numerical modelling campaign is an adequate tool in obtaining the experimental results of FRCC strengthened piers.

Table 6.4 Theoretical, experimental, and numerical results for CFRCC piers

| <b>Value</b>  | <b>Theoretical results</b> | <b>Experimental results (mean)</b> | <b>Numerical results (mean)</b> |
|---|----------------------------|------------------------------------|---------------------------------|
| <b>Maximum horizontal force – positive direction [kN]</b> | -                          | 215,69                             | 223,50                          |
| <b>Maximum displacement – positive direction [mm]</b>     | -                          | 21,02                              | 22,15                           |
| <b>Ductility – positive direction</b>                     | -                          | 1,39                               | 1,64                            |
| <b>Initial stiffness – positive direction [kN/mm]</b>     | -                          | 16,18                              | -                               |
| <b>Maximum horizontal force – negative direction [kN]</b> | -                          | 206,40                             | 223,50                          |
| <b>Maximum displacement – negative direction [mm]</b>     | -                          | 18,80                              | 22,15                           |
| <b>Ductility – negative direction</b>                     | -                          | 1,44                               | 1,64                            |
| <b>Initial stiffness – negative direction [kN/mm]</b>     | -                          | 21,33                              | -                               |



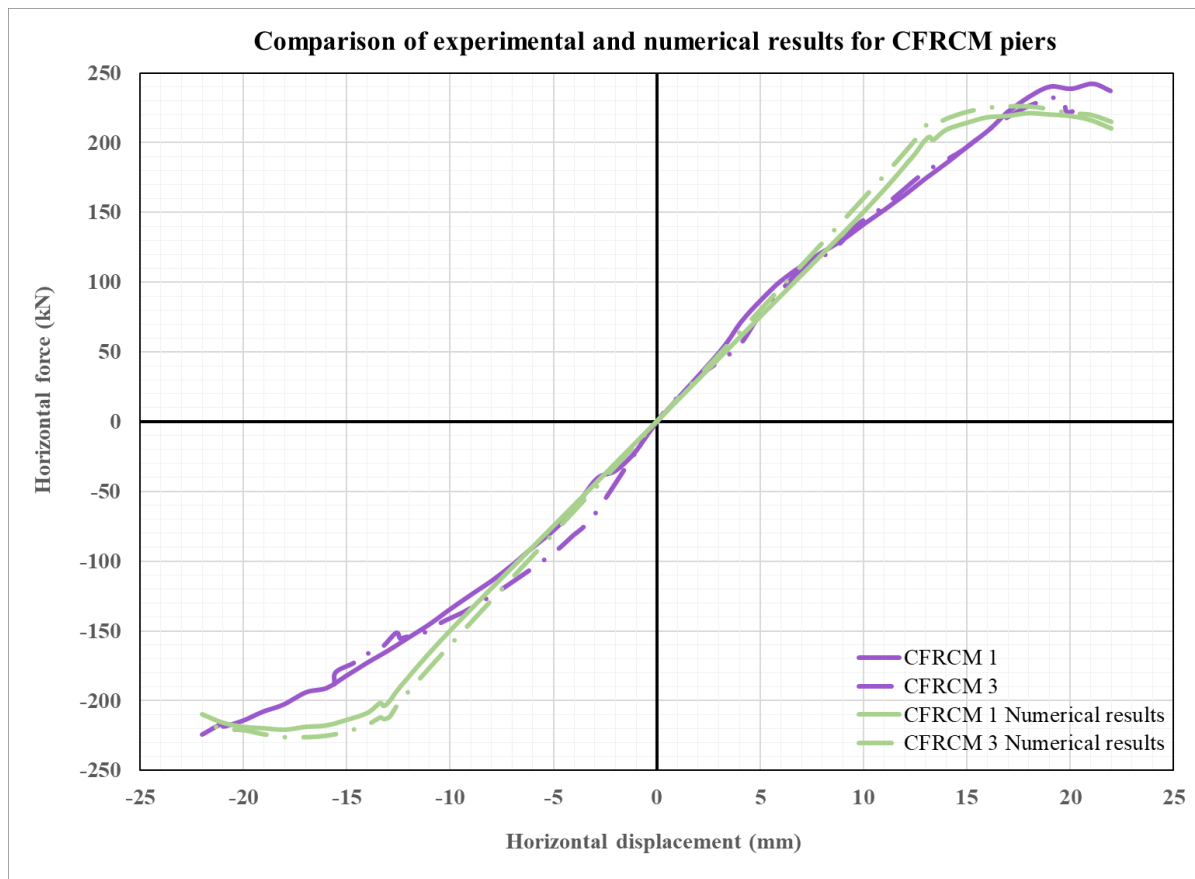


Figure 6.5 Comparison of envelope and pushover curves for CFRCM piers – experimental and numerical results

### 6.3 Research Hypothesis Verification

In the following chapter the increase of the ductility and shear load capacity of masonry piers will be analysed when innovative clamping details are used. At the end of chapter 1, two hypotheses were proposed, which will be accepted or rejected based on the results of the experimental testing and the numerical modelling campaign.

#### 6.3.1 Ductility

The ductility of masonry piers was analysed both in the experimental and numerical stage of this dissertation for all three series of masonry piers. It was observed and concluded that the ductility increased after the strengthening of masonry piers. Both FRCM and CFRCM piers showed a similar or higher ductility in the experimental campaign (subsection 4.4.4) and in the numerical modelling (subsection 5.5). What remained to be determined is whether the inclusion of clamping details affects the increase in ductility. The comparison involves examining the results from the FRCM and CFRCM series. In Table 6.5, the ductility of the FRCM and CFRCM series in both the experimental and numerical campaigns are illustrated. The values from the experimental campaign and the numerical modelling campaign represent

the mean values that were obtained. Meanwhile, the value from the numerical campaign remains consistent in both the negative and positive directions, so an absolute value is presented.

The differences in ductility are given as a numerical value ( $\Delta$ ) and a percentage value (%) in Table 6.5. In the experiment, the ductility in the positive direction is increased by 0,05 or 3,73 % when clamping details were added. On the other hand, in the negative direction the ductility increased by 0,29 or 25,22 %. Finally, in the numerical modelling campaign, CFRCM piers have a 0,20 or 13,89 % higher ductility than the FRCM piers. From these results it can be deduced that with the addition of clamping details an increase in ductility can be expected in regards to a typical single sided FRCM system. Unfortunately, due to the inadequacy of the results obtained from CFRCM 2 pier, this conclusion needs to be confirmed using a larger sample size.

With everything stated above, hypothesis **H<sub>1</sub>**: “Increase in ductility of the brick masonry pier strengthened with the novelty layout of the FRCM system with innovative clamping details is larger than the increase in ductility of the brick masonry pier strengthened with a standard single sided FRCM system.” **is accepted.**

Table 6.5 Comparison of the ductility of FRCM and CFRCM piers

| Value  | FRCM | CFRCM | $\Delta$ | %     |
|--|------|-------|----------|-------|
| <b>Ductility – positive direction (experimental)</b> | 1,34 | 1,39  | 0,05     | 3,73  |
| <b>Ductility – negative direction (experimental)</b> | 1,15 | 1,44  | 0,29     | 25,22 |
| <b>Ductility (numerical)</b>                         | 1,44 | 1,64  | 0,20     | 13,89 |

### 6.3.2 Shear load capacity

The shear load capacity of masonry piers was analysed both in the experimental and numerical stage of this dissertation for all three series of masonry piers. The shear load capacity was denominated as the maximum horizontal force of the pier achieved in the experimental and numerical campaign. It was observed and concluded that the shear load capacity increased after the strengthening of masonry piers. Both FRCM and CFRCM piers showed a higher maximum horizontal force in the experimental campaign (subsection 4.4.4) and in the numerical modelling campaign (subsection 5.5). What remained to be seen was did the clamping details have an influence on the increase of the shear load capacity. The results that need to be compared are the results from the FRCM and CFRCM series. In Table 6.6 the shear load

capacities of the FRCM and CFRCM series from the experimental and numerical campaign are demonstrated. The values from the experimental campaign and the numerical modelling campaign represent the mean values that were obtained. Meanwhile, the value from the numerical campaign remains consistent in both the negative and positive directions, so an absolute value is presented.

The differences in the shear load capacity are given as a numerical value ( $\Delta$ ) in kilonewtons and a percentage value (%) in Table 6.6. In the experiment, the maximum horizontal force in the positive direction was increased by 11,17 kN or 5,46 % when clamping details were added. On the other hand, in the negative direction the addition of clamping details did not result in an increase. The values were the same. Finally, in the numerical modelling campaign, CFRCM piers had a 13,50 kN or 6,43 % higher shear load capacity than the FRCM piers. From these results no apparent connection can be made between the addition of clamping details and the increase of the shear load capacity in regards to a typical single sided FRCM.

With everything stated above, hypothesis **H**<sub>2</sub>: “Increase in shear load capacity of the brick masonry pier strengthened with the novelty layout of the FRCM system with innovative clamping details is larger than the increase in shear load capacity of the brick masonry pier strengthened with a standard single sided FRCM system.” **is dismissed**.

Table 6.6 Comparison of the shear load capacities of FRCM and CFRCM piers

| Value  | FRCM   | CFRCM  | $\Delta$ [kN] | %    |
|--|--------|--------|---------------|------|
| <b>Maximum horizontal force – positive direction [kN] (experimental)</b> | 204,52 | 215,69 | 11,17         | 5,46 |
| <b>Maximum horizontal force – negative direction [kN] (experimental)</b> | 206,40 | 206,40 | 0,00          | 0,00 |
| <b>Maximum horizontal force [kN] (numerical)</b>                         | 210,00 | 223,50 | 13,50         | 6,43 |

## 7 CONCLUSION

The research conducted in this dissertation was focused on the improvement of the one-sided application of the FRCM system on masonry piers by introducing innovative clamping details on the sides of the pier. The primary idea was to increase the shear load capacity and ductility of masonry piers subjected to seismic activity. Three types of elements were examined: URM piers, masonry piers strengthened on one side with the FRCM coating (denominated as FRCM) and masonry piers strengthened on one side with the FRCM coating with additional clamping details on the sides (denominated as CFRCM). Through an extensive experimental and numerical modelling campaign, the behaviour of masonry piers was observed. A typical quasi-static cyclic displacement-controlled test was used for the experiment. The numerical model was developed in DIANA FEA software using the micro modelling approach.

After both the experimental and numerical modelling campaign were conducted, the most significant conclusions are drawn as follows:

- The use of FRCM reinforcement increases the shear load capacity and ductility of URM piers.
- The use of FRCM reinforcement leads to a typical corner-to-corner diagonal shear failure.
- Addition of clamping details in the single-sided FRCM strengthening of masonry piers results in an increase of the ductility.
- Addition of clamping details in the single-sided FRCM strengthening of masonry piers did not result in an increase of the shear load capacity.
- Addition of clamping details in the single-sided FRCM strengthening of masonry piers leads to a more stable behaviour of the strengthened masonry pier until failure.
- The numerical micro-modelling approach, although conservative, adequately represents the behaviour of unreinforced and reinforced masonry piers.

These conclusions indicate the potential of such a new and innovative method for strengthening of masonry piers but also highlight the need for further exploration of the field and the topic. Future research should be directed towards increasing the number of samples used in the experimental campaign and the adaptation of the system for practical use.

## 8 RECOMMENDATIONS FOR FUTURE RESEARCH

Based on the conducted theoretical evaluation, the knowledge obtained experimentally and numerically, the following recommendations are given for future research:

- Investigate whether increasing the number of samples in the experimental campaign would have an impact on the enhancement of the shear load capacity when FRCM clamping details are used.
- With a potential increase in shear load capacity when a larger number of samples are used, explore the viability of updating the current version of the CNR-DT 215/2018 standard dedicated to the contribution of the FRCM reinforcement to the shear load capacity by adding the effect of the clamping details.
- Upgrade the small-scale experimental campaign by examining the mechanical properties of the components of the FRCM system for the purposes of a more detailed theoretical evaluation.
- Analyse and compare other types of detailed numerical modelling to properly confirm the results obtained in the numerical modelling campaign.
- Research the modification of the number of transversal connectors used on the face and the sides of the masonry pier and the influence this modification has on the shear load capacity and ductility.
- Research the modification of the number of meshes applied on one side of the pier and the influence this modification has on the shear load capacity and ductility.
- Analyse and compare the use of different types of fibres used in the FRCM system and its influence on the shear load capacity and ductility.

In addition to the mentioned suggestions, it is possible to conduct various other research related to the shear load capacity and ductility of FRCM-reinforced masonry piers. It seems useful to explore the influence of the clamping details in piers subjected to flexure. In essence, such piers would potentially benefit from adding FRCM reinforcement along the cross end-sections where the tensile and compressive strength are spent. Another possibility that should be explored is the use of other types of masonry elements and/or mortar in masonry piers and the influence of clamping details on their shear load capacity and ductility. Finally, the influence of the clamping details should be observed in masonry piers with larger thicknesses since they are sometimes thicker than 60 cm in older URM buildings.

## LITERATURE

- [1] F. Yavartanoo, T.H.K. Kang, Retrofitting of unreinforced masonry structures and considerations for heritage-sensitive constructions, *J. Build. Eng.* 49 (2022) 103993. <https://doi.org/10.1016/j.job.2022.103993>.
- [2] G. Barbieri, L. Biolzi, M. Bocciarelli, L. Fregonese, A. Frigeri, Assessing the seismic vulnerability of a historical building, *Eng. Struct.* 57 (2013) 523–535. <https://doi.org/10.1016/j.engstruct.2013.09.045>.
- [3] A. Drougkas, L. Licciardello, J.G. Rots, R. Esposito, In-plane seismic behaviour of retrofitted masonry walls subjected to subsidence-induced damage, *Eng. Struct.* 223 (2020) 111192. <https://doi.org/10.1016/j.engstruct.2020.111192>.
- [4] M.R. Valluzzi, On the vulnerability of historical masonry structures: analysis and mitigation, *Mater. Struct. Constr.* 40 (2007) 723–743. <https://doi.org/10.1617/s11527-006-9188-7>.
- [5] M. Stepinac, P.B. Lourenço, J. Atalić, T. Kišiček, M. Uroš, M. Baniček, M. Šavor Novak, Damage classification of residential buildings in historical downtown after the ML5.5 earthquake in Zagreb, Croatia in 2020, *Int. J. Disaster Risk Reduct.* 56 (2021). <https://doi.org/10.1016/j.ijdr.2021.102140>.
- [6] M. Stepinac, T. Kišiček, T. Renić, I. Hafner, C. Bedon, Methods for the assessment of critical properties in existing masonry structures under seismic loads-the ARES project, *Appl. Sci.* 10 (2020). <https://doi.org/10.3390/app10051576>.
- [7] L. Lulić, K. Ožić, T. Kišiček, I. Hafner, M. Stepinac, Post-earthquake damage assessment-case study of the educational building after the zagreb earthquake, *Sustain.* 13 (2021). <https://doi.org/10.3390/su13116353>.
- [8] I. Hafner, D. Lazarević, T. Kišiček, M. Stepinac, Post-Earthquake Assessment of a Historical Masonry Building after the Zagreb Earthquake–Case Study, *Buildings.* 12 (2022). <https://doi.org/10.3390/buildings12030323>.
- [9] M. Tomažević, *Earthquake-Resistant Design of Masonry Buildings*, 1<sup>st</sup> edition, Imperial College Press, 57 Shelton Street, Covent Garden, London, United Kingdom (1999).
- [10] R. Marques, P.B. Lourenço, Structural behaviour and design rules of confined masonry walls: Review and proposals, *Constr. Build. Mater.* 217 (2019) 137–155. <https://doi.org/10.1016/j.conbuildmat.2019.04.266>.
- [11] Đurđica Matošević, V. Sigmund, I. Guljaš, Cyclic testing of single bay confined masonry walls with various connection details, *Bull. Earthq. Eng.* 13 (2015) 565–586.

- <https://doi.org/10.1007/s10518-014-9627-8>.
- [12] S. Brzev, *Earthquake-Resistant Confined Masonry Construction*, 1<sup>st</sup> edition, National Information Center of Earthquake Engineering, Indian Institute of Technology Kanpur, Kanpur, India (2007).
- [13] A. Gupta, V. Singhal, *Strengthening of Confined Masonry Structures for In-plane Loads: A Review*, *IOP Conf. Ser. Mater. Sci. Eng.* 936 (2020). <https://doi.org/10.1088/1757-899X/936/1/012031>.
- [14] M. ElGawady, P. Lestuzzi, M. Badoux, *Retrofitting of masonry walls using shotcrete*, *2006 NZSEE Conf.* (2006) 45–54.
- [15] C. D’Ambra, G.P. Lignola, A. Prota, *Simple method to evaluate FRCM strengthening effects on in-plane shear capacity of masonry walls*, *Constr. Build. Mater.* 268 (2021) 121125. <https://doi.org/10.1016/j.conbuildmat.2020.121125>.
- [16] M.M. Maraş, H.Ç. Kılınç, *Comparison on Repair and Strengthening Techniques for Unreinforced Masonry Structures*, *Int. J. Eng. Res. Appl.* 6 (2016) 1–5.
- [17] S.W. Chuang, Y. Zhuge, *Seismic Retrofitting of Unreinforced Masonry Buildings – A Literature Review*, *Aust. J. Struct. Eng.* 6 (2005) 25–36. <https://doi.org/10.1080/13287982.2005.11464942>.
- [18] S.A. Babatunde, *Review of strengthening techniques for masonry using fiber reinforced polymers*, *Compos. Struct.* 161 (2017) 246–255. <https://doi.org/10.1016/j.compstruct.2016.10.132>.
- [19] L.A.S. Kouris, T.C. Triantafillou, *State-of-the-art on strengthening of masonry structures with textile reinforced mortar (TRM)*, *Constr. Build. Mater.* 188 (2018) 1221–1233. <https://doi.org/10.1016/j.conbuildmat.2018.08.039>.
- [20] P. Zampieri, N. Simoncelo, C.D. Tetougueni, C. Pellegrino, *A review of methods for strengthening of masonry arches with composite materials*, *Eng. Struct.* 171 (2018) 154–169. <https://doi.org/10.1016/j.engstruct.2018.05.070>.
- [21] M.J. Simonič, V. Bosiljkov, S. Gostič, R. Žarnić, *Ispitivanje i analiza nosivosti na posmik zidova ojačanih s FRP-om*, *Gradjevinar.* 66 (2014) 533–548. <https://doi.org/10.14256/JCE.960.2013>.
- [22] A. Cascardi, R. Dell’Anna, F. Micelli, F. Lionetto, M.A. Aiello, A. Maffezzoli, *Reversible techniques for FRP-confinement of masonry columns*, *Constr. Build. Mater.* 225 (2019) 415–428. <https://doi.org/10.1016/j.conbuildmat.2019.07.124>.
- [23] N. Gattesco, C. Amadio, C. Bedon, *Experimental and numerical study on the shear behavior of stone masonry walls strengthened with GFRP reinforced mortar coating and*

- steel-cord reinforced repointing, *Eng. Struct.* 90 (2015) 143–157.  
<https://doi.org/10.1016/j.engstruct.2015.02.024>.
- [24] P. Triller, M. Tomažević, M. Lutman, M. Gams, Seismic Behavior of Strengthened URM Masonry - An Overview of Research at ZAG, *Procedia Eng.* 193 (2017) 66–73.  
<https://doi.org/10.1016/j.proeng.2017.06.187>.
- [25] L. Garcia-Ramonda, L. Pelá, P. Roca, G. Camata, In-plane shear behaviour by diagonal compression testing of brick masonry walls strengthened with basalt and steel textile reinforced mortars, *Constr. Build. Mater.* 240 (2020) 117905.  
<https://doi.org/10.1016/j.conbuildmat.2019.117905>.
- [26] H. Maljaee, B. Ghiassi, P.B. Lourenço, D. V. Oliveira, FRP-brick masonry bond degradation under hygrothermal conditions, *Compos. Struct.* 147 (2016) 143–154.  
<https://doi.org/10.1016/j.compstruct.2016.03.037>.
- [27] R. Ramirez, H. Maljaee, B. Ghiassi, P.B. Lourenço, D. V. Oliveira, Bond behavior degradation between FRP and masonry under aggressive environmental conditions, *Mech. Adv. Mater. Struct.* 26 (2019) 6–14.  
<https://doi.org/10.1080/15376494.2018.1534164>.
- [28] T. Kišiček, M. Stepinac, T. Renić, I. Hafner, L. Lulić, Strengthening of masonry walls with FRP or TRM, *Gradjevinar.* 72 (2020) 937–953.  
<https://doi.org/10.14256/JCE.2983.2020>.
- [29] L. De Lorenzis, N. Galati, L. Ombres, In-plane shear strengthening of natural masonry walls with NSM CFRP strips and FRCM overlay, (2005) 847–856.
- [30] R. Cucuzza, M. Domaneschi, G. Camata, G. Carlo, A. Formisano, D. Brigante, FRCM retrofitting techniques for masonry walls : a literature review and some laboratory tests, *Structural Integrity Procedia*, 00 (2022).
- [31] A. Incerti, F. Ferretti, C. Mazzotti, FRCM strengthening systems efficiency on the shear behavior of pre-damaged masonry panels: an experimental study, *J. Build. Pathol. Rehabil.* 4 (2019) 1–13. <https://doi.org/10.1007/s41024-019-0053-9>.
- [32] M. Angiolilli, A. Gregori, M. Pathirage, G. Cusatis, Fiber Reinforced Cementitious Matrix (FRCM) for strengthening historical stone masonry structures: Experiments and computations, *Eng. Struct.* 224 (2020) 111102.  
<https://doi.org/10.1016/j.engstruct.2020.111102>.
- [33] L. Estevan, F.J. Baeza, D. Bru, S. Ivorra, Stone masonry confinement with FRP and FRCM composites, *Constr. Build. Mater.* 237 (2020) 117612.  
<https://doi.org/10.1016/j.conbuildmat.2019.117612>.



- [34] F. Ferretti, A. Incerti, A.R. Tilocca, C. Mazzotti, In-Plane Shear Behavior of Stone Masonry Panels Strengthened through Grout Injection and Fiber Reinforced Cementitious Matrices, *Int. J. Archit. Herit.* 15 (2021) 1375–1394. <https://doi.org/10.1080/15583058.2019.1675803>.
- [35] E. Bertolesi, M. Buitrago, E. Giordano, P.A. Calderón, J.J. Moragues, F. Clementi, J.M. Adam, Effectiveness of textile reinforced mortar (TRM) materials in preventing seismic-induced damage in a U-shaped masonry structure submitted to pseudo-dynamic excitations, *Constr. Build. Mater.* 248 (2020) 118532. <https://doi.org/10.1016/j.conbuildmat.2020.118532>.
- [36] K. Toska, L. Hofer, F. Faleschini, M. Angelo, C. Pellegrino, Seismic behavior of damaged RC columns repaired with FRCM composites Section A-A Section A-A, *Eng. Struct.* 262 (2022) 114339. <https://doi.org/10.1016/j.engstruct.2022.114339>.
- [37] F.S. Murgo, C. Mazzotti, Masonry columns strengthened with FRCM system: Numerical and experimental evaluation, *Constr. Build. Mater.* 202 (2019) 208–222. <https://doi.org/10.1016/j.conbuildmat.2018.12.211>.
- [38] E. Grande, G. Milani, Modeling of FRCM strengthening systems externally applied on curved masonry substrates, *Eng. Struct.* 233 (2021) 111895. <https://doi.org/10.1016/j.engstruct.2021.111895>.
- [39] P. Zampieri, Horizontal capacity of single-span masonry bridges with intrados FRCM strengthening, *Compos. Struct.* 244 (2020) 112238. <https://doi.org/10.1016/j.compstruct.2020.112238>.
- [40] E. Garavaglia, M.R. Valluzzi, S. Perego, C. Tedeschi, Probabilistic damage evolution in masonry strengthened with FRCM subjected to aggressive environment, *Constr. Build. Mater.* 239 (2020) 117718. <https://doi.org/10.1016/j.conbuildmat.2019.117718>.
- [41] J. Donnini, Durability of glass FRCM systems: Effects of different environments on mechanical properties, *Compos. Part B Eng.* 174 (2019) 107047. <https://doi.org/10.1016/j.compositesb.2019.107047>.
- [42] E. Franzoni, M. Santandrea, C. Gentilini, A. Fregni, C. Carloni, The role of mortar matrix in the bond behavior and salt crystallization resistance of FRCM applied to masonry, *Constr. Build. Mater.* 209 (2019) 592–605. <https://doi.org/10.1016/j.conbuildmat.2019.03.059>.
- [43] I. Boem, Masonry Elements Strengthened with TRM: A Review of Experimental, Design and Numerical Methods, *Buildings.* 12 (2022). <https://doi.org/10.3390/buildings12091307>.

- [44] F. Ferretti, A. Incerti, B. Ferracuti, C. Mazzotti, FRCM strengthened masonry panels: The role of mechanical anchorages and symmetric layouts, *Key Eng. Mater.* (2017) 334–341. <https://doi.org/10.4028/www.scientific.net/KEM.747.334>.
- [45] N. Gattesco, E. Rizzi, I. Boem, A. Dudine, M. Gams, A new method of seismic strengthening stone masonry with CRM coatings on one side, *Constr. Build. Mater.* 407 (2023) 133565. <https://doi.org/10.1016/j.conbuildmat.2023.133565>.
- [46] F. Parisi, C. Menna, A. Prota, Fabric-reinforced cementitious matrix (FRCM) composites: Mechanical behavior and application to masonry walls, (2018). <https://doi.org/10.1016/B978-0-08-102293-1.00010-3>.
- [47] F.G. Carozzi, C. Poggi, Mechanical properties and debonding strength of Fabric Reinforced Cementitious Matrix (FRCM) systems for masonry strengthening, *Compos. Part B Eng.* 70 (2015) 215–230. <https://doi.org/10.1016/j.compositesb.2014.10.056>.
- [48] A. Bellini, M. Bovo, C. Mazzotti, Experimental and numerical evaluation of fiber-matrix interface behaviour of different FRCM systems, *Compos. Part B Eng.* 161 (2019) 411–426. <https://doi.org/10.1016/j.compositesb.2018.12.115>.
- [49] T. Celano, L.U. Argiento, F. Ceroni, C. Casapulla, Literature review of the in-plane behavior of masonry walls: Theoretical vs. experimental results, *Materials.* 14 (2021). <https://doi.org/10.3390/ma14113063>.
- [50] H. Pirsaeheb, M. Javad Moradi, G. Milani, A Multi-Pier MP procedure for the non-linear analysis of in-plane loaded masonry walls, *Eng. Struct.* 212 (2020) 110534. <https://doi.org/10.1016/j.engstruct.2020.110534>.
- [51] T. Celano, L.U. Argiento, F. Ceroni, C. Casapulla, In-plane behaviour of masonry walls: Numerical analysis and design formulations, *Materials.* 14 (2021). <https://doi.org/10.3390/ma14195780>.
- [52] F. da Porto, G. Guidi, E. Garbin, C. Modena, In-Plane Behavior of Clay Masonry Walls: Experimental Testing and Finite-Element Modeling, *J. Struct. Eng.* 136 (2010) 1379–1392. [https://doi.org/10.1061/\(asce\)st.1943-541x.0000236](https://doi.org/10.1061/(asce)st.1943-541x.0000236).
- [53] CNR DT 215/2018, Guide for the Design and Construction of Externally Bonded Fibre Reinforced Inorganic Matrix Systems for Strengthening Existing Structures, *ACI Comm.* 440. (2018) 144.
- [54] S. Casacci, C. Gentilini, A. Di Tommaso, D. V. Oliveira, Shear strengthening of masonry wallettes resorting to structural repointing and FRCM composites, *Constr. Build. Mater.* 206 (2019) 19–34. <https://doi.org/10.1016/j.conbuildmat.2019.02.044>.
- [55] G. Ramaglia, F. Fabbrocino, G.P. Lignola, A. Prota, Impact of FRP and FRCM on the

- ductility of strengthened masonry members, *Structures*. 28 (2020) 1229–1243. <https://doi.org/10.1016/j.istruc.2020.09.025>.
- [56] F. Ferretti, C. Mazzotti, FRM/SRG strengthened masonry in diagonal compression: experimental results and analytical approach proposal, *Constr. Build. Mater.* 283 (2021) 122766. <https://doi.org/10.1016/j.conbuildmat.2021.122766>.
- [57] E. Grande, G. Milani, M. Imbimbo, Theoretical model for the study of the tensile behavior of FRM reinforcements, *Constr. Build. Mater.* 236 (2020) 117617. <https://doi.org/10.1016/j.conbuildmat.2019.117617>.
- [58] F. Ceroni, P. Salzano, Design provisions for FRM systems bonded to concrete and masonry elements, *Compos. Part B Eng.* 143 (2018) 230–242. <https://doi.org/10.1016/j.compositesb.2018.01.033>.
- [59] F.G. Carozzi, A. Bellini, T. D’Antino, G. de Felice, F. Focacci, Ł. Hojdys, L. Laghi, E. Lanoye, F. Micelli, M. Panizza, C. Poggi, Experimental investigation of tensile and bond properties of Carbon-FRM composites for strengthening masonry elements, *Compos. Part B Eng.* 128 (2017) 100–119. <https://doi.org/10.1016/j.compositesb.2017.06.018>.
- [60] F.G. Carozzi, G. Milani, C. Poggi, Mechanical properties and numerical modeling of Fabric Reinforced Cementitious Matrix (FRM) systems for strengthening of masonry structures, *Compos. Struct.* 107 (2014) 711–725. <https://doi.org/10.1016/j.compstruct.2013.08.026>.
- [61] P.E. Mezrea, M. Ispir, I.A. Balci, I.E. Bal, A. Ilki, Diagonal tensile tests on historical brick masonry wallets strengthened with fabric reinforced cementitious mortar, *Structures*. 33 (2021) 935–946. <https://doi.org/10.1016/j.istruc.2021.04.076>.
- [62] A. Mandor, A. El Refai, Assessment and modeling of the debonding failure of fabric-reinforced cementitious matrix (FRM) systems, *Compos. Struct.* 275 (2021) 114394. <https://doi.org/10.1016/j.compstruct.2021.114394>.
- [63] E. Grande, G. Milani, Numerical simulation of the tensile behavior of FRM strengthening systems, *Compos. Part B Eng.* 189 (2020) 107886. <https://doi.org/10.1016/j.compositesb.2020.107886>.
- [64] P. Colombi, T. D’Antino, Analytical assessment of the stress-transfer mechanism in FRM composites, *Compos. Struct.* 220 (2019) 961–970. <https://doi.org/10.1016/j.compstruct.2019.03.074>.
- [65] A. Bellini, S.K. Shahreza, C. Mazzotti, Cyclic bond behavior of FRM composites applied on masonry substrate, *Compos. Part B Eng.* 169 (2019) 189–199. <https://doi.org/10.1016/j.compositesb.2019.04.009>.

- [66] P. Triller, M. Tomažević, M. Gams, Seismic strengthening of clay block masonry buildings with composites: an experimental study of a full scale three-storey building model, *Bulletin of Earthquake Engineering*. 17 (2019). <https://doi.org/10.1007/s10518-019-00609-0>.
- [67] A. Cascardi, M. Leone, M.A. Aiello, Transversal joining of multi-leaf masonry through different types of connector: Experimental and theoretical investigation, *Constr. Build. Mater.* 265 (2020) 120733. <https://doi.org/10.1016/j.conbuildmat.2020.120733>.
- [68] A. Cascardi, M. Leone, M.A. Aiello, Shear behavior of multi leafs masonry panels with transversal connections, *Key Eng. Mater.* 817 (2019) 359–364. <https://doi.org/10.4028/www.scientific.net/KEM.817.359>.
- [69] J. Donnini, G. Maracchini, S. Lenci, V. Corinaldesi, E. Quagliarini, TRM reinforced tuff and fired clay brick masonry: Experimental and analytical investigation on their in-plane and out-of-plane behavior, *Constr. Build. Mater.* 272 (2021) 121643. <https://doi.org/10.1016/j.conbuildmat.2020.121643>.
- [70] A. Incerti, F. Ferretti, A.R. Tilocca, C. Mazzotti, Influence of Masonry Texture on the Shear Strength of FRCM Reinforced Panels: An Interdisciplinary Approach, *RILEM: Structural Analysis of Historical Constructions*. (2019). <https://doi.org/10.1007/978-3-319-99441-3>.
- [71] M. Guadagnuolo, G. Faella, G. Frunzio, L. Massaro, D. Brigante, The capacity of GFRP anchors in concrete and masonry structures, *Structural Integrity Procedia*. 00 (2022).
- [72] N. Gattesco, E. Rizzi, I. Boem, L. Facconi, F. Minelli, A. Dudine, M. Gams, Full-scale cyclic tests on a stone masonry building to investigate the effectiveness of a one-side application of the composite reinforced mortar system, *Eng. Struct.* 296 (2023) 116967. <https://doi.org/10.1016/j.engstruct.2023.116967>.
- [73] M. Gams, M. Tomažević, T. Berset, Seismic strengthening of brick masonry by composite coatings: an experimental study, *Bull. Earthq. Eng.* 15 (2017) 4269–4298. <https://doi.org/10.1007/s10518-017-0136-4>.
- [74] J. Donnini, G. Chiappini, G. Lancioni, V. Corinaldesi, Tensile behaviour of glass FRCM systems with fabrics' overlap: Experimental results and numerical modeling, *Compos. Struct.* 212 (2019) 398–411. <https://doi.org/10.1016/j.compstruct.2019.01.053>.
- [75] S. Babaeidarabad, A. Nanni, In-plane behavior of unreinforced masonry walls strengthened with fabric-reinforced cementitious matrix (FRCM), *Am. Concr. Institute, ACI Spec. Publ.* 2015-Janua (2015) 69–80. <https://doi.org/10.14359/51688019>.
- [76] M. Giaretton, D. Dizhur, E. Garbin, J.M. Ingham, F. da Porto, In-Plane Strengthening of

- Clay Brick and Block Masonry Walls Using Textile-Reinforced Mortar, *J. Compos. Constr.* 22 (2018) 04018028. [https://doi.org/10.1061/\(asce\)cc.1943-5614.0000866](https://doi.org/10.1061/(asce)cc.1943-5614.0000866).
- [77] A. Bellini, A. Incerti, M. Bovo, C. Mazzotti, Effectiveness of FRCM Reinforcement Applied to Masonry Walls Subject to Axial Force and Out-Of-Plane Loads Evaluated by Experimental and Numerical Studies, *Int. J. Archit. Herit.* 12 (2018) 376–394. <https://doi.org/10.1080/15583058.2017.1323246>.
- [78] C. D’Ambra, G.P. Lignola, A. Prota, E. Sacco, F. Fabbrocino, Experimental performance of FRCM retrofit on out-of-plane behaviour of clay brick walls, *Compos. Part B Eng.* 148 (2018) 198–206. <https://doi.org/10.1016/j.compositesb.2018.04.062>.
- [79] J. Scacco, B. Ghiassi, G. Milani, P.B. Lourenço, A fast modeling approach for numerical analysis of unreinforced and FRCM reinforced masonry walls under out-of-plane loading, *Compos. Part B Eng.* 180 (2020) 107553. <https://doi.org/10.1016/j.compositesb.2019.107553>.
- [80] G. Maddaloni, M. Di Ludovico, A. Balsamo, G. Maddaloni, A. Prota, Dynamic assessment of innovative retrofit techniques for masonry buildings, *Compos. Part B Eng.* 147 (2018) 147–161. <https://doi.org/10.1016/j.compositesb.2018.04.038>.
- [81] Đ. Peulić, *Konstruktivni elementi zgrada*, 1<sup>st</sup> edition, Croatiaknjiga, Ilica 42, Zagreb, Croatia (2002).
- [82] EN 1992-1-1:2004, Eurocode 2: Design of concrete structures - Part 1-1: General rules and rules for buildings (2004).
- [83] HRN 1130-3:2008, Steel for the reinforcement of concrete -- Weldable reinforcing steel -- Part 2: Technical delivery conditions for class B (2008).
- [84] Z. Sorić, T. Kišiček, *Betonske konstrukcije 1*, 1<sup>st</sup> edition, Sveučilište u Zagrebu, Građevinski fakultet, Fra Andrije Kačića-Miošića 26, Zagreb, Croatia (2014).
- [85] EN 1996-1-1:2005, Eurocode 6: Design of masonry structures - Part 1-1: General rules for reinforced and unreinforced masonry structures (2005).
- [86] T. Renić, I. Hafner, T. Kišiček, Ductility of hybrid FRP – steel reinforced concrete sections, *Proc. 2nd Int. Conf. CoMS 2020/21*, Ljubljana, Slovenija, (2021) 118–126.
- [87] CEN/TC 250/SC 8, Final Document EN1998-3:2018 NEN SC8 PT3, Working Draft (2018).
- [88] HRN EN 998-2:2016, Specification for mortar for masonry -- Part 2: Masonry mortar (2016).
- [89] F. Net, Rete termosaldada in fibra di vetro - 300, Available online: <https://fibrenet.it/wp-content/uploads/FB-10-STC-022-IT-01-FB-VAR320R12-1.pdf>.

- [90] Rofix SismaDur FRCM, Available online: <https://www.rofix.hr/proizvod/rofix-sismadur-slim-tankoslojni-mort-za-konsolidiranje-na-bazi-nhl-a#downloads>.
- [91] F. Net, FB-TUP10-VAR1A, GFRP bars with bow - diameter 10 mm. Available online: <https://fibrenet.it/en/product/grfp-bar-with-one-sided-fraying-high-toughness-fb-tup10-var1a/>.
- [92] HRN EN 1996-1-1:2012, Eurocode 6: Design of masonry structures -- Part 1-1: General rules for reinforced and unreinforced masonry structures (EN 1996-1-1:2005+A1:2012).
- [93] HRN EN 1052-3:2004, Methods of test for masonry -- Part 3: Determination of initial shear strength (EN 1052-3:2002).
- [94] A. Jäger, M. Gams, Practical design of masonry subjected to horizontal loads based on Eurocode 6 shear model, Brick Block Mason. Trends, Innov. Challenges - Proc. 16th Int. Brick Block Mason. Conf. IBMAC, Padua, Italy, (2016) 689–694. <https://doi.org/10.1201/b21889-86>.
- [95] HRN EN 12390-1:2012, Testing hardened concrete -- Part 1: Shape, dimensions and other requirements for specimens and moulds (EN 12390-1:2012).
- [96] HRN EN 12390-3:2019, Testing hardened concrete -- Part 3: Compressive strength of test specimens (EN 12390-3:2019).
- [97] HRN EN 206:2021, Concrete -- Specification, performance, production and conformity (EN 206:2013+A2:2021).
- [98] HRN EN 771-1:2015, Specification for masonry units -- Part 1: Clay masonry units (EN 771-1:2011+A1:2015).
- [99] HRN EN 772-1:2015, Methods of test for masonry units -- Part 1: Determination of compressive strength (EN 772-1:2011+A1:2015).
- [100] HRN EN 772-16:2011, Methods of test for masonry units -- Part 16: Determination of dimensions (EN 772-16:2011).
- [101] HRN EN 1015-2:2000/A1:2008, Methods of test for mortar for masonry -- Part 2: Bulk sampling of mortars and preparation of test mortars (EN 1015-2:1998/A1:2006).
- [102] HRN EN 1015-11:2019, Methods of test for mortar for masonry -- Part 11: Determination of flexural and compressive strength of hardened mortar (EN 1015-11:2019).
- [103] A. Aşıkoğlu, G. Vasconcelos, P.B. Lourenço, B. Pantò, Pushover analysis of unreinforced irregular masonry buildings: Lessons from different modeling approaches, Eng. Struct. 218 (2020). <https://doi.org/10.1016/j.engstruct.2020.110830>.
- [104] F.S. Murgo, F. Ferretti, C. Mazzotti, A discrete-cracking numerical model for the in-

- plane behavior of FRCM strengthened masonry panels, *Bulletin of Earthquake Engineering*. (2021). <https://doi.org/10.1007/s10518-021-01129-6>.
- [105] G.P. Lignola, A. Bilotta, F. Ceroni, Assessment of the effect of FRCM materials on the behaviour of masonry walls by means of FE models, *Eng. Struct.* 184 (2019) 145–157. <https://doi.org/10.1016/j.engstruct.2019.01.035>.
- [106] E. Ricci, D. V. Oliveira, E. Sacco, B. Ghiassi, Modelling of masonry arches strengthened at extrados with FRCM, *Proc. Int. Mason. Conf.*, Milan, Italy, (2018) 2150–2162.
- [107] A.M. D’Altri, V. Sarhosis, G. Milani, J. Rots, S. Cattari, S. Lagomarsino, E. Sacco, A. Tralli, G. Castellazzi, S. de Miranda, A review of numerical models for masonry structures, Elsevier Ltd, Amsterdam, Netherlands, (2019). <https://doi.org/10.1016/B978-0-08-102439-3.00001-4>.
- [108] A.W. Page, Finite Element Model for Masonry, *J. Struct. Div.* 106 (1980) 935–935. <https://doi.org/10.1061/jsdeag.0005406>.
- [109] H.R. Lotfi, P.B. Shing, Interface model applied to fracture of masonry structures, *J. Struct. Eng.* 120 (1994) 63–80.
- [110] P.B. Lourenço, J.G. Rots, Multisurface Interface Model for Analysis of Masonry Structures, *J. Eng. Mech.* 123 (1997) 660–668. [https://doi.org/10.1061/\(asce\)0733-9399\(1997\)123:7\(660\)](https://doi.org/10.1061/(asce)0733-9399(1997)123:7(660)).
- [111] D. V. Oliveira, P.B. Lourenço, Implementation and validation of a constitutive model for the cyclic behaviour of interface elements, *Comput. Struct.* 82 (2004) 1451–1461. <https://doi.org/10.1016/j.compstruc.2004.03.041>.
- [112] J.P. Plassiard, M. Eymard, I. Alachek, O. Plé, Pushover tests on unreinforced masonry wallettes retrofitted with an innovative coating: Experimental study and finite element modelling, *Materials*. 14 (2021). <https://doi.org/10.3390/ma14226815>.
- [113] F. Nerilli, S. Marfia, E. Sacco, Nonlocal damage and interface modeling approach for the micro-scale analysis of FRCM, *Comput. Struct.* 254 (2021) 106582. <https://doi.org/10.1016/j.compstruc.2021.106582>.
- [114] J.G. Rots, Numerical simulation of cracking in structural masonry, *Heron*. 36 (1991).
- [115] M. Betti, L. Galano, A. Vignoli, Comparative analysis on the seismic behaviour of unreinforced masonry buildings with flexible diaphragms, *Eng. Struct.* 61 (2014) 195–208. <https://doi.org/10.1016/j.engstruct.2013.12.038>.
- [116] E. Bertolesi, G. Milani, C. Poggi, Simple holonomic homogenization model for the non-linear static analysis of in-plane loaded masonry walls strengthened with FRCM composites, *Compos. Struct.* 158 (2016) 291–307.

- <https://doi.org/10.1016/j.compstruct.2016.09.027>.
- [117] J. Rots, *Structural Masonry: An Experimental/Numerical Basis for Practical Design Rules*, A.A. Balkema, Rotterdam, Netherlands, (1997).
- [118] B. Ghiassi, G. Milani, *Numerical modeling of masonry and historical structures*, Elsevier Ltd, Amsterdam, Netherlands, (2019).
- [119] F. Aras, G. Altay, Investigation of mechanical properties of masonry in historic buildings, *Građevinar*. 5 (2015) 461–469. <https://doi.org/10.14256/jce.1145.2014>.
- [120] C. D'Ambra, G.P. Lignola, A. Prota, F. Fabbrocino, E. Sacco, FRCM strengthening of clay brick walls for out of plane loads, *Compos. Part B Eng.* 174 (2019) 107050. <https://doi.org/10.1016/j.compositesb.2019.107050>.
- [121] L.M. Heffler, *Variability of Unit Flexural Bond Strength and its Effect on Strength in Clay Brick Unreinforced Masonry Walls subjected to Vertical Bending*, Master Thesis. Faculty of Engineering and Build Environment, University of Newcastle, (2009).
- [122] R.B. Petersen, *In-plane Shear Behaviour of Unreinforced Masonry Panels Strengthened with Fibre Reinforced Polymer Strips*, PhD. Thesis., The University of Newcastle, Australia (2009).
- [123] *FIB Model Code:2010 Volume 2*, 1st ed., International Federation for Structural Concrete, Lausanne, (2012).



## CURRICULUM VITAE

Ivan Hafner was born on June 26<sup>th</sup>, 1993 in Zagreb, Croatia. He graduated from Jordanovac Elementary School in 2008 and enrolled in XV. Gymnasium which he finished in 2012. In the same year, he enrolled in the undergraduate level at the Faculty of Civil Engineering, University of Zagreb. He completed his undergraduate studies in 2015 obtaining a bachelor's degree in civil engineering. After that, he continued his education at the Faculty of Civil Engineering, University of Zagreb by enrolling into the graduate/master level specializing in structural engineering. In 2017 he obtained his master's degree in the field of structural engineering and successfully defended his master thesis entitled "Comparative analysis of different outrigger structural system variants in a high-rise building".

Starting in October of 2017, he was employed as an investor representative in charge of cost estimation and financial analysis of project participants' offers at VMD d.o.o where he supervised on-site activities on a high-profile residential project.

Since February of 2019, he is employed as a research and teaching assistant at the Chair of Concrete and Masonry Structures, Department of Structures, Faculty of Civil Engineering, University of Zagreb. He is enrolled in the teaching, research, and professional activities at the department. As a lecturer, he is involved in multiple courses at the undergraduate and graduate level. He was a part of numerous scientific research project which resulted in conference and journal papers. In his scientific work, he published 24 research papers and attended 17 conferences and 11 international workshops and training schools. In two instances, he was a part of an employee exchange programme in 2021 and 2022 visiting Delft University of Technology.

He is enrolled in the postgraduate doctoral programme at the Faculty of Civil Engineering, University of Zagreb since October of 2019. His research proposal titled "Improving the seismic response of masonry piers with single sided FRCM coating using innovative clamping details" was approved in February of 2023. The approval was given by the committee which included his mentor prof. Tomislav Kišiček, asst. prof. Matija Gams and asst. prof. Mislav Stepinac.

## LIST OF PUBLISHED WORKS BY THE AUTHOR

### 1) Journal papers – Scientific and Review Papers

**Kišiček, Tomislav; Renić, Tvrtko; Lazarević, Damir; Hafner, Ivan**

Compressive Shear Strength of Reinforced Concrete Walls at High Ductility Levels. // Sustainability, 12 (2020), 11; 4434, 16 doi:10.3390/su12114434 (international peer review, article, scientific)

**Stepinac, Mislav; Kišiček, Tomislav; Renić, Tvrtko; Hafner, Ivan; Bedon, Chiara**

Methods for the Assessment of Critical Properties in Existing Masonry Structures under Seismic Loads — The ARES Project. // Applied Sciences-Basel, 10 (2020), 5; 1576, 15 doi:10.3390/app10051576 (international peer review, article, scientific)

**Kišiček, Tomislav; Stepinac, Mislav; Renić, Tvrtko; Hafner, Ivan; Lulić, Luka**

Strengthening of masonry walls with FRP or TRM. // Građevinar : Journal of the Croatian Association of Civil Engineers 72 (2020), 10; 937-953 doi:10.14256/JCE.2983.2020 (international peer review, review paper, scientific)

**Hafner, Ivan; Vlašić, Anđelko; Kišiček, Tomislav; Renić, Tvrtko**

Parametric Analysis of the Shear Lag Effect in Tube Structural Systems of Tall Buildings. // Applied Sciences-Basel, 11 (2020), 1; 278, 16 doi:10.3390/app11010278 (international peer review, article, scientific)

**Lulić, Luka; Ožić, Karlo; Kišiček, Tomislav; Hafner, Ivan; Stepinac, Mislav**

Post-Earthquake Damage Assessment—Case Study of the Educational Building after the Zagreb Earthquake. // Sustainability, 13 (2021), 11; 6353, 25 doi: 10.3390/su13116353 (international peer review, article, scientific)

**Hafner, Ivan; Lazarević, Damir; Kišiček, Tomislav; Stepinac, Mislav**

Post-earthquake assessment of a historical masonry building after the Zagreb earthquake – Case study. // Buildings, 12 (2022), 3; 323, 25 doi: 10.3390/buildings12030323 (international peer review, article, scientific)

**Kišiček, Tomislav; Renić, Tvrtko; Hafner, Ivan; Stepinac, Mislav**

Simplified Rules for Serviceability Control of FRPRC Elements. // Polymers, 14 (2022), 2513 doi: 10.3390/polym14122513 (international peer review, article, scientific)

**Hafner, Ivan; Kišiček, Tomislav; Gams, Matija**

Review of Methods for Seismic Strengthening of Masonry Piers and Walls. // Buildings, 13 (2023), 1 doi: 10.3390/buildings13061524 (international peer review, review paper, scientific)

## **2) Papers in Conference Proceedings – Scientific Papers in Conference Proceedings**

### **Hafner, Ivan; Vlašić, Anđelko; Skokandić, Dominik**

Usporedna analiza različitih varijanti primjene outrigger sustava na primjeru visoke zgrade. // Proceedings of the CoNstruction 17 / Popara, Mladen ; Milošević, Olivera ; Borojević, Svetlana (ed.).

Novi Sad: University of Novi Sad, 2017. p. 49-59. (presentation, international peer review, full paper (in extenso), scientific)

### **Renić, Tvrtko; Hafner, Ivan; Kišiček, Tomislav**

Ductility of hybrid FRP – steel reinforced concrete sections. // Proceedings of the 2nd International Conference CoMS 2020/21 / Šajna, Aljoša ; Legat, Andraž ; Jordan, Sabina ; Horvat, Petra ; Kemperle, Ema ; Dolenc, Sabina ; Ljubešek, Metka ; Michelizza, Matej (ed.). Ljubljana: Slovenian National Building and Civil Engineering Institute, 2021. p. 118-126. (<https://www.bib.irb.hr/1126998>) (presentation, international peer review, full paper (in extenso), scientific)

### **Hafner, Ivan; Renić, Tvrtko; Koščak, Janko; Kišiček, Tomislav; Stepinac, Mislav**

Assessment of Existing Masonry Structures (The ARES project). // Proceedings of the 2021 session of the 13th fib International PhD Symposium in Civil Engineering / Gatuingt, Fabrice ; Torrenti, Jean-Michel (ed.). Pariz, 2021. p. 211-217. (<https://www.bib.irb.hr/1139903>) (presentation, international peer review, full paper (in extenso), scientific)

### **Kišiček, Tomislav; Renić, Tvrtko; Hafner, Ivan; Stepinac, Mislav**

Maximum FRP Bar Diameter and Bar Spacing for Crack Control in Flexural Reinforced Concrete Members. // 10th International Conference on FRP Composites in Civil Engineering, Proceedings of CICE 2020/2021 / Ilki, Alper ; Ispir, Medine ; Inci, Pinar (ed.). Cham, Switzerland: Springer Nature Switzerland AG, 2021. p. 621-631 doi:10.1007/978-3-030-88166-5\_53 (presentation, international peer review, full paper (in extenso), scientific)

### **Hafner, Ivan; Kišiček, Tomislav; Renić, Tvrtko; Ožić Karlo**

An insight into The Masonry Quality Index (MQI) method for the visual assessment of existing masonry structures. // Proceedings of the 1st Croatian Conference on Earthquake Engineering - 1CroCEE / Lakušić, Stjepan ; Atalić, Josip (ed.).

Zagreb: University of Zagreb, Faculty of Civil Engineering, 2021. p. 643-653

doi:10.5592/CO/1CroCEE.2021.188 (presentation, international peer review, full paper (in extenso), scientific)

**Lulić, Luka; Renić, Tvrtko; Škofić, Michele; Hafner, Ivan; Kišiček, Tomislav; Stepinac, Mislav**

Damage assessment after the Zagreb earthquake – the case study of the educational building.

// Proceedings of the 1st Croatian Conference on Earthquake Engineering - 1CroCEE /

Lakušić, Stjepan ; Atalić, Josip (ed.).

Zagreb: University of Zagreb, Faculty of Civil Engineering, 2021. p. 655-660

doi:10.5592/CO/1CroCEE.2021.197 (presentation, international peer review, full paper (in extenso), scientific)

**Kišiček, Tomislav; Stepinac, Mislav; Renić, Tvrtko; Hafner, Ivan; Lulić, Luka**

Calculation of masonry in-plane shear strengthening. // Proceedings of the 1st Croatian Conference on Earthquake Engineering - 1CroCEE / Lakušić, Stjepan ; Atalić, Josip (ed.).

Zagreb: University of Zagreb, Faculty of Civil Engineering, 2021. p. 797-807

doi:10.5592/CO/1CroCEE.2021.209 (presentation, international peer review, full paper (in extenso), scientific)

**Hafner, Ivan; Renić, Tvrtko; Kišiček, Tomislav; Stepinac, Mislav**

Seismic strengthening of stone masonry structures – state of the art. // Proceedings of the 2nd International Conference CoMS 2020/21 / Šajna, Aljoša ; Legat, Andraž ; Jordan, Sabina ; Horvat, Petra ; Kemperle, Ema ; Dolenc, Sabina ; Ljubešek, Metka ; Michelizza, Matej (ed.). Ljubljana: Slovenian National Building and Civil Engineering Institute, 2020. p. 124-132.

(<https://www.bib.irb.hr/1112050>) (presentation, international peer review, full paper (in extenso), scientific)

**Hafner, Ivan; Kišiček, Tomislav**

Procjena stanja postojećih zidanih konstrukcija: Pregled metoda. // 9th Symposium on Doctoral Studies in Civil Engineering, Conference proceedings / Lakušić, Stjepan (ed.).

Zagreb: University of Zagreb, Faculty of Civil Engineering, 2020. p. 21-32 doi:

10.5592/CO/PhDSym.2020.02 (presentation, international peer review, full paper (in extenso), scientific)

**Lulić, Luka; Stepinac, Mislav; Damjanović, Domagoj; Duvnjak, Ivan; Bartolac, Marko; Hafner, Ivan**

The role of flat-jack testing after recent earthquakes. // Proceedings of the 3rd European Conference on Earthquake Engineering & Seismology / Arion, Cristian ; Scupin, Alexandra ; Tigianescu, Alexandru (ed.).

Bukurešt: Conspress, 2022. p. 289-296 (presentation, international peer review, full paper (in extenso), scientific)

**Kišiček, Tomislav; Renić, Tvrtko; Hafner, Ivan; Lulić, Luka**

The Influence of Shear Crack Angle on FRP Wall Strengthening. // Proceedings of fib Symposium 2023: Building for the Future: Durable, Sustainable, Resilient / Ilki, Alper ; Çavunt, Derya ; Çavunt, Yavuz Selim (ed.).

Istanbul, 2023. p. 1059-1069 doi: 10.1007/978-3-031-32511-3\_108 (presentation, international peer review, full paper (in extenso), scientific)

**Hafner, Ivan; Kišiček, Tomislav; Gams, Matija**

Improving the Seismic Response of Masonry Piers with Single-Sided FRCM Coating Using Clamping Details – Numerical Modelling. // Proceedings of 13th International Conference on Structural Analysis of Historical Constructions (SAHC2023) / Endo, Yohei ; Hanazato, Toshikazu (ed.).

Kyoto, 2023. p. 1189-1201 doi: 10.1007/978-3-031-39603-8\_96 (presentation, international peer review, full paper (in extenso), scientific)

**3) Conference Abstracts – Short Communications in Proceedings and Journals****Stepinac, Mislav; Kišiček, Tomislav; Renić, Tvrtko; Hafner, Ivan; Lulić, Luka; Ožić, Karlo**

The role of assessment in the proper rehabilitation of existing structures. // Proceedings of the 1st Croatian Conference on Earthquake Engineering - 1CroCEE / Lakušić, Stjepan ; Atalić, Josip (ed.).

Zagreb: University of Zagreb, Faculty of Civil Engineering, 2021. p. 639-642  
doi:10.5592/CO/1CroCEE.2021.187 (presentation, international peer review, short communication, scientific)

**4) Extended Abstracts in Proceedings and Journals****Renić, Tvrtko; Stepinac, Mislav; Kišiček, Tomislav; Hafner, Ivan**

Assessment and Rehabilitation of Existing Structures. // ISDEE Proceedings  
Tirana, Albanija, 2020. p. 1-2 (presentation, international peer review, extended abstract, scientific)

**Renić, Tvrtko; Stepinac, Mislav; Kišiček, Tomislav; Hafner, Ivan**

Seismic Strengthening of Masonry Structures. // ISDEE Proceedings  
Tirana, Albanija, 2020. p. 1-2 (presentation, international peer review, extended abstract, scientific)